

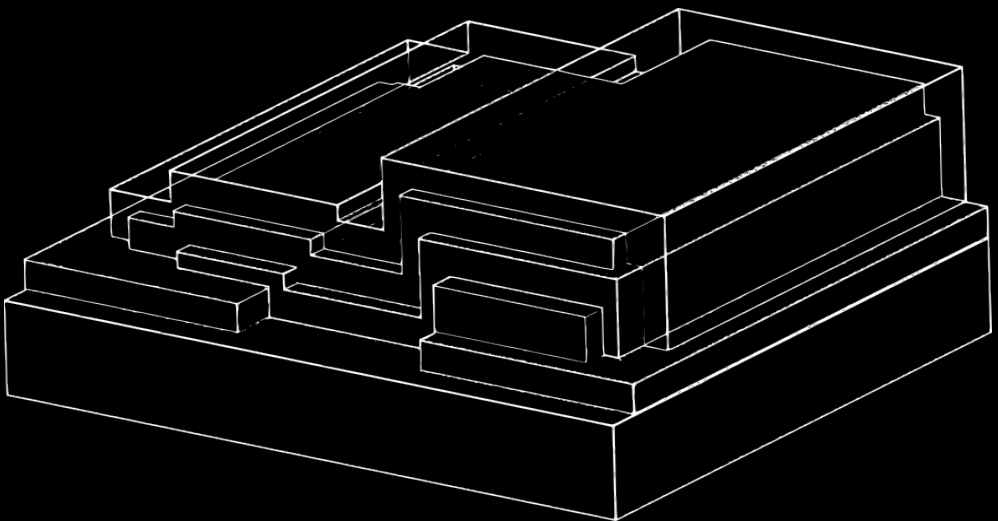
eman ta zabal zazu



Universidad del País Vasco Euskal Herriko Unibertsitatea

Growth and characterization of an all solid-state high voltage Li-ion thin film battery

Iñaki Madinabeitia Terrones



Doctoral Thesis

2021

PhD Thesis

Growth and characterization of an all solid-state high voltage Li-ion thin film battery

A dissertation submitted to the University of the Basque Country in partial fulfillments of the requirements for the degree of Doctor in Philosophy

Author:

Iñaki Madinabeitia Terrones

Supervisors:

Dr. Miguel Ángel Muñoz Márquez

Dr. Fco. José Fernández Carretero

Tutor:

Prof. Dr. Fco. Javier Zúñiga Lagares

November 2021

Gurasuentzat

*“Never let the fear of
striking out keep you
from playing the game”*

-Babe Ruth-

Acknowledgements

When I graduated, I didn't have in mind doing a thesis, in fact, I had completely ruled it out. The thought of planning your life for four years makes anyone shudder. However, as the years went by, I began to miss the research, the uncovering of the hidden... the science. And suddenly I was in an interview with Miguel Ángel and Alberto, a new experience was about to begin.

Sometimes, people ask you, are you sure you want to do a PhD? Actually, you are never quite sure, you always have that nagging feeling in your head. But as someone once said, *no risk, no gain*. I've always found that phrase a bit exaggerated, but no one refutes that it gives you the extra motivation we often need. And here I am... writing the last part of my thesis. Looking back and remembering all that I have experienced in the last few years. It has been a period full of results worthy of celebration, but also of some scientific frustration. Even so, would not trade it for the world. It has been an experience I want to remember, as well as all those who have lent me a hand both scientifically and emotionally.

Mi más sincero agradecimiento a Miguel Ángel, Fran y Alberto, por darme esta oportunidad y apoyarme durante todos estos años. Giorgio e Iñigo, que haría yo sin vosotros... Grazie mille/eskerrik asko por todos los consejos e hipótesis planteadas en esta tesis. Mila esker Jokin eta Ane irakatsitako guztiagatik, tesi honen parte zarete. A vosotr@s también, Begoña, Elena, Maider y Antonio, y en general al grupo de investigación, por el tiempo que me habéis dedicado. Thanks to you too Hamideh, the stay was full of complications due to the pandemic but very fruitful. Rosalia y Coca, muchas gracias por ayudarme a interpretar los resultados indescifrables del XPS, os estoy muy agradecido. Ezin ahaztu teknikari zein administrazio kideak diren guztiak, haiek gabe ezin izango baitzen burututakoa burutu, eskerrik asko Maria J., Maria E., Fran, Yan, eta aipatu gabe utzi ditudan guztioi.

Los procesos de sputtering no son fáciles de controlar, en este sentido me gustaría agradecer a mis compañeros y amigos Santi e Iñigo por su paciencia y el buen humor transmitido durante el festival de muestras que hemos tenido. Eskerrik asko zuri ere Anastasia, ez galdu irribarrea. Quiero agradecer en general a todo el grupo de superficies por su disposición en el transcurso de esta tesis. Y como no, agradezco también a mis compañeros de grupo. Inés, Patxi, Yolanda y todos los que me habéis acompañado en esta aventura, eskerrik asko. Pero la tesis no ha sido solo trabajar, mila-mila esker kafe orduak alaitu dizkidazuen guztioi... muxu potolo bana.

Lan orduetatik kanpo eduki dudan babesari ere esker berezi bat eman nahiko nioke. Kuadrillia... zer egingo nuke zuek gabe. Pisukide izan nituen Eñaut ta Oierrekin bizi izandako abenturetatik hasi eta Elkororekin izandako domeka ilunkeretako berriketetara. Ezin aipatu gabe utzi Elgetakin jandako pitxopoteko menu berezia, baita Andu eta Jorgerekin egindako bizikleta buelta luzeak ere. Edo Maite eta Naiakin ordu txikitararte egondako gau luzeak. Edota Borraxitok sukaldaturiko bazkari bereziak. Eutsi goiari Borrax! Ekintza soilak dirudite, baina norbera indarrez betetzeko gai dira. Ahaztu gabe, eskerrik asko *Pipar bete* taldeko kide zareten guztioi, besarkada handi bat.

Etxekoei zer esanik ez... Beraiek gabe ez litzateke hau guztia posible izango. Ezer zorretan eskatu gabe txiki-txikitatik guztia eman didatelako, eskerrik asko Aitta ta Ama. Zuentzat da tesi hau. Ta hermanita, eskerrik asko emandako gomendio eta laguntza guztiagatik, *gràcies a tu també Ferran*, no perdis mai el teu somriure.

Eta azkenik, nire bizitzan agertu den pertsona espezial horri... Tesi honetan zehar bidelagun izan dudan horri... Burugogor zein maitagarria den horri... Egoera txarrei buelta eman eta irribarre bat ateratzeko gai izan dan horri... Bihotz-bihotzez eskerrik asko Maitte. Tesi honen parte zara.

Guztioi...

...MILA-MILA ESKER...

...zuek gabe ez zen posible izango.

This work has received the financial support from European H2020 project MONBASA (Monolithic Batteries for Spaceship Applications, Grant No. 687561) and Basque Government through Elkartek 2017 program with the project Elkartek CIce2017 (KK-2017/00066).

Abstract

All solid-state Li-ion batteries are attracting increasing attention as the next generation of advanced electric energy storage systems. They promise to overcome some of the most important challenges related to conventional liquid electrolyte-based batteries namely, reduced electrochemical stability window, toxicity and Li dendrite formation that can ultimately become a fire hazard. These directly impact on energy density, environmental friendliness, and safety. Solid electrolytes typically offer wide electrochemical stability windows, paving the way to integrate high voltage cathodes and permitting the fabrication of higher energy density batteries. In addition, all solid-state configurations also allow downscaling the whole battery to micrometric thin-film components, envisioning the fabrication of compact microbatteries for low power energy supply. In this thesis, a $\text{LiNi}_{0.5}\text{Mn}_{1.5}\text{O}_4$ (LNMO)/lithium phosphorus oxynitride (LiPON)/lithium all-solid-state high voltage rechargeable Li-ion thin-film battery has been successfully developed. Throughout the thesis, each part of the battery has been studied separately before assembling the complete pack.

A cobalt-free spinel LNMO was selected as cathode material. It is one of the most promising and environmentally-friendly cathodes, with high specific theoretical capacity ($146.6 \text{ mAh}\cdot\text{g}^{-1}$) and high operating voltage (4.7 V vs Li/Li^+), as well as acceptable electronic and Li-ion conductivities. Here, LNMO thin film cathodes have been deposited by means of industrially scalable alternating current (AC) magnetron sputtering on functional and cost-effective stainless-steel current collectors. The effect of the post-deposition annealing and film thickness on the electrochemical performance is discussed, correlating the observed structural and morphological evolution with the final electrochemical response. Moreover, the effect of iron diffusion from the current collector substrate into the cathode film is analyzed. The addition of interfacial passivation layers (including CrN) between the current collector and the electrode is proposed to prevent Fe diffusion, with a direct positive influence on the electrochemical behavior.

Concerning the solid electrolyte, State-of-the-Art LiPON was selected. In the past few decades, various solid oxide electrolytes with some special structures and relatively high Li^+ conductivity have been studied. Nevertheless, despite a significant progress in the development of new materials, nowadays the most used electrolyte material in thin-film form is still LiPON. Its electrical and chemical stability, high electronic resistivity ($>10^{14} \Omega\cdot\text{cm}$), and large electrochemical window of $0\text{-}5.5 \text{ V vs Li/Li}^+$ have been key aspects for its selection, being able to use it in combination with many different electrode materials. Here, LiPON is prepared by reactive radiofrequency (RF) magnetron sputtering deposition from a Li_3PO_4 target, at room temperature and using nitrogen as a reactive sputter gas.

First, the determination of the optimum nitrogen flow rate for the optimal LiPON layer was carried out, based on the resulting ionic conductivity measured by means of electrochemical impedance spectroscopy. Additionally, the obtained films were characterized morphologically by scanning electron microscopy, structurally by X-ray diffraction, and elementally by X-ray photoelectron spectroscopy. The maximum conductivity was reached with an N₂-saturated background pressure, reaching $2.48 \cdot 10^{-6} \text{ S} \cdot \text{cm}^{-1}$.

Anode wise, the use of Li metal as a negative electrode is living an intense upturn lately, to profit from its high theoretical specific capacity ($3860 \text{ mAh} \cdot \text{g}^{-1}$), the lowest negative electrochemical potential (-3.040 V vs SHE), and low density ($0.59 \text{ g} \cdot \text{cm}^{-3}$). In this case, Li metal thin films (thickness approx. $1 \mu\text{m}$) were prepared by thermal evaporation. The morphological and compositional characterization of the anode has been carried out by scanning electron microscopy and X-ray induced photoelectron spectroscopy. The functionality of the evaporated lithium as an anode was demonstrated, optimizing its deposition on the LiPON solid electrolyte.

Finally, a LNMO/LiPON/evaporated Li thin-film battery was fabricated. To validate the successful implementation of the different thin film battery components, a comparison of the electrochemical performance at different C-rates of the microbattery using evaporated lithium as well as lithium foil (commonly employed) was done. Importantly, it was found that in the absence of the liquid electrolyte, the evaporated lithium is able to improve the interfacial contact and thus its electrochemical performance. All in all, this thesis proves the successful fabrication of a functional and cost-effective microbattery, for its implementation as power source in future portable devices operating in the low power regime.

Resumen

Las baterías de iones de litio de estado sólido están generando un creciente interés como la próxima generación de sistemas avanzados de almacenamiento de energía eléctrica. Prometen superar algunos de los retos más significativos relacionados con las baterías convencionales basadas en electrolitos líquidos, como son una ventana de estabilidad electroquímica reducida, alta toxicidad y el crecimiento de dendritas de litio que, en última instancia, pueden ocasionar problemas de seguridad por sobrecalentamiento y fuego. Esto repercute directamente en la densidad energética, el respeto al medio ambiente y la seguridad. Los electrolitos sólidos ofrecen amplias ventanas de estabilidad electroquímica, que facilitan la integración de cátodos de alto voltaje, permitiendo la fabricación de baterías con mayor densidad energética. Además, al tratarse de una configuración de estado sólido es viable la reducción de escala de la batería hasta espesores micrométricos, posibilitando la fabricación de microbaterías compactas orientadas al suministro de energía de baja potencia. En este trabajo se ha investigado con éxito en el desarrollo de una batería Li-ion recargable de capa delgada de estado sólido y alto voltaje, compuesta por $\text{LiNi}_{0.5}\text{Mn}_{1.5}\text{O}_4$ (LNMO)/oxinitruro de fósforo de litio (LiPON)/litio metálico. Cada uno de estos componentes ha sido desarrollado y caracterizado específicamente y se ha completado su integración en una microbatería de capa delgada.

El material catódico seleccionado es la espinela libre de cobalto LNMO. Además de ser respetuoso con el medio ambiente, actualmente es uno de los cátodos de baterías de Li-ion más prometedores debido a su elevada capacidad teórica específica ($146.6 \text{ mAh}\cdot\text{g}^{-1}$) y su alto voltaje operativo (4.7 V vs Li/Li^+), así como a su aceptable conductividad electrónica e iónica. A lo largo de esta tesis, se han desarrollado capas finas funcionales de LNMO sobre colectores de corriente restables de acero inoxidable mediante la técnica de pulverización catódica de corriente alterna (AC). Se ha estudiado el efecto del tratamiento térmico posterior a la deposición y el espesor de la capa en su rendimiento electroquímico, correlacionándolo directamente con su evolución estructural y morfológica. Además, se ha analizado específicamente el efecto de la interdifusión en la interfase colector de corriente/cátodo debido al tratamiento térmico, proponiéndose la aplicación de capas protectoras (entre otras CrN) para su prevención y la mejora del comportamiento electroquímico del cátodo.

En cuanto al electrolito sólido, se ha seleccionado el LiPON. En las últimas décadas, se ha investigado sobre electrolitos sólidos con diferentes composiciones, consiguiendo conductividades iónicas relativamente altas. Sin embargo, a pesar de estos avances, el material electrolítico más utilizado en forma de capa fina sigue siendo el LiPON. Entre los aspectos claves de su

selección destacan su estabilidad eléctrica y química, su alta resistividad electrónica ($>10^{14} \Omega \cdot \text{cm}$) y su gran ventana electroquímica de 0 a 5.5 V vs Li/Li⁺, posibilitando así, su utilización en combinación con diferentes electrodos. Esta capa delgada se ha preparado mediante la tecnología de pulverización catódica reactiva radiofrecuencia (RF) partiendo de un blanco de Li₃PO₄. La deposición se ha llevado a cabo a temperatura ambiente y utilizando nitrógeno como gas reactivo. En primer lugar, se han determinado las condiciones de deposición óptimas para maximizar la conductividad iónica del LiPON depositado. Por otra parte, las capas obtenidas se han caracterizado morfológicamente por microscopía electrónica de barrido, estructuralmente por difracción de rayos X y elementalmente por espectroscopia de fotoelectrones de rayos X. La máxima conductividad iónica obtenida ha sido de $2.48 \cdot 10^{-6} \text{ S} \cdot \text{cm}^{-1}$, correspondiente al proceso realizado utilizando solo N₂ como gas de deposición.

Con relación al ánodo, se ha utilizado el litio metálico, en línea con los últimos desarrollos en la tecnología de baterías Li-ion, debido a su alta capacidad específica teórica ($3860 \text{ mAh} \cdot \text{g}^{-1}$), menor potencial electroquímico negativo conocido (-3.040 V vs SHE), y baja densidad ($0.59 \text{ g} \cdot \text{cm}^{-3}$). Se han preparado capas finas de litio (espesor aproximado de $1 \mu\text{m}$) por evaporación térmica en vacío. La caracterización morfológica y composicional del material se ha llevado a cabo mediante microscopía electrónica de barrido y espectroscopia de fotoelectrones inducidos por rayos X. La funcionalidad del litio evaporado como ánodo ha sido demostrada, optimizando su deposición sobre el electrolito LiPON.

Por último, se ha desarrollado y ensamblado una batería de capa fina compuesta por LNMO/LiPON/Litio metálico. Esta microbatería ha sido ensayada en descarga a diferentes ratios C y ha demostrado su mejora frente al uso de ánodos de lámina de litio (solución comúnmente empleada). Se ha demostrado el aumento en el rendimiento electroquímico de la batería debido a la mejora en el contacto interfacial electrolito-ánodo cuando se utiliza litio evaporado como ánodo. En definitiva, esta tesis demuestra la viabilidad técnica de la fabricación de una microbatería funcional para su implementación como fuente de energía en futuros dispositivos autónomos que operen en el régimen de baja potencia.

Laburpen luzea

1991.urtean ezagutzera eman zenetik etengabe doa gorantz litio-ioi baterien eskaera. Gaur egun, bateria horiek hainbat gailu elektronikoren energia iturri moduan erabiltzen dira; horien artean, mugikorak, ordenagailu eramangarriak edota ibilgailu elektrikoak aurki daitezke. Teknologia hobetuz doan heinean, energia kontsumoa ere gorantz doa. Premia honi aurre egiteko, merkatuan aurki daitezkeenak baino energia dentsitate handiagoa duten baterien garapena beharrezkoa da. Hori dela eta, bateriaren osagai desberdinen (anodo, katodo eta elektrolitoa) ezaugarri elektrokimikoak hobetu ditzaketen material berriak identifikatu eta ikertu behar dira.

Hala ere, likido egoerako elektrolitoek tentsio altuan (4-5 V vs Li/Li⁺) duten egonkortasun urriak mugatzen du litio-ioi baterien teknologia konbentzionala. Horrez gain, erabiltzen diren disolbatzaileak oso sukoiak dira (thermal runaway mekanismoa); zirkuitulabur, gainkarga edo berotze kasuetan segurtasuna murriztuz. Hori dela eta, tentsio altuko katodoen merkaturatze eta eskala handiko produktiorako konponbide interesgarriena egoera solidoko bateriak dira. Ohiko litio-ioi bateriek ez bezala, aipaturiko bateria horietan elektrolito likidoa egoera solidoko elektrolito batengatik ordezkutzen da. Horrela, segurtasun eta egonkortasun hobea bermatzen da; era berean, ahalmena biderkatu, karga denbora murriztu eta balio-bizitza luzatzen delarik. Egoera solidoko baterien barruan geruza meheko bateriak aurki daitezke (mikrobateria moduan ezagunak), mikrometro azpiko lodiera duten elektrodo eta elektrolitoengatik bereziak. Geruza meheko bateria horiek geruzaz geruza substratu baten gainean osatzen dira.

Elektrodo positiboari dagokionez, LiCoO₂ moduko oxido laminarrak, Li_xMn₂O₄ espinelak, LiMPO₄ (M = Fe, Mn edo Co) erako fosfatoak eta banadio oxidoak gehien ikertzen diren materialak dira. Horien artean, LiNi_{0.5}Mn_{1.5}O₄ (LNMO) tentsio altuko espinela da erakargarriena; merkea, ez toxikoa eta energia dentsitate altua daukalako. Bere ezaugarrien artean 4.75 V vs Li/Li⁺-eko lan tentsioa eta 146.6 mAh·g⁻¹-ko biltegitratze ahalmena aurkitu ditzakegu. Elektrolito solidoari dagokionez, esan beharra dago azken hamarkadetan egitura bereziak eta eroankortasun ioniko nahiko handiak dituzten zenbait material aztertu direla. Material berrien garapenean aurrerapen handiak egin diren arren, gaur egun, geruza mehe moduan gehien erabiltzen den material elektrolitikoa LiPON-a da. Lan honetan aukeratu izanaren arrazoiaren artean haren egonkortasun elektrikoa eta kimikoa, erresistibitate elektronikoa handia (10¹⁴ Ω·cm⁻¹) eta leiho elektrokimikoa handia (0-5.5 V vs Li/Li⁺) daude. Material anodikorakoan aldiz, litio metalikoaren aldeko apustua egin da, azken bolada honetan gorakada handia ari baita izaten. Horren arrazoiak bere ahalmen espezifikoa teorikoa handia (3860

mAh·g⁻¹), potentzial elektrokimiko negatibo ezagun txikiena (-3.040 V vs SHE) eta dentsitate txikia (0.59 g·cm⁻³) dira.

Egun, geruza meheak egiteko gehien erabiltzen diren teknikak hutsune ganberan oinarritzen dira. Horien artean, entzunenak laser-ablazioa (PLD, pulsed laser deposition), lurrinketa termikoa eta ihintadura-katodikoa (magnetron sputtering) dira. Ikerketa honetan azken teknika hori erabiliko da, lorturiko estaldurak akats gutxikoak, konposizio egokidunak eta uniformeak direlako. Ihintadura-katodikoaren prozesuan elektroik kolisio bitartez sorturiko argoi ioiak lortu nahi den geruzaren material iturria kolpatzen dute. Talka horren ondorioz bertatik partikulak ateratzen dira, ganbera guztia zeharkatu eta substratuan ezartzen direlarik.

Mikrobaterietan teknika honen erabilerak baterien diseinu eta arkitektura berriei atea ireki die, bateria flexible eta tamaina txikikoak lortzea ahalbidetuz. Gaur egun txartel inteligentetan, irrati-maiztasun identifikazio etiketetan, gailu elektroniko txikietan eta gauzen Interneta delakoaren kontzeptuan (IoT, Internet Of Things) aurki daitezke.

Lan honetan, LNMO/LiPON/litio lurrunduaz osaturiko geruza mehe eta goitentsioko bateria bat garatu da. Karakterizazio hobea burutzeko asmoz, bateria bere osotasunean ikertu aurretik, osagai bakoitzaren ezaugarri fisiko-kimiko, morfologiko eta elektrokimikoak ikertuko dira.

LNMO film meheak maiztasun ertaineko korrante alternodun ihintadura-katodiko duala erabiliz altzairu herdoilgaitzeko substratuen gainean ezarri dira. Prozesua giro-temperaturan burutu denez, lorturiko laginak amorfoak eta elektrokimikoki ez-aktiboak dira. Hori dela eta, LNMO geruzaren espinela desordenatu kristalizazio fasea lortzeko beharrezkoa izan da 600 °C-ko deposizio-osteko suberaketa egitea. Berotze tenperatura hori gainditzeak geruzaren fase-osotasunaren okertzea dakar. Elektrolito likido komertzial erabiliz, geruza optimoarekin eginiko errendimendu elektrokimikoaren probak bat datoz literaturan aurki daitezkeen beste ihintadura-katodikoez lorturiko LNMO filmenekin. Hala ere, film meheko elektrodo optimizatu horien ziklo-errendimendua askoz ere hobea da katodo arruntenekin alderatuz. Horrek LNMO material elektroaktiboaren potentzial handia nabarmentzen du, izan ere, elektrodoen formulazioan ez dago ez gehigarri ezta aglutinatzaile eroalerik ere. Ondorioz, lan honetan MF-AC ihintadura-katodikoa proposatzen da film meheko baterien osagaien ekoizpen industrialerako hautagai gisa.

Zoritxarrez, eginiko tratamendu termikoaren ondorioz altzairu herdoilgaitzeko substratutik LNMO film mehera Fe elementuaren difusioa aurkitu da, Fe₂O₃ bigarren mailako fasea eratuz. Honela, 1 μm bitarteko lodierako laginetan lehen

kargan *plateau* itzulezin bat agertzen da. Honek bereziki geruza mehei eragiten die, non *plateau*-a askoz iraupen luzeagokoa den. Gainera, film lodietan ere nahi ez den bigarren mailako fasea agertu izanak aplikatu daitekeen lodiera praktiko handiena mugatzen du, batez ere, C altuetan. Fe-aren barne difusioarekin zerikusia duten arazoak konpontzeko asmotan, Au, CrN, TiN eta Al difusio-hesi estaldurak ikertu dira. Horien artean, arrakastatsuen Tecnalian sintetizaturiko CrN geruza izan da, lehenengo zikloko *plateau*-aren desagertzea ekarriz. Horrez gain, C altuetan biltegitatzeko ahalmen handiagoa ere lortu du. Emaiza horiek LNMO film meheko katodoen erabilera bermatzen dute mikrobateria funtzional gisa, honi errentagarritasuna ere gehituz altzairu herdoilgaitz substratuak erabiliz.

Laginean eginiko hobekuntzen artean, aipatu beharrekoa da katodoaren gainean ezarritako estaldura babeslea. Honek LNMO-aren gainazalak eta elektrolito likidoaren arteko albo-erreakzioak minimizatzeke balio du. Al_2O_3 geruza nanometriko bat nahikoa da katodoaren azaleko erreakzio itzulezin nagusiak murriztu eta eraginkortasun Coulombikoa hobetzeko. Bizi-itxaropen luzeagoa lortu den arren, geruza mehe honek laginaren litio-ioien biltegitatze ahalmen espezifikoa murriztea ere ekarri du.

Elektrolito solidoa RF ihintadura-katodiko bidez fabrikatu da, Ar eta N_2 gasen ehuneko desberdinak erabiliz. Lorturiko laginek egitura leuna eta oso trinkoa erakutsi dute, kristalizazio-seinurik gabea. LiPON film mehen izaera amorfoa XRD difraktogramaren bidez berretsi da. Filmen eroankortasun ionikoa bi zunden bitartezko EIS metodoa erabiliz neurtu da. Giro-tenperaturaren eginiko neurketen emaitzak ez da nahikoa izan geruzen eroankortasun ionikoa lortzeko. Arrheniusen ekuazioa erabiliz giro-tenperaturako eroankortasun ionikoa kalkulatzeko posible da, horretarako $100\text{ }^\circ\text{C}$ eta $250\text{ }^\circ\text{C}$ arteko tenperaturetako eroankortasun ionikoak kalkulatu behar dira. Tenperatura igo ahala, eroankortasun ionikoa ere handituz doa. Gainera, eginiko prozesu guztien artean N_2 gasarekin eginikoak lortu du emaitz hobereena. Prozesu horrek, giro-tenperaturaren $2.48 \cdot 10^{-6}\text{ S}\cdot\text{cm}^{-1}$ -eko eroankortasun ionikoa lortu du, zein, literaturarekin bat datorren. Aktibazio-energiaren joera aldiz, alderantzizkoa izan da: 0.585 eV -tik 0.530 eV -ra jaitsi delarik N_2 -ren ehuneko igo ahala. Hau da, geroz eta N_2 gehiago izan, orduan eta onuragarriagoa da LiPON sistema elektrolitikoan N kantitate optimoa sartzeko. XPS bitartez laginen konposizioa hobeto uler daiteke. Esan bezala, laginen arteko desberdintasun nagusiak N 1s espektroan ikusi dira. Ar bakarrik erabili den prozesuko laginek ez dute eskualde horretan seinalerik ematen, aldiz, Ar- N_2 eta N_2 prozesuetako laginetan seinale zabala antzematen da; non, Nd eta Nt kontribuzioak bereizten diren. Emaitz horiek bat datoz proposaturiko ordezkapen-eredu teorikoekin, nitrogenoa eraginkortasunez sartzeko deli LiPON sarean iradokiz.

Anodoari dagokionez, altzairu herdoilgaitzeko substratuen gainean $1\ \mu\text{m}$ lodierako litio geruza ezarri da lurruntze termiko bitartez. Film horiek egitura granulatu eta dentsoa dute, substratutik induzituriko zimurtasuna erakutsiz. XPS teknika erabiliz gainazalaren azterketa elementala burutu da, lurrundutako litioaren errektibotasun handia dela eta, oxido eta karbonato-espezieak (Li_2CO_3 eta $\text{Li}_2\text{O}/\text{Li}_2\text{O}_2$) agertu dira. Poluitzaile horiek litioak O_2 -arekin, CO_2 -arekin eta H_2O -arekin erreakzionatzean sortu dira, airearekin kontaktuan egon gabe. Anodoaren karakterizazio elektrokimikoa elektrolito komertzial likidoarekin (LP30) eta aurrez eginiko LNMO katodoak erabiliz egin da. Lehendabiziko C/20 ziklotan, litio xaflen adinako biltegitratze ahalmena erakutsi du, hots, $113.94\ \text{mAh}\cdot\text{g}^{-1}$. Honek esan nahi du C balio baxuetan LNMO-an zeharreko litio-ioi mugimenduak ez duela anodoaren menpekotasunik. Zoritxarrez, lurrundutako litioaren karga txikia dela eta, eginiko bateriak ziklo bizona urria erakutsi du. Hala ere, litiozko geruza meheko anodoen funtzionaltasunaren froga garbia izan da.

Azkenik, aurrez aztertutako geruza mehe optimoak hartu eta tentsio altuko eta egoera solidoko mikrobateria eratu da. Osagai bakoitza leundutako altzairu herdoilgaitzeko substratu batetik hasita modu sekuentzian ezarri da, kasu bakoitzean dagokion maskara erabiliz.

Geruza meheko bateriaren arrakasta balioztatzeko, egoera berean osaturiko litio-xafladun bateriekin konparatu da. Litio-xaflak elektrolito solidoari itsaspen urria duela ikusi denez, elektrolito likidozko tanta bat gehitu beharra izan da. Horrela, kontaktua eta propietate elektrokimikoak hobetu dira. Lurrundutako litioa, aldiz, elektrolito solidoaren zimurtasunera egoki moldatu da, osagai likidoa gehitzeko beharra izan gabe. Lorturiko biltegitratze ahalmen handiak mikrobateria funtzional eta errentagarri baten fabrikazioaren arrakasta erakusten du, potentzia baxuko erregimenean lan egiten duten etorkizuneko gailu eramangarrietan energia-iturri gisa inplementatzeko.

CONTENTS

Chapter 1

Introduction

1.1. Global energy scenario	1
1.2. Li-ion battery	3
1.2.1. Basics of Li-ion batteries	4
1.2.2. All solid-state batteries	6
1.3 All solid-state thin film batteries	7
1.3.1. Main component materials	9
<i>Positive electrode materials</i>	9
<i>Negative electrode materials</i>	12
<i>Inorganic solid-state electrolyte materials</i>	14
1.3.2. Laboratory scale thin film batteries.....	17
1.3.3. Commercial thin film batteries.....	19
1.4. Scope of the thesis	21
References.....	23

Chapter 2

Experimental techniques

2.1. Thin film deposition.....	31
2.1.1. Thin film nucleation and growth	32
2.1.2. Magnetron sputtering.....	35
<i>Power sources</i>	38
<i>Equipment used in this work</i>	41
2.1.3. Thermal evaporation.....	42
<i>Equipment used in this work</i>	43

2.2. Thickness, roughness, and weight characterization	44
2.2.1. Contact profilometry.....	44
<i>Roughness analysis</i>	45
2.2.2. Ellipsometry	45
2.3. Structural, morphological, and elemental characterization	46
2.3.1. X-ray diffraction	46
2.3.2. Raman spectroscopy.....	48
2.3.3. Electronic microscopy	50
<i>Scanning electron microscopy</i>	51
<i>Transmission electron microscopy</i>	53
<i>Electron energy loss spectroscopy</i>	55
2.3.4. X-ray photoelectron spectroscopy	55
2.4. Electrochemical characterization	58
2.4.1. Electrochemical cells.....	58
2.4.2. Cyclic voltammetry.....	60
2.4.3. Galvanostatic cycling.....	61
2.4.4. Electrochemical impedance spectroscopy.....	63
<i>In-plane ionic conductivity of the solid electrolyte</i>	66
References.....	69

Chapter 3

Synthesis and characterization of $\text{LiNi}_{0.5}\text{Mn}_{1.5}\text{O}_4$ (LNMO) thin film cathode

3.1. Introduction.....	73
3.2. Main objectives of the chapter.....	75
3.3. Experimental set-up and deposition optimization	75
3.4. Characterization of as-deposited sample	79
3.5. Effect of the post-deposition thermal treatment.....	82
3.5.1. Structural characterization.....	82
3.5.2. Surface morphology.....	87

3.5.3. Electrochemical performance	89
<i>Cycling voltammetry</i>	89
<i>Rate performance</i>	91
<i>Electrochemical Impedance Spectroscopy</i>	94
3.6. Effect of the post-deposition annealing time	99
3.6.1. Surface morphology and structural characterization.....	99
3.6.2. Electrochemical characterization	100
3.6.3. In-depth elemental distribution analysis.....	102
3.7. Effect of the thin film thickness	103
3.7.1. Surface morphology and structural characterization.....	104
3.7.2. Electrochemical characterization	108
3.7.3. Fe interdiffusion from the stainless steel substrate	112
3.8. Comparison with commercial cathode.....	116
3.9. Conclusions.....	119
References.....	121

Chapter 4

Improvement of $\text{LiNi}_{0.5}\text{Mn}_{1.5}\text{O}_4$ (LNMO) thin film cathode

4.1. Introduction.....	125
4.2. Main objectives of the chapter.....	126
4.3. Current collector/cathode interface: coating of the stainless steel substrate	126
4.3.1. Experimental set-up of CrN coating	129
4.3.2. Structural characterization.....	130
4.3.3. Surface morphology and compositional analysis	133
4.3.4. Electrochemical characterization	136
4.3.5. CrN layer in-depth study	140
4.4. Cathode/liquid electrolyte interface: cathode protection coating. 142	
4.4.1. Experimental set-up of Al_2O_3 coating and initial tests.....	142
4.4.2. Surface morphology and structural characterization.....	144

4.4.3. Electrochemical characterization of different Al ₂ O ₃ thickness.....	146
4.5. Conclusions.....	148
References.....	150

Chapter 5

Synthesis and characterization of LiPON thin film solid electrolyte

5.1. Introduction.....	153
5.2. Main objectives of the chapter.....	153
5.3. Experimental set-up and initial deposition tests	154
5.4. Characterization of LiPON films.....	157
5.4.1. Surface morphology.....	157
5.4.2. Structural characterization.....	159
5.4.3. Ionic conductivity	160
5.4.4. Analysis of the surface composition.....	164
5.5. Conclusions.....	169
References.....	171

Chapter 6

All solid-state high voltage thin film battery

6.1. Introduction.....	173
6.2. Main objectives of the chapter.....	174
6.3. Lithium anode.....	174
6.3.1 Characterization of the evaporated lithium anode	175
<i>Morphological and compositional characterization</i>	175
<i>Electrochemical characterization</i>	177
6.4. Sequential deposition of ASSB components.....	178
6.5. Initial tests of the all solid-state thin film battery.....	181
6.6. Interface effect study of the all solid-state thin film battery.....	183
6.6.1. CrN passivation layer in the current collector/cathode interface ..	189

6.7. Conclusions..... 194
References..... 196

Chapter 7

General conclusions and perspectives

7.1. General conclusions 199
7.2. Perspectives..... 202

Appendix

A.1. List of abbreviations 205
A.2. List of contributions 209
 A.2.1. Conferences..... 209
 A.2.2. Publications..... 209

Chapter 1

Introduction

1.1. Global energy scenario

Global energy demand continues growing, driven by increasing prosperity and living standards in the emerging world. The United Nations (UN) Human Development Index (HDI) suggests that the increase in energy consumption up to around 100 Gigajoules (GJ) per head are associated with substantial improvement in human well-being and development.^[1] Nonetheless, significant inequalities in energy consumption and access to energy persist. Nowadays, about 80% of the world's population today live in countries where the average energy consumption is still less than 100 GJ per head. According to BP energy outlook report (data from 2019),^[1] in order to promote social equality and to reduce the percentage of the population below 100 GJ to a one-third by 2040, the world would require an increase of about 25% in energy production, which is equivalent to China's total energy consumption in 2017.

Inevitably, this increase will bring severe consequences, unless the current energy scenario transits towards green, non-polluting alternatives. The World Resources Institute (WRI) estimates that total greenhouse gases equaled 49.4 billion tons CO₂ emissions in 2016, with carbon emissions from energy production being the largest source (about 65% of the total).^[2] Far from reaching a maximum, these emissions keep increasing year by year, as evidenced in **Figure 1.1**. The inset graph also shows the increasing trend of the global average temperature anomaly relative to the average temperature in the 1961-1990 period. The global average temperature has already risen by 1.1 °C since pre-industrial times.^[3] Scientific evidence suggests that the dominant cause of climate change is the release of greenhouse gases. The polar ice caps are melting, and

the sea level is rising (5 mm per year in the five-year period 2014-2019). In some regions, extreme weather events and floods are becoming more frequent, and others are experiencing heat waves and droughts.^[4] Moreover, the consequences are expected to intensify in the coming decade.

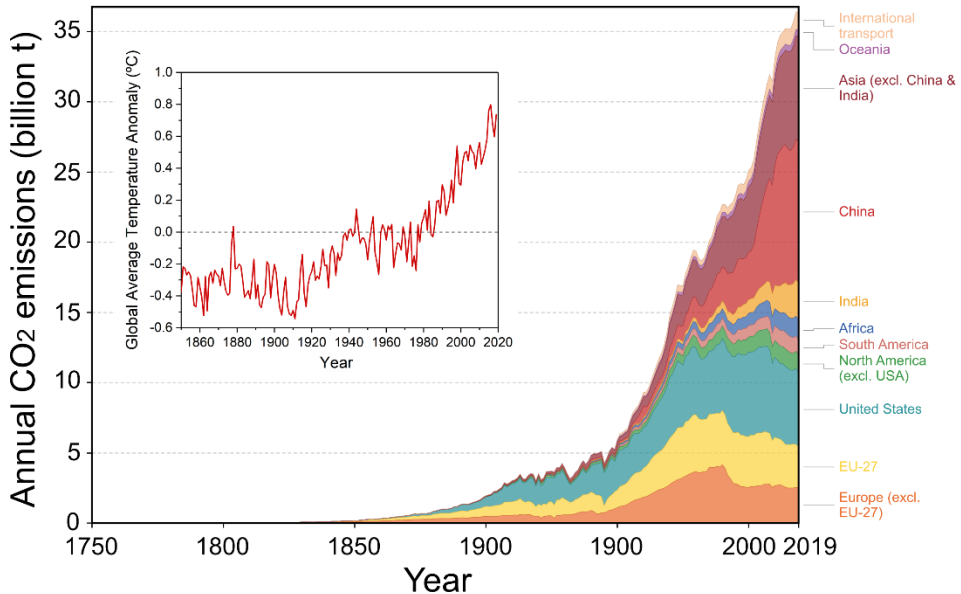


Figure 1.1: Annual production-based emissions of carbon dioxide (CO₂) from 1750 to 2019, measured in tons per year by world regions (fossil fuels and cement production only – land use change is not included). Inset graph shows the global average land-sea temperature anomaly relative to the 1961-1990 average temperature. (source: Our World in Data, Global Carbon Budget 2020, and Met Office Hadley Centre).^[5-7]

A rapid and sustained decline in carbon emissions is likely to require a series of policy measures, led by a significant increase in carbon prices.^[2] In the 2015 Paris climate agreement, after 20 years of negotiation, 195 countries agreed to target a maximum global temperature rise of 2 °C compared to the pre-industrial era.^[8] Reducing greenhouse gas emissions passes through mitigation, adaptation, and resilience. Delaying these policies measures and societal shifts may lead to significant economic costs and disruption. After withdrawing the agreement in 2017, at the beginning of 2021, the United States rejoined the treaty, which is very good news considering that USA was responsible for 14.75% of the total CO₂ emitted in 2018. These policies undoubtedly need to be accompanied by shifts in societal behaviors and preferences.

A transition to a lower carbon energy system needs a fundamental restructuring of the global energy system, with a more diverse energy mix, greater consumer choice, more localized energy markets, and increasing levels of integration and competition. These changes underlie the basic beliefs about how the global energy system may restructure into a low-carbon transition, and therefore declining the role of fossil fuels.^[2]

Renewable energy, led by wind and solar power, is the fastest growing source of energy over the next 30 years. Last year, the increase in renewable capacity accounted for 90% of the entire global power sector's expansion.^[9] Nevertheless, the intermittency associated with wind and solar energy production implies the need of smart solutions to balance the energy system and ensure the availability of energy independently of punctual variabilities in the consumer's demand. For that, the ability to store the generated energy is fundamental and, in this context, electrochemical energy storage in general, and batteries in particular, outstands as one of the preferred and most advanced options.

1.2. Li-ion battery

Batteries can be classified into several different categories depending on their characteristics and/or purposes. In general, they fall into two categories: primary and secondary,^[10] depending on whether they are non-rechargeable (single-use) or rechargeable, respectively. Primary batteries include zinc anode cells (zinc-carbon, zinc chloride and alkaline), and lithium batteries (lithium-iron sulfide and lithium-Manganese oxide) for example. Meanwhile, lead-acid (Pb-Acid), nickel-cadmium (Ni-Cd), nickel-metal hydride (Ni-MH), and lithium-ion batteries belong to the secondary batteries. Among them, the Li-ion batteries (LIB) are a subfamily of particular interest that are nowadays behind the transition from internal combustion engine vehicles to electric propulsion ones. Their importance lies on the contribution towards CO₂ emissions reduction: if the entire cycle life is considered, the electric vehicles will release between 17 to 21% less CO₂ than a diesel engine and between 26 to 30% less than a gasoline engine mounted in a vehicle with similar characteristics.^[11]

In the last three decades of 20th century, J. B. Goodenough and M. S. Whittingham developed the electroactive materials that were used in 1987 by A. Yoshino and co-workers (*Asahi Kasei Co.*) to design and develop the first commercial Li-ion battery.^[12] These three researchers were awarded the 2019 Nobel Prize in chemistry for the development of LIBs. The Li-ion battery was first commercialized by *Sony Co.* in 1991, followed by *A&T Battery Co. Ltd.* (a *Toshiba Battery* and *Asahi Kasei Co.* co-venture) in 1992.^[13] The high specific energy

density ($125 \text{ Wh}\cdot\text{kg}^{-1}$), the good performance (up to 500 cycles), and the absence of memory effect (as occurs with Ni-Cd or Ni-MH batteries) were responsible for its great success in the society. Among the main applications of LIBs, their use as power source for portable electronics outstands, including all current cell phones and laptops. Nevertheless, in recent years the scope of application has been diversified, extended to bicycles or, most importantly, the full electric vehicles.

1.2.1. Basics of Li-ion batteries

A battery is an electrochemical energy storage system. It consists of two electrochemically active compounds, known as electrodes, separated by an electronically insulating but ionically conductive medium, the electrolyte (**Figure 1.2**). In fact, a single electrode/electrolyte/electrode system is known as cell, while the combination of several cells constitutes the battery.

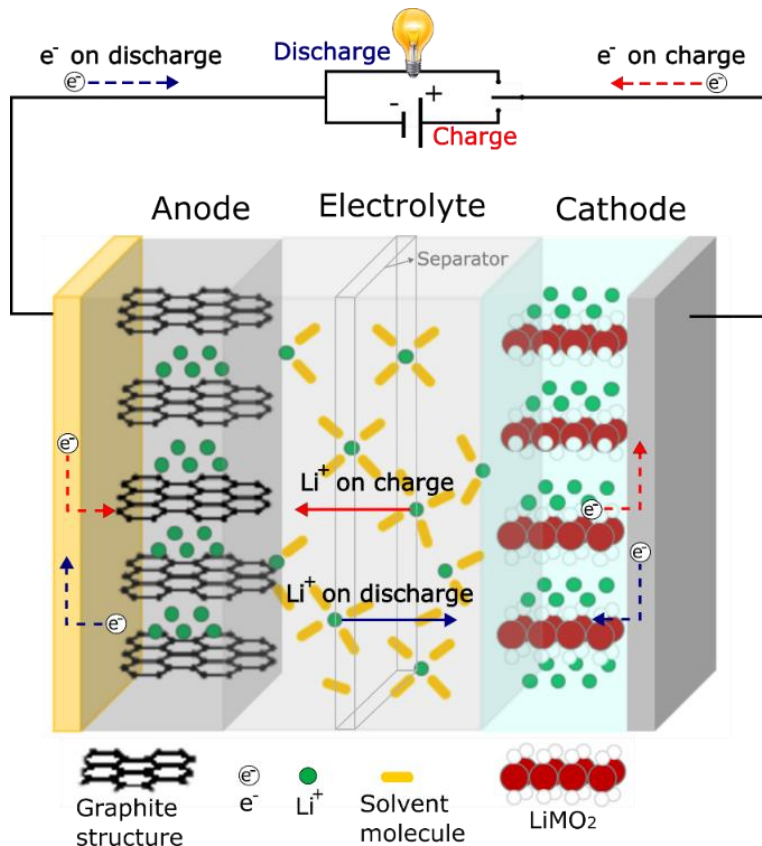


Figure 1.2: Schematic representation of a typical Li-ion cell. Typically, a copper current collector is used in the negative electrode while an aluminum collector is used for the positive electrode.

The two electrodes are responsible for exchanging lithium ions and electrons through oxidation (anode or negative electrode) and reduction (cathode or positive electrode) reactions. The electrolyte is responsible for transporting the lithium ions between the two electrodes during battery operation. In the case of liquid-based electrolytes, a separator is required to avoid both electrodes contacting and short-circuiting. Lithium ions transfer from the anode to the cathode during discharge through the electrolyte, due to the potential difference between electrodes. Meanwhile, the electrons move through the external circuit and provide energy to the external load. Traditionally, the positive electrode is referred to as the cathode.^[14]

When the negative electrode is oxidized and the positive electrode reduced, the battery is considered discharged. In a rechargeable battery, the electrochemical reactions are reversible, so the process can be reversed by applying an external electrical source that will reduce the negative electrode and oxidize the positive one, charging again the battery. This electron and ion transfer can be translated into delivered or applied energy.

The energy provided by a battery can be expressed in kWh, that can be normalized to weight or volume, hence obtaining specific energy (kWh/kg) and energy density ($\text{kWh}\cdot\text{L}^{-1}$), respectively. For instance, focusing on the previous example and selecting LiCoO_2 as the positive electrode with a redox potential of 3.8 V vs Li/Li^+ and graphite as the anode (redox potential of about 0.1 V vs Li/Li^+), the overall energy density of the cell remains between 150-200 $\text{Wh}\cdot\text{kg}^{-1}$.^[15]

The process of lithium-ion insertion into the electrode takes place typically by intercalation mechanism, without changing the crystalline structure of the electrode. During charge and discharge, the lithium ions go back and forth between the electrodes, being the whole phenomenon of intercalation and deintercalation reversible. Ideally, this phenomenon could continue infinitely. However, capacity loss and a subsequent reduction of the lifetime occurs due to materials degradation and other irreversible chemical reactions.^[16] For many years, most battery research has been based on liquid electrolyte systems. Despite the advantages of high conductivity and excellent wetting of electrode surfaces, liquid electrolytes often suffer from inadequate electrochemical and thermal stability, low ion selectivity and poor safety.^[17]

1.2.2. All solid-state batteries

In this scenario, all solid-state batteries (ASSB) – where the liquid electrolyte is substituted by a solid Li-ion conducting material – are attracting increasing attention, considering the important advantages that removing organic liquid components from the battery brings. In particular, ASSBs overcome classical technological limits associated with liquid electrolytes in terms of i) wider electrochemical window, ii) non-flammability, and iii) reduced Li dendrite formation.^[18,19] Importantly, widening the voltage stability window also allows the integration of high voltage cathodes paving the way towards building higher energy density batteries.^[20]

Moreover, the solid electrolyte can also act as a separator, without the need to incorporate an additional component in the battery stack. Therefore, the implementation of solid-state technology implies a significant increase in energy density. This means an increase in the amount of energy stored per volume or mass of a device, constituting a critical characteristic for any energy storage application.^[19]

Two approaches have been pursued for the development of mechanically and electrochemically stable Li-ion conducting solid electrolyte materials, *viz.* the use of polymers (organic) and the use of ceramic materials (inorganic). On the one hand, polymer-based electrolytes have been widely reported (polyethylene oxide (PEO)-based formulations) due to their easy processability, non-toxic properties, low-cost, and good chemical stability. However, they are limited by a low Li-ion conductivity at room temperature thus restricting the operation to high temperatures, usually *ca.* 70°C. On the other hand, ceramic materials are lately receiving increasing attention due to their competitive ionic conductivity at room temperature, as well as thermal and electrochemical stability.^[21] They could withstand operating temperatures range from –50 to 200 °C or higher, in which conventional liquid electrolytes would freeze, boil or decompose. The low variation of the ionic conductivity with temperature hinges on the low activation energies for fast ion conduction ensuring reliable operation.^[19] Moreover, the fact that solid-state batteries have operated for more than 10000 cycles is an irrefutable proof of the inherently slower reactivity of solids compared to liquids, resulting in longer device lifetimes for solid-state cells.^[22]

An indicator of the great potential of this technology is the growing interest of the automotive industry in new processing methods for integrating solid-state batteries into electric vehicles in the medium to long term. Not surprisingly, car manufacturers have partnered with solid-state battery start-ups or have developed their own programs. *e.g.*, Volkswagen has been associated with *Quantumscap*, General Motors with *Sakti3* (later acquired by *Dyson*) or *Toyota*, who has created his own program (AIST).

Furthermore, a particularly relevant advantage of solid electrolytes, in particular ceramic electrolytes, is the possibility of downscaling their thickness to thin film format ($< 1 \mu\text{m}$).^[23] This enables the development of all solid-state thin film batteries, introduced in the next section. In addition, as the electrolyte does not take part in the electrochemical reaction, the reduction in terms of mass also implies the increase of the energy density of the cell.^[24]

1.3 All solid-state thin film batteries

The upcoming era of the Internet of Things (IoT), with an unprecedented proliferation of interconnected energy-demanding autonomous devices, requires the development of a new generation of high-energy-density powering systems able to fulfill the needs of those devices working in the low-power regime.^[25,26]

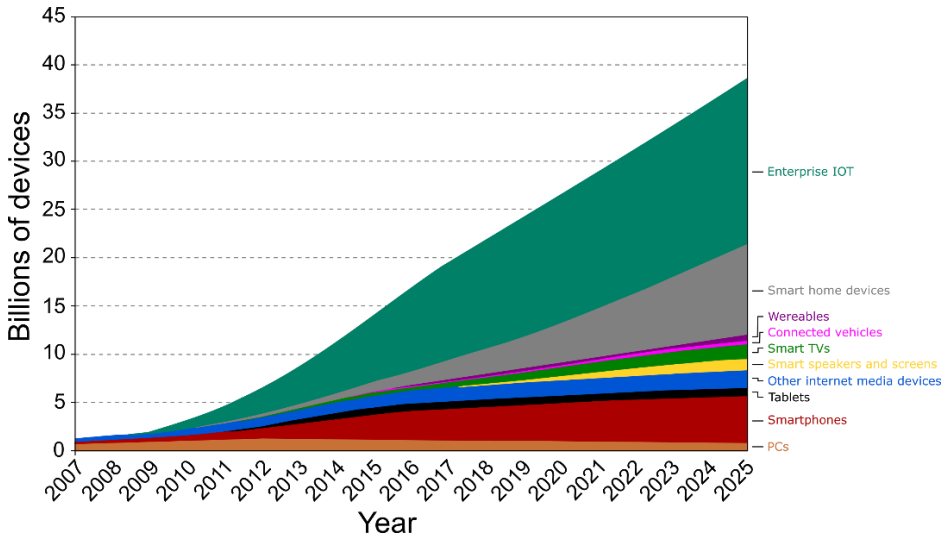


Figure 1.3: Global connected and IoT device installed forecast. (source: Strategy Analytics, Global Connected and IoT Device Forecast Update report 2019).^[27]

As shown in **Figure 1.3**, the number of devices connected to the internet reached 22.0 billion worldwide at the end of 2018, according to the latest research from Strategy Analytics.^[27] With an estimation of 38.6 billion devices by 2025, and 50 billion by 2030. Enterprise IoT remains the leading segment, accounting for more than half of the market. Among others, the emerging applications are wearable electronics, autonomous sensors, RFID tags, energy harvesting systems, credit cards, data smart cards, and also in high-added value batteries for aerospace applications, such as satellites.^[14]

The use of solid components for all the functional parts of the battery (cathode, anode and electrolyte) opens up new avenues for the development of thin film microbatteries, where the thickness of each functional layer is reduced to *ca.* 1 μm or less.^[28,29] This way, compact, light and high energy density batteries are envisioned, with capacities typically in the range of 0.1 to 5 mAh (*i.e.* perfectly suited for IoT devices).^[26,30]

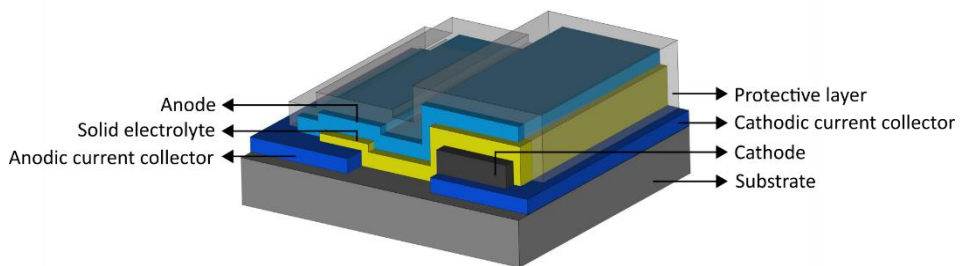


Figure 1.4: Drawing of a typical All Solid-State thin film lithium-ion battery.

As shown in the **Figure 1.4**, all solid-state thin film microbatteries are formed by a stack of thin film layers sequentially deposited on a substrate in the form of coatings through microfabrication technologies, using masks and selective etching processes to define the functional area of each cell component. Back in 1994, Bates and co-workers developed and patented the first thin film microbattery, fabricated by magnetron sputtering at Oak Ridge National Laboratory (ORNL).^[31] Magnetron sputtering belongs to the Physical vapor deposition (PVD) vacuum technology, which are, along with evaporation (thermal and electron beam) and pulsed laser deposition (PLD), the most widely used techniques for processing thin film components still nowadays. Protective layers (casings) are used to protect the batteries from environmental influences, such as moisture.^[24] The following chapter explains in more detail the techniques used for the deposition of thin film batteries in this thesis.

Currently, as seen in the **Table 1.1** there are already thin film batteries at the laboratory level that outperform any commercially available batteries, highlighting the potential of the technology as high-performing power source for the low-power regime.^[32] In this sense, the development of new materials in the form of a thin layer for each part of the battery is a field of extensive progress nowadays.^[33] The following section reviews the most commonly used materials for the different components of the battery.

Table 1.1: Comparison of the performance of conventional technologies against state-of-the-art estimates for thin film batteries.

Technology	Specific Energy (Wh·kg ⁻¹)	Energy density (Wh·l ⁻¹)	Cycle life (number of cycles)	Charge/discharge efficiency (%)
Pb-Acid	35-40	80-90	300	50-95
Ni-Cd	40-60	50-150	400	70-90
Ni-MH	60-120	140-300	600	66-92
Li-ion (Liquid electrolyte)	100-265	250-693	500	80-95
Li-Polymer	155–220	255–380	500	70-98
Li/Li-ion thin film	255-430	375-1050	>1000	94-99

1.3.1. Main component materials

In this section, the most widely used electrode active materials and solid inorganic electrolytes are presented. Notably, the majority of the works have been focused on the study of electrode materials,^[34–39] while most of the publications opt for using metallic lithium as anode and the well-known lithium phosphorous oxynitride (LIPON) as electrolyte.^[40–45] The portfolio of materials appeared in literature is wide.^[24,46] **Figure 1.5** presents a compilation of the most relevant electrode materials, compared by operating voltage and specific capacity.

Positive electrode materials

Among the electrode materials, the most extensively used ones are the intercalation materials.^[24] Within this group, several crystalline structures can be distinguished: Layered, Olivine and spinel structures.

Layered electrode structure. The layered lithium transition metal oxides, with a general composition of $\text{Li}(\text{Ni}_x\text{Mn}_y\text{Co}_z)\text{O}_2$ (NMC), are the most common option as active material in the cathodes. This family includes the lithium cobalt oxide (LiCoO_2 , LCO), firstly proposed in 1980 and nowadays the most used positive electrode material in commercial lithium-ion batteries.^[47] LCO crystallizes in a layered $\alpha\text{-NaFeO}_2$ structure, resulting in a nominal voltage of 3.8 V vs Li/Li^+ and a theoretical capacity of $148 \text{ mAh}\cdot\text{g}^{-1}$.^[48] For this reason, it has attracted immense attention for its downscaling to thin film, including PVD processes which have been investigated for 30 years.^[24] A initial specific capacity of $113.8 \text{ mAh}\cdot\text{g}^{-1}$ and a long-term stability during cycling was obtained in sputter-deposited LCO films.^[49,50] Nevertheless, high materials cost, toxicity and poor thermal stability encourage researchers to seek for alternatives.

A potential substitute is the isostructural LiNiO_2 , which is relatively cheaper, less toxic, less susceptible to electrolyte decomposition due to the more negative redox potential (0.25 V), and higher specific capacity (up to $200 \text{ mAh}\cdot\text{g}^{-1}$).^[51] However, some problems related to structural instability have hampered their commercial application. The close ionic radius of Li^+ (0.76 Å) and Ni^{2+} (0.69 Å) make them easily interchangeable, thus blocking the Li^+ ion mobility inside the crystalline structure.^[52,53] The incorporation of other transition metals can improve the structural stability and increase its thermal stability. Layered NMC materials in which Ni, Mn and Co are combined in the $\alpha\text{-NaFeO}_2$ structure, shows a very good cyclability and satisfactory structural and thermal stability, including high capacities (e.g. $160 \text{ mAh}\cdot\text{g}^{-1}$ for $\text{LiNi}_{1/3}\text{Mn}_{1/3}\text{Co}_{1/3}\text{O}_2$).^[54] This material is increasing importance also in PVD research. Nevertheless, in layered structures the ionic conduction is highly anisotropic and it depends on the orientation of the deposited layer, being this effect conditioned strongly by the substrate material.^[54]

Another example of layered electrode structure is the vanadium oxide and, particularly, the vanadium pentoxide (V_2O_5). This material is considered a promising cathode electrode material owing to its high discharge capacity (about $400 \text{ mAh}\cdot\text{g}^{-1}$), low cost and abundance.^[55] Moreover, due to its intermediate redox potential, it can be used either as positive or negative electrode material in different types of batteries.^[24] The major drawbacks of the V_2O_5 are its poor structural stability, low electronic conductivity and slow electrochemical kinetics. Even so, the non-necessity of a crystalline phase for operation makes vanadium oxide one of the most attractive materials for thin film batteries, allowing its direct deposition on polymer substrates as well.

Olivine structure. Recently, in the last decade there has been a great interest in lithium transition-metal phosphates LiMPO_4 ($M = \text{Fe, Co, Ni, Mn}$) as promising cathode materials, with a capacity of about $170 \text{ mAh}\cdot\text{g}^{-1}$ and high stability during electrochemical cycling.^[35,56,57] The most common option and a potential low-cost cathode among them is the LiFePO_4 (LFP), with an operating voltage of 3.45 V vs Li/Li^+ .^[24] The operating voltage increase when Fe is replaced by other transition metal, following the sequence $\text{Fe} < \text{Mn} < \text{Co} < \text{Ni}$. The main drawback of this family of materials is associated to its low electronic and ionic conductivity (e.g. electronic conductivity $10^{-9} \text{ S}\cdot\text{cm}^{-1}$ and Li^+ diffusion coefficient of $10^{-13} - 10^{-14} \text{ cm}^2\cdot\text{s}^{-1}$ were reported for LFP)^[58], which limits the electrochemical performance of the electrode. In spite of this, it is one of the most widely used materials in the automotive industry, as it has good thermal and chemical stability, which improves its safety.^[59]

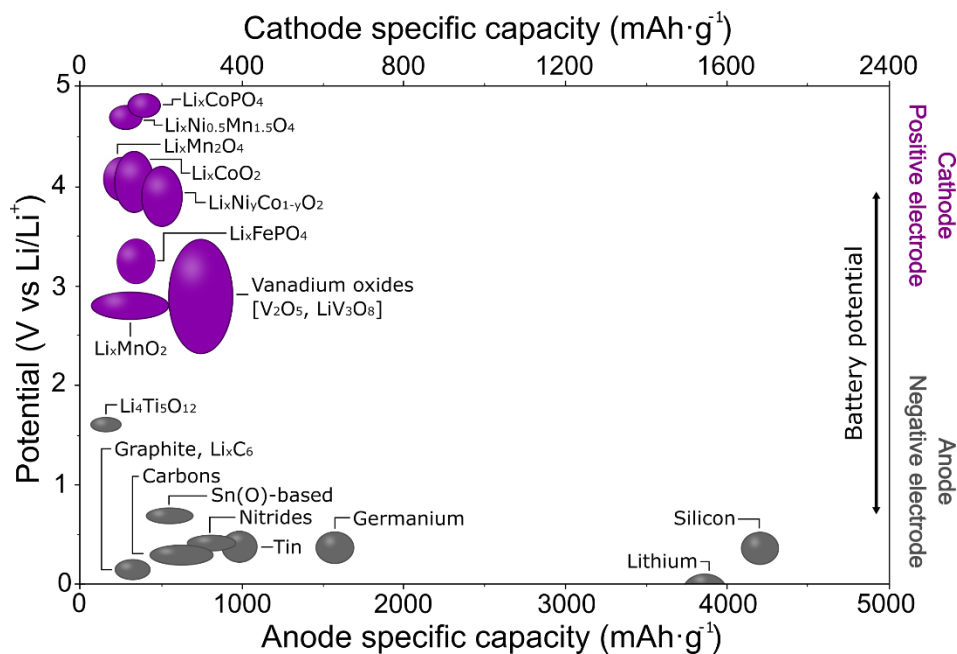


Figure 1.5: Voltage versus capacity for positive- and negative electrode materials. The purple materials are normally used as cathode while the gray ones are used as anodes. The potential difference between the employed materials determines the potential of the battery.

Spinel structure. The lithium manganese oxide, LiMn_2O_4 (LMO) is an attractive cathode material on account of its low cost, environmental friendliness, and good thermal stability.^[60,61] The theoretical capacity of LMO is $148 \text{ mAh}\cdot\text{g}^{-1}$. However, only $100\text{-}120 \text{ mAh}\cdot\text{g}^{-1}$ can be practically realized because of structural instability issues related to Jahn-Teller distortions (phase transition from cubic to tetragonal

phase) upon 3 V vs Li/Li⁺ cycling.^[62] Moreover, in conventional cells the liquid electrolyte could lead to the formation of oxygen vacancies as a result of the dissolution of manganese in the electrolyte resulting in poor cycle stability and capacity fading.^[63]

Several studies have been working on stabilizing the structure and enhancing capacity and operational voltage. To that end, a whole spinel family of Mn-based oxides has been studied, obtained by the partial substitution of the Mn cation in LMO by a transition metal (LiMn_{2-x}M_xO₄, where M = Ni, Co, Fe, Cu, or Cr).^[64-66] In particular, the nickel-substituted spinel LiMn_{1.5}Ni_{0.5}O₄ (LNMO) has attracted great attention due to a higher capacity ($C_{th.} = 146.6 \text{ mAh}\cdot\text{g}^{-1}$) and operating voltage compared to the spinel parent compound LiMn₂O₄. Firstly reported by Tarascon *et al.* in 1991,^[67] a 4.7 V vs Li/Li⁺ operating voltage was proven by Zhong *et al.* and Amine *et al.* in 1997, corresponding to the nickel redox reaction (from Ni²⁺ to Ni⁴⁺).^[39,68] Moreover, LMNO presents high charge/discharge rate capability and good electronic and Li-ion conductivities.^[36,69,70] All these properties, along with the non-toxic nature of the constituent elements, have turned this material into one of the most appealing cathode options for the next generation of high-power thin film batteries.^[71]

Negative electrode materials

Graphite is an excellent negative electrode material given its low potential against Li/Li⁺ and its high specific capacity of 372 mAh·g⁻¹. In addition, there are numerous research projects underway to further improve the anodic properties.^[72-74]

Many investigations are focused on the carbon family elements, group 14 of the periodic table, due to their high energy density, which makes them very useful for future all solid-state thin film batteries. This group includes silicon, tin, and germanium. Their popularity has also been boosted due to their availability, relative stability, high capacity, and low potential.^[24] To be precise, the Si has a theoretical capacity of 4200 mAh·g⁻¹ and the potential of 0.4 V vs Li/Li⁺, the Sn 994 mAh·g⁻¹ and 0.6 V vs Li/Li⁺, and the Ge 1625 mAh·g⁻¹ and 0.5 V vs Li/Li⁺. Nevertheless, there remains a lot of research works to be done on these materials, since they show a large irreversible capacity loss during the first 5-10 cycles (*e.g.* 500-1000 mAh·g⁻¹ in Si), being more evident in thin film materials.^[75-77] This effect can be attributed to their substantial volumetric expansion during lithiation (420% for Si, 370% for Ge and 260% for Sn) and the associated loss of the surface contact.^[78]

The spinel $\text{Li}_4\text{Ti}_5\text{O}_{12}$ (LTO) is the main oxide-based alternative. With a theoretical specific capacity of $175 \text{ mAh}\cdot\text{g}^{-1}$, LTO possesses very appealing properties like negligible volume expansion during (de)lithiation, outstanding cycle performance, stability and reduced cost.^[79,80] In addition, LTO is suitable for being processed by PVD as corroborated by the increasing number of articles dealing with LTO thin film electrodes.^[81–83]

The conversion-type materials are also frequently used as anodic materials. This group includes metal oxides, nitrides, sulfides, fluorides.^[84] Its general formula is M_xA_y , where M is a metal (mainly transition-metal: Fe, Co, Ti, Ni, Mn, Sn, etc.), and A an anionic species (mainly from O, N, F, S, P, etc.). These materials undergo a conversion reaction from its oxidized form to the metallic state, that can be expressed as: $\text{M}_x\text{A}_y + (y+n)\text{Li}^+ + (y+n)\text{e}^- \rightarrow x\text{M}^0 + y\text{Li}_n\text{A}$. Such conversion reaction can often involve more Li-ions than the intercalation reactions, which potentially results in much higher capacities and energy densities. Nevertheless, the materials within this family also suffer from the severe problems of high hysteresis, low-rate capability, and rapid capacity loss. This is attributed to the significant chemical reorganization during reactions and poor ionic and electronic conductivity.^[24]

With a theoretical capacity of $1491 \text{ mAh}\cdot\text{g}^{-1}$ SnO_2 is one of the most attractive materials within this group. This high capacity is achieved by the incorporation of up to 8.4 lithium ions per formula unit in the processes.^[24] Unfortunately, in thin film batteries SnO_2 shows a rapid capacity fade when cycled with liquid electrolyte.^[84]

Nitrides have also attracted a considerable amount of attention. In these compounds, Li_3N is formed as a reaction product, having a higher ionic conductivity (up to $1.2 \times 10^{-3} \text{ S}\cdot\text{cm}^{-1}$) than the insulating Li_2O formed in oxide materials.^[85] For instance, SnN_x thin films achieves specific capacities up to $700 \mu\text{Ah}\cdot\text{cm}^{-2}\cdot\mu\text{m}^{-1}$ in cells with liquid electrolyte, showing a good long-term stability, although a strong degradation within the first 100 cycles was also observed.^[86]

Finally, not to mention the material that is typically applied as foil in bulk-type batteries: the metallic lithium. The use of Li metal as a negative electrode in thin film batteries is living an intense upturn lately, to profit from its high theoretical specific capacity ($3860 \text{ mAh}\cdot\text{g}^{-1}$), the lowest negative electrochemical potential (-3.040 V vs SHE), and low density ($0.59 \text{ g}\cdot\text{cm}^{-3}$).^[20,87] It is usually deposited by thermal evaporation technique, although details or characteristics of its deposition are rarely given.

Inorganic solid-state electrolyte materials

An ideal electrolyte is characterized by high ionic conductivity, low electronic conductivity, low-resistivity, and stable electro material interfaces. As mentioned above, solid electrolytes are divided into organic and inorganic electrolytes. This section is focused on the inorganic ones (particularly oxides), which are suitable for the implementation in thin film batteries (thickness < 1 μm).

Garnet-type electrolyte

Garnet-type Li-ion conductors have been intensively studied as solid electrolytes for LIBs following the first report by Thangadurai *et al.*^[88] They studied the Lithium metal oxides with the nominal composition of $\text{Li}_5\text{La}_3\text{M}_2\text{O}_{12}$ (M = Nb, Ta), resulting in a bulk conductivity of $\sim 10^{-6} \text{ S}\cdot\text{cm}^{-1}$ at 25°C. Among the investigated compounds with garnet-related structures, $\text{Li}_7\text{La}_3\text{Zr}_2\text{O}_{12}$ (LLZO) exhibits a high lithium ion conductivity ($> 10^{-4} \text{ S}\cdot\text{cm}^{-1}$ at RT in its cubic crystalline form), good thermal and chemical stability against reactions with prospective electrode materials, environmental benignity, and availability of the raw materials.^[89] Unfortunately, LLZO stabilizes in a less-conductive tetragonal structure at low temperatures ($\sigma \sim 10^{-6} \text{ S}\cdot\text{cm}^{-1}$ at RT), so innovative solutions need to be applied to stabilize the high conducting cubic phase down to RT. The most common option involves structural doping in either the Li, La or Zr sites. In particular, replacement of Li^+ by Al^{3+} or Ga^{3+} , the substitution of La^{3+} by Ca^{2+} , Sr^{2+} , and Ba^{2+} ^[24] or Ta-doping in the Zr-site or Nb-doped LLZO are proven strategies to ultimately obtain a cubic garnet stable in the whole range of operating temperatures (down to RT).

However, PVD deposition of garnet-type materials is not entirely straightforward. The main problem is the large mass difference between cations (Li^+ , La^{3+} and Zr^{2+}). This makes the dynamics of each element in the plasma totally different and generates many stoichiometric changes, making a great challenge the stoichiometric transfer from the target to the thin film. For instance, Zr-containing garnets are thermodynamically stable between 600-700 °C. Lower temperature deposition could lead to amorphous phase and its consequently low conductivity or secondary phases formation like $\text{La}_2\text{Zr}_2\text{O}_7$, while high temperatures result in a loss of lithium.^[24] Despite the great challenges, several studies have been successful in mitigating these side effects. With a post-annealing at 600 °C Saccoccio *et al.* were able to deposit at various temperatures $\text{Li}_{6.4}\text{La}_3\text{Zr}_{1.4}\text{Ta}_{0.6}\text{O}_{12}$ on MgO substrate.^[90] In addition, strategies like $\text{Li}_{6.25}\text{Al}_{0.25}\text{La}_3\text{Zr}_2\text{O}_{12}$ deposition alternating with Li_3N layers have been used to balance the Li-loss during annealing^[91] or also three target (LLZ, Li_2O and either Ga_2O_3 or Al) co-sputtering to deposit Ga- and Al-substituted LLZ.^[92]

LiPON-type electrolytes

Lithium phosphorus oxynitride ($\text{Li}_3\text{PO}_{4-x}\text{N}_x$, commonly referred as LiPON) is a popular glassy amorphous Li-ion solid electrolyte. First fabricated in the 1990s by Bates et al, [23,93,94] it is usually prepared by reactive RF magnetron sputtering deposition from a Li_3PO_4 target, using nitrogen as a reactive sputter gas without substrate heating (to avoid crystallization). The low deposition temperatures avoid interdiffusion of the elements from/towards the substrate and/or the electrode material. Besides, the deposition of thin and flexible layers permits avoiding cracking during operation due to volumetric changes in the cell. Moreover, it has the advantages of isotropic conduction properties due to its amorphous structure.

In thin film form, pure Li_3PO_4 was reported to have a relatively low ionic conductivity of $7 \times 10^{-8} \text{ S}\cdot\text{cm}^{-1}$. [95] Therefore, efforts were made to improve its ionic conductivity with the insertion of nitrogen in the system. This way, a higher ionic conductivity could be achieved, along with a good electrical and chemical stability, high electronic resistivity ($>10^{14} \Omega\cdot\text{cm}$), and large electrochemical window of 0-5.5 V vs Li/Li^+ , being able to use in combination with many different electrode materials. [96] To date, the highest ionic conductivities reported was $9.78 \times 10^{-6} \text{ S}\cdot\text{cm}^{-1}$. [97,98] Notably, it is important to highlight that crystalline LiPON presents a much lower ionic conductivity of $1.4 \times 10^{-13} \text{ S}\cdot\text{cm}^{-1}$, thus reflecting the need of keeping the amorphous structure for ensuring low resistivity of the film. [99] All in all, the low deposition temperatures makes LiPON the ideal candidate for all solid-state thin film batteries.

NASICON-type electrolytes

The so-called NASICON or sodium super ionic conductors are crystalline solids of the general formula $\text{A}_1\text{B}_2(\text{PO}_4)_3$ where A is a monovalent cation and B is either a single or combination of tri-, tetra- and pentavalent ions. [100] In 1976, Hong [101] and Goodenough [102] originally reported first 3D NASICON material, $\text{Na}_{1+x}\text{Zr}_2\text{Si}_x\text{P}_{3-x}\text{O}_{12}$ as inorganic solid electrolyte providing an excellent structural strength and outstanding ionic conductivity. [102]

Its implementation in lithium-ion batteries was not long in coming. Among the NASICON-type electrolytes the $\text{LiM}_2(\text{PO}_4)_3$ ($\text{M} = \text{Ge}, \text{Ti}, \text{Hf}, \text{etc.}$) compound family has been thoroughly investigated, particularly $\text{LiTi}_2(\text{PO}_4)_3$ for its high ionic conductivity. [103] In addition, the partial replacement of M^{4+} ions by trivalent ions (general formula $\text{Li}_{1+x}\text{Al}_x\text{M}_{2-x}(\text{PO}_4)_3$ where $\text{M} = \text{Ge}, \text{Ti}$) gives rise to higher Li-ion

conductivities, as high as $7.4 \times 10^{-4} \text{ S}\cdot\text{cm}^{-1}$ for $\text{Li}_{1+x}\text{Al}_x\text{Ti}_{2-x}(\text{PO}_4)_3$ (LATP)^[102] and $2.4 \times 10^{-4} \text{ S}\cdot\text{cm}^{-1}$ for $\text{Li}_{1+x}\text{Al}_x\text{GeM}_{2-x}(\text{PO}_4)_3$ (LAGP).^[102]

In the case of thin films, an important advantage of this type of materials is that they require a relatively low deposition temperature to obtain the crystalline phase. Sun *et al.* were able to deposit LAGP thin film by sputtering at 600 °C (using a target of the same chemical composition). Tan *et al.* carried out a deposition temperature study for nitrogen-incorporated LATP based thin film electrolytes, varying the temperature from 25 to 500 °C. The crystallinity of the sample increase with the temperature as well the ionic conductivity, obtaining a maximum of about $1.2 \times 10^{-5} \text{ S}\cdot\text{cm}^{-1}$ at 30 °C for a sample deposited at 500 °C.^[102]

Perovskite-type electrolytes

The ideal perovskite structure has a general formula of ABO_3 and a cubic unit cell (A is typically alkaline-earth or rare-earth elements, whereas B is typically transition metal ions).^[104] The advantages of the perovskite-type electrolytes over other electrolytes include wide tolerance factor that allow doping with most ions, a high bulk Li-ion conductivity and a simple crystal structure with a clear Li transmission mechanism.^[105] The Li ions can be introduced in the perovskite materials on the A site through aliovalent doping creating compositions such as $\text{Li}_{3x}\text{La}_{2/3-x}\text{TiO}_3$ (LLTO). Inaguma *et al.* pioneered the analysis of this material, being for $\text{Li}_{0.34}\text{La}_{0.56}\text{TiO}_3$ the highest achieved Li-ion conductivity in the perovskite family with a total value of $7 \times 10^{-5} \text{ S}\cdot\text{cm}^{-1}$.^[104] Although perovskite-type solid electrolytes have demonstrated to be stable at high potentials, they still suffer from several significant problems, such as poor stability against lithium metal (being reduced around 1.5 V vs Li/Li⁺ making it unsuitable for its use with lithium and graphite negative electrodes), high interface resistance, etc.^[105]

For the thin film form, the most used PVD technique for this type of material is PLD.^[106–110] Very few thin films are published using sputtering or evaporation.^[107] The deposition temperature is a key parameter for the ionic conductivity of LLTO thin films growth by PLD. The thin film remains in an amorphous state up to temperatures (deposition or post-annealing) below 700 °C. This leads to an increase in ionic conductivity due to the absence of grain boundaries. According to Lee *et al.* and Ahn *et al.* the optimum deposition temperature is 400°C.^[109,111] Moreover, the deposition of single phase LLTO thin films remains very challenging. The perovskite phase growth competes with an insulating $\text{La}_2\text{Ti}_2\text{O}_7$ phase when prepared in the deposition temperature higher than 700 °C and

using high oxygen pressure by PLD.^[106] F. Aguesse *et al.* have achieved higher ionic conductivity with an epitaxial growth of LLTO on different (001) oriented substrates such as LaAlO₃, SrTiO₃ and MgO using Li-rich targets. Nonetheless, the presence of the secondary phase remains, strongly hindering the migration of lithium ions and reducing the overall conductivity compared to bulk properties.^[106]

1.3.2. Laboratory scale thin film batteries

At the laboratory level, different research groups have been developing thin film lithium-ion batteries with new materials over the last few years.^[28] One of the main ways of replacing conventional liquid electrolyte batteries is by means of high voltage solid-state batteries. Kuwata *et al.* fabricated a thin film battery with 150 nm-thick LiCoMnO₄ (LCMO) cathode, Li₃PO₄ solid electrolyte and Lithium anode that was able to operate at potentials above 5 V vs Li/Li⁺, which is among the highest voltages reported for a thin film battery.^[112] It showed a good cycling performance, with an initial discharge capacity of 107 mAh·g⁻¹ (76% of the theoretical discharge capacity, 145 mAh·g⁻¹) and a capacity retention of 99.4% after 20 cycles.^[112] Later, Li *et al.* observed in a LCMO/LiPON/Li battery cell that limiting the charge and discharge cut-off voltages to 5.0 V and 1.4 V, respectively, reduces the degradation of the battery at high voltages and enables the use of the capacity under 3 V vs Li/Li⁺ associated with a cubic-tetragonal phase transitions without appreciable capacity fade with cycling.^[113] This way, a specific capacity of about 170.7 μAh·cm⁻²·μm⁻¹ with a capacity retention of 99.85% within the first 100 cycles was obtained.^[113]

Additionally, a high-voltage battery consisting of LNMO cathode, LiPON electrolyte, and Li metal anode was developed by Li and co-workers.^[22] This solid-state lithium battery delivers remarkable capacity retention of 90% over 10 000 cycles with discharge capacities of about 122 mAh·g⁻¹, and a high Coulombic efficiency (99.98 %). Moreover, it shows a strong adhesion of the cell components, without element interdiffusion after 1000 cycles.^[22]

Besides high voltage cathodes, some studies focus on increasing the specific capacity of the battery. Using an LCO/LiPON/Si thin film battery a specific capacity of 3000 mAh·g⁻¹ relative to the silicon anode was obtained by Wang and co-workers.^[114] Nonetheless, they found a great initial irreversible capacity loss on the first cycle, that could be due to lithium accumulation and chemical changes

in the interfacial layer between cathode and solid electrolyte, as well as first cycle irreversibility of the silicon anode.^[114]

Among the ongoing solid-state thin film battery research, flexible batteries are gaining special importance. Which will be beneficial for future applications such as wearable electronics. A MoO₃/LiPON/Li battery stack deposited on flexible polyimide substrate by Glenneberg *et al.* showed a very high cycling stability and excellent rate capability.^[45] Obtaining an initial capacity of 180 $\mu\text{Ah}\cdot\text{cm}^{-2}\cdot\mu\text{m}^{-1}$ at C/2 and around 15% of discharge capacity fade after 550 full cycles (between 1 and 3.5 V vs Li/Li⁺) at 10C.^[45] Unfortunately, bending experiments carried out on this battery stack showed a cathode delamination and severe cracking effect in the electrolyte and the anode.^[24] Not to mention that polymer-type substrates are very susceptible to heat treatment. Thus, a flexible all solid-state thin film battery consisting of LTO/LiPON/Li was fabricated using an yttria-stabilized zirconia (YSZ) ceramic sheet.^[115] This flexible material withstands processing temperatures up to 1200 °C and shows good insulation properties.^[115]

A recent objective of the scientific community is the development of 3D thin film batteries that can provide high power and high areal energy density storage. Ideally, the 3D geometry maximizes the volume of active material per unit area, while keeping its thickness small to allow for fast Li diffusion.^[116] Talin *et al.* have obtained a 3D thin film battery of LCO/LiPON/Si using a 3D-structured Si wafer substrate. The resulting low specific areal capacity (10 $\mu\text{Ah}\cdot\text{cm}^{-2}$ at 0.6C) may be due to the inhomogeneity of the deposited layers resulting in non-homogeneous current density distribution. Conversely, Xia and co-workers obtained a 3D structure by changing the sputtering growth parameters when depositing the thin film cathode. The battery was made up of LMO/LiPON/Li.^[117] A further improvement in cycling performance were observed comparing to the counterpart 2D cathode. The deep insertion of LiPON electrolyte into the 3D cathode has allowed the increase in surface area, exhibiting large specific capacity (121 $\text{mAh}\cdot\text{g}^{-1}$ at 1C), superior rate capability (83 $\text{mAh}\cdot\text{g}^{-1}$ at 20C), and good cycle performance (over 90% of capacity retention after 500 cycles).^[117] However, the commercialization of 3D batteries is hampered by processing cost and scalability.

To sum up, the developing of new functional materials (including both electrodes and electrolytes) with good electrochemical properties and integrating them into thin film batteries by PVD fabrication techniques remains challenging. Different properties of the new materials should be improved, such as their stability during

cycling and electrochemical compatibility. In this sense, it is necessary to control the interface phenomena between the electrodes and the electrolyte, especially when the material is synthesized as a solid coating.





1.3.3. Commercial thin film batteries

The market for all solid-state thin film batteries is growing fast in recent years, and despite its initial development arose in the USA (*Cymbet*, *Excellatron*, *BrightVolt*, etc.), it is expected to expand to the rest of the world in the short term.

Today as discussed above the main driver of this technology is the growth of IoT, including smart cards, wireless microsensors, radio frequency identification (RFID) tags, toys, and medical devices, such as tiny defibrillators. They also can be used to hold energy gathered from solar cells or other green technologies.^[118]

Table 1.2 shows some examples of the current commercially available all solid-state thin film batteries.

Table 1.2: Some available commercial all solid-state batteries.

				
	Cymbet corp.	STMicroelectronics	IPS	TDK corp.
	<i>Enerchip CBC050</i>	<i>EnFilm EFL700A39</i>	<i>Thinergy MEC202</i>	<i>CeraCharge 1812</i>
Composition	Cathode: LiCoO ₂ Electrolyte: LiPON Anode: Li	Cathode: LiCoO ₂ Electrolyte: LiPON Anode: Li	Cathode: LiCoO ₂ Electrolyte: LiPON Anode: Li	Electrodes: Li ₃ V ₂ (PO ₄) ₃ Electrolyte: Li _{1.3} Al _{0.3} Ti _{1.7} (PO ₄) ₃
Nominal voltage (V vs Li/Li⁺)	3.8	3.9	3.9	1.4
Nominal capacity (mAh)	0.05	0.7	2.2	0.1
Thickness (μm)	200	220	170	1100
Size (mm²)	8.0 x 8.0	25.7 x 25.7	25.4 x 50.8	4.4 x 3.3

At laboratory scale, despite progress in the development of new materials, nowadays the most used electrolyte material in thin film form is still LiPON. The LCO cathode used in most commercially available cells provides a specific capacity of about $150 \text{ mAh}\cdot\text{g}^{-1}$ and voltages of about 4 V vs Li/Li⁺. The energy density of the thin film batteries presented in this section are in the range of 27 to $45 \text{ Wh}\cdot\text{l}^{-1}$, well below the values provided above.

LCO/LiPON/Li batteries offer the longest cycle life. *Cymbet Corporation* and *STMicroelectronic* cells operate reliably over 5000 and 4000 cycles respectively, albeit not under deep discharge condition, whereas *Infinite Power Solutions (IPS)* technology exceeds 10000 cycles at 100% depth-of-discharge (corresponding to more than 15 years). The estimated time to fully charge these batteries is usually about 20 minutes. Regarding self-discharge rate *Cymbet* and *STMicroelectronics* are very similar, losing 2.5% and 3% per year, respectively, during storage at ambient conditions. In the *IPS* case, this feature is dated as <1% per year. All values remain below the value of a conventional LCO-based battery, which can lose up to 4% per year.

In the case of *TDK* a novel technology is presented. It is based on a multilayer technology containing purely ceramic electrode and electrolyte materials. CeraCharge is the world's first rechargeable battery to be designed as a surface-mount technology (SMT)-compatible component. Accordingly, this results in further advantages such as easy placement of components and the use of conventional reflow soldering processes. The CeraCharge 1812 battery offers a 100 μAh nominal capacity, a nominal voltage of 1.5 V, and a $9 \text{ Wh}\cdot\text{l}^{-1}$ of energy density, along with a cycle life of 1000 cycles.

1.4. Scope of the thesis

In this thesis, an all solid-state thin film Li-ion battery comprised of a high-voltage LNMO cathode, a LiPON ceramic electrolyte (both deposited by magnetron sputtering), and a metallic Li anode (thermally evaporated) has been developed. The structural and electrochemical properties of each electroactive component of the battery have been analyzed separately before the building up of the cell for the characterization of the cycling performance. These analyses are divided into different chapters, as visually represented in **Figure 1.6**.

Chapter 2 is devoted to briefly describe the different fabrication and characterization techniques used during the thesis for the development of this work.

Chapter 3 presents the optimization of the selected cathode, LNMO. For this goal, the material is deposited on SS substrates, by mid-frequency alternating current (AC) magnetron sputtering. The chapter includes the optimization of the magnetron sputtering process to achieve coatings with controlled thickness, morphology, chemical composition, and crystallographic structure. Each deposited cathode is subjected to specific electrochemical tests. Furthermore, at the end of the chapter, the optimum cathode is compared with a commercial cathode. This work was carried out in collaboration with Dr. Jokin Rikarte in the framework of the European H2020 project MONBASA (Monolithic Batteries for Spaceship Applications, Grant No. 687561).

Chapter 4 is dedicated to the study of the different interfaces formed between the LNMO layer and other components of the cell, *i.e.*, substrate-cathode and electrolyte-cathode interfaces. The addition of protective layers is analyzed, aiming to avoid detrimental interactions/reactions between the different components.

Chapter 5 describes the synthesis and characterization of LiPON thin film solid electrolyte deposited by RF magnetron sputtering. The study focuses on the effect of N₂ flux during the deposition process to obtain the optimum LiPON composition, by analyzing its structure, elemental composition, and ionic conductivity.

After separately analyzing the structural and electrochemical properties of each electroactive component of the battery, **Chapter 6** is focused on the build-up of a high voltage all solid-state thin film battery by combining the optimized functional films (cathode and electrolyte). To complete the cell, lithium metal

anode has been used based on a previous work carried out within the group at *CIC energiGUNE* by Dr. Ane Etxebarria Dueñas.

Chapter 7 summarizes the overall conclusions from the whole research work. The future perspectives of all solid-state thin film battery are also presented.

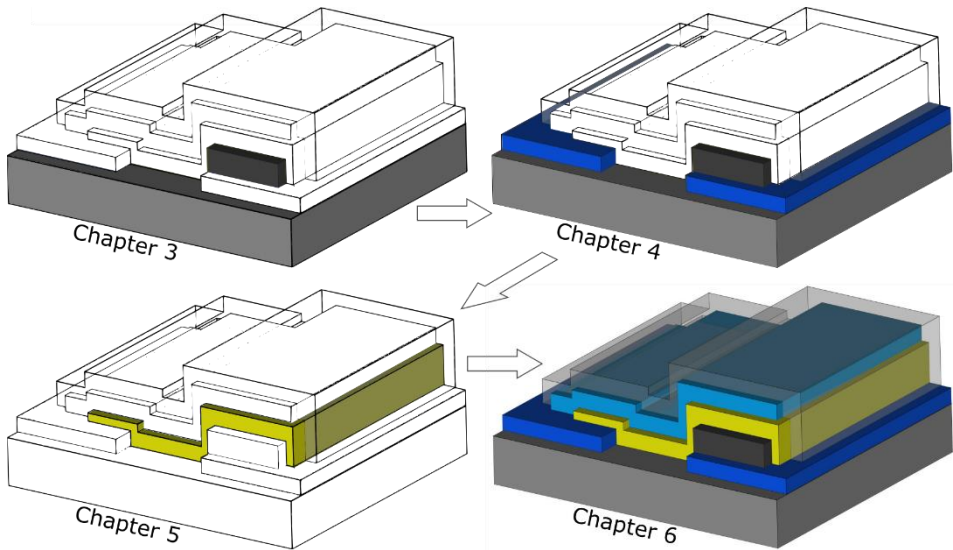


Figure 1.6: Summary outline of the components studied in this thesis in chronological order.

References in Chapter 1

- [1] British Petroleum, *BP Energy Outlook 2019*, 2019.
- [2] British Petroleum, *BP Energy Outlook 2020*, 2020.
- [3] “Cambio climático,” can be found under <https://es.greenpeace.org/es/trabajamos-en/cambio-climatico/>, 2019.
- [4] “Consecuencias del cambio climático | Acción por el Clima,” can be found under https://ec.europa.eu/clima/change/consequences_es, 2019.
- [5] P. Friedlingstein, M. O’Sullivan, M. W. Jones, R. M. Andrew, J. Hauck, A. Olsen, G. P. Peters, W. Peters, J. Pongratz, S. Sitch, C. Le Quére, J. G. Canadell, P. Ciais, R. B. Jackson, S. Alin, L. E. O. C. Aragão, A. Arneeth, V. Arora, N. R. Bates, M. Becker, A. Benoit-Cattin, H. C. Bittig, L. Bopp, S. Bultan, N. Chandra, F. Chevallier, L. P. Chini, W. Evans, L. Florentie, P. M. Forster, T. Gasser, M. Gehlen, D. Gilfillan, T. Gkritzalis, L. Gregor, N. Gruber, I. Harris, K. Hartung, V. Haverd, R. A. Houghton, T. Ilyina, A. K. Jain, E. Joetzjer, K. Kadono, E. Kato, V. Kitidis, J. I. Korsbakken, P. Landschützer, N. Lefèvre, A. Lenton, S. Lienert, Z. Liu, D. Lombardozzi, G. Marland, N. Metz, D. R. Munro, J. E. M. S. Nabel, S. I. Nakaoka, Y. Niwa, K. O’Brien, T. Ono, P. I. Palmer, D. Pierrot, B. Poulter, L. Resplandy, E. Robertson, C. Rödenbeck, J. Schwinger, R. Séférian, I. Skjelvan, A. J. P. Smith, A. J. Sutton, T. Tanhua, P. P. Tans, H. Tian, B. Tilbrook, G. Van Der Werf, N. Vuichard, A. P. Walker, R. Wanninkhof, A. J. Watson, D. Willis, A. J. Wiltshire, W. Yuan, X. Yue, S. Zaehle, *Earth Syst. Sci. Data* 2020, 12, 3269.
- [6] C. Morice, “Met Office Hadley Centre observations datasets,” can be found under <https://www.metoffice.gov.uk/hadobs/hadcrut4/index.html>, 2016.
- [7] H. Ritchie, M. Roser, “CO₂ and Greenhouse Gas Emissions - Our World in Data,” can be found under <https://ourworldindata.org/co2-and-other-greenhouse-gas-emissions>, 2020.
- [8] Naciones Unidas, *United Nations Framework Convention on Climate Change Paris Agreement*, 2015.
- [9] “Renewables are stronger than ever as they power through the pandemic,” can be found under <https://www.iea.org/news/renewables-are-stronger-than-ever-as-they-power-through-the-pandemic>, 2021.

-
- [10] F. Schipper, D. Aurbach, *Russ. J. Electrochem.* 2016, 52, 1095.
- [11] “Eléctricos, híbridos, diésel y gasolina: ¿cuántas emisiones producen en su vida útil?” can be found under <https://www.caranddriver.com/es/coches/planeta-motor/a30780438/emisiones-contaminantes-segun-tipo-coche>, 2020.
- [12] A. Yoshino, K. Sanechika, T. Nakajima, *Secondary Battery*, 1987, US4668595A.
- [13] M. Yoshio, R. J. Brodd, A. Kozowa, *Lithium-Ion Batteries. Science and Technologies*, Springer, 2009.
- [14] S. Moitzheim, B. Put, P. M. Vereecken, *Adv. Mater. Interfaces* 2019, 6, 1.
- [15] A. Etxebarria Dueñas, Doctoral Thesis, Study of Li Metal Anode Surface: Interaction with Atmospheric Gases and Impact of Impurities in Electrochemistry, Euskal Herriko Unibertsitatea, 2020.
- [16] M. Farag, Doctoral Thesis, Thermal-Electrochemical Modeling and State of Charge Estimation for Lithium Ion Batteries in Real-Time Applications, mcmaster university, 2017.
- [17] A. Manthiram, X. Yu, S. Wang, *Nat. Rev. Mater.* 2017, 2, 1.
- [18] Z. Wu, Z. Xie, A. Yoshida, Z. Wang, X. Hao, A. Abudula, G. Guan, *Renew. Sustain. Energy Rev.* 2019, 109, 367.
- [19] T. Famprakis, P. Canepa, J. A. Dawson, M. S. Islam, C. Masquelier, *Nat. Mater.* 2019, 18, 1278.
- [20] S. Xia, X. Wu, Z. Zhang, Y. Cui, W. Liu, *Chem* 2019, 5, 753.
- [21] J. Janek, W. G. Zeier, *Nat. Energy* 2016, 1, 1.
- [22] J. Li, C. Ma, M. Chi, C. Liang, N. J. Dudney, *Adv. Energy Mater.* 2015, 5, 1.
- [23] N. J. Dudney, B. J. Neudecker, *Curr. Opin. Solid State Mater. Sci.* 1999, 4, 479.
- [24] S. Lobe, A. Bauer, S. Uhlenbruck, D. Fattakhova-Rohlfing, *Adv. Sci.* 2021, 8, 2002044.
- [25] M. Armand, M. Tarascon, *Nature* 2008, 451, 652.

- [26] G. Qian, X. Liao, Y. Zhu, F. Pan, X. Chen, Y. Yang, *ACS Energy Lett.* 2019, 4, 690.
- [27] D. Mercer, *Global Connected and IOT Device Forecast Update*, 2019.
- [28] A. Rambabu, S. B. Krupanidhi, P. Barpanda, *Proc. Indian Natl. Sci. Acad.* 2019, 85, 121.
- [29] J. F. M. Oudenhoven, L. Baggetto, P. H. L. Notten, *Adv. Energy Mater.* 2011, 1, 10.
- [30] N. J. Dudney, *Electrochem. Soc. Interface* 2008, 17, 44.
- [31] J.B.Bates, G.R.Gruzalski, N.J.Dudney, C.F.Luck, X. Yu, *Solid State Ionics* 1994, 70–71, 619.
- [32] J. F. Ribeiro, M. F. Silva, J. P. Carmo, L. M. Gonçalves, M. M. Silva, J. H. Correia, *NanoScience And Technology*, 2012, pp. 575–619.
- [33] X. Liang, F. Tan, F. Wei, J. Du, *IOP Conf. Ser. Earth Environ. Sci.* 2019, 218.
- [34] C. F. Xiao, J. H. Kim, D. Choi, Y. C. Park, J. H. Kim, J. Park, Y. J. Kim, H. S. Kim, *J. Alloys Compd.* 2019, 801, 550.
- [35] M. Zhang, N. Garcia-Araez, A. L. Hector, *J. Mater. Chem. A* 2018, 6, 14483.
- [36] D. Liu, W. Zhu, J. Trottier, C. Gagnon, F. Barray, A. Guerfi, A. Mauger, H. Groult, C. M. Julien, J. B. Goodenough, K. Zaghib, *RSC Adv.* 2014, 4, 154.
- [37] J. Liu, A. Manthiram, *Chem. Mater.* 2009, 21, 1695.
- [38] T. Ohzuku, K. Ariyoshi, S. Takeda, Y. Sakai, *Electrochim. Acta* 2001, 46, 2327.
- [39] Q. Zhong, A. Bonakdarpour, M. Zhang, Y. Gao, J. R. Dahn, *J. Electrochem. Soc.* 1997, 144, 205.
- [40] N. J. Dudney, *J. Power Sources* 2000, 89, 176.
- [41] Y. Su, J. Falgenhauer, A. Polity, T. Leichtweiß, A. Kronenberger, J. Obel, S. Zhou, D. Schlettwein, J. Janek, B. K. Meyer, *Solid State Ionics* 2015, 282, 63.
- [42] J. F. Whitacre, C. W. West, V. B. Ratnakumar, *J Electrochem Soc* 2003, 150,

A1676.

- [43] P. Schichtel, M. Geiß, T. Leichtweiß, J. Sann, D. A. Weber, J. Janek, *J. Power Sources* 2017, 360, 593.
- [44] W. Y. Liu, Z. W. Fu, Q. Z. Qin, *Thin Solid Films* 2007, 515, 4045.
- [45] J. Glenneberg, F. Andre, I. Bardenhagen, F. Langer, J. Schwenzel, R. Kun, *J. Power Sources* 2016, 324, 722.
- [46] Y. Di Zhang, Y. Li, X. H. Xia, X. L. Wang, C. D. Gu, J. P. Tu, *Sci. China Technol. Sci.* 2015, 58, 1809.
- [47] T. Ohzuku, R. J. Brodd, *J. Power Sources* 2007, 174, 449.
- [48] C. M. Julien, A. Mauger, O. M. Hussain, *Materials (Basel)*. 2019, 12, 1.
- [49] X. Zhu, Z. Guo, G. Du, P. Zhang, H. Liu, *Surf. Coatings Technol.* 2010, 204, 1710.
- [50] B. Wang, J. B. Bates, F. X. Hart, B. C. Sales, R. A. Zuhr, J. D. Robertson, *J. Electrochem. Soc.* 1996, 143, 3203.
- [51] J. A. Coca, Doctoral Thesis, Electrochemical and Surface Study of Lithium-Rich Transition Metal Oxides Used as Cathodes in Lithium-Ion Batteries, University of Liverpool, 2019.
- [52] Q. Tao, L. Wang, C. Shi, J. Li, G. Chen, Z. Xue, J. Wang, S. Wang, H. Jin, *Mater. Chem. Front.* 2021, 5, 2607.
- [53] Z. Ye, L. Qiu, W. Yang, Z. Wu, Y. Liu, G. Wang, Y. Song, B. Zhong, X. Guo, *Chem. - A Eur. J.* 2021, 27, 4249.
- [54] N. Nitta, F. Wu, J. T. Lee, G. Yushin, *Mater. Today* 2015, 18, 252.
- [55] D. Yu, Y. Qiao, X. Zhou, J. Wang, C. Li, C. Chen, Q. Huo, *J. Power Sources* 2014, 266, 1.
- [56] N. H. Kwon, T. Drezen, I. Exnar, I. Teerlinck, M. Isono, M. Graetzel, *Electrochem. Solid-State Lett.* 2006, 9, 7.
- [57] G. X. Wang, S. Needham, J. Yao, J. Z. Wang, R. S. Liu, H. K. Liu, *J. Power Sources* 2006, 159, 282.

- [58] L. X. Yuan, Z. H. Wang, W. X. Zhang, X. L. Hu, J. T. Chen, Y. H. Huang, J. B. Goodenough, *Energy Environ. Sci.* 2011, 4, 269.
- [59] V. Fuentes, “Las baterías de litio-ferrofosfato ganan terreno en el vehículo eléctrico en China, gracias a su durabilidad,” can be found under <https://www.motorpasion.com/coches-hibridos-alternativos/baterias-litio-ferrofosfato-ganan-terreno-vehiculo-electrico-china-gracias-a-su-durabilidad>, 2020.
- [60] M. M. Thackeray, *Prog. Solid State Chem.* 1997, 25, 1.
- [61] C. Schilcher, C. Meyer, A. Kwade, *Energy Technol.* 2016, 4, 1604.
- [62] A. Yamada, M. Tanaka, K. Tanaka, K. Sekai, *J. Power Sources* 1999, 81–82, 73.
- [63] Q. Liu, S. Wang, H. Tan, Z. Yang, J. Zeng, *Energies* 2013, 6, 1718.
- [64] T. Ohzuku, S. Takeda, M. Iwanaga, *J. Power Sources* 1999, 81–82, 90.
- [65] R. Thirunakaran, B. ramesh babu, N. Kalaiselvi, P. Periasamy, T. prem kumar, n g Renganathan, M. Raghavan, N. Muniyandi, 2016, 24, 51.
- [66] G. Singh, A. Panwar, A. Sil, G. Sudipto, *Ceram. - Silikaty* 2009, 53, 260.
- [67] J. M. Tarascon, *J. Electrochem. Soc.* 1991, 138, 2859.
- [68] K. Amine, H. Tukamoto, H. Yasuda, Y. Fujita, *J. Power Sources* 1997, 68, 604.
- [69] T. F. Yi, J. Mei, Y. R. Zhu, *J. Power Sources* 2016, 316, 85.
- [70] X. Fang, M. Ge, J. Rong, Y. Che, N. Aroonyadet, X. Wang, Y. Liu, A. Zhang, C. Zhou, *Energy Technol.* 2014, 2, 159.
- [71] A. Manthiram, K. Chemelewski, E. S. Lee, *Energy Environ. Sci.* 2014, 7, 1339.
- [72] F. Lyu, Z. Sun, B. Nan, S. Yu, L. Cao, M. Yang, M. Li, W. Wang, S. Wu, S. Zeng, H. Liu, Z. Lu, *ACS Appl. Mater. Interfaces* 2017, 9, 10699.
- [73] W. J. Lee, T. H. Hwang, J. O. Hwang, H. W. Kim, J. Lim, H. Y. Jeong, J. Shim, T. H. Han, J. Y. Kim, J. W. Choi, S. O. Kim, *Energy Environ. Sci.* 2014, 7, 621.

-
- [74] M. Li, W. Wang, M. Yang, F. Lv, L. Cao, Y. Tang, R. Sun, Z. Lu, *RSC Adv.* 2015, 5, 7356.
- [75] J. Graetz, C. C. Ahn, R. Yazami, B. Fultz, *Electrochem. Solid-State Lett.* 2003, 6, A194.
- [76] B. Laforge, L. Levan-Jodin, R. Salot, A. Billard, *J. Electrochem. Soc.* 2008, 155, A181.
- [77] M. Wu, X. Li, Q. Zhou, H. Ming, J. Adkins, J. Zheng, *Electrochim. Acta* 2014, 123, 144.
- [78] W. Li, X. Sun, Y. Yu, *Small Methods* 2017, 1, 1600037.
- [79] T. F. Yi, S. Y. Yang, Y. Xie, *J. Mater. Chem. A* 2015, 3, 5750.
- [80] B. Zhao, R. Ran, M. Liu, Z. Shao, *Mater. Sci. Eng. R Reports* 2015, 98, 1.
- [81] F. Wunde, F. Berkemeier, G. Schmitz, *J. Power Sources* 2012, 215, 109.
- [82] C. L. Wang, Y. C. Liao, F. C. Hsu, N. H. Tai, M. K. Wu, *J. Electrochem. Soc.* 2005, 152, A653.
- [83] M. Hirayama, K. Kim, T. Toujigamori, W. Cho, R. Kanno, *Dalt. Trans.* 2011, 40, 2882.
- [84] S. H. Yu, X. Feng, N. Zhang, J. Seok, H. D. Abruña, *Acc. Chem. Res.* 2018, 51, 273.
- [85] B. A. Boukamp, R. A. Huggins, *Mater. Res. Bull.* 1978, 13, 23.
- [86] L. Baggetto, N. A. M. Verhaegh, R. A. H. Niessen, F. Roozeboom, J. C. Jumas, P. H. L. Notten, *J. Electrochem. Soc.* 2010, 157, A340.
- [87] Z. Jiang, Q. Han, S. Wang, H. Wang, *ChemElectroChem* 2019, 6, 2970.
- [88] C. Wang, K. Fu, S. P. Kammampata, D. W. McOwen, A. J. Samson, L. Zhang, G. T. Hitz, A. M. Nolan, E. D. Wachsman, Y. Mo, V. Thangadurai, L. Hu, *Chem. Rev.* 2020, 120, 4257.
- [89] R. Murugan, V. Thangadurai, W. Weppner, *Angew. Chemie Int. Ed.* 2007, 46, 7778.
- [90] M. Saccoccio, J. Yu, Z. Lu, S. C. T. Kwok, J. Wang, K. K. Yeung, M. M. F. Yuen,

- F. Ciucci, *J. Power Sources* 2017, 365, 43.
- [91] R. Pfenninger, M. Struzik, I. Garbayo, E. Stilp, J. L. M. Rupp, *Nat. Energy* 2019, 4, 475.
- [92] M. Rawlence, A. N. Filippin, A. Wäckerlin, T. Y. Lin, E. Cuervo-Reyes, A. Remhof, C. Battaglia, J. L. M. Rupp, S. Buecheler, *ACS Appl. Mater. Interfaces* 2018, 10, 13720.
- [93] J. B. Bates, N. J. Dudney, G. R. Gruzalski, R. A. Zuhr, A. Choudhury, C. F. Luck, J. D. Robertson, *Solid State Ionics* 1992, 53–56, 647.
- [94] B. Wang, B. S. Kwak, B. C. Sales, J. B. Bates, *J. Non. Cryst. Solids* 1995, 183, 297.
- [95] J. F. M. Oudenhoven, L. Baggetto, P. H. L. Notten, *Adv. Energy Mater.* 2011, 1, 10.
- [96] L. Li, X. Xue, S. Liu, H. Zhou, *Ionics (Kiel)*. 2017, 23, 1451.
- [97] P. D. Mani, S. Saraf, V. Singh, M. Real-Robert, A. Vijayakumar, S. J. Duranceau, S. Seal, K. R. Coffey, *Solid State Ionics* 2016, 287, 48.
- [98] K. F. Chiu, C. C. Chen, K. M. Lin, C. C. Lo, H. C. Lin, W. H. Ho, C. S. Jiang, *J. Vac. Sci. Technol. A Vacuum, Surfaces, Film.* 2010, 28, 568.
- [99] B. Wang, B. C. Chakoumakos, B. C. Sales, B. S. Kwak, J. B. Bates, *J. Solid State Chem.* 1995, 115, 313.
- [100] K. J. Rao, *Structural Chemistry of Glasses*, Elsevier, 2002.
- [101] H. Y. P. Hong, *Mater. Res. Bull.* 1976, 11, 173.
- [102] J. B. Goodenough, H. Y. P. Hong, J. A. Kafalas, *Mater. Res. Bull.* 1976, 11, 203.
- [103] F. Zheng, M. Kotobuki, S. Song, M. O. Lai, L. Lu, *J. Power Sources* 2018, 389, 198.
- [104] J. Christopher, S. Muy, A. Grimaud, H. Chang, N. Pour, S. F. Lux, O. Paschos, *Am. Chem. Soc.* 2016.
- [105] J. Lu, Y. Li, *J. Mater. Sci. Mater. Electron.* 2021, 32, 9736.

-
- [106] F. Aguesse, V. Roddatis, J. Roqueta, P. García, D. Pergolesi, J. Santiso, J. A. Kilner, *Solid State Ionics* 2015, 272, 1.
- [107] K. K. Bharathi, H. Tan, S. Takeuchi, L. Meshi, H. Shen, J. Shin, I. Takeuchi, L. A. Bendersky, *RSC Adv.* 2016, 6, 61974.
- [108] J. K. Ahn, S. G. Yoon, in *Electrochim. Acta*, Pergamon, 2004, pp. 371–374.
- [109] J.-K. Ahn, S.-G. Yoon, C. S. Kim, *J. Vac. Sci. Technol. B Microelectron. Nanom. Struct.* 2005, 23, 2089.
- [110] S. I. Furusawa, H. Tabuchi, T. Sugiyama, S. Tao, J. T. S. Irvine, *Solid State Ionics* 2005, 176, 553.
- [111] J. Z. Lee, Z. Wang, H. L. Xin, T. A. Wynn, Y. S. Meng, *J. Electrochem. Soc.* 2017, 164, A6268.
- [112] N. Kuwata, S. Kudo, Y. Matsuda, J. Kawamura, *Solid State Ionics* 2014, 262, 165.
- [113] H. Li, W. C. West, M. Motoyama, Y. Iriyama, *Thin Solid Films* 2016, 615, 210.
- [114] Z. Wang, D. Santhanagopalan, W. Zhang, F. Wang, H. L. Xin, K. He, J. Li, N. Dudney, Y. S. Meng, *Nano Lett.* 2016, 16, 3760.
- [115] A. Sepúlveda, J. Speulmanns, P. M. Vereecken, *Sci. Technol. Adv. Mater.* 2018, 19, 454.
- [116] A. A. Talin, D. Ruzmetov, A. Kolmakov, K. McKelvey, N. Ware, F. El Gabaly, B. Dunn, H. S. White, *ACS Appl. Mater. Interfaces* 2016, 8, 32385.
- [117] Q. Xia, S. Sun, J. Xu, F. Zan, J. Yue, Q. Zhang, L. Gu, H. Xia, *Small* 2018, 14, 1.
- [118] B. Smith, “Applications of Thin Film Batteries,” can be found under <https://www.azom.com/article.aspx?ArticleID=15741>, 2018.

Chapter 2

Experimental techniques

This chapter describes the basic principles of the deposition technologies employed to grow the different components of the battery, as well as the main characterization techniques employed to determine the microstructural, morphological, elemental, and electrochemical properties of the prepared materials.

2.1. Thin film deposition

This section describes the different techniques used in this thesis for the deposition of the thin films and coatings. Thin film deposition consists of growing a very thin layer of material (between a few nanometers and about 100 micrometers) onto the surface of the selected substrate. Thin film deposition manufacturing technologies are extensively used in today's semiconductors, photovoltaics, electronic devices, decorative and protective films, CDs, optical anti-reflective treatments, and, also, in thin film battery industries.^[1] But what makes it useful is that there is the possibility of sequentially deposit several materials to form well-defined multilayer systems.^[2]

Thin film deposition techniques are generally divided into two groups: chemical vapor deposition (CVD) and physical vapor deposition (PVD). The CVD is based on the reaction of a gas mixture on a given surface inside a vacuum chamber leaving a chemically deposited thin film coating. While the PVD refers to a process in which the material goes from a condensed phase to a vapor phase, using mechanical, electromechanical, or thermodynamic processes, and going then back to a thin film condensed phase on a substrate.^[3]

Among the PVD techniques, the most relevant processes for the all solid-state thin film batteries are magnetron sputtering, evaporation (thermal and electron beam), and pulsed laser deposition (PLD). The first two techniques are well-established in the present industry, as they are efficient in depositing large surface areas in the square meter range at significantly high deposition rates, including roll-to-roll processes, whereas PLD has been limited to smaller substrate sizes with low deposition rates.

The selected processes for this thesis are magnetron sputtering and thermal evaporation, which are two of the most widely used PVD techniques. Before describing in detail these two techniques, the following section explains the process of thin film growth.

2.1.1. Thin film nucleation and growth

Figure 2.1 shows schematically the growth of the thin film coating.^[4] Depending on the energy at which a vapor phase material impinges on the substrate, it can diffuse over the surface to a greater or lesser extent, and even return to the vapor phase (in case of excessively high incoming energy). As they diffuse through the surface of the substrate, there are favorable positions for the anchoring of the adsorbed atoms, namely surface defects such as vacancies, steps, kinks or adatoms, generating a suitable place for nucleation. These nucleation sites are formed by individual atoms or small aggregates of atoms, on which the layer begins to grow with the arrival of new atoms from the vapor phase.

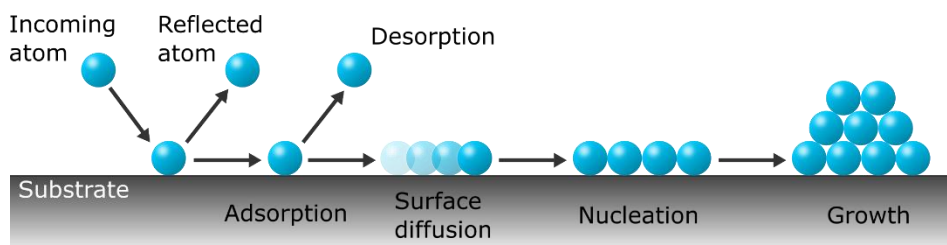


Figure 2.1: Schematic of the nucleation and growth steps of the coating.

There are different ways to increase diffusion by applying energy. This energy can be received either by elevating the substrate temperature or by bombarding with high energetic ions (transferring linear energy). In this way, the density and the crystallinity of the obtained layer can be enhanced. However, if the applied energy is excessive, it can generate high stresses inside the layer that will result in crack formation.^[5]

According to the ratio between the binding energy between the atoms (E_B) and the interaction energy of the atom with the substrate (E_{adh}) different types of mechanisms can be distinguished: Volmer-Weber model ($E_B > E_{adh}$), Frank-van der Merwe model ($E_B < E_{adh}$), and Stranski-Krastanov model (combination).^[4,5] In the first model, the E_B is assumed to be larger than the E_{adh} , so there is a poor chemical or structural affinity between the substrate and the material to be deposited. In this case, the atoms diffuse along the surface until they find other atoms that are already fixed to the substrate, thus interacting with each other, and forming small nuclei. This type of growth is characterized by the formation of islands that cover the substrate completely as they grow. The second model is based on the consideration that E_{adh} is greater than E_B , which occurs when the substrate and the material to be deposited are chemically affine or have a similar crystalline structure. The incoming atoms are attached to the substrate as they arrive to the surface. When new atoms arrive, the surface is gradually covered to form of a monolayer that will grow in a layer-by-layer fashion. Finally, the Stranski-Krastanov model is an intermediate situation between the two previous models. One or more monolayers are formed first (Frank-van der Merwe model), with a subsequent formation of islands (Volmer-Weber model). In other words, upon reaching a critical layer thickness, which depends on the strain and chemical potential of the deposited film, the growth continues through nucleation and coalescence of adsorbed islands.

Figure 2.2 shows the progression of each model step by step.

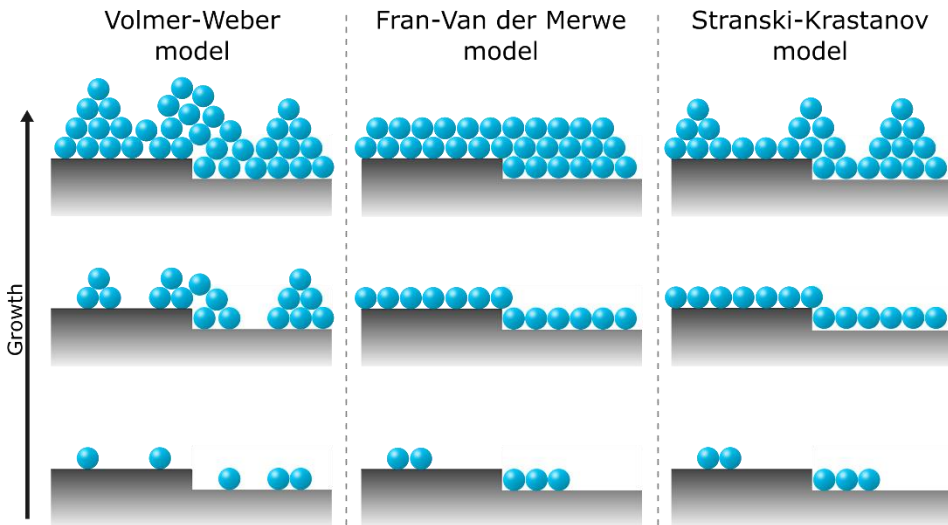


Figure 2.2: Schematic representation of the different growth models.

Several growth models correlate the deposition variables, such as temperature, with the structure and properties of the coating. Considering the substrate temperature (T_s) and the melting temperature of the deposited material (T_m), Movcham and Demchysim (1969)^[6] developed a model that predicted the coating growth structure (structure zones model, SZM), which was later completed by Thornton and Messier by adding the working pressure variable.^[7] Depending on the ratio between T_s and T_m (T_s/T_m), several zones can be distinguished. **Figure 2.3** shows the schematic diagram of the different growth zones according to the ratio T_s/T_m .^[4,6]

Zone I ($0 < \frac{T_s}{T_m} < 0.1$):

The zone I is associated with the lowest value of T_s/T_m . In this case, the substrate temperature is so low that the incident atoms have not enough energy to diffuse widely, being the surface diffusion negligible and forcing the atoms to remain in the vicinity of the contact zone. This, along with shadowing effects on the surface (produced by roughness and elevated regions) leads to columnar-type structures with multiple intermediate paths in the direction of arrival of the atoms. This phenomenon is favored at high working pressures, due to the thermalization of the atoms before reaching the substrate surface.

Zone T ($0.1 < \frac{T_s}{T_m} < 0.3$):

The zone T is known as the transition zone where some surface diffusion of adatoms can occur. The layer structure develops competitively between adjacent crystals with different orientations. This results in a typical V-shaped grains near the nucleation layer which culminates in a columnar morphology at higher film thicknesses.^[8]

Zone II ($0.3 < \frac{T_s}{T_m} < 0.5$):

As the substrate temperature increases, the migration of atoms between the formed grain boundaries is favored. The preferred orientation of the crystal is thereby revealed. This results in columnar coatings whose width increases with temperature. In addition, the tops of the faceted columns give rise to a rougher surface than the previous zone.

Zone III ($0.5 < \frac{T_s}{T_m} < 1$):

Due to the high temperature of the substrate, it can be considered that bulk annealing of the layer is taking place during deposition in zone III. The structure is dominated by the phenomena of internal diffusion and recrystallization, caused by the segregation of impurities from the substrate towards the surface of the grains. These impurities hinder crystal growth and give rise to secondary nucleation phenomena. As a result, the morphology of the layers evolves from columnar type (low T) to more isotropic or equiaxed crystallite shape (high T).

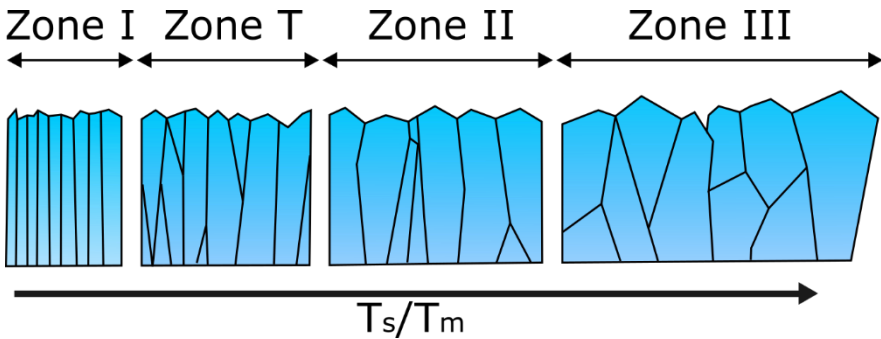


Figure 2.3: Diagram of the different structural zones as a function of T_s/T_m .

2.1.2. Magnetron sputtering

Sputtering is the process whereby atoms or molecules of a solid material are extracted or ejected from it by the bombardment of high kinetic energy ions.^[9] These charged particles transfer their linear momentum to the surface atoms of the solid material, known as target, producing a cascade of atomic collisions that results in the emission of a flow of particles from the target to the substrate located at a certain distance, where they condense to form a coating.^[5]

The sputtering process is shown in **Figure 2.4**. The process starts when the substrate is placed in the vacuum chamber and an inert gas, usually Argon, is leaked in the chamber. A negative potential difference is then applied between the substrate and the target. Free electrons flow off from the negatively charged target and collide with the Argon atoms present in the chamber, predominantly close to the target. This collision drives the Ar outer shell electrons off, forming positive Argon ions. These ionized particles generate a glowing plasma near the surface of the target, as illustrative example, **Figure 2.5** shows an image of the target, substrate and plasma during the sputtering process. The negatively charged target attracts the positive Ar ions to its surface at a very high velocity. Upon collision, a large energy transfer occurs between the positive Ar ion and the atoms of the target surface. When the transferred energy is higher than the binding energy of the target atom in the crystalline network, a cascade effect of

collisions between atoms will result in the sputtering of atoms from the surface of the target that will travel through the vacuum chamber to be deposited as a thin film on the surface of the substrate. Besides the atomic sputtering, secondary electrons are emitted from the target surface and sustain the glow discharge. [1,9]

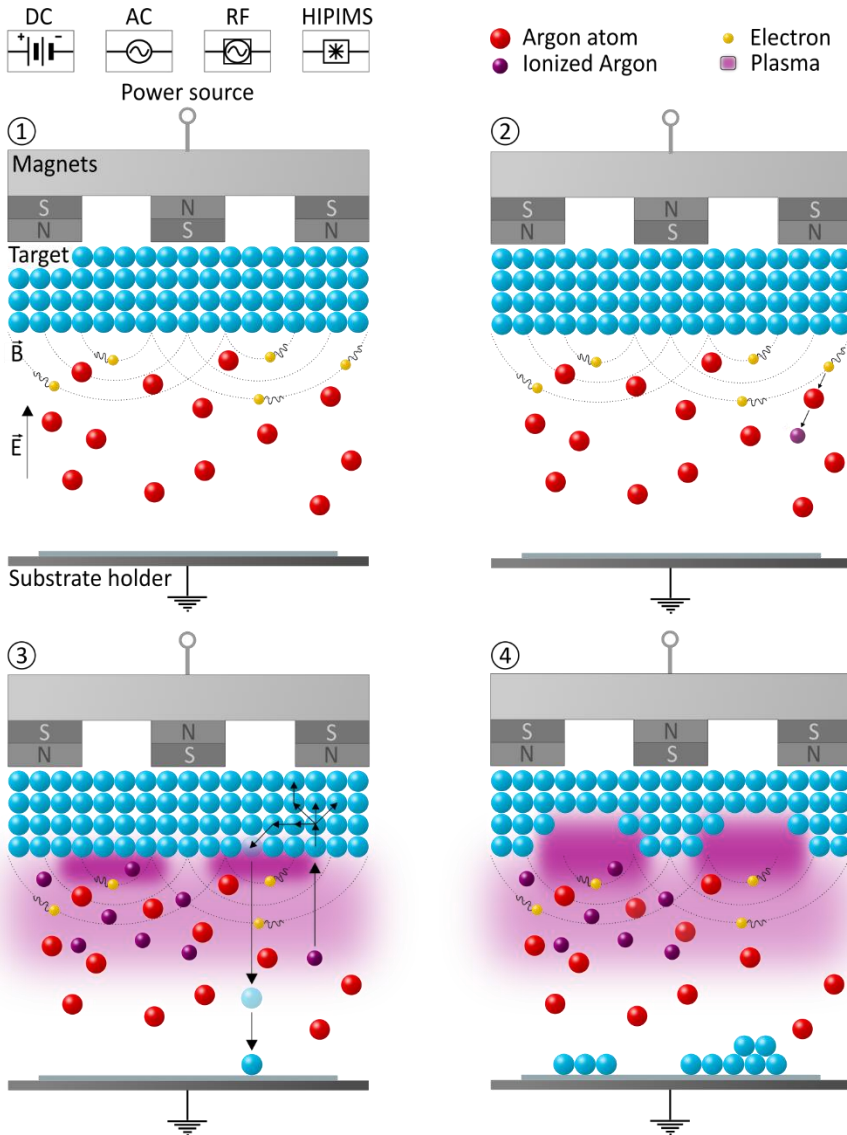


Figure 2.4: Diagram of the different steps of a magnetron sputtering process. In the top, the various sputtering power sources are listed: direct current (DC), alternating current (AC), radiofrequency (RF) and high-power impulse magnetron sputtering (HIPIMS).

In magnetron sputtering deposition magnets are employed in the negative cathode to trap electrons near the target surface, thus increasing the Argon ionization and thereby raising the deposition rate. Depending on the magnets layout, there are two types of magnetron configurations. On the one hand, when the magnetic fluxes of the outer and inner poles are the same, the configuration is the so called balanced. In this case, the magnetic field confines the plasma just nearby the target surface. Therefore, the substrate is hardly bombarded by species different from those present in the target, being suitable for heat-sensitive substrates. On the other hand, the unbalanced configuration is based on the disequilibrium of the magnetic flux through one of the poles, orienting the magnetic field lines towards the chamber walls or the substrate. In this way, the plasma is not tightly confined in the target region but can flow towards the substrate (as well as the secondary electrons). Hence, the substrate receives additional bombardment from species other than the target during thin film growth, the ionic energy can be tuned by a substrate bias.^[10,11] Note that the magnetic lines drawn in the previous figure correspond to the balanced configuration, which is the one we used for this work.

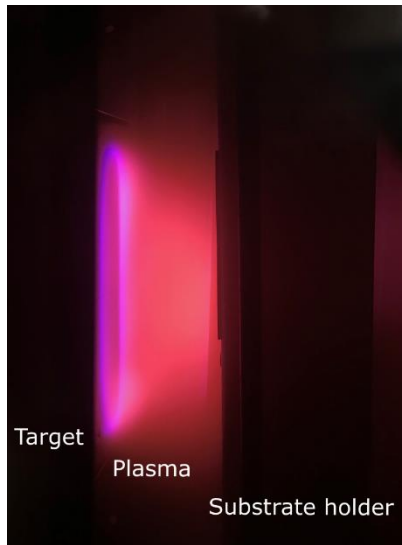


Figure 2.5: Plasma during AC magnetron sputtering process at Tecnalia.

During sputtering processes, it is possible to use a non-inert gas, other than argon, such as oxygen or nitrogen. These gases are often used instead of or in combination with argon. By introducing a non-inert gas, which is also ionized, we can induce chemical reactions with the target material vapor cloud and produce new molecular compounds which will be deposited on the substrate. This

variation of the sputtering technique is known as reactive sputtering and is widely used in the manufacturing of composite coatings. For example, starting from a chromium target, it is possible to obtain a chromium nitride layer by using nitrogen as process gas. Moreover, the partial pressure of the non-inert gas used will influence the stoichiometry and the characteristics of the produced molecular film, obtaining layers of desired properties. However, care must be taken with the surface poisoning of the target, since it is known that some of these reactive gas ions can chemically react irreversibly with the atoms on the target surface and ultimately change the elemental concentration, the conductivity, and the sputtering ability of the target. If this poisoning occurs, the target surface can be reconditioned by sputtering the top layer using only argon as the process gas.^[12]

Power sources

There are several different types of power supplies used to drive the magnetron sputtering heads. They differ by the way the potential is applied to the magnetron head in terms of time and intensity. **Figure 2.6** shows the voltage profiles of the different power sources used.

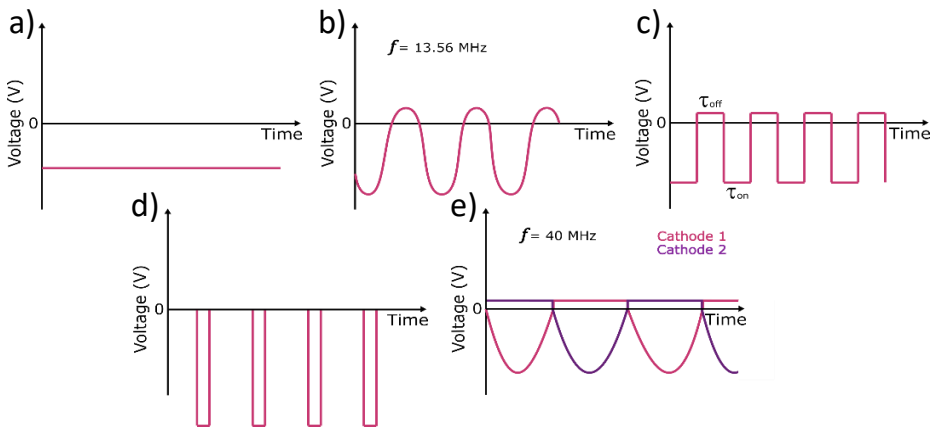


Figure 2.6: Voltage profiles for the different power supplies, a) DC, b) RF, c) pulsed DC, d) HIPIMS, and e) Mid Frequency AC dual.

Direct Current (DC)

DC power sources provide a constant potential difference as a function of time (typically in the -2 to -5 kV range).^[13] It is generally used with electrically conductive target materials and is characterized by its easy control and relatively low energy cost. However, DC sputtering has some limitations when dealing with

dielectric materials (e.g. aluminum oxide or silicon oxide). The surface of these materials becomes charged as it is bombarded by positively charged ions, this positive charge cannot be compensated due to their insulating nature. Increasing the charge excessively could counteract the applied potential difference and thus quench the plasma. This charge buildup can also result in film quality issues induced by electric arc discharge in the plasma.^[13]

The solution to this problem lies in using a time-varying voltage signal whose polarization changes, in such a way that when its charge sign changes, electrons are injected into the target, canceling the positive charge generated on the surface.

Radio Frequency (RF)

In RF sputtering a sinusoidal voltage signal is applied to the magnetron head that alternates the electrical potential of the current to prevent charge accumulation on certain types of dielectric targets. The sinusoidal signal applied has a frequency of 13.56 MHz, which is the one used internationally for RF power equipment.^[14]

By switching the electrical potential with RF sputtering, the surface of the target material can be "cleaned" of a charge buildup upon each voltage cycle. While the sinusoidal cycle is on the negative voltage region, the positively charged ions are accelerated towards the target and sputtering occurs along with charge accumulation. Conversely, when the cycle is at positive voltages, the plasma electrons are accelerated towards the material and neutralize the positive charge accumulated previously.

The RF signal is usually non-symmetrical with respect to zero voltage. The difference in mobility between electrons and ions makes the signal mostly negative. In other words, the lower mass of the electrons needs lower accelerating voltage and time to counteract the charge present on the target.^[5]

Pulsed DC

An alternative to the RF signal that also enables the sputtering of dielectric materials is the pulsed DC signal. This technique consists of a bipolar rectangular signal divided into τ_{on} and τ_{off} (the time when the voltage value is negative and when it is positive, respectively). The duty cycle (η) is defined as the time ratio the load is *on* compared to the time the load is *off* ($\eta=100 \cdot \tau_{on}/(\tau_{on} + \tau_{off})$).^[5] The higher the duty cycle the longer the time it will be at the negative voltage, and hence sputtering off atoms from the target surface. Typically, the positive part

consists of a low voltage and short duration (between ten and twenty percent of the turn-on time), enough to "clean" the target surface from charge accumulation and prepare it for the next voltage cycle.

The pulsed DC power supply has a significantly reduced cost with respect to more expensive RF power supplies. However, pulsed DC processes typically result in electric arc discharge that can be reduced/eliminated by pulsing the DC voltage in the 10-350 kHz range with duty cycles in the 50-90% range.^[15]

HIPIMS

HIPIMS or high-power impulse magnetron sputtering is a relatively recent technique based on the application of a short-lasting high voltage pulses. It generates a high-density plasma that results in a high degree and velocity ionization of the target material without overheating.^[16]

This powerful pulsing ionizes the gas atoms at much higher energy levels than conventional sputtering, greatly increasing the probability of ionizing collisions. The layers deposited with this technique are characterized by high-performance dense coating with good adhesion and uniformity even on complex-shaped substrates.

However, its high-power requirements may demand more energy (30-80%) for equivalent deposition rates than conventional magnetron sputtering.^[16] Moreover, besides its high cost in terms of instrumentation, HIPIMS increases the probability of electric arc discharge at the cathode or target surface.

Mid Frequency AC

Medium frequency AC sputtering is mostly replacing RF sputtering for the coating of dielectric or non-conductive materials since it works in the kHz rather than MHz range (20 to 70 kHz, among them 40 kHz is the most used). This way, requires less sophisticated and expensive power sources (25 to 300 kW), being adaptable to large-scale applications.^[17]

The most efficient use of AC sputtering is with two targets. As the potential continually switches, the compound buildup is maintained at a constant level. This prevents the "disappearing anode" problem present in RF or DC pulsed sputtering, while increasing the deposition rates. AC sputtering provides more efficient use of the power being supplied to the process, in contrast to RF sputtering, where only 50% of the applied power is used.

This technique generally involves the use of dual magnetrons to confine the electrons close to the target and to reduce electric arc discharge for process control, including the abovementioned balanced or unbalanced configurations.^[17]

Equipment used in this work

In this thesis, two different magnetron sputtering systems were used depending on the material to be deposited.

The system mainly used for the cathode deposition at *Tecnalia*, is a semi-industrial Cemecon CC800/8 machine based on mid-frequency (MF) AC dual magnetron sputtering technology, with the additional capability of working in RF and DC modes (**Figure 2.7**). The Cemecon system is composed of four rectangular magnetron heads (88 mm x 200 mm targets), a sample holder with planetary motion, and a substrate heater with medium temperature ability. The system was upgraded with an ion-source IMC75 and gas feedback control from *Gencoa*. The IMC75 ion source will allow the surface preparation of the current collector by etching/cleaning with Ar ions. Whereas the feedback control (including a penning PEM and Speedflo devices from *Gencoa*) allows the precise control of the O₂ partial pressure, hence, of the reactive processes. Also, the included CCD-spectrometer is very useful to control the cathode plasma spectrum. These enhancements in the system were carried out by *Gencoa* as part of the Horizon2020 European project MONBASA (Monolithic Batteries for Spaceship Applications, Grant Agreement No. 687561).

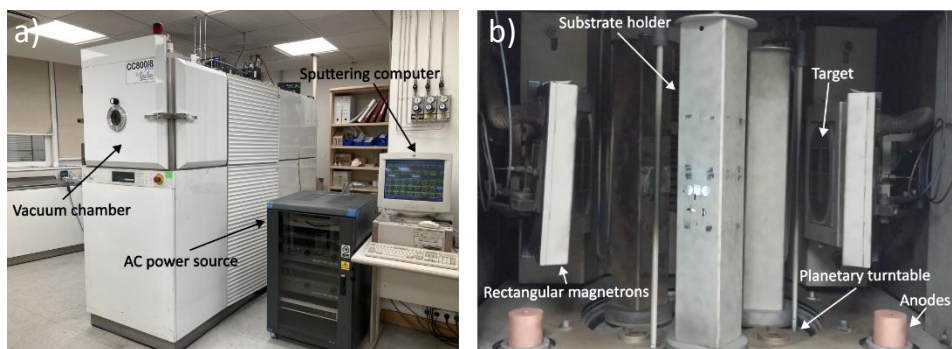


Figure 2.7: a) General view, and b) vacuum chamber of the Cemecon CC800/8 system

The deposition of the ceramic electrolyte was carried out using the magnetron sputtering system at *CIC energigUNE* which is an R&D Pfeiffer classic 500 SP system (**Figure 2.8**) equipped with RF and DC power sources that allow deposition

at low temperatures. During this thesis, the process chamber was equipped with two circular magnetrons (2" targets), a full-face erosion magnetron head (FFE75, 75 mm target from *Gencoa*), ion source IMC75, and feedback control, both from *Gencoa* as well. The FFE75 cathode allowed the decrease of the target to surface distance and, at the same time, it allowed to increase the power applied to the target. The fast entry antechamber modified with an air tight transfer arm allowed the manipulation of air-sensitive samples.

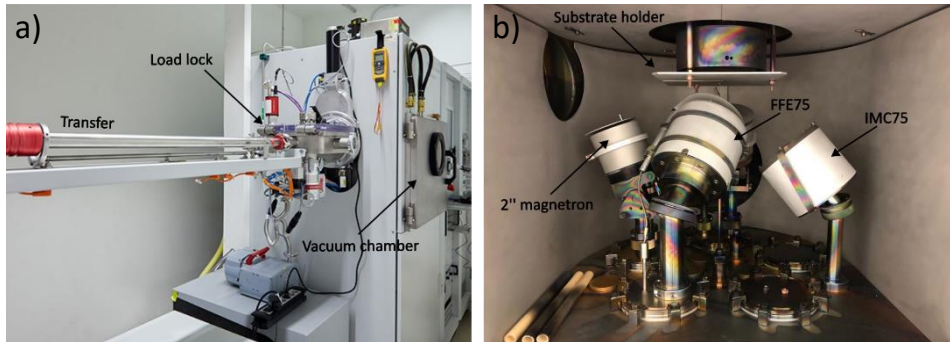


Figure 2.8: a) General view, and b) vacuum chamber of the Pfeiffer classic 500 SP.

2.1.3. Thermal evaporation

Along with magnetron sputtering, thermal evaporation is one of the most widely used PVD techniques in thin film deposition. This method consists of heating a solid material to its melting point inside an ultra-high vacuum chamber (10^{-8} mbar), thus producing a certain vapor pressure of evaporated material that will land in the substrate, adhering as a coating or film.^[18]

Figure 2.9 shows the operation diagram of thermal evaporation. The material to be deposited is usually placed at the bottom of the chamber (typically in a vertical crucible); while the substrate is held upside down at the top of the chamber, orienting the surfaces to be coated towards the heated source material. The Materials deposited by this technique can be pure atomic elements, including metals and non-metals, or even molecules such as oxides and nitrides.^[19]

There are two ways of heating the source material: filament heating and electron beam heating (e-beam evaporation). The first, most often used and the selected illustration for **Figure 2.9**, consists of an electrically resistive heating element or filament (usually tungsten). This method offers the security of using a low voltage, although a very high current is required during the process.^[19] The second method is based on an e-beam gun, where a small and very hot filament

emits electrons that are accelerated by a high voltage to generate an electron beam with considerable energy that will release its energy in the target material. Electron beam systems require of additional safety features.^[7]

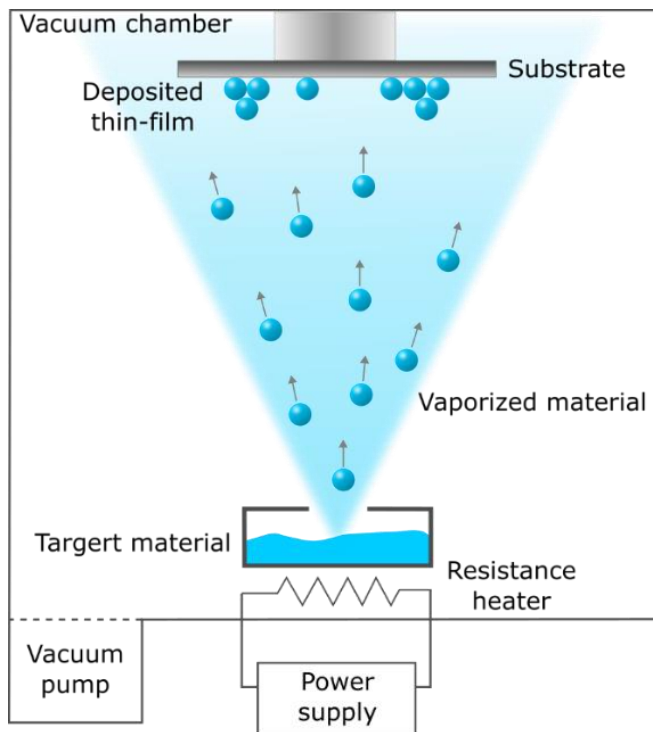


Figure 2.9: Schematics of a typical thermal evaporation system. The source material is heated by a resistance heater driven by a given electrical current.

Equipment used in this work

Figure 2.10 shows the ultra-high vacuum system (10^{-8} mbar) used to thermally evaporate Lithium thin films, being able to deposit from tens of nanometers up to tens of microns. The use of gate valves allows to keep the source or the evaporation chamber in vacuum. In this thesis the Li sources used are commercially available chromate-free metal vapor sources (alvasources, from *Alvatec*). The system permits the sample insertion without exposing to air using an air-tight container (sample transfer arm).

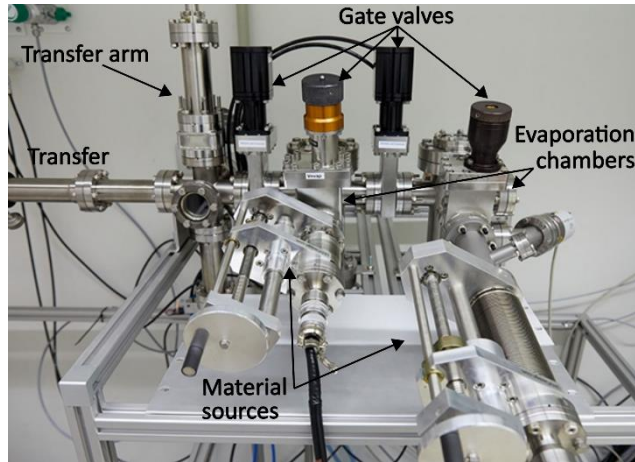


Figure 2.10: Thermal evaporation system at CIC energiGUNE.

2.2. Thickness, roughness, and weight characterization

The mass of the deposited thin films is determined by weighting the SS substrate before and after film deposition using a high precision analytical balance (Mettler Toledo, XP205 model). For air-sensitive samples, this action has been performed in an Ar-filled glove box (H_2O and O_2 levels below 0.1 ppm).

Several techniques have been used to determine the thin film thickness. Among them, the most often used is contact profilometry. For sensitive samples, the scanning electron microscope was employed (described in section 2.3.3.).

2.2.1. Contact profilometry

Mechanical or contact profilometry is a 2D surface analysis technique based on a diamond tip mounted on a stylus whose height variations are accurately recorded. This is used to determine the thin film thickness by measuring the vertical displacement of the tip during a linear scanning of the stylus across the film surface while a constant force on the stylus is maintained.

Successive and parallel scans enable the obtention of the three-dimensional map with nanometer resolution on the vertical axis. Numerous stylus tips are available for different applications, with a radius ranging from 50nm to 25 μ m, and with a high aspect ratio for the characterization of deep and narrow trenches.^[20]

The equipment used in this work was the Veeco Dektak 150 surface profilometer located at *Tecnalia*. Sample preparation for thin film thickness measurement was performed by covering partially single crystal silicon substrates (selected for their

atomically flat surface) with Kapton strips during deposition. The step profiles were recorded at a probing speed of 0.20 mm/s and with a distance between points of 1.5 μm. To improve the statistics, measurements were made at several points on the step.

Roughness analysis

By means of contact profilometry, we can also reproduce the topographic profile of a surface in such a way that information about its roughness can be obtained. The values used to quantify roughness can be interpreted as statistical parameters of profile heights distribution, the most common variables used to characterize the roughness of a surface are: R_a (arithmetic roughness average), R_t (maximum peak-to-valley distance in the analyzed segment), and R_z (average value of different R_t), see **Figure 2.11**.

$$R_a = \frac{1}{L} \int_0^L |y| dx \tag{2.1}$$

$$R_t = y_{\max} - y_{\min} \tag{2.2}$$

$$R_z = \frac{1}{L} \int_0^L R_t dx \tag{2.3}$$

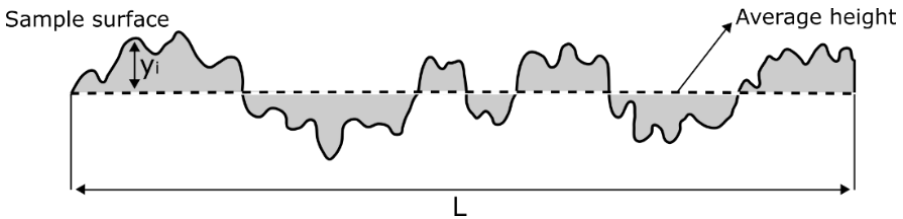


Figure 2.11: Profilometer analysis interpretation with respect to the mean line.

2.2.2. Ellipsometry

Spectroscopic ellipsometry is an optical analysis technique based on the change of polarization state of the light incident on the material to be studied. As it is an optical technique, this analysis is non-destructive and can be used to determine the thickness of thin films, refractive index, extinction coefficient, etc.

The fact that this technology measures changes in polarization state, rather than absolute light intensity, makes ellipsometry a highly sensitive technique even at thin layers of just a few angstroms (Å), being hard to measure with a contact profilometer.^[21]

The spectroscopic ellipsometer GES5 SEMILAB located at *CIC nanoGUNE* was used for thickness measurements of some thin films.

2.3. Structural, morphological, and elemental characterization

This section describes the different techniques used for the structural, morphological, and elemental characterization of the samples prepared in this thesis. The most important techniques are the following: X-ray diffraction (XRD), Raman spectroscopy, electron microscopy (EM), and X-ray photoelectron spectroscopy (XPS).

2.3.1. X-ray diffraction

The crystalline materials show a structure that is the result of the periodic three-dimensional repetition of a specific elemental block, known as unit cell. This periodic distribution of atoms, ions, or molecules, results in the formation of crystalline features such as the so-called crystalline planes. Each crystal belongs to a particular space group, which specifies the symmetry relationship within the unit cell and is characterized by unique cell dimensions. The crystalline structure of a material can be determined by diffraction experiments with different types of incident probes (photons, electrons, neutrons, etc.), which in all cases have an equivalent wavelength comparable to the atomic spacings in the crystal (1 – 10 Å range).^[22]

X-ray diffraction is probably the most employed method to determine the phase, crystal structure, and purity of crystalline solids.^[23] This technique is based on the constructive interference of monochromatic X-rays with the atomic network of crystalline samples. **Figure 2.12** shows Bragg's condition for the reflection of X-rays by a crystal. The monochromatic X-ray beams IB_1 and IB_2 are incident to the planes at an angle of θ_{hkl} , and are scattered by atoms a and y , respectively. These planes with Miller indices hkl are represented as parallel sets of atoms (drawn as black dots in the figure) and with an interplanar spacing of d_{hkl} . Each plane reflects a portion of the incident radiation. Diffracted beams are obtained when reflections in successive parallel atomic planes interfere additively (constructive interference). This takes place when the difference in the path between the reflected beams (RB_1 and RB_2) by two adjacent planes is an integer multiple of their wavelength.^[24,25] Bragg's law, **equation 2.4**, defines the conditions to obtain constructive scattering:

$$n\lambda = 2d_{hkl} \cdot \sin\theta_{hkl} \quad (2.4)$$

Where n is an integer, λ is the wavelength of the incident X-rays, d_{hkl} is the distance between the planes, and θ is the angle between the plane and the incident X-ray beam.

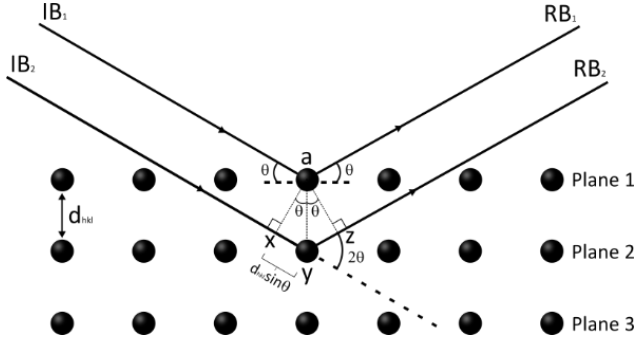


Figure 2.12: Conditions for diffraction and derivation of Bragg’s law.

X-ray diffractometers consist of three basic elements: the X-ray tube (the specific X-ray wavelengths are characteristic of the target material in the tube anode: Cu, Co, Fe, Mo, or Cr), the sample holder, and the X-ray detector.^[26] In the most used measuring configuration of the X-ray diffractometer, the sample rotates in the path of the collimated incident beam at an angle θ while the X-ray detector is mounted on a rotating arm at an angle 2θ (goniometer) to collect the diffracted X-rays,^[27] see Figure 2.13.

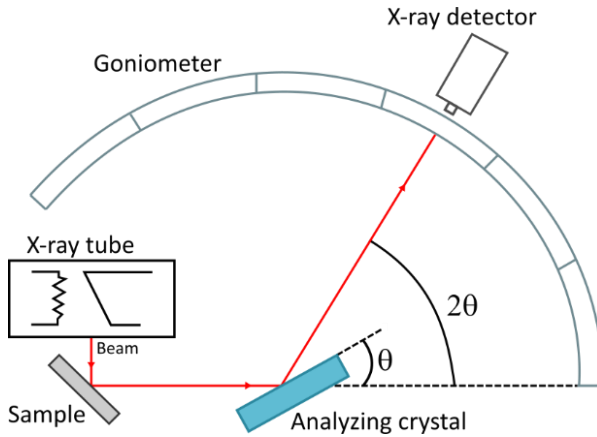


Figure 2.13: Schematic diagram of a diffractometer system (modified from ^[27]).

The obtained diffractogram plots the intensity of the diffracted beam as a function of the 2θ angle. A series of maximums, called Bragg’s reflections, appear in the diffractogram and correspond to the beforementioned constructive interference of waves elastically scattered by the atomic planes of the crystal.

The position and intensity of these peaks can be used to extract information about the crystal structure of the sample under study. In this way, the qualitative analysis of the crystalline structure was carried out by direct comparison with a database using the specific software (Diffract.eva), the Powder Diffraction File database (PDF-2 2010), and the Crystallography Open Database (COD) cards. These databases include interplanar distances, relative intensities, cell parameters, etc.

XRD data were collected using two different diffractometers available at *CIC energiGUNE*: a dichromatic Bruker D8 Advance D8 (Cu $K_{\alpha 1,2}$ $\lambda = 1.5406 \text{ \AA}$, 1.5444 \AA) and a monochromatic Bruker D8 Discover (Cu $K_{\alpha 1}$ $\lambda = 1.5406 \text{ \AA}$) suitable for highly crystalline materials. Both systems can operate in both divergent and parallel beam geometries and are equipped with LYNXEYE (ADVANCE) and LYNXEYE XE (DISCOVER) one-dimensional detectors and with photon energy discrimination to filter out fluorescence radiation. Regarding the sample holders, for the air-sensitive materials (*e.g.* LiPON), an air-tight sample holder with Kapton foil was used, whereas the rest of the measurements at room temperature were carried out using zero-background monocrystalline silicon sample holders. The in-situ temperature dependence XRD analysis of the LNMO sample was measured using the Bruker Advance D8 diffractometer with Co anode X-ray source (Co $K_{\alpha 1,2}$ $\lambda = 1.78897 \text{ \AA}$, 1.79285 \AA). The sample, placed on an alumina holder, was introduced in a high-temperature oven chamber (Anton Paar HTK 1200, Rigaku) and XRD patterns were collected at different temperatures. To simplify the comparison with previously reported XRD patterns of LNMO, the XRD data were recalculated as if Cu radiation was used in all cases by applying Bragg's law (equation 2.4).

2.3.2. Raman spectroscopy

Raman spectroscopy is one of the vibrational spectroscopy techniques most widely used. This family of characterization techniques is defined as non-destructive elemental and structural characterization tool based on the measurement of the vibrational energy of a compound. To each chemical bond corresponds a specific vibrational energy that is considered as a distinctive fingerprint and can be used to determine the structures of compounds by comparing it with the fingerprints of other known compounds.^[28]

The origin of Raman spectra relies on the electronic polarization induced in a material when ultraviolet, visible, or near-infrared radiation is applied, hence, changing its vibrational modes. When monochromatic radiation with a frequency ν_i interacts with matter, most of the radiation is elastically scattered (Rayleigh

scattering, $\nu_s = \nu_i$), while a small part (perhaps 1 part in 10 million) of the incident radiation inelastically interacts with the material ($\nu_s \neq \nu_i$). Unlike Rayleigh scattering, the inelastic scattering provides information about the molecular composition of the sample and is known as Raman scattering, which results in frequency shifts that are characteristic of the chemical nature of the sample, independent of the incident radiation.

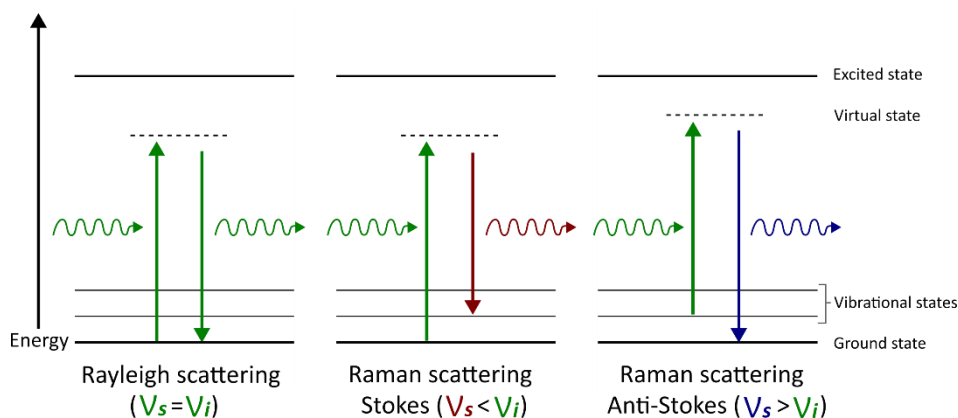


Figure 2.14: Energy-level diagram showing the states involved in Raman scattering.

The Raman shift occurs because photons exchange part of their energy with molecular vibrations in the material. The incident photon transiently brings the molecule to a higher vibrational (or rotational) virtual energy level. The excited molecule soon leaves this state to pass to a stable energy level by emitting a photon. The frequency at which this photon is released depends on the energy jump made. When there is a loss of energy ($h\nu_i > h\nu_s$, where h is the Planck constant) the Raman scattering is designated as Stokes, but when energy is gained it is known as Anti-Stokes (see **Figure 2.14**). The Raman spectroscopy is usually represented using Stokes Raman light as it is more intense than Anti-Stokes. Nonetheless, both represent the same vibrational information of the molecule.^[29]

In a typical Raman experiment, the sample under study is illuminated with a monochromatic laser beam. Electromagnetic radiation from the illuminated spot is collected with a lens and sent through a monochromator. Elastically scattered radiation at the wavelength corresponding to the laser line (Rayleigh Scattering) is filtered out by either a notch filter, edge pass filter, or a bandpass filter, while the rest of the collected light is dispersed onto a detector. **Figure 2.15** shows the diagram of the used Raman spectrometer. The Raman spectrum results are

represented by the scattered optical intensity as a function of the normalized wavenumber ν ($\nu = \nu/c = 1/\lambda$), expressed in cm^{-1} . The typical Raman technique ranges from 100 to 10000 cm^{-1} .^[5]

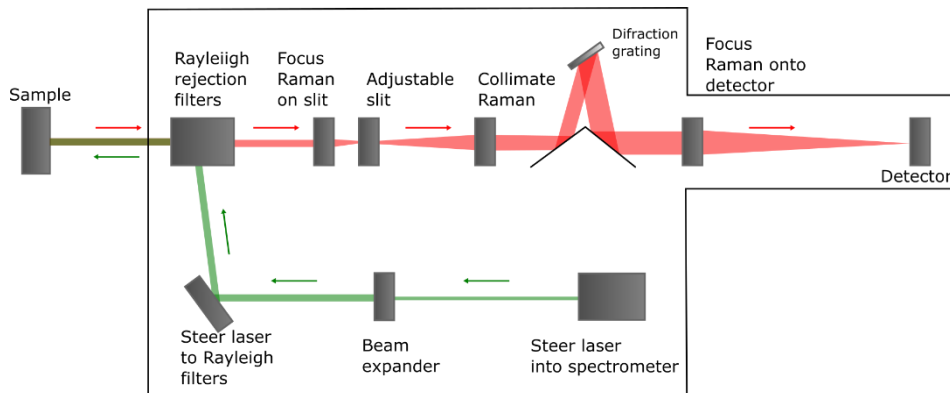


Figure 2.15: Diagram of the Raman spectrometer.

The Raman measurements were carried out using the inVia Renishaw confocal microscope with Raman spectrometer available at *CIC energiGUNE*. This instrument allows a high spatial resolution, in addition to a high-performance video camera and long-distance objectives, high precision motorized platform, and dual-wavelength laser (532 nm and 785 nm). In this work, the sample analysis was performed with a 50× magnification objective and using a green (532 nm wavelength) laser source with a 2.0 μm spot size operating at 0.5 mW. Before measuring the samples related to this thesis, the instrumentation was calibrated using a silicon crystal as a reference (520 cm^{-1}). For the materials under study, we first acquire a general spectrum, focusing subsequently on more accurate measurements at various locations and adjusting the measurement region to the range of interest while increasing the accumulations and exposure time.

2.3.3. Electronic microscopy

The atomic structure, and therefore its properties, are reflected in the morphology of the sample. Therefore, the initial guess about the structure of a material can be obtained from a visual analysis of the material's morphology. In this case, there are submicrometric features that require the use of a microscope with high resolving power. Electron microscopy (EM) is a widespread experimental technique to obtain morphological, structural, and compositional information of the sample under study. EM is based on the analysis of different properties through an electron beam probe. This beam is obtained by the

excitation of a metal filament (cathode) that by thermionic effect emits electrons that are accelerated by the potential difference set between cathode and anode. The voltage range used in EM is in the 5-300 kV range, which results in high energy electrons with an associated wavelength between 0.20-0.5 Å.^[30] To guarantee the adequate functioning of the EM, it is important to avoid electron interaction with air particles, so a high vacuum environment is needed in the analysis chamber.

Depending on the interaction of the electron beam with the sample, there are different types of electron microscopy. The possible interactions are shown in **Figure 2.16**. With the appropriate electron microscopy method, all the desired information (morphological, structural, compositional, etc.) could be obtained.^[31] The most commonly used EM methods are Scanning Electron Microscopy (SEM) and Transmission Electron Microscopy (TEM).

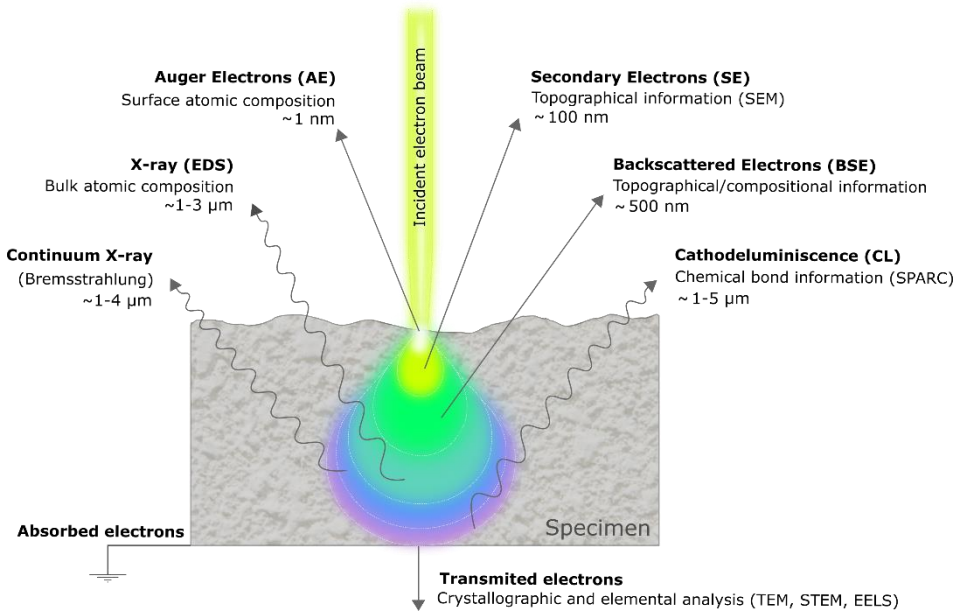


Figure 2.16: General *pear* model sketch of the electron beam interactions on the sample.

Scanning electron microscopy

The scanning electron microscopy (SEM) uses specific detectors to collect the electrons generated from the interaction of the electron beam with the sample surface to create an image that captures the surface characteristics of the sample and can provide information on the shapes, textures, and chemical composition of its constituents. In the SEM, the electron beam, with working voltages in the

range of 3 kV (low vacuum mode) to 30 kV (high vacuum mode), goes through the condenser and objective lenses and is systematically focused and displaced (scanned) along the sample surface by the scanning coils, see **Figure 2.17**.^[32]

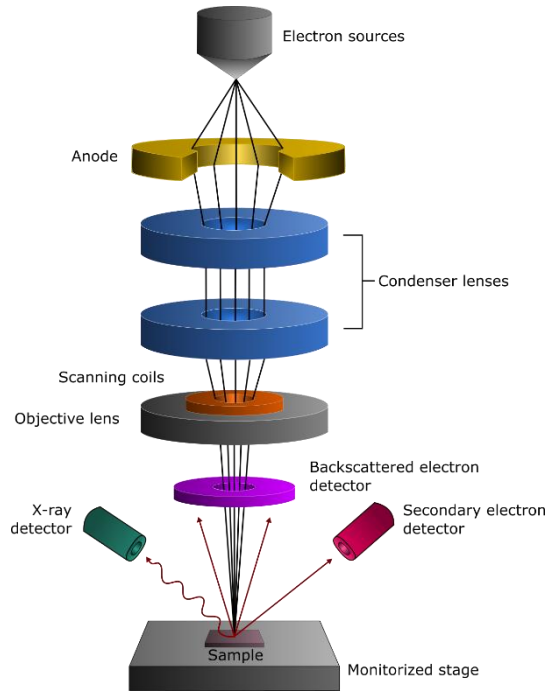


Figure 2.17: Schematic drawing of a Scanning Electron Microscope (SEM) (modified from ^[32]).

The SEM can detect, among the interactions between the electron beam and the sample, secondary electrons (SE), backscattered electrons (BSE), and the X-ray signal (EDS).^[33] SE are produced when an electron of the beam passes close to an atomic nucleus in the sample, providing enough energy to one or more of the atom inner electrons to escape the sample. These electrons have very low energy (below 5 eV), so they can only escape the samples when they are ejected from near surface atoms. This is precisely why they provide valuable topographical information about the sample (allows to obtain 3-5 nm resolution) and are the most used in SEM measurements. When a secondary electron is ejected from the atom, an electron from higher energy shells can relax to fill this hole. The excess energy caused by this displacement can be corrected by emitting a new electron from the outermost shell. This is the so-called Auger process, and the Auger electrons (AE) can be used to obtain information about the composition of very small parts of the sample surface. The aforementioned excess of energy can also be balanced by the emission of X-rays; these are characteristic of each element

in the sample and are therefore used to obtain information on the composition of the sample (EDS). Unlike the low-energy EA, X-rays provide analytical information from a considerable volume of the sample since they can travel much longer distances in the solid. Finally, BSE are produced when an electron in the beam collides head-on with the nucleus of an atom in the sample and is repelled in the opposite direction out of the sample. The intensity of this effect varies proportionally with the atomic number of the atoms in the sample. For this reason, they are used to obtain a superficial image with atomic contrast, which also provides information about the surface elemental composition of the sample.

An FEI Quanta-200FEG Scanning electron microscopy available at *CIC energiGUNE* was used for the morphological and compositional study of the samples. An accelerating voltage of between 5 kV and 30 kV was selected for different samples analyzed in this work. Surface and cross-sectional studies were carried out on the thin films to obtain information on the thickness and uniformity (complementing section 2.2.). For the latter, the cutting was performed using a diamond tip in the case of the samples deposited in a silicon wafer and polishing with the sample embedded in epoxy resin for the stainless steel discs. For the air-sensitive species (*e.g.* LiPON) the SEM transfer chamber (from Gatan company) was used.

Transmission electron microscopy

In transmission electron microscopy (TEM), the accelerated electrons are incident on a thin specimen (<100 nm) that allows the electrons to pass-through the sample. Depending on the thickness and the type of atoms in the sample, part of the electrons are scattered while others pass directly through the sample without interaction. All of them are conducted and modulated by lenses to form a final image onto a phosphorescent screen or on a CCD camera, that can provide thousands of magnifications with a resolution unattainable by any other instrument.^[34] The TEM images are a combination of different gray intensities that correspond to the degree of scattering of the incident electrons. **Figure 2.18** shows a diagram of the TEM configuration.^[32]

The TEM image as described above provides information about the structure of the sample, whether it is amorphous or crystalline. In case the sample is crystalline, it may be possible that several families of the periodic planes satisfy the Bragg (**equation 2.5**) condition and coherently diffract the incident electronic wave providing reciprocal space information on the crystal structure beyond the TEM real space image. Besides, the microscope has a series of apertures (located

in the image plane) that enable selecting an area of the sample while obtaining the diffraction of the selected area. The diffraction pattern obtained by this method is known as electron diffraction pattern. This diagram consists of ordered points (in the case of single crystals) or concentric rings (randomly oriented crystalline phases) around a central point (non-deflected transmitted electrons) that provide information about the orientation and structure of the existing crystal(s).^[5]

$$Rd_{hkl} = \lambda L \quad (2.5)$$

Where R is the radius of the diffraction rings, L is the distance between the sample and the viewing screen or CCD camera, λ is the associated electron wavelength and d_{hkl} corresponds to the interplanar spacing. The values of the camera distance and the wavelength associated to the incident electrons are known parameters, so by measuring the diameters of the rings it is possible to obtain the interplanar spacings corresponding to the crystalline phase presented in the analyzed area.

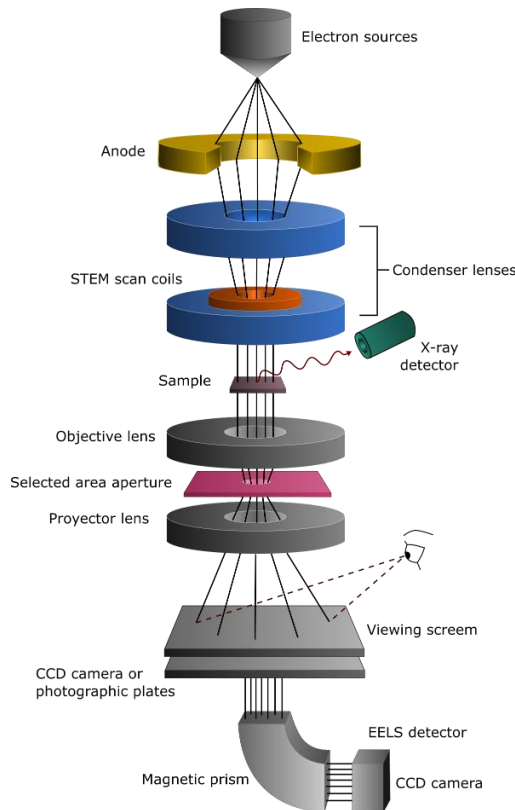


Figure 2.18: Schematic drawing of a Transmission electron microscopy (TEM) (modified from ^[32]).

The equipment used in this work is the Tecnai G2 F20 TEM that, based on a 200kV field emission gun (FEG), excels in versatility and flexibility by combining high performance in TEM/STEM imaging modes and EDS spectroscopy. Scanning Transmission Electron Microscopy (STEM) mode is based on scanning the sample through the scanning coils and recording the intensity of the signal produced by the sample directly on a detector (thus obtaining an XY map of the signal intensity distribution).

Electron energy loss spectroscopy

Another electron spectroscopy refinement that can be carried out with the TEM is electron energy loss spectroscopy (EELS) which provides a wide range of structural and chemical information from a small volume of sample. This information results from the analysis of the energy loss suffered by the electrons of the incident beam due to their inelastic interactions with the atoms of the sample.^[5] When the electron beam passes through the sample, it is conducted towards a magnetic prism whose function is to disperse the electrons according to their kinetic energy and focus them at different points in a plane to form the energy loss spectrum (**Figure 2.18**). This technique provides information about the chemical state, being able to create elemental and chemical mapping and low loss plasmon spectroscopy.

The EELS work carried out in this thesis was performed at *CIC nanoGUNE* within the MONBASA project.

2.3.4. X-ray photoelectron spectroscopy

X-ray photoelectron spectroscopy (XPS) is employed to determine the chemical composition of the materials surface^[35] including elemental composition, empirical formula, chemical state, and electronic state of the elements. This technique consists of the irradiation of a solid surface with an X-ray beam that will induce the emission of core level photoelectrons from the sample atoms while simultaneously measuring the kinetic energy of the core level photoelectrons emitted from the upper 1-10 nm of the analyzed material.^[35,36] The kinetic energy (KE) provided to the photoelectron depends upon the incident photon energy ($h\nu$) and the energy required to remove out the electron from the atom to the vacuum level, known as binding energy (BE). This relationship is expressed in **Equation 2.6**,^[30] ϕ is the work function of the spectrometer, that is the energy required to bring the electron from its zero binding energy (or Fermi) level to that of the spectrometer.

$$KE = h\nu - BE - \phi \quad (2.6)$$

By measuring the KE and considering that the energy of the incident photon and the work function of the spectrometer is known, the value of BE can be determined from the above equation. In this way, the information of the electronic structure of the atom is obtained and, since this structure is particular to each chemical element, the chemical composition of the sample can be determined. This is because the BE depends upon several factors: i) The element from which the electron is emitted, ii) the orbital from which the electron is ejected, and iii) the chemical environment of the atom from which the electron was emitted.^[36] **Figure 2.19** shows the photoemission process involved in XPS surface analysis.

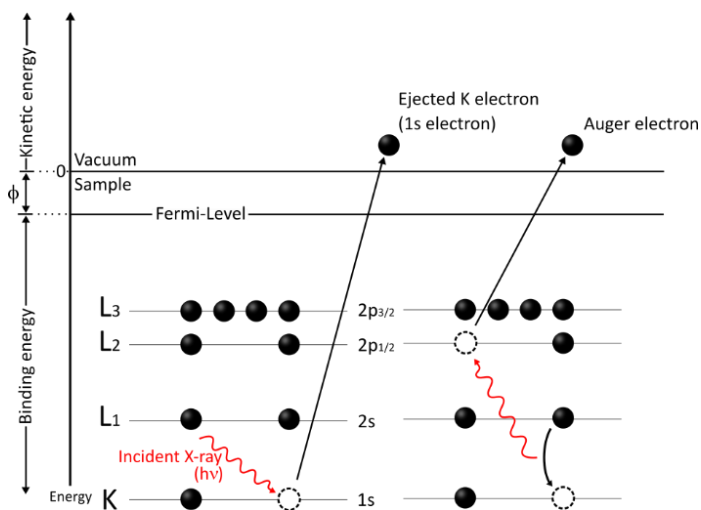


Figure 2.19: The photoemission process of 1s electron and Auger relaxation effect (KLL). The spheres represent electrons and the bars are energy levels within the material.

To avoid possible collision between photoelectrons and gas molecules in the spectrometer, and to minimize surface contamination of residual gases, XPS measurements are carried out in an ultra-high vacuum chamber (UHV, $< 10^{-8}$ Torr). A typical XPS system consists of an X-ray source, an electron energy analyzer, and a photoelectron detector, see **Figure 2.20**.

The standard X-ray source is supplied with aluminum (K_{α} 1486.6 eV) and magnesium (K_{α} 1253.6 eV) anodes. The photoelectrons extracted from the sample are transferred to an electron energy analyzer through the electron lens system and separated according to their kinetic energy. The most used configuration in XPS is the so-called Fixed Analyzer Transmission (FAT) where the electron lens system retards the photoelectrons to a fixed energy (called pass energy), improving the energy resolution of the analyzer (≤ 0.1 eV). The Fixed

Retard Ratio (FRR) configuration is typically used when measuring Auger spectroscopy. There are different types of analyzers, such as the hemispherical electrostatic analyzer (HSA), the cylindrical mirror analyzer (CMA), and the spherical mirror analyzer (SMA). The HSA is the most widely used among them.^[37]

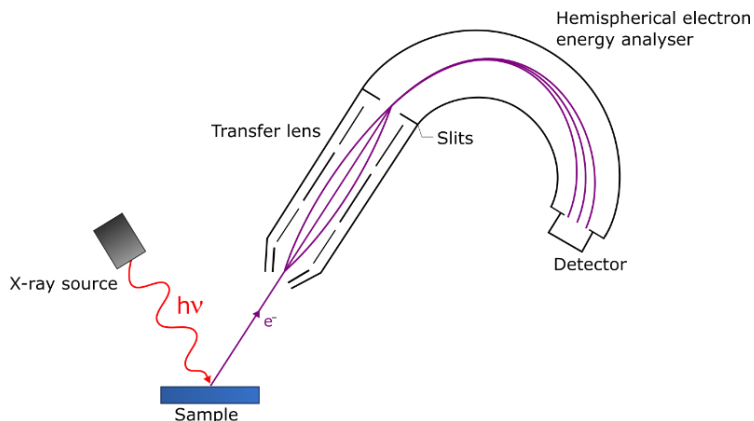


Figure 2.20: Schematic of a hemispherical analyzer (HSA) with the path of electrons from the sample to the detector.

In the photoelectron spectrum, obtained by counting the electrons ejected in a range of KE, and hence BE, appear peaks from atoms emitting those electrons in particular characteristic energy. Therefore, the spectrum is displayed as a plot of a number of electrons (intensity) versus electron BE. The specific energies and intensities of the photoelectron peaks make possible the identification and quantification of all the elements in the surface of the sample under study (except hydrogen and helium which can only be detected in a dedicated synchrotron-based system). Auger electron emission can also occur when a solid is irradiated by X-rays. These electrons differ from photoelectrons and are characterized by the fact that their kinetic energy is independent of the irradiation energy.

As mentioned above, the photoelectrons that reach the detector are from the first 10 nm of the surface, even though the incident X-rays can penetrate up to 10 μm into the sample. This is because the maximum distance that the photoelectrons can travel in the solid before losing energy or being trapped is limited, known as Inelastic Mean Free Path (IMFP). This distance depends on their kinetic energy and the compound (higher photon energy, higher IMFP).^[23] A possible alternative to obtain elemental information at higher depths is removing the outermost surface layers progressively by ion bombardment (usually Ar^+). A technique widely used to clean the surfaces from atmospheric contamination.

In this work, the composition evolution of the thin film surfaces was analyzed using a Phoibos 150 XPS system from SPECS GmbH operated in FAT mode, based on the hemispherical analyzer with a 2D delay line detector, and a non-monochromatic dual Mg/Al K_{α} X-ray source. An air-tight transfer tool was used to move sensitive samples from the glove box to the XPS, either in a vacuum or argon atmosphere. Before specific region analysis, a survey spectrum was recorded from all samples, the used standard parameters were 0.5 eV step size, pass energy of 60 eV, dwell time of 0.1 s, and 1 scan. The particular regions of the elements present on the survey signal were acquired with higher resolution (particularly for the Li 1s region, where longer accumulation times are needed, owing to the very low sensitivity factor of electrons in Li 1s orbitals). Experimental data were treated with the CasaXPS program. The binding energy of every spectra was calibrated using the aliphatic carbon signal which was set at 284.6 eV. The background of inelastically scattered photoelectrons was simulated by a Shirley function and a Voigt profile (30% Gaussian, 70% Lorentzian) was employed for peak deconvolution.

2.4. Electrochemical characterization

The main electrochemical techniques used during this work are the following: cyclic voltammetry, galvanostatic cycling, and electrochemical impedance spectroscopy (EIS). For this purpose, the cells were assembled in different geometries.

2.4.1. Electrochemical cells

Three types of cells were used during the thesis according to the needs of each application: CR2032 type coin cell, 3 electrodes Swagelok cell, and pouch cell. Among them, the most widely used was the coin cell. An important part of this project is focused on the electrochemical characterization of LNMO thin films deposited on stainless steel discs by AC-MF magnetron sputtering. These stainless steel discs are used as spacers in coin cells, so the cathode implementation in this type of substrate will guarantee an easy integration in the coin cell. **Figure 2.21a** shows the components and configuration of the CR2032 used in this work. Cap, case, spacer and wave spring are made of 316L stainless steel, while a propylene gasket is used to prevent short-circuiting. Throughout the electrochemical study carried out, a half-cell set-up was assembled, where the lithium metal acts as a counter and a reference electrode. This set-up is often used for better evaluation of the cathode and anode individually. Therefore, the air-tight CR2032 coin cells were used to test the LNMO thin films against Li-foil ($\varnothing = 14$ mm), as working and counter electrodes, respectively. A glass fiber (GE Healthcare, GF/D grade) was used as a separator and was embedded with 1 M of

LiPF₆ in dimethyl carbonate (DMC) and ethylene carbonate (EC) (1:1 v/v, Solvionic, 99.9%) liquid electrolyte. The cell was assembled in an Ar-filled glove box (H₂O and O₂ levels below 0.1 ppm) using a manual or hydraulic clammer.

The Swagelok™ cell consists of a Teflon body sealed with oxidation and reduction resistant stainless steel plungers and their corresponding nuts and ferrules to guarantee the air tightening. **Figure 2.21b** shows the three-electrode cell, which is designed for measurements where working, counter and reference electrode are needed. In this thesis, we use this system to study the performance of the commercial electrode ($\varnothing = 12$ mm) with a larger amount of liquid electrolyte. The coin cell is not designed to hold such an amount of electrolyte, so the reference electrode cavity of the Swagelok was used for this purpose. But always maintaining the two-electrode set-up used in the coin cell (cathode-separator-anode).

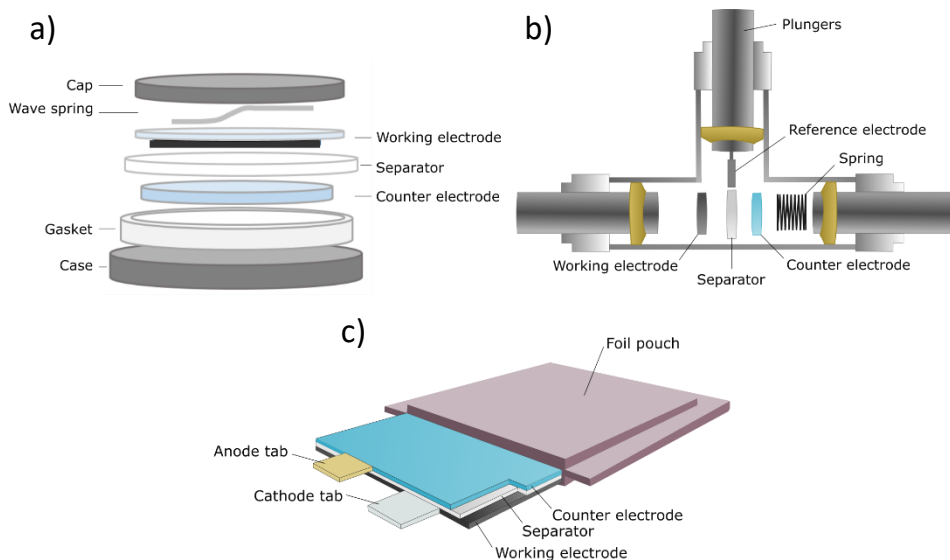


Figure 2.21: Configuration and elements of the different electrochemical cells, a) coin cell, b) Swagelok-type cell, and c) pouch cell (modified from ^[38]).

The third cell used in this project is a pouch cell. These cells are based on the cathode-separator-anode stack packaging with an aluminum-plastic film casing, see **Figure 2.21c**.^[38] Aluminum and nickel tabs (positive and negative terminal, respectively) are used as electrical contacts, incorporating an adhesive polymer tape that allows the immediate hot sealing of the tabs while guaranteeing the air-tightening. The encapsulation material is made up of aluminum foil sandwiched between multiple layers of polymers such as polyethylene terephthalate (PET),

polyamide (PA), and cast polypropylene (CPP). In this way, when a safety problem occurs, the battery, being soft-packed, tends to bulge, without exploding as may be the case with steel cells. Therefore, besides providing more safety, it reduces considerably the weight and enables the manufacture of flexible batteries with tunable geometry up to some extent. In this project, the use of pouch cells is oriented to all solid-state batteries. Note that when a solid electrolyte is deposited, the use of the separator is not required. Moreover, with the absence of the liquid electrolyte, the safety problems would also disappear. The pouch cell provides a better control of the applied pressure to the cell with respect to the coin cell set-up. Since the pressure reduction is an important factor owing to the fragility of the used ceramic electrolyte, the pouch cell will allow for better electrochemical performance.

The assembled cells were connected to a VMP3 multichannel potentiostat (Bio-Logic Science Instrument) and MACCOR series 4000 battery tester to perform electrochemical measurements. Before any measurement is carried out on the cell, it is important to check the voltage difference between the positive and negative terminals of the cell. This voltage difference is known as Open Circuit Voltage (OCV) and is the difference between the reduction potential of the electrodes. If the OCV is zero, the battery is short-circuited and cannot be used.

2.4.2. Cyclic voltammetry

The cyclic voltammetry (CV) technique is used to obtain information about the different redox reactions that take place at the electrode, the voltage at which they occur, and their reversibility. This technique applies a voltage ramp, *i.e.* a linear potential variation with time, between two defined potential values. Thus, the current flowing through the cell is monitored and plotted as a function of the applied potential.^[39] **Figure 2.22** shows the voltage evolution with time for the CV measurements, along with a possible current response.

The peaks that appear in the CV measurement correspond to the reduction and oxidation reactions that the sample undergoes. For a specific measurement, the initial (E_i) and final potentials (E_f) are selected in such a way that the redox reaction of interest (E_r) occurs in that range. When the value reaches E_f the applied potential to the electrode is reversed and scanned back to the initial value.

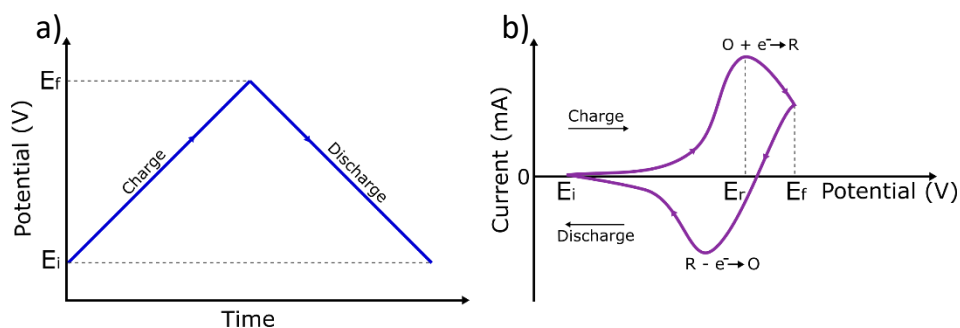


Figure 2.22: a) Example of the voltage evolution with time for a CV measurements and b) Current response of the electrode in a one-electron redox reaction.

As mentioned before, when the anodic scan (charge) reaches the E_R value, the current flow begins to increase. The O species of the electrode are reduced to R. As the potential moves forward, the concentration of O decreases due to its consumption in the reaction. Once the E_R value is passed, its concentration is depleted, the maximum is reached and the current decreased again. Conversely, during the cathodic scan (discharge), the R species are oxidized to O, reversing the reaction. This reaction can be expressed by $O + e^- \leftrightarrow R$. Note that the second reaction takes place only if the process is reversible and the current flow shape is very similar to that of the charge. Moreover, several redox processes can occur, giving rise to a more complicated CV than one-electron transfer reactions shown in **Figure 2.22**.^[40]

The scan rate (mV/s) is an important parameter to consider cyclic voltammetry experiments. Measurements made at different scan rates can be used to identify if the redox process is reversible or irreversible (fast or slow electron transfer). In reversible processes, the potential does not change with the current peak. Besides, the current peak intensity variation with scan rate can be useful to determine whether the redox process is diffusion or adsorption controlled.

2.4.3. Galvanostatic cycling

In contrast with the previous technique, in this case, a constant current is applied to the cell and the voltage changes over time are recorded, along with the redox reaction information or the electrode ion capacity in the selected voltage range.

During charge, the applied current causes the reduction of the O species to R at a constant rate, moving the electrode potential to the characteristic value of this redox couple (E_r). When the voltage is plotted versus time, this reduction reaction appears as a steady line, known as a plateau (two-phase reaction). Once the

voltage reaches the desired final value (E_f), the inverse constant current value is applied to return it to its initial value (E_i), thereby completing a cycle. In this case also, considering a reversible process, with the corresponding redox reaction plateau (from R to O). A schematic sketch of the voltage curve over time and the corresponding current values are shown in **Figure 2.23**.

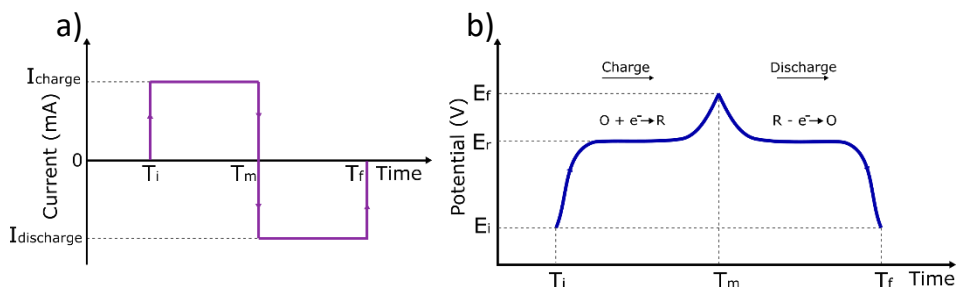


Figure 2.23: a) Example of the applied constant current for charging and discharging (I_{charge} and $I_{\text{discharge}}$, respectively) over time for galvanostatic measurements, and b) Voltage response of the electrode. T_i refers to the start of the charge at E_i , T_m is the moment when the desired voltage value is reached (E_f), and T_f refers to the end of the cycle. The redox plateau is observed at E_r .

To evaluate the current applied to a cell, the theoretical gravimetric capacity of the material under study is considered. This concept is defined as the amount of charge that can be extracted from a battery per unit mass of the electroactive material ($\text{mAh}\cdot\text{g}^{-1}$). The number of ions inserted into the electrode is determined by Faraday's law, hence the theoretical gravimetric capacity (C_{Theo}) is expressed as follows:

$$C_{\text{Theo}} = \frac{n \cdot F}{3600 \cdot PM} \quad (2.7)$$

Where n is the number of charge carriers, F the Faraday constant (96485.3383 C/mol), *i.e.* theoretically 1 gram-equivalent weight of the material will deliver 96485 C, the factor 3600 is used to obtain the result in $\text{mAh}\cdot\text{g}^{-1}$, and PM is the molecular weight of the substance (expressed as kg/mol).

According to the applied current, two tests can be performed in particular: C-rate capability test and cycle life test. The first one consists of a series of charge/discharge cycles made at different current densities. The applied current intensity is determined from the previously defined C_{Theo} of the material, corresponding to each cycle the expression C_{Theo}/n , where n is the number of hours needed to deliver/recover such capacity (n hours to charge, n hours to discharge). Instead, the cycle life test consists of cycling a cell at a specific C-rate,

usually at 1C (charge/discharge in 1 h, $n = 1$), until its capacity drops to 80% of its initial value, the limit established as the end of the cell life.

In those galvanostatic tests, the parameter used to study the reversibility of the redox processes is the coulombic efficiency (CE). The CE is defined as the ratio between the amount of charge provided by the cell during the discharge and the needed charge take up during the charge cycle (expressed as %). The corresponding equation is as follows:

$$CE = \frac{C_{\text{discharge}}}{C_{\text{charge}}} \cdot 100 \quad (2.8)$$

where $C_{\text{discharge}}$ is the amount of charge provided by the battery during the discharge cycle, and C_{charge} is the amount of charge that enters the battery during the charging cycle.

Also, the galvanostatic technique can be used for the analysis of the variation in the capacity of the active material concerning the variation in the cell voltage (dQ/dV). This parameter is known as the differential capacity and provides direct information on the electrochemical reactions taking place in the cell. The profile obtained is very similar to that of the CV explained in the previous section. But in this case, it is more useful to observe the voltage hysteresis between the charge and discharge redox peaks (the lower the difference, the higher the efficiency).^[41]

2.4.4. Electrochemical impedance spectroscopy

Electrochemical Impedance spectroscopy (EIS) is a widespread non-invasive electrical analysis technique that measures the frequency-dependent impedance response of an electrochemical system when exposed to an alternating current (AC) or voltage signal.^[42] The sweep in frequencies allows separating the different impedance contributions of each element of the cell from the total output signal, rendering it useful for the study of either the electrolyte or the electrode performance.^[43]

A single frequency voltage signal that varied sinusoidally with time $V(t) = V_m \cdot \sin(\omega t)$ is applied to the cell, where V_m is the amplitude and ω the variable angular frequency (frequency (f) = $\omega/2\pi$). As a result, a steady-state current $I(t) = I_m \cdot \sin(\omega t + \theta)$ is measured, being θ the phase shift of the $I(t)$ generated with respect to $V(t)$ (the phase shift is zero for purely resistive behavior).^[43,44] Impedance can be defined as the ratio of voltage and current:

$$Z(\omega) = \frac{V(t)}{I(t)} = |Z| e^{-i\theta} \quad (2.9)$$

This complex impedance number can be expressed in terms of real (Z') and imaginary (Z'') components. The real part is related to the resistance, while the imaginary part refers to the capacitance and inductance elements.

$$Z(\omega) = |Z|/\cos \theta - i|Z|/\sin \theta = Z'(\omega) - iZ''(\omega) \quad (2.9)$$

The Impedance results can be represented in different kinds of plots, generally, in batteries-related areas, the most used ones are Bode and Nyquist plots. Bode plot consists of two separate graphs, one for the magnitude of the frequency response, and the other for the phase shift. Whereas Nyquist plot represents the imaginary part Z'' versus the real part Z' . The second mode is the most used to study the EIS experimental data, since it allows an easy comparison of the kinetic factors of the different signals.^[44]

One of the advantages of using the EIS technique is that the electrical and electrochemical processes can be modeled by equivalent circuits. In a system that is based on a single conduction mechanism, the Nyquist plot is represented as a semicircle of diameter R (value related to the resistance of the material). **Figure 2.24a** shows the Nyquist plot along with the equivalent circuit that can be used for fitting. The maximum point on the semicircle (with ω_m) corresponds to $\omega_m \cdot RC = 1$, where RC is known as time constant or relaxation time, commonly used to determine the effect behind the semicircle. Note that the imaginary part is represented negatively in Ω (sometimes also in $\Omega \cdot \text{cm}^2$). However, when dealing with a more complex system, such as a stack of subsequently deposited layers (cathode-anode-electrolyte), different factors must be considered. Among them the ionic conductivity through the electrolyte, charge transfer, or mass transport at the electrode/electrolyte interface. The sum of all these contributions to the total impedance results in a series of semicircles and other inputs to the Nyquist plot. Moreover, these effects can be superimposed in a way that they cannot be distinguished.^[43,44] **Figure 2.24b** shows a typical Nyquist plot of a cathode/electrolyte/anode stack and the equivalent circuit.^[45,46]

The EIS technique provides the ability to analyze the properties of the ionic and electronic transport inside the electrodes, as well as the Solid Electrolyte Interphase (SEI) layer behavior. The measurements usually are carried out in the frequency range from a few mHz (or even tens of μHz) to several tens of kHz.^[46] This impedance range is divided into three different frequency regions: high frequencies, medium frequency, and low frequency. Each region provides specific information about the battery operation.

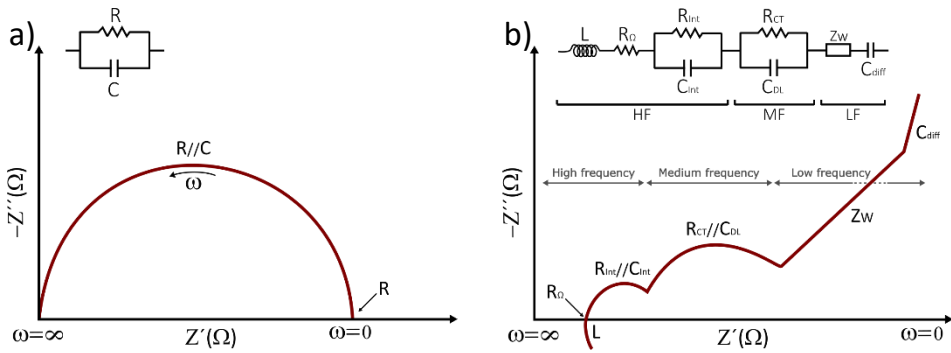


Figure 2.24: Nyquist plot and equivalent circuit of a) $R//C$ element that leads to a semicircle, and b) typical profile of a lithium-ion battery cell with its different components represented as inductances, resistances and $R//C$ elements.

High frequency (HF):

At high frequencies, there is a setup-associated inductance (L), mainly associated to the measurement cables and connections. The ohmic resistance (R_Ω) value is taken from the point at which this inductive tail intersects the X-axis. This resistance is due to the ohmic losses produced when a current flows through a cell and is associated with the ionic conduction at the electrolyte and electronic conduction at the electrodes and current collectors.^[44] Note that the expected electronic resistance associated with contacts and cables, which should also be incorporated in R_Ω contribution, is much lower than that related to the ionic-electronic mobility of the cell and can thus be neglected.

In series with the R_Ω appears the $R_{int}-CPE_{int}$ couple contribution, related to the electrode/electrolyte interface, referring to the SEI layer. This resistance effect, represented by the real part of the semicircle, is associated with the kinetics of the measured electrochemical process, *i.e.* the resistance experienced by the ions when crossing the interphase layer. Whereas the imaginary part represents the electrical double layer effect that is formed on the surface of the interphase. This effect is caused by the formation of two layers of opposite polarity, happening when the layer acts as a molecular dielectric, storing charge electrostatically.

Medium frequency (MF):

Another semicircle (or more than one depending on the cell) is found in the medium frequencies range. On one hand, as in the previous case, the real part is termed as resistance, charge-transfer resistance (R_{CT}). The Li^+ intercalation on the electrode material results in a faradaic charge transfer reaction. The speed at

which the electrochemical reaction occurs is then represented by the resistance of this reaction (R_{CT}). On the other hand, the different ohmic contributions, contribute to a general capacitive effect, such as the contact resistance, particle surface, or carbon coating.^[44] Hence, the capacitive effect associated with this frequency, known as double-layer capacitance (C_{DL}), comes from the accumulation of charge at those interfaces.

Low frequency (LF):

The first diffusional line appearing in the low-frequency range is related to the diffusion or transport mechanisms of the lithium ions inside the material, this contribution is known as the mass-transfer effect.^[23] This type of diffusion can be either solid or liquid phase. The first of them represents the diffusion of ions inside the active material particles, while the liquid phase diffusion refers to the transport of ions in the liquid electrolyte.^[44] This charge-transfer mechanism is represented using different Warburg elements (Z_w).

The last contribution, until reaching the lowest measured frequency, is related to the intercalation capacity (C_{diff}). This contribution is associated to the accumulation of charge in the intercalation electrodes. It refers to the inability to insert the lithium-ion into the structure at certain voltages, accumulating the charge around it.

It should be noted that the capacitive charge accumulation reactions described above are not ideal. With the application of constant phase elements (CPE) instead of pure capacity (C), we could make a better interpretation of the EIS result, taking into account any inhomogeneities, roughness, or crystallinity effects of the cell.^[23] One of the features of the CPE is that has properties of R and C, being its behavior defined as $Z=A(i\omega)^{-\alpha}$, where ($0<\alpha<1$); this way, when $\alpha=0$ acts as a pure resistance, whereas when $\alpha=1$ tends to work as pure capacitance. In addition, one of the parameters to consider when comparing different equivalent circuits with RC contributions is the time constant, also called tau. It is equal to the product of the circuit resistance and the circuit capacitance ($\tau = R \cdot C$) and is defined as a time which represents the speed response of an RC system to a given change.

In-plane ionic conductivity of the solid electrolyte

The ionic conductivity of thin films was also determined by performing EIS measurements but, in this case, using an in-plane test geometry with a two-probe method. **Figure 2.25a** shows the commonly used arrangement of two top electrodes deposited on the surface of the thin film. An insulating oxide material

must be used for the substrate, in this way, the electrical leakage through the substrate can be avoided.

The typical Nyquist plot obtained in the EIS measurements of the deposited solid electrolyte thin film is shown in **Figure 2.25b**. The equivalent circuit used to fit the spectra is composed by the high-frequency resistance R_{Ω} (related to the resistance of the electrode and the other metallic parts), the R_{TF} - CPE_{TF} couple (ascribed to the thin film resistance and capacitance including defects features such as roughness or impurities), and low-frequency element CPE_{CB} (corresponding to the charge accumulation at the blocking electrode).^[47] Note that in this section the CPE has already been applied.

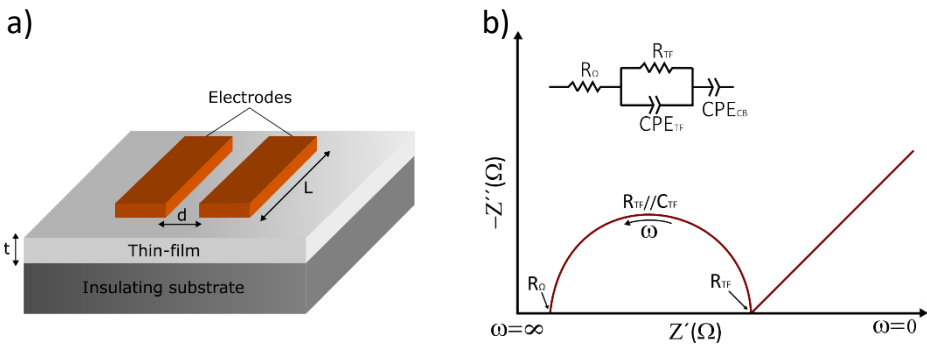


Figure 2.25: a) Two electrode configuration used in the EIS measurement, and b) a typical impedance spectra of a thin film solid electrolyte.

The ionic conductivity of the layer (σ) was calculated using the resistance value obtained from the semicircle of the Nyquist plot. The resistance depends on the characteristics of the material and its shape as follows:

$$R = \rho \frac{L}{A} \tag{2.10}$$

Where ρ is the material’s resistivity ($\rho=1/\sigma$), L is the material length, and A the contact section area. By applying it to the **Figure 2.25a** case, and assuming $t \ll d$, the ionic conductivity equation is ($S \cdot cm^{-1}$):

$$\sigma = \frac{d}{R \cdot L \cdot t} \tag{2.11}$$

Where d is the distance between electrodes, L is the length of the electrodes, t is the thickness of the thin film and R is the electrolyte resistance determined by the impedance spectroscopy.

A Linkam HFS600E-PB4 four tips stage was used for the in-plane measurements that were connected to Biologic EC-Lab potentiostat. **Figure 2.26** shows an image of the stage, along with the configuration used in this thesis. The sample to be characterized is placed on the top of the heating plate and the tips are positioned on the electrodes. The stage is hermetically sealed, allowing a controlled environment within the chamber, being important to characterize air-sensitive samples, Argon is typically used. Therefore, before the Argon connection of the Linkam, the sample is introduced in the stage in an Ar-filled glove box (H_2O and O_2 levels below 0.1 ppm). The Linkam allows a working temperature to range from $-195\text{ }^\circ\text{C}$ to $600\text{ }^\circ\text{C}$ (Water-cooled needed from $300\text{ }^\circ\text{C}$, to avoid damage to the stage).

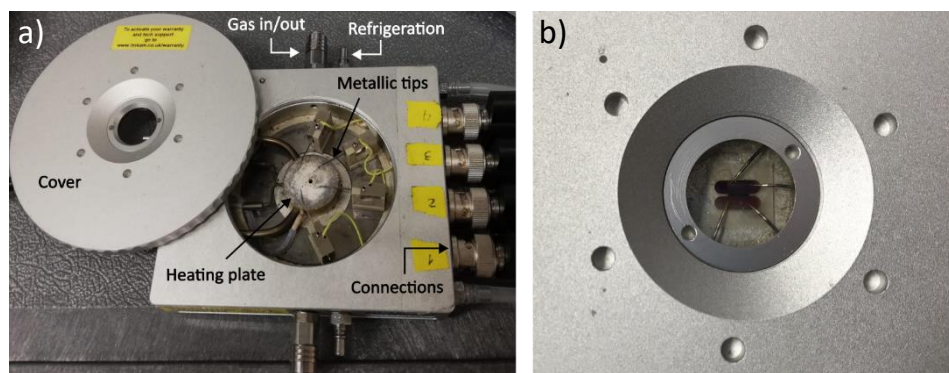


Figure 2.26: a) Linkam stage, and b) in-plane measurement set-up used in this thesis (two probes in each electrode).

References in Chapter 2

- [1] M. Hughes, “What Is Thin Film Deposition?,” can be found under <http://www.semicore.com/news/81-what-is-thin-film-deposition>, 2014.
- [2] S. Lobe, A. Bauer, S. Uhlenbruck, D. Fattakhova-Rohlfing, *Adv. Sci.* 2021, 8, 2002044.
- [3] A. V. Rane, K. Kanny, V. K. Abitha, S. Thomas, in *Synth. Inorg. Nanomater.*, Elsevier, 2018, pp. 121–139.
- [4] J. M. Albella, *Láminas Delgadas y Recubrimientos. Preparación, Propiedades y Aplicaciones*, Consejo Superior De Investigaciones Científicas (CSIC), 2003.
- [5] S. Domínguez Meister, Doctoral Thesis, Recubrimientos Protectores Nanoestructurados Preparados Por Magnetron Sputtering, Universidad de Sevilla, 2016.
- [6] B. A. Movchan, A. Demchish, *Phys. Met. Metallogr.* 1969, 28, 83.
- [7] J. A. Thornton, *Annu. Rev. Mater. Sci.* 1977, 7, 239.
- [8] M. Mühlbacher, Doctoral Thesis, High-Resolution Characterization of TiN Diffusion Barrier Layers, Linköping University, 2015.
- [9] I. V. Tudose, F. Comanescu, P. Pascariu, S. Bucur, L. Rusen, F. Iacomì, E. Koudoumas, M. P. Sucheà, in *Funct. Nanostructured Interfaces Environ. Biomed. Appl.*, Elsevier, 2019, pp. 15–26.
- [10] B. Window, N. Savvides, *J. Vac. Sci. Technol. A Vacuum, Surfaces, Film.* 1986, 4, 196.
- [11] J. T. Gudmundsson, D. Lundin, in *High Power Impuls. Magnetron Sputtering Fundam. Technol. Challenges Appl.*, Elsevier, 2019, pp. 1–48.
- [12] N. Hardy, “What is Reactive Sputtering?,” can be found under <http://www.semicore.com/news/67-reactive-sputtering-basics>, 2013.
- [13] M. Hughes, “What is DC Sputtering?,” can be found under <http://www.semicore.com/news/94-what-is-dc-sputtering>, 2016.
- [14] M. Hughes, “What is RF Sputtering?,” can be found under

- <http://www.semicore.com/news/92-what-is-rf-sputtering>, 2016.
- [15] M. Hughes, “What is Pulsed DC Sputtering?,” can be found under <http://www.semicore.com/news/95-what-is-pulsed-dc-sputtering>, 2016.
- [16] M. Hughes, “What is HIPIMS? High Power Impulse Magnetron Sputtering,” can be found under <http://www.semicore.com/news/93-what-is-hipims>, 2016.
- [17] M. Hughes, “What is MF or Mid-Frequency AC Sputtering?,” can be found under <http://www.semicore.com/news/97-what-is-mf-ac-sputtering>, 2017.
- [18] A. Etxebarria Dueñas, Doctoral Thesis, Study of Li Metal Anode Surface: Interaction with Atmospheric Gases and Impact of Impurities in Electrochemistry, Euskal Herriko Unibertsitatea, 2020.
- [19] N. Hardy, “What is Thin Film Deposition By Thermal Evaporation?,” can be found under <http://www.semicore.com/news/71-thin-film-deposition-thermal-evaporation>, 2013.
- [20] “Perfilometría Mecánica,” can be found under <https://www.espe-innovativa.edu.ec/cencinat/perfilometria-mecanica/>, 2017.
- [21] “Elipsometría,” can be found under <http://www.grupoalava.com/ingenieros/productos/nanotecnologia/elipsometria/>, 2021.
- [22] I. Madinabeitia, Undergraduate Thesis Project, Desarrollo de Composites de Base de Nanopartículas de FeNi Obtenidas Por El Método de Explosión Eléctrica de Hilo Para Aplicaciones de Alta Frecuencia, Euskal Herriko Unibertsitatea, 2014.
- [23] M. Zarrabeitia, Doctoral Thesis, Low and High Voltage Stability of Na-Ion Battery Materials: Study of Structural , Transport and Interfacial Properties, Euskal Herriko Unibertsitatea, 2016.
- [24] B. A. Pederson, Doctoral Thesis, Structure and Regulation of Glycogen Synthase in the Brain, University of California, 2019.
- [25] E. L. Thomas, Doctoral Thesis, Crystal Growth and the Search for Highly Correlated Ternary Intermetallic Antimonides and Stannides, Southern University and Agricultural and Mechanical College, 2002.

- [26] J. R. Connolly, *Introduction to X-Ray Powder Diffraction*, 2007.
- [27] A. A. Bunaciu, E. gabriela Udriștioiu, H. Y. Aboul-Enein, *Crit. Rev. Anal. Chem.* 2015, *45*, 289.
- [28] B. Campanella, V. Palleschi, S. Legnaioli, *ChemTexts* 2021, *7*, 5.
- [29] “Raman spectroscopy in more detail,” can be found under <https://www.renishaw.es/es/raman-spectroscopy-in-more-detail--25806>, n.d.
- [30] J. Rikarte Ormazabal, Doctoral Thesis, Surfaces & Interphases in Thin-Film & Conventional Li-Ion Batteries, Euskal Herriko Unibertsitatea, 2019.
- [31] M. Ezzahmouly, A. Elmoutaouakkil, M. Ed-Dhahraouy, H. Khallok, A. Elouahli, A. Mazurier, A. ElAlbani, Z. Hatim, *Heliyon* 2019, *5*, e02557.
- [32] B. J. Inkson, *Scanning Electron Microscopy (SEM); and Transmission Electron Microscopy (TEM) for Materials Characterization*, Elsevier Ltd, 2016.
- [33] “Microscopía Electrónica de Barrido,” can be found under <http://www.scai.uma.es/areas/micr/sem/sem.html>, 2016.
- [34] “Microscopia electrónica de transmisión,” can be found under <http://www.upv.es/entidades/SME/info/753329normalc.html>, 2020.
- [35] J. F. Moulder, W. F. Stickle, P. E. Sobol, K. D. Bomben, *Handbook of X-Ray Photoelectron Spectroscopy*, Physical Electronics Inc., 1995.
- [36] Thermo Fisher Scientific Inc., “Thermo Scientific XPS: What is XPS,” can be found under <https://xpssimplified.com/whatisxps.php>, n.d.
- [37] H. Seyama, M. Soma, B. K. G. Theng, in *Dev. Clay Sci.*, Elsevier, 2013, pp. 161–176.
- [38] D. J. Heydecke, *Jauch Quartz GmbH Jauch Batter. Solut. GmbH* 2018, 1.
- [39] M. Falk, Doctoral Thesis, Investigation of Surface Film Formation on Based Liquid Electrolytes Using the Secondary Ion Mass Spectrometry, Universidad de Gießen, 2014.
- [40] N. Elgrishi, K. J. Rountree, B. D. McCarthy, E. S. Rountree, T. T. Eisenhart, J. L. Dempsey, *J. Chem. Educ.* 2018, *95*, 197.

- [41] J. A. Coca, Doctoral Thesis, Electrochemical and Surface Study of Lithium-Rich Transition Metal Oxides Used as Cathodes in Lithium-Ion Batteries, University of Liverpool, 2019.
- [42] P. Schichtel, Doctoral Thesis, Preparation and Impedance Characterization of All-Solid-State Thin Film Battery Systems, Universidad de Gießen, 2018.
- [43] I. Garbayo Senosiain, Doctoral Thesis, Integration of Thin Film-Based Micro Solid Oxide Fuel Cells in Silicon Technology, Universitat de Barcelona, 2013.
- [44] V. J. Ovejas Benedicto, Doctoral Thesis, Determination of the State of Health of Li-Ion Batteries : The Irreversible Entropy Production Approach, Universitat Politècnica de Catalunya, 2017.
- [45] D. Andre, M. Meiler, K. Steiner, H. Walz, T. Soczka-Guth, D. U. Sauer, *J. Power Sources* 2011, 196, 5349.
- [46] M. Grossi, B. Riccò, *J. Sensors Sens. Syst.* 2017, 6, 303.
- [47] S. Larfaillou, D. Guy-Bouyssou, F. Le Cras, S. Franger, *ECS Trans.* 2014, 61, 165.

Chapter 3

Synthesis and characterization of $\text{LiNi}_{0.5}\text{Mn}_{1.5}\text{O}_4$ (LNMO) thin film cathode

3.1. Introduction

The selected cathode for this thesis is the high-voltage spinel $\text{LiNi}_{0.5}\text{Mn}_{1.5}\text{O}_4$ (LNMO). As discussed in the introduction the LNMO has become one of the most studied positive electrodes for the development of LIBs due to its enhanced cycling behavior namely, high operating voltage of 4.75 V vs Li/Li^+ and specific capacity of $146.6 \text{ mAh}\cdot\text{g}^{-1}$.^[1-3]

Two types of structures have been reported for the LNMO spinel: the ordered space group of $\text{P4}_3\text{32}$ (simple cubic phase) and the disordered space group of Fd-3m (face-centered spinel).^[2-6] Where the ordered phase displays Ni and Mn atoms regularly ordered in 16d octahedral sites while, in the disordered structure, Ni and Mn are randomly occupying the 16d sites. The **Figure 3.1** shows the schematic representation for both atomic structures. The main difference between them is the valency of Mn ions; only Mn^{4+} ions are present in the ordered phase, whereas a small amount of Mn^{3+} ions are found in the disordered one. The larger ionic radius of Mn^{3+} results in better electronic conductivity and Li^+ diffusion path.^[1,7,8] Hence, the disordered LNMO has a better electrochemical performance than the ordered one. The annealing temperature to which the LNMO is subjected during synthesis plays an important role in the final

crystallographic structure.^[1,9] For this reason, the electrode fabrication method is also a factor of paramount importance.

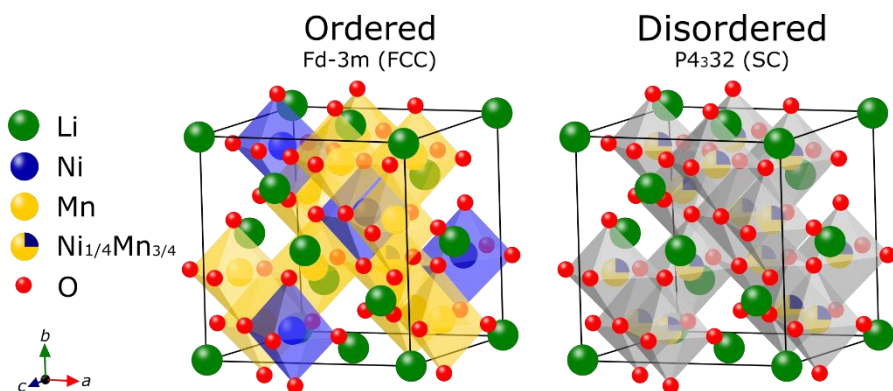


Figure 3.1: Schematic representation of both LNMO spinel structures. In the ordered spinel, left panel, the Ni, Mn, and Li atoms are situated in the 4a, 12d, and 4c sites, respectively, while O ions occupy the 8c and 24e sites. In this case, Ni and Mn atoms are ordered regularly in the 16d sites. In the disordered spinel, right panel, the Ni and Mn, Li and O atoms are situated in the 16d octahedral sites, 8a tetrahedral sites and 32e sites, respectively. The Ni and Mn atoms randomly occupy the 16d sites.

Looking at the literature, the deposition of LNMO thin films has been carried out using different techniques, such as sol-gel,^[10,11] electrostatic spray deposition,^[12] spin-coating,^[13] pulsed laser deposition,^[14,15] and radio-frequency (RF) magnetron sputtering deposition.^[6,16] In particular, RF sputtering is considered one of the best suited techniques for processing thin film components for batteries, owing to its high deposition rates, reproducibility of the target material with a customized thin film shape, repeatability, solvent-free method, and ability to scale-up for industrial production (*e.g.* roll-to-roll systems).^[17–19]

When using thin film growth methods, the substrate where the oxide thin film is deposited plays a key role in the layer growth. The present work focuses on studying the behavior of LNMO deposited by mid-frequency alternating current (AC) magnetron sputtering in an easily accessible substrate, *viz.* stainless steel (SS), typically used in coin cell configuration as current collector or spacer.^[6,20] In stark contrast with previous literature, mostly focused on non-scalable Pt-coated Al_2O_3 substrates,^[21,22] the stability, acceptable electrical conductivity, availability and low cost of SS makes it one of the preferred substrates for building up

batteries,¹ ready for scale-up to industrial scale. Nevertheless, chemical and electrochemical compatibility of the substrate with the cathode material needs to be carefully analyzed, since interdiffusion issues during the thermal treatment have been reported in literature.^[23]

3.2. Main objectives of the chapter

This chapter is focused on the synthesis and the characterization of LNMO thin film cathodes. They have been grown on stainless steel substrates by mid-frequency AC magnetron sputtering.

The study includes the optimization of the magnetron sputtering process to achieve coatings with controlled thickness, morphology, chemical composition, and crystallographic structure, along with electrochemical tests that can be used to correlate the thin film properties with the electrochemical performance.

3.3. Experimental set-up and deposition optimization

For this investigation, the selected magnetron sputtering system is the semi-industrial CemeCon CC800/8 unit located in *Tecnalia*. A modification on the original PVD set-up allows to perform deposition processes based on the Mid-Frequency AC dual magnetron sputtering technology.

As explained in the chapter 2, in the AC sputtering method the cathode and the anode switch the polarity every half cycle. When two targets are used, this results in a more efficient use of the power; unlike RF, where only 50% of the applied power is transferred to the system. Therefore, a higher deposition rates could be obtained, which is an important parameter in industrial applications. The magnetron sputtering process chamber layout employed for the LNMO deposition is shown in **Figure 3.2**. The spinel LNMO single-phase (*Toshima Manufacturing Co., Ltd.*) and graphite (*Cemecon AG*) targets were placed in the magnetrons connected to the AC power source. The latter was selected due to its low sputtering rate but remained shielded throughout the deposition process. In this way, it is ensured that only the LNMO is deposited. The substrates were posted on one of the rectangular faces of the static holder while facing the LNMO target. The sample holder was placed in a fixed position that enabled the highest possible deposition rate.

¹ As a quick comparison. On one side, the conductivity of SS is $1.3 \text{ S}\cdot\text{m}^{-1}$, while for a Cu is $59 \text{ S}\cdot\text{m}^{-1}$. Indeed, SS conductivity is one of the lowest one among conductive materials. However, it is still an acceptable value. On the other side, world production of SS is ~60 million tones, much larger than copper, whose world production is not even 20 million tones. Finally, the cost of SS is ~3 \$-kg, instead for Cu is ~10 \$-kg.^[56]

The physical and chemical properties of the obtained thin films are directly dependent on the sputtering process parameters such as pressure into the chamber, applied power to the cathode, the distance between the target and the substrate, the deposition time, etc. Therefore, a study to determine the influence of the deposition parameters on coating properties was performed.

The ceramic nature of the cathode material needs careful control of the applied power and a ramp rate procedure to avoid thermal shock of the target. After the initial tests, it was observed that the minimum power to ignite the plasma was 100 W, while higher powers, *i.e.* 600 W, result in crack formation and risk of target breakdown. Therefore, the AC power for LNMO deposition was fixed at 300 W ($0.85 \text{ W}\cdot\text{cm}^{-2}$ per target) with $1.5 \text{ W}\cdot\text{sec}^{-1}$ ramp rate, as suggested by our collaborators from the company *Gencoa Ltd.* within the MONBASA H2020 project.^[24] Other parameters such as the target size or substrate-to-target distance were kept fixed due to the geometry of the sputtering chamber.

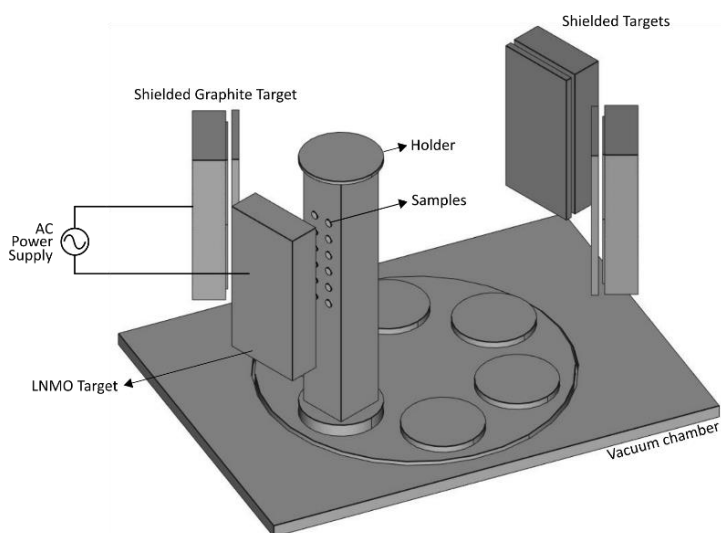


Figure 3.2: Schematic view of the CemeCon CC800/8 magnetron sputtering system at *Tecnalia*.

In this work, the LNMO films were deposited on 316L Stainless Steel (SS) current collector discs (*Hohsen Corp.*, diameter 16 mm, thickness 0.5 mm) that are typically used as spacers in the coin cells, hence being possible its direct integration in a CR2032 coin cell. In turn, atomically flat Si (100) single crystal substrates were used for thickness and cross-section measurements of the LNMO films. Prior to the sputtering process, to ensure good surface cleanliness (without contaminants) and hence good contact between the two materials, the samples were immersed in an ultrasonic bath with alkaline detergent (10 % concentration

and pH 10 to 12) at 70 °C for 20 minutes and rinsing them afterward in deionized water (with ionic conductivity lower than $1 \mu\text{S}\cdot\text{cm}^{-1}$).

Before the initial deposition tests, the process chamber was evacuated down to a base pressure of $2\cdot 10^{-5}$ mbar, SS substrates were placed at 25 cm above the base of the holder and the substrate-to-target distance was set at 75 mm. Three sputtering processes were carried out with different constant flow rates of highly pure Ar, namely 50, 250, and 402 sccm that resulted in working pressures of $2.20\cdot 10^{-3}$, $5.70\cdot 10^{-3}$, and $1.05\cdot 10^{-2}$ mbar, respectively. The increase in the argon pressure led to a clear increase in the thickness of the deposited LNMO films, see **Figure 3.3**. The deposition rate at the lowest Ar flow is $6.40 \pm 1.37 \text{ nm}\cdot\text{min}^{-1}$, increasing considerably to $8.38 \pm 0.09 \text{ nm}\cdot\text{min}^{-1}$ with 250 sccm, and to $9.56 \pm 0.08 \text{ nm}\cdot\text{min}^{-1}$ for the highest flow tested.

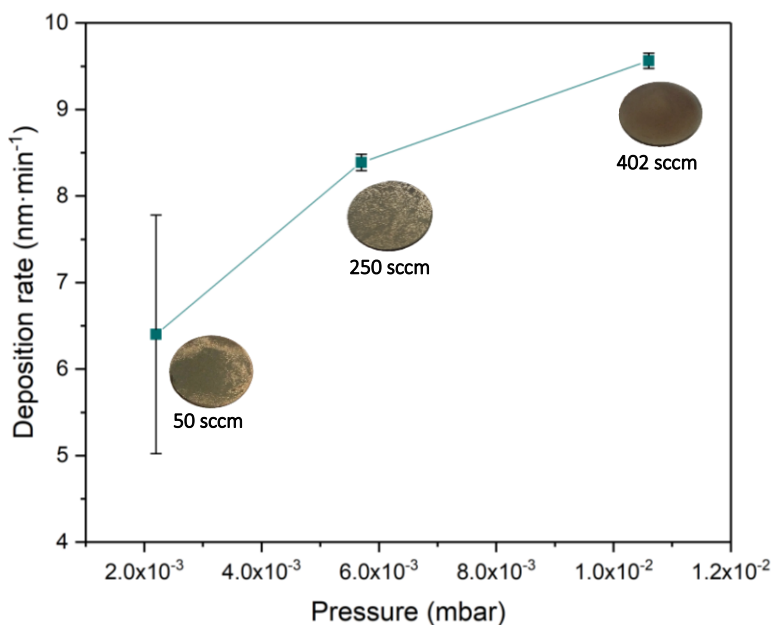


Figure 3.3: Deposition rate of processed carried out with 50 sccm, 250 sccm and 402 sccm.

The LNMO coatings deposited with 50 and 250 sccm suffered from delamination from the SS substrate (3h duration processes), being more evident in the first case. This is due to the known fact that a decrease of the sputtering pressure leads to an increase of the film internal stress, with a negative effect on the adhesion of this film to the substrate. Thus, due to both positive effects (deposition rate and good film adhesion), the sputtering process for LNMO

cathode deposition was decided to be carried out in the upper range of pressures of the equipment (above 0.01 mbar).

Once we determined the working pressure and the applied power to the target, we need to optimize the position of the substrates on the holder. This position was determined by analyzing the deposition rate at different heights within the holder. For this purpose, 10 silicon substrates masked with a Kapton strip were placed at different heights within the holder prior to running a deposition process with the selected conditions. Once the films were grown on the Si substrates, the thickness of the films was measured at the step edge of the Kapton shadow mask by means of a stylus profilometer. **Figure 3.4** shows the deposition rate of the selected positions. The first silicon was positioned at 12 cm from the base of the sample holder tower, obtaining a value of $3.49 \pm 0.19 \text{ nm}\cdot\text{min}^{-1}$. This value increases as moving towards the center of the holder, achieving $9.56 \pm 0.09 \text{ nm}\cdot\text{min}^{-1}$ at 25.5 cm. And decrease again to $3.90 \pm 0.41 \text{ nm}\cdot\text{min}^{-1}$ at 36 cm, where the last silicon was placed. For further clarity a colored contour plot is overlaid with the holder drawing, making clear the non-uniformity of the thickness along the length of the holder.

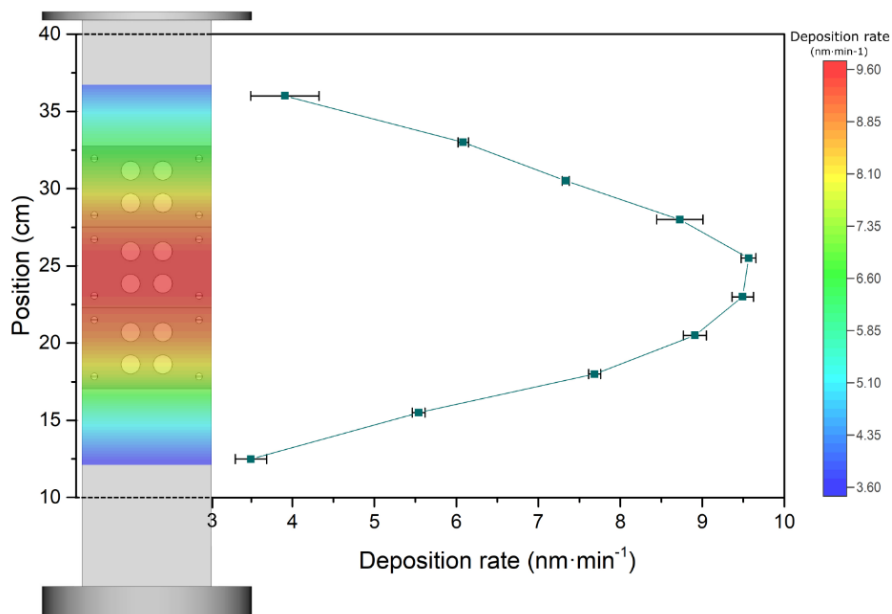


Figure 3.4: Deposition rate along the holder (represented also by color scale) and a holder drawing indicating the final position of the masks.

Throughout this thesis, the components of the thin film battery are deposited sequentially. To avoid possible short-circuits, each part of the battery must have its specific mask size and shape. In our case, a SS disk-centered circular mask will be used for all battery parts. For the cathode, three SS foils with four 12 mm-diameter holes were fabricated and placed in the center of the tower, ensuring the maximum deposition rate and uniformity, as well as keeping the SS substrates in front of the target. In total, we are able to grow 12 LNMO films at once.

3.4. Characterization of as-deposited sample

In this section the characterization of the optimal film achieved in the previous section is presented. This film was deposited with a constant flow rate of 402 sccm of highly pure Ar, working at a constant pressure of $1 \cdot 10^{-2}$ mbar. The spinel LNMO single-phase target was biased at $0.85 \text{ W} \cdot \text{cm}^{-2}$ and the substrate-to-target distance was fixed to 75 mm. The substrates were positioned in the middle of the holder, at 25 cm from the base of the sample holder tower. For this section, the deposition process lasted for 3 hours.

The parameter space to be explored in the analysis of the as-deposited sample (LNMO_AD) was rather broad, so we focused on the structural, morphological, and elemental characterization.

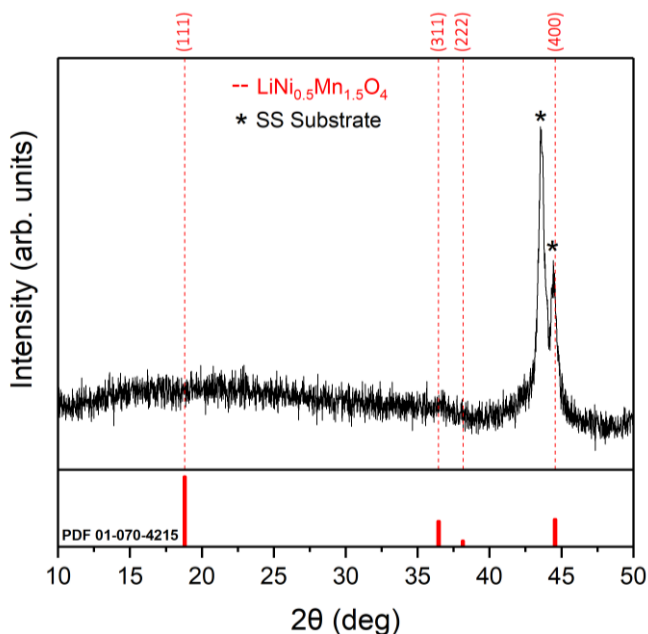


Figure 3.5: XRD pattern of LNMO_AD. Red dashed fiducial lines correspond to miller indexes of spinel LNMO, taken from reference PDF 01-070-4215 (attached graph).

XRD patterns were measured to study the crystallographic structure of the deposited LNMO film. Data were collected in the 10° to 50° 2θ range with a step size of 0.019° . The obtained diffractogram is presented in **Figure 3.5**, only two reflections related to the α - and γ -phases of the SS substrate at $2\theta = 43.6^\circ$ and $2\theta = 44.5^\circ$ can be observed, respectively.^[23] There is no sign of the spinel LNMO phase represented by PDF 01-070-4215 reference, revealing the amorphous nature of the sample.

The morphology of the LNMO_AD was studied by means of SEM, **Figure 3.6**.² As seen in the cross-section image, see **Figure 3.6a**, the coating is uniform, defect-free, and with columnar growth. As expected, the thickness of the obtained layer is about $1.71\ \mu\text{m}$, corresponding to a deposition rate of $9.5\ \text{nm}\cdot\text{min}^{-1}$. Looking at the top view image, **Figure 3.6b**, a granular surface morphology can be observed. This is in accordance with the zone T of the SZM model,^[25] as the LNMO melting temperature (T_m) is close to $1700\ \text{K}$ ^[26] and during the sputtering process the substrate temperature (T_s) reaches around $338.5\ \text{K}$ (measured by 575CMSS direct contact thermometer, *PTC Metrology*TM), the T_s/T_m ratio is slightly lower than 0.2 (the zone T corresponds to $0.1 < T_s/T_m < 0.3$). The observed structures are typical of amorphous or quasi-amorphous films, as supported by the XRD patterns shown in **Figure 3.5**.

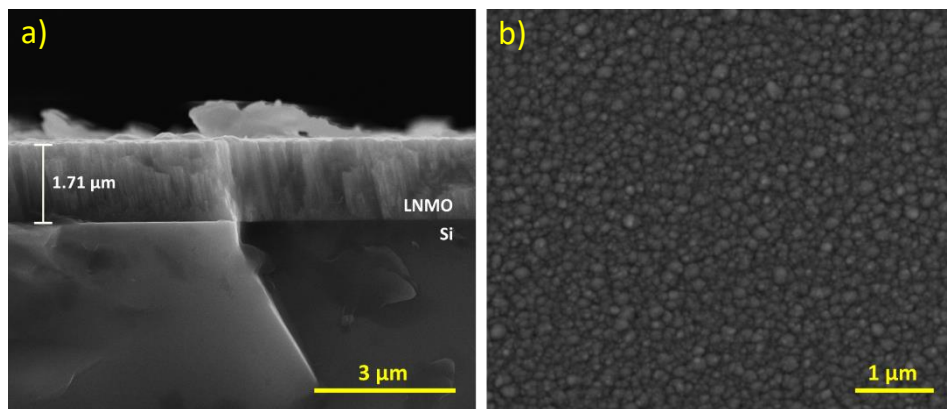


Figure 3.6: SEM images corresponding to LNMO_AD deposited on silicon, a) cross-section, and b) top view.

The preferential sputtering of some elements and their interaction with the plasma could lead to some changes in the final composition of the deposited

² The microscopy works corresponding to this section have been conducted in the *Laboratorio de Microscopias Avanzadas* at *Instituto de Nanociencia de Aragon - Universidad de Zaragoza*. We acknowledge the LMA-INA for offering access to their instruments and expertise.

coating compared to the original composition of the target. So, in order to validate the viability of the sputtering process an elemental characterization of LNMO_AD was performed by means of XPS, with a non-monochromatic Mg K_{α} source operated at 100 W. Survey spectra were acquired with 0.5 eV step size, pass energy of 60 eV, and accumulation of 1 scan. Particular regions of the elements present on the survey scan were acquired with higher resolution (step size of 0.1 eV, pass energy of 30 eV, and accumulation of 3 scans). In the LNMO_AD survey spectrum, only C and O can be identified at binding energy values corresponding to adventitious carbon and surface oxides, see **Figure 3.7**. Some Li is also detected on the surface related to the presence of lithium carbonate species. Nevertheless, transition metals (Ni and Mn) peaks were not detected, see inset graphs of **Figure 3.7**. These results suggest that the deposited film was covered by a layer of surface contaminants, mainly consisting of organic species, resulting from exposure to air.^[27,28]

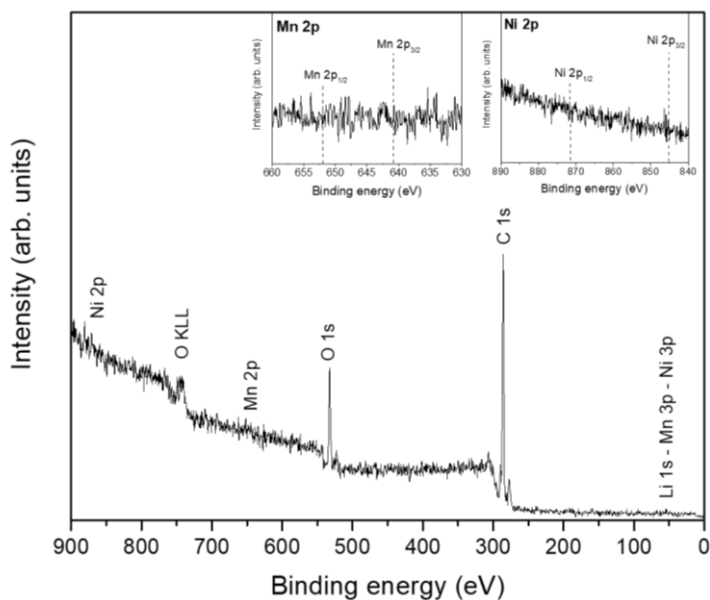


Figure 3.7: XPS survey and Ni 2p and Mn 2p regions (inset graphs) for LNMO_AD.

To verify whether the deposited film contains such transition metals, a bulk elemental analysis must be carried out. Energy Dispersive X-Ray Spectroscopy is a suitable technique for obtaining information about the concentration of constitutive elements (except Li) up to a depth of 1-2 μm . With this technique, Mn and Ni signals were detected. The analysis of the EDS data results in the determination of the film stoichiometry, for this, the stoichiometry of Ni, and O

elements for LNMO_AD was determined taking the Mn value as 1.5. The obtained values are listed in **Table 3.1**

Table 3.1: Stoichiometry of the LNMO_AD film as determined from EDS analysis and expected theoretical values, both normalized to 1.5 Mn.

	Mn	Ni	O
LNMO_AD	1.50	0.51	4.38
Theoretical	1.50	0.50	4.00

Looking at **Table 3.1** it can be concluded that the chemical composition of the LNMO_AD perfectly matched the theoretical stoichiometry of LNMO. The Ni stoichiometry differs only by 2%, while there is an excess of oxygen of 9.5%. The significant increase in O can be due to the presence of surface contamination species, but the small increase in Ni might be related to experimental error. This result gives good feedback for further developments in LNMO films deposited by AC magnetron sputtering.

As outlined in this section, the LNMO_AD sample is amorphous, therefore a post-annealing process is needed to achieve the specific crystallographic structure of LNMO that displays electrochemical activity as the cathode in Li-ion batteries. In the following section, the effect of the post-deposition thermal treatment will be discussed.

3.5. Effect of the post-deposition thermal treatment

The thermal annealing of the LNMO thin film is an important field of research in the development of functional LNMO cathodes. A wide range of temperatures was tested to check its influence on the LNMO film properties.

The explored parameters for the optimization of the post-deposition annealing process are divided into three different parts: structural characterization (XRD and Raman Spectroscopy), surface morphology (SEM), and electrochemical performance (C-rate, CV, and EIS).

3.5.1. Structural characterization

The evolution with temperature of the XRD patterns of LNMO-coated SS substrate can be seen in **Figure 3.8**, data were collected in the 15° to 45° 2θ range with a step size of 0.02° . The temperature was increased from RT up to 900°C , with a ramp step of $5^\circ\text{C}\cdot\text{min}^{-1}$. Diffraction patterns were recorded at 100°C steps, from RT to 400°C , and every 50°C , from 400°C to 900°C . For the sake of clarity,

results are displayed in three plots defined on the base of (a) low, (b) intermediate, and (c) high annealing temperature range.

Figure 3.8a displays the diffractograms measured at room temperature and after annealing at 200 °C, 300 °C, 400 °C, 450 °C, 500 °C. From room temperature up to 300 °C, only two reflections at $2\theta = 43.7^\circ$ and $2\theta = 44.6^\circ$ are observed that can be related to the α - and γ -phases of the SS substrate.^[23] This means that the deposited LNMO film is amorphous even after the first annealing step. At 300 °C, a broad and weak diffraction peak is also seen at $2\theta = 18.6^\circ$ that corresponds to LNMO (111) diffraction lines. After annealing at 400 °C, 500 °C and even up to 550 °C, being the diffractograms of this last annealing temperature shown in **Figure 3.8b**, the reflection at $2\theta = 18.6^\circ$ becomes progressively more intense and narrower. This feature is originated by an increase of the degree of crystallization of the thin film with temperature. Besides, two weak peaks at $2\theta = 36.5^\circ$ and $2\theta = 38.1^\circ$, corresponding to LNMO (311) and (222) diffraction lines, appear in diffractogram with no significant evolution upon annealing.

Figure 3.8b shows the diffractograms measured after annealing at 550 °C, 600 °C, 650 °C, and 700 °C. At 550 °C, the peak corresponding to the α -phase of SS substrate almost disappears, suggesting that a structural change starts to take place in the outermost surface region of the substrate. After annealing at 600 °C and 650 °C, a strong narrowing and intensification of the LNMO (111) diffraction line and a progressive splitting of LNMO (311) reflection in two peaks are observed. At temperatures above 650 °C, a very weak peak appears at $2\theta = 30.3^\circ$, while at 700 °C, the new reflections resulting from LNMO (311) splitting gain intensity. Particularly, the one at $2\theta = 35.6^\circ$ becomes more intense than the one corresponding to LNMO (311). In addition, the LNMO (111) reflection becomes asymmetric owing to the appearance of a shoulder at $2\theta = 18.4^\circ$, the LNMO (222) peak almost disappears and overlapping between the γ -phases of the SS substrate and a new feature is foreseen. The XRD pattern evolution unveils that a gradual structural change is taking place in the deposited film above 650 °C. Particularly, the new contributions to the diffractograms can be related to a new phase formed upon diffusion of Fe atoms from SS substrate towards the thin film. According to previous reports,^[23,29] Fe atoms can occupy tetrahedral sites of the LNMO spinel structure during their migration towards the surface while forming a disordered spinel $\text{LiFe}_y\text{Mn}_{2-y}\text{O}_4$ (LFMO) phase (with $0 < y < 0.6$) (PDF 01-075-319). Therefore, above 650 °C the two identified phases, namely LNMO and LFMO, are thus coexisting in the annealed thin film.

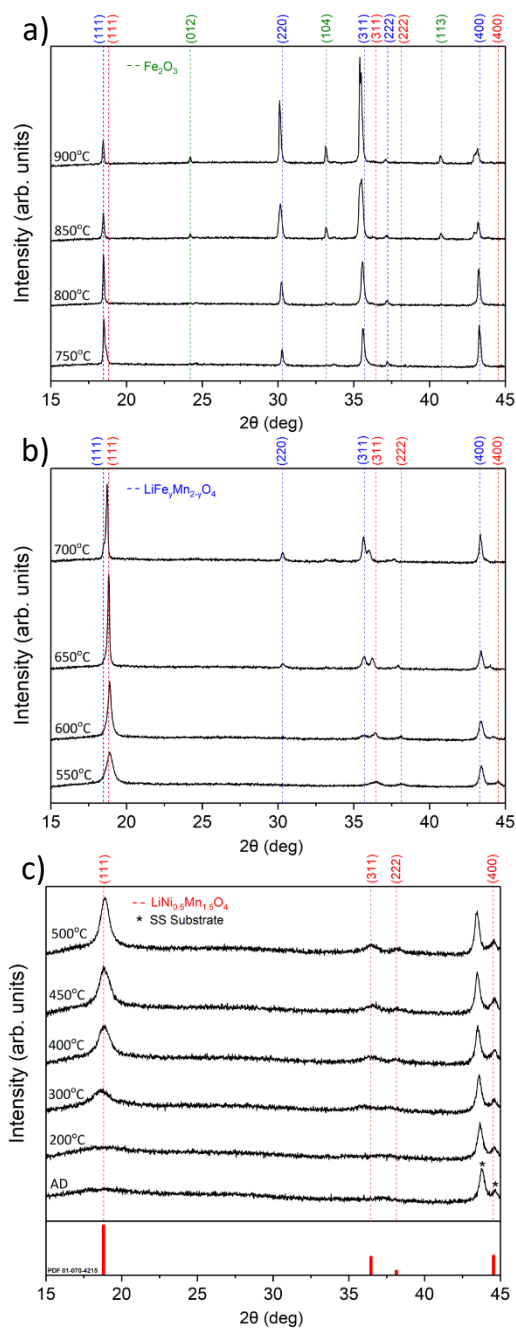


Figure 3.8: XRD patterns of LNMO thin films deposited on SS substrates measured during in-situ annealing at a) high, b) intermediate, and c) low temperatures. Red, blue, and green dashed lines correspond to Miller indexes of spinel LNMO, spinel LFMO and corundum Fe_2O_3 , respectively.

Figure 3.8c shows the diffractograms measured after annealing at 750 °C, 800 °C, 850 °C, and 900 °C. At 750 °C, the shape of the LNMO (111) diffraction line changes: the shoulder observed at $2\theta = 18.4^\circ$, corresponding to LFMO (111) is more intense than the original LNMO (111) peak, meaning that the film is slowly changing towards the new phase. This is further supported by the fact that the LNMO (311) reflection disappears and a new weak reflection corresponding to LFMO (222) is observed at $2\theta = 37.1^\circ$. After annealing at 800 °C, reflections corresponding to spinel LNMO disappear and only those related to LFMO are observed. Finally, at 850 °C and 900 °C additional diffraction lines appear at $2\theta = 24.1^\circ$, $2\theta = 33.1^\circ$ and $2\theta = 40.7^\circ$ that can be related to hematite (Fe_2O_3 , R3cH space group) (PDF 01-088-2359).^[30] The evolution of the XRD pattern at high temperatures shows that the second spinel LFMO phase, appearing at intermediate annealing temperature, finally replaces the desired spinel LNMO phase.

According to the XRD results, the deposited LNMO thin films undergo structural changes during annealing. Further characterization was then performed on these samples to identify any related morphological and compositional feature of interest for electrochemical applications. As the cathode begins to show signs of crystallization at 300 °C, from now on, the study will focus on analyzing the cathode properties from that temperature every 150 °C (*i.e.* 300 °C, 450 °C, 600 °C, 750 °C, and 900 °C). The samples will be identified as follows: LNMO_AD (as-deposited sample), LNMO_300, LNMO_450, LNMO_600, LNMO_750, and LNMO_900.

Although the XRD study was carried out by progressively increasing the temperature, for further characterization, the LNMO films were annealed at the desired temperature with a commercial oven (*Carbolite*) for 1 hour in air, with a ramp step of $5^\circ\text{C}\cdot\text{min}^{-1}$, and then left cooling slowly inside the oven switched off.

Despite having the same stoichiometry, LNMO can crystallize in ordered or disordered spinel structures depending on the synthesis conditions.^[2,22,31] In general, the disordered spinel phase is considered more suitable than the ordered one for electrochemical applications due to its high electronic and Li-ion conductivity.^[2,32] This feature is hard to be clearly distinguished by XRD without high resolution data accompanied by Rietveld refinement, in contrast, Raman spectroscopy is a fast tool to determine the cation ordering without complex data processing: the $F_{2g(1)}$, E_g , $F_{2g(2)}$, $F_{2g(3)}$, and A_{1g} vibrational modes at 340 cm^{-1} , 400 cm^{-1} , 500 cm^{-1} , 610 cm^{-1} , and 640 cm^{-1} respectively, are the expected ones for the disordered spinel LNMO.^[2,4,31,32] **Figure 3.9** shows the Raman spectra from LNMO_AD, LNMO_300, LNMO_450, LNMO_600, LNMO_750, and LNMO_900

samples. For LNMO_AD and LNMO_300, an asymmetric broad band appeared at 600 cm^{-1} , followed by a long tail that extends down to 400 cm^{-1} . This hints at the mainly amorphous nature of the film. By increasing the temperature up to $450\text{ }^\circ\text{C}$, the previously identified peaks become more intense, still the disordered spinel phase is not yet identified. In the case of LNMO_600, several peaks are detected at the expected positions of the disordered spinel LNMO, confirming that this annealing temperature resulted on the desired phase. The intense peaks at 640 and *ca.* 600 cm^{-1} are typically ascribed to Mn-O stretching modes, whereas the peaks around 500 and 404 cm^{-1} can be correlated to Ni-O stretching vibrations.^[10] Importantly, the degree of disordering (Ni and Mn cations randomly distributed in the 16d octahedral sites of the spinel structure) is reflected in the splitting of the $F_{2g(3)}$ vibrational mode. This way, two distinct peaks at *ca.* 593 and *ca.* 612 cm^{-1} are expected for high ordering, whereas a broad single peak is observed in disordered structures.^[33] The same behavior is also observed in the case of LNMO_750, whereas the LNMO_900 Raman spectrum considerably differs from the rest: broadened peaks, vibrational bands related to LNMO are hardly distinguished and new bands are detected around 475 cm^{-1} and 710 cm^{-1} . This result further corroborated the structural changes occurring in the cathode after annealing at $900\text{ }^\circ\text{C}$, as a result of Fe diffusion, in agreement with XRD measurements, **Figure 3.8**.

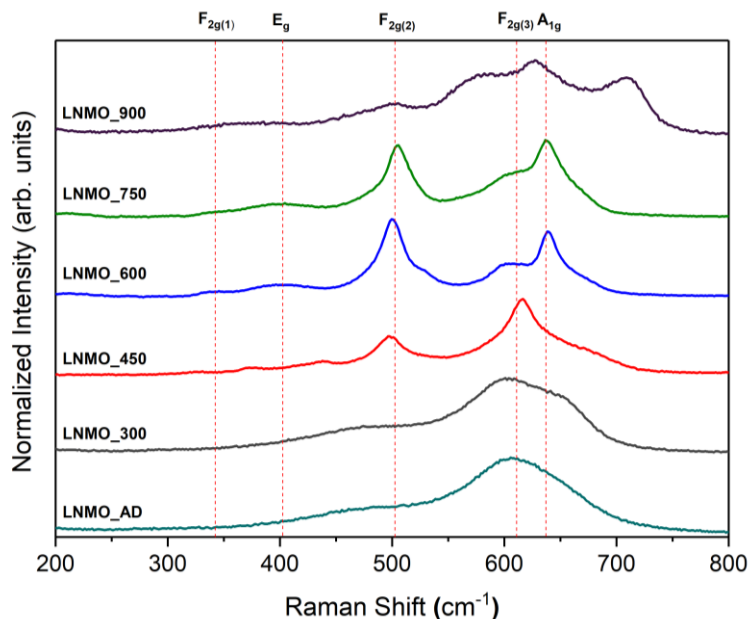


Figure 3.9: Raman spectra corresponding to LNMO_AD, LNMO_300, LNMO_450, LNMO_600, LNMO_750, and LNMO_900. Dashed lines correspond to LNMO vibrational modes.

3.5.2. Surface morphology

In general, structural changes are accompanied by morphological ones. Therefore, the film morphology was studied by means of SEM as can be seen on the micrographs of **Figure 3.10**: a) LNMO_AD, b) LNMO_300, c) LNMO_450, d) LNMO_600, e) LNMO_750 and f) LNMO_900.

Indeed, the surface morphology of LNMO_AD and LNMO_300 is similar, in both cases, the LNMO film is uniform, defect-free, and shows granular morphology. Only a slight increase of the grain size is appreciated in LNMO_300 with respect to LNMO_AD. The observed structures are typical of amorphous or quasi-amorphous films, as confirmed by the lack of diffraction features in the XRD data shown in **Figure 3.8c**.

The morphology of LNMO_450 changes considerably with respect to samples annealed at lower temperature. The granular morphology is replaced by thin and elongated flake-like particles (long- and short-axis of 300 nm and 50 nm long, respectively). In the LNMO_600 case, the surface becomes denser with more compact particles. The flake-like particles are still visible, but they increased in thickness (the short-axis has grown to 100 nm). The observed morphology is compatible with the observed intense and narrow LNMO reflections of the XRD pattern, and it is comparable with those reported in the literature for samples that have been prepared under similar experimental conditions.^[6]

Finally, a further morphology change is also observed at high annealing temperatures. The LNMO_750 shows large, around 500 nm, and mostly quasi-rectangular-shaped particles. When the temperature reaches 900 °C, the crystallites increase up to 1 μm with a better-defined shape. Most of the particles present octahedrons-like shape with triangular faces, which is in accordance with the reported in the literature.^[23] This drastic modification in terms of morphology reflects the phase change highlighted by XRD in **Figure 3.8**.

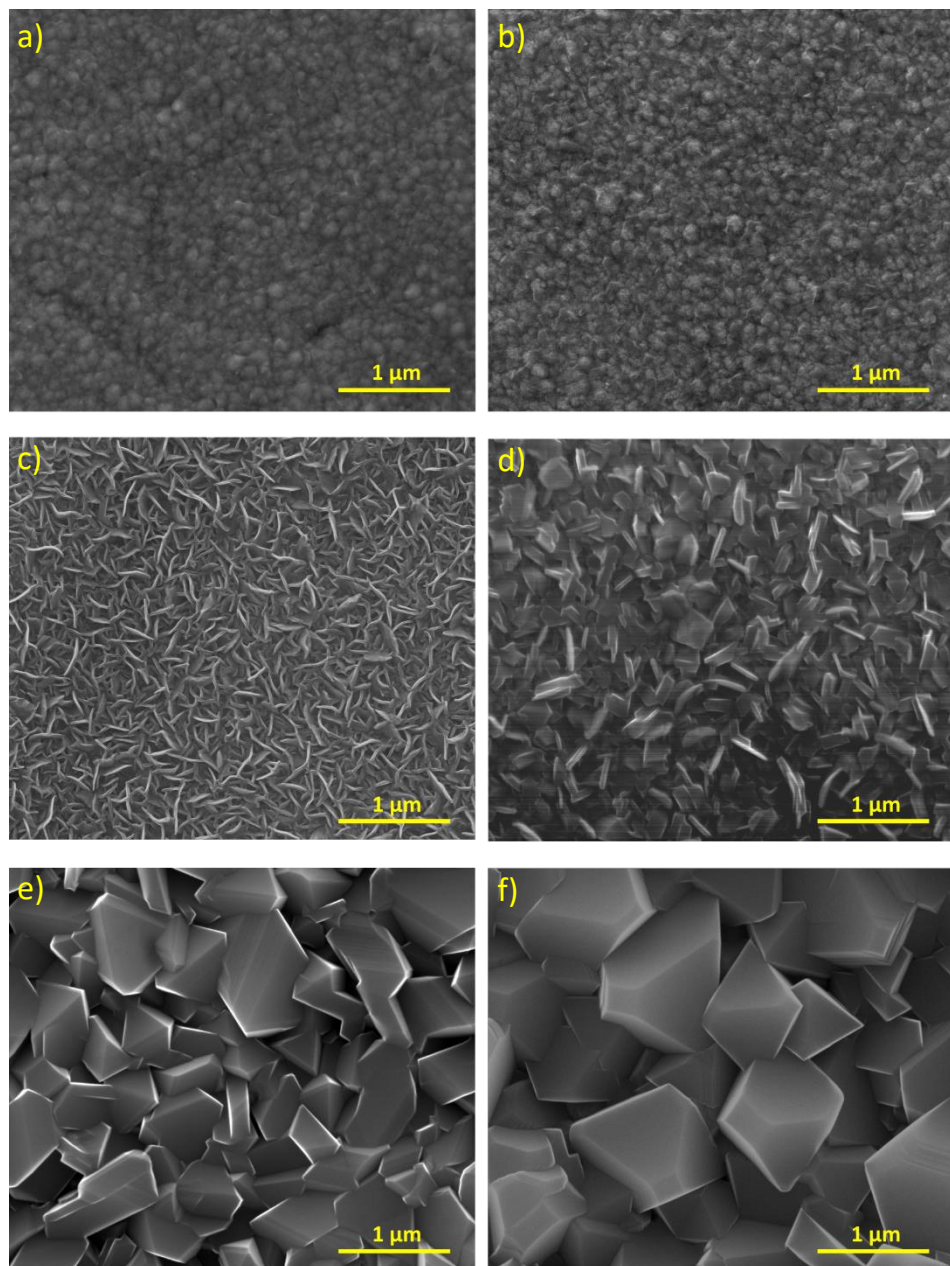


Figure 3.10: SEM micrographs corresponding to a) LNMO_AD, b) LNMO_300, c) LNMO_450, d) LNMO_600, e) LNMO_750, and f) LNMO_900.

3.5.3. Electrochemical performance

After identifying the optimal growth parameters for obtaining spinel LNMO, the fabricated electrodes, i.e. LNMO_AD, LNMO_300, LNMO_450, LNMO_600, LNMO_750, and LNMO_900, were mounted in an airtight CR2032 coin cell against Li foil ($\varnothing = 14$ mm), using a 1 M of LiPF₆ in DMC and EC (1:1 v/v) as liquid electrolyte and glass fiber (*GE Healthcare*, GF/D grade) as separator, to study the electrochemical properties via CV, C-rate and EIS.

Cycling voltammetry

The first electrochemical test, the CV, was carried out at room temperature, the analyzed voltage window was in the 3.5 - 5.0 V vs Li/Li⁺ range, and the scan rate was fixed at 0.05 mV·s⁻¹.

The as-deposited sample, as well as LNMO_300, do not show any relevant electrochemical activity in the selected electrochemical windows, as otherwise expected. There is only a slight increase in current as the voltage approaches 5.0 V vs Li/Li⁺ in the LNMO_AD case, see inset graph of **Figure 3.11a**, which can be related to the decomposition of the electrolyte at such high voltages.^[21] In this way, the need for a post-deposition annealing treatment of the sample has been confirmed in order to make it electrochemically active. As confirmed by the XRD measurements, **Figure 3.8**, the cathode annealed at 300 °C begins to show signs of crystallinity. This is reflected in the fact that the CV shows a weak broad redox peak at 4.6 V vs Li/Li⁺ in the forward scan (from 3.5 to 5 V vs Li/Li⁺) and at 4.2 V vs Li/Li⁺ in the reverse scan (from 5 to 3.5 V vs Li/Li⁺), see inset graph in **Figure 3.11b**, along with the increase of the current at 5 V vs Li/Li⁺ as in the previous case. As the temperature increases to 450 °C, the redox peaks related to nickel and manganese become more noticeable (**Figure 3.11c**). Nevertheless, the expected pure disordered spinel LNMO behavior was achieved at 600 °C.^[15,21,31]

LNMO_600 shows two intense reversible peaks around 4.7 V vs Li/Li⁺, see **Figure 3.11d**. In the forward scan, the peaks observed at 4.69 V vs Li/Li⁺ and 4.77 V vs Li/Li⁺ correspond to Ni oxidation from 2⁺ to 3⁺ and from 3⁺ to 4⁺, respectively. In the reverse scan, the peaks indicating Ni reduction are observed at 4.64 V vs Li/Li⁺ and 4.70 V vs Li/Li⁺. Lithium is successfully (de)inserted in LNMO_600. Besides, the low voltage hysteresis between oxidation and reduction peaks (< 0.1 V) hints at the absence of parasitic reactions at this high voltage. Apart from the Ni-related peaks, a broad weak irreversible band around 4.1 - 4.2 V vs Li/Li⁺ is observed in the forward scan. This can be attributed to the electrochemical

activity of Mn species in 3^+ oxidation state, as already reported in the literature for LNMO film.^[16,23]

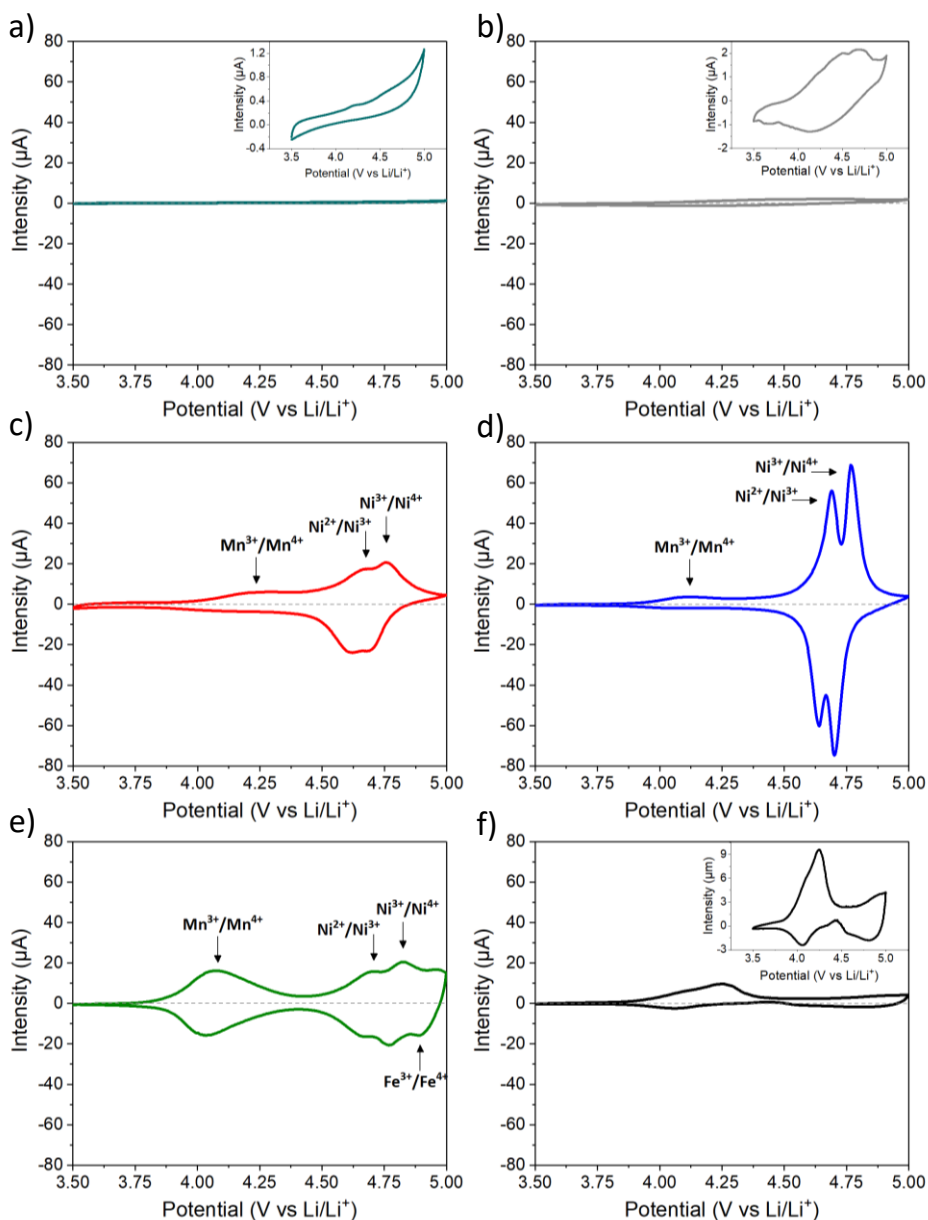


Figure 3.11: CV of a) LNMO_AD, b) LNMO_300, c) LNMO_450, d) LNMO_600, e) LNMO_750, and f) LNMO_900. Inset graphs show a zoomed view of corresponding temperature

The intensity of the LNMO redox peaks was highly reduced by increasing the temperature to 750 °C, **Figure 3.11e**, as well as a new contribution at higher voltages (4.85 V vs Li/Li⁺). This new redox peak can be related to a Fe³⁺/Fe⁴⁺ reaction of the LFMO phase formed upon diffusion of Fe atoms from SS substrate towards thin film.^[23] As mentioned above, under this annealing condition, two identified phases are coexisting in the deposited thin film, leading to several redox reactions corresponding to the LNMO and LFMO phases, see **Figure 3.8**. However, the LNMO_900 sample, **Figure 3.11f**, does not show any relevant electrochemical activity, the peak at high voltages reduces the intensity, while the peak around 4 V vs Li/Li⁺ increases with respect to the others. This is most likely due to the LNMO phase disappearance and the combination of the new formatted Fe₂O₃ hematite phase with LFMO, resulting in a clear deterioration of the electrochemical response of the material.^[34]

Rate performance

Figure 3.12 shows the CE along with the current C-rate of the cathodes measured in the range from C/10 to 10C, and back to C/10 (5 cycles at each C-rate step). Specific capacities and currents were determined for the exact mass of positive electrode loading, calculated by weighing the SS substrate before and after LNMO deposition.

At C/10 the discharge specific capacity of the LNMO_AD sample (**Figure 3.12a**), was near zero, 2.1 mAh·g⁻¹. As seen in the CV, electrochemical behavior improves as the sample increase in crystallization. Thereby, for the samples LNMO_300 (**Figure 3.12b**), LNMO_450 (**Figure 3.12c**), and LNMO_600 (**Figure 3.12d**) the obtained discharge specific capacity was 20.2, 89.3, and 119.0 mAh·g⁻¹, respectively. This last value, corresponding to the sample with spinel structure, is almost 80% of the theoretical one (146.6 mAh·g⁻¹); a value in accordance with the reported LNMO thin film capacity in the literature.^[16,20,23] Unfortunately, as the annealing temperature increases, the concentration of LNMO phase fades while secondary phases appear, as a result, the discharge specific capacity at C/10 drops considerably. This is the case of the samples LNMO_750 and LNMO_900, **Figure 3.12e** and **Figure 3.12f**, respectively. In the first case the obtained value is rather stable (as in the previous cases) around 91 mAh·g⁻¹, whereas at 900 °C the discharge specific capacity decreases progressively from 97.8 mAh·g⁻¹ down to 60.3 mAh·g⁻¹. This can be caused by a phase change during cycling, leading to irreversible reactions and therefore decreasing the amount of available lithium ion in subsequent cycles.^[35] Also, it has been reported that the formation of impurities within LNMO film can affect the electrode performance.^[15,36] In this

sense, XPS measurements carried out in the LNMO_900 sample unveiled Fe atom diffusion from the substrate towards the film surface.^[37]

In all samples, the very high charge capacity observed in the first cycle is followed by its progressive decrease until it equals the value of the discharge capacity that is rather stable. Following this trend, CE also increases in the first cycles, from 74% up to 94% in the case of LNMO_600 at C/10. Despite the observed improvement, CE is very low at this rate, having also a direct relationship with the post-annealing temperature, obtaining 50%, 77%, 93%, 92% and 83% for LNMO_AD, LNMO_300, LNMO_450, LNMO_750, and LNMO_900, respectively.

At 1C, charge and discharge specific capacities of LNMO_AD, LNMO_300, and LNMO_900 decay to zero. Whereas the discharge specific capacity of LNMO_450, LNMO_600, and LNMO_750 was 48.9, 104.9, and 63.2 $\text{mAh}\cdot\text{g}^{-1}$, respectively; this corresponds to 54%, 88%, and 68% of the initial value. The worsening of the capacity retention with increasing C-rate is consistent with a reduction of the efficiency of Li-ion (de)insertion in the material crystal lattice and is aligned with the intrinsic low ionic and electronic conductivities of the LNMO. The slight difference between charge and discharge leads to a CE of 99.1%, 99.2%, and 98.2% as the temperature increases.

In the cycling range from 1C to 10C, a pronounced decrease of charge and discharge capacities is observed. LNMO_450 and LNMO_750 fall by 82% and 90%, respectively. Particularly, the LNMO_600 can deliver a discharge capacity 50.4 $\text{mAh}\cdot\text{g}^{-1}$ (in contrast with the other samples, this only drops 51% from 1C to 10C), which correspond to 42% of its initial capacity. In addition, at this high C-rates, its CE reaches almost 100% value.

Finally, when the cell is cycled back to C/10, the initial capacity is recovered, 92.2%, 99.6%, and 95.6% for LNMO_450, LNMO_600, and LNMO_750, respectively. The obtained best result corresponds again to the LNMO_600 sample, suggesting that the interface between LNMO_600 and the electrolyte remains more stable.^[23] Even operating at this low rate, the charge capacity is slightly higher than the discharge one, decreasing the CE to low values (94%-95% for LNMO_600). The used electrolyte is unstable above 4.3 V vs Li/Li⁺. As the C-rate decreases, the duration of the charge-discharge cycle increases, and, consequently, parasitic reactions related to electrolyte decomposition and their contribution to electrochemistry are also increased. So, the improvement of CE

with increasing C-rate relies on the decreasing contribution of electrolyte decomposition reaction to charge capacity.

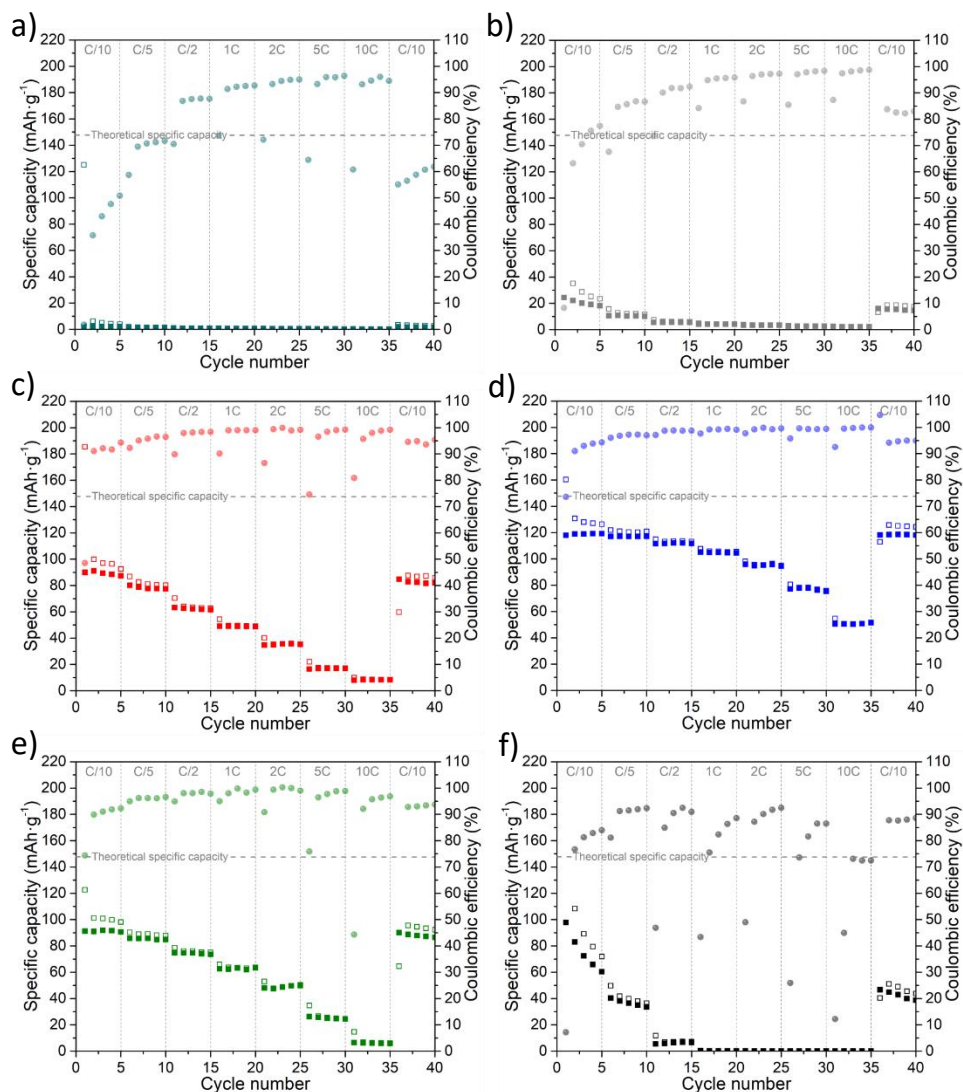


Figure 3.12: Charge (hollow squares), discharge (filled squares) specific capacities, and corresponding coulombic efficiency (filled circle) at different C-rates of a) LNMO_AD, b) LNMO_300, c) LNMO_450, d) LNMO_600, e) LNMO_750, and f) LNMO_900. As reference, a dashed line indicates the theoretical specific capacity of the LNMO, which is equal to $146.6 \text{ mAh}\cdot\text{g}^{-1}$.

Therefore, looking at **Figure 3.12**, the rate performance improves as the sample crystallizes until it reaches 600°C . At this temperature a turning point is found, if

the temperature continues increasing the Fe diffusion alters, even more, the crystalline structure of the sample, and hence its electrochemical activity. For more information, the following section will analyze the Electrochemical Impedance Spectroscopy behavior of the samples.

Electrochemical Impedance Spectroscopy

The EIS measurements were carried out on the assembled CR2032 coin cells. Thus, a two-electrode configuration was employed. Hence, the contribution of the LNMO working electrode, and the lithium anode (counter/reference electrode) will be reflected. The data were collected in the 5 mHz – 101 kHz frequency range at some significant potentials within the range of the battery charge (from 3.5 to 5 V vs Li/Li^+). As an example, **Figure 3.13** highlights the selected voltage points in the CV scan of LNMO_600. In all cases the same criteria were used to choose the points: at the beginning of the cycle (V_1 , 3.5 V vs Li/Li^+), at $\text{Mn}^{3+}/\text{Mn}^{4+}$ reaction voltage (V_2 , around 4.1 V vs Li/Li^+), halfway through the cycle (V_3 , at 4.4 V vs Li/Li^+), at the voltages corresponding to the double oxidation of nickel (from 2^+ to 3^+ and from 3^+ to 4^+ , V_4 and V_5 , respectively), and finally, at the charge cut-off voltage (V_6 , 5 V vs Li/Li^+).

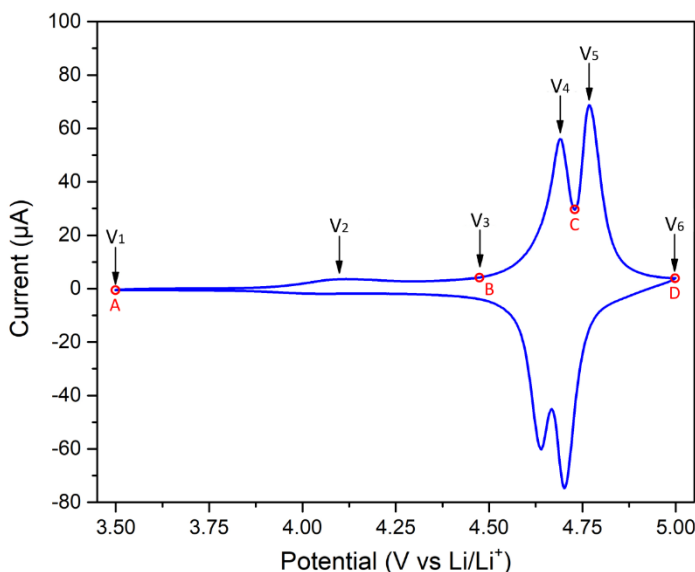


Figure 3.13: CV curve of LNMO_600 sample at 0.05 mV/s scan rate. EIS measurements were carried out at the highlighted voltage points. Red points are placed to visualize the position of the different phases of the LNMO.

Figure 3.14 shows the Nyquist plots, corresponding to the selected potential values for all annealing temperatures (note the difference in the axis scale); for sake of clarity, the zoomed graphs are gathered in the inset graph. The LNMO_AD shows a long arc at LF as the main feature at all potentials, which can be associated with a great semicircle in this frequency region. This long arc reveals that the insulating behavior of the sample is directly related to the electron conductivity of the active material.^[38] As it can be seen from the inset graphs, a well-defined semicircle is revealed at HF. This feature is present at all voltages, and therefore, seems to be independent of the intercalation degree or polarization.^[39] Considering the involved frequency region, this semicircle is most probably associated with the formation of a passivating interfacial layer.^[40]

In the LNMO spinel crystallized sample, *i.e.* LNMO_600, and to a lesser degree in the LNMO_450 and LNMO_300 samples, the impedance associated with the LF semicircle tends to close on the real axis as the potential becomes more positive, thus evidencing its strong potential dependency. In addition, at voltages between 4.10 and 4.75 V vs Li/Li⁺, the impedance curve shows an additional semicircle at MF and a clear tail related to the ion diffusion at LF. However, at high voltages, the large arc at LF is once again visible. The fact that the dispersion tends to close on the real axis as the potential increases and it raises again at high voltages can be explained by assuming a change in the electronic conductivity of the electrode due to the Li⁺ deinsertion. Indeed, this assumption is supported by previous results which suggest that the electronic character of the material switched from semiconductor to conductor depending on the Li⁺ intercalation degree.^[12] As the annealing temperature increases, *i.e.* LNMO_750 and LNMO_900, the semicircle at intermediate voltages in the MF range is also visible. However, at these temperatures the trend has changed, the lowest impedance is achieved at 4.1 V vs Li/Li⁺. This may be related to the newly formed Fe₂O₃ hematite and LFMO secondary phases.

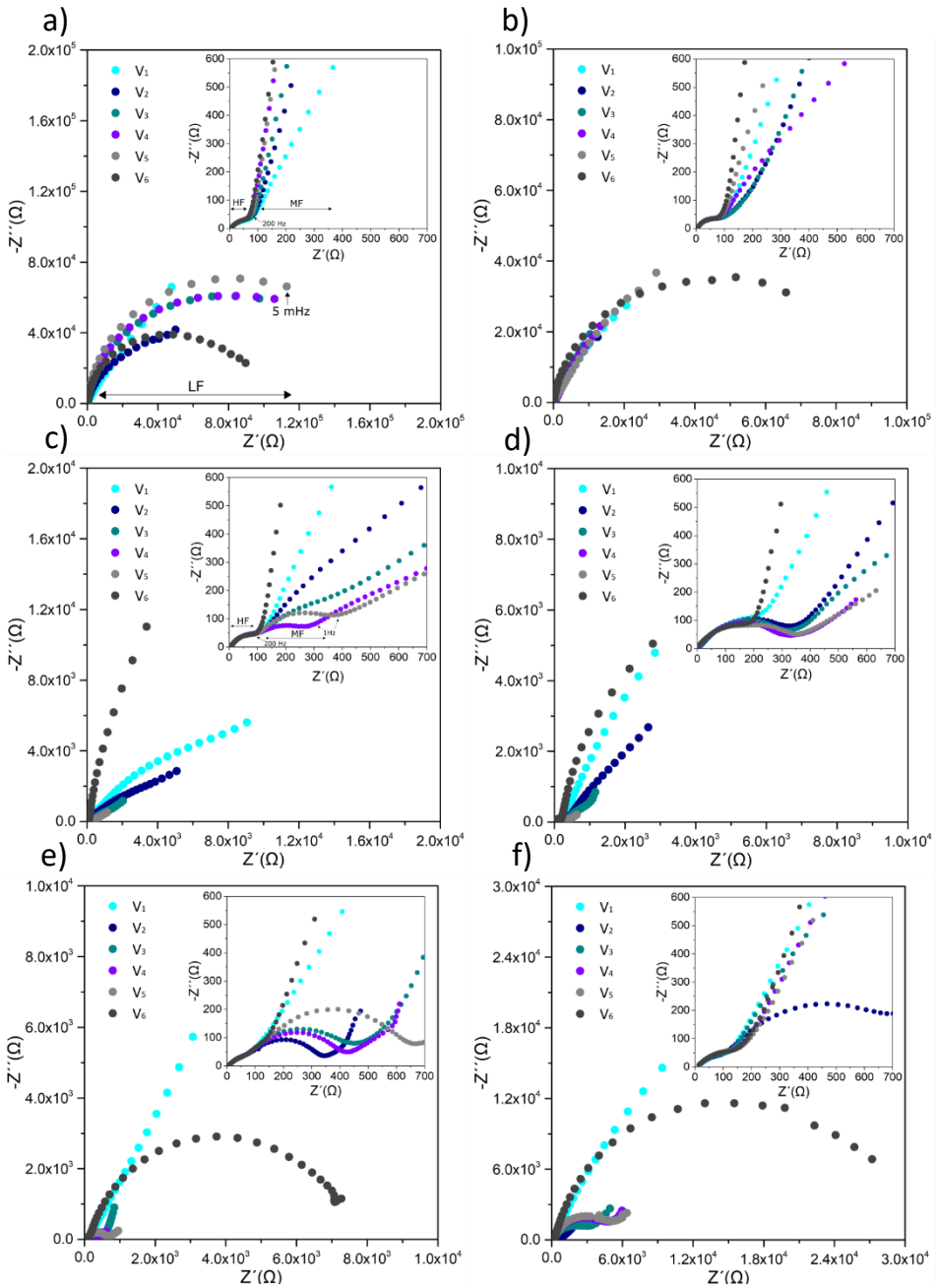


Figure 3.14: Nyquist plots of LNMO cathodes upon charge at different voltage for a) LNMO_AD, b) LNMO_300, c) LNMO_450, d) LNMO_600, e) LNMO_750, and f) LNMO_900. The inset graph shows the zoomed impedance spectrum (same range in all).

Equivalent electrical circuits can be used in order to approximate the experimental impedance data. In this way, the behavior of the abovementioned electrochemical processes can be analyzed quantitatively. In this section, the impedance data were fitted with an equivalent circuit similar to the one used by Levi and co-workers.^[41] The HF part of the equivalent circuit is modelled with the electrolyte ohmic resistance (R_{Ω}), corresponding to the Li^+ resistance across the electrolyte, in series with the $R_{\text{Int}}\text{-CPE}_{\text{Int}}$ contribution of the interfacial layers. Note that the expected electronic resistance associated with contacts and cables, already incorporated in R_{Ω} , is much lower than that of Li^+ mobility and can thus be neglected. The semicircle at MF, is ascribed to a charge-transfer resistance and a double layer capacitance ($R_{\text{CT}}\text{-C}_{\text{DL}}$), connected in parallel. Finally, the LF range is modelled with two contributions: i) RC semicircle associated with bulk electronic resistance (R_e) and charge accumulation capacitance at the surface/crystallites domains which is represented with a constant phase element (CPE_e),^[42] and ii) the Warburg diffusion element (Z_w) in series with the active mass capacitance (C_{diff}), that are used to describe the sloping line ascribed to the solid-state diffusion of the Li^+ in the crystal and the active mass capacitance, respectively.

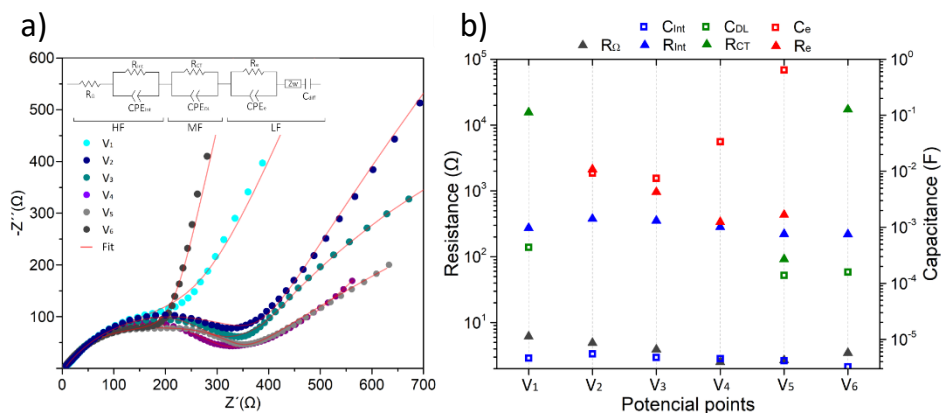


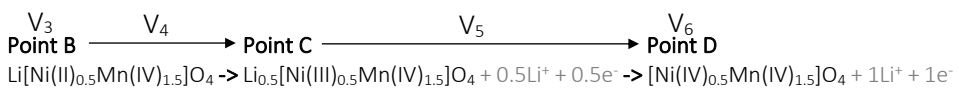
Figure 3.15: The fits of Nyquits plots of LNMO_600 at different voltages, a) The equivalent circuit and the fitted data, and b) R_{Ω} (dark gray triangles), $R_{\text{Int}}\text{-C}_{\text{Int}}$ (blue triangles and squares, respectively), $R_{\text{CT}}\text{-C}_{\text{DL}}$ (green triangles and squares, respectively) and $R_e\text{-C}_e$ (red triangles and squares, respectively) behavior vs voltage (represented as log scale).

Figure 3.15a shows the Nyquist plots of LNMO_600 fitted with the proposed equivalent circuit (see inset drawing). In this section, we focus on this sample in which is, according to the previous structural and electrochemical characterization, the most representative LNMO spinel sample. The overall trend of the resistance and capacitance values, calculated from fitting, are reported in

Figure 3.15b. During the fitting procedure, the diffusion elements of Z_w and C_{diff} were substituted by CPEs in order to consider any roughness or other deviations from the ideal interfacial behavior.^[42,43]

Previously it was observed that the position and the size of the first semicircle in HF do not vary significantly with the voltage, *i.e.*, they are resistive processes independent of oxidation or changes in the system. The low-resistance contribution of R_{Ω} (in the range 3-6 Ω in all cases) is followed by the R_{int} in the 200-300 Ω range and a $\text{CPE}_{\text{int-T}}$ value of about $5 \cdot 10^{-5}$ F with 0.6 of $\text{CPE}_{\text{int-P}}$. As can be seen in the figure above, the latter values result in capacitance effects of the same order of magnitude (10^{-6}) for all measured voltages, suggesting that they correspond to the same process: the formation of a passivating layer on the electrode/electrolyte interface.

The lithiated and non-lithiated phases show an $R_{\text{CT}}\text{-CPE}_{\text{DL}}$ contribution, which is not distinguished in most of the intermediate phases, with a charge transfer resistance of around 15 k Ω and a capacitance value in the order of 10^{-4} (see V_1 and V_6 in **Figure 3.13**). The absence of the $R_{\text{e}}\text{-CPE}_{\text{e}}$ contribution may be related to the low electronic conductivity of the cathode and the slow kinetics of the electrochemical reactions.^[12] When the electrode undergoes the manganese oxidation process, from point A going through V_2 to point B (from V_1 to V_3 , see **Figure 3.13**), appears the $R_{\text{e}}\text{-CPE}_{\text{e}}$ contribution and $R_{\text{CT}}\text{-C}_{\text{DL}}$ disappears. The phase change improves the electronic conductivity of the sample. As can be seen in the following equation, V_4 and V_5 were measured during the phase change of the cathode, while V_6 (mentioned above) analyze the delithiated phase.



In this way, in the potential value V_4 , the contribution of the charge-transfer is not discernible either. Although it can be overlapped with the previous semicircle being undifferentiated, as it is possible to appreciate in LNMO_450 and LNMO_750 samples. On the contrary, in V_5 , both contributions are observed, *i.e.* $R_{\text{CT}}\text{-C}_{\text{DL}}$ and $R_{\text{e}}\text{-CPE}_{\text{e}}$. The increase in the concentration of Li^+ and e^- enabled the charge transfer between the electrode and the electrolyte, obtaining only 19 Ω of R_{CT} , much lower than the one corresponding to V_6 . As Mohamedi and co-workers stated,^[12] this confirms the transition from semiconductor in totally lithiated phase to conductor in intermediate phases, and getting back to semiconductor in delithiated phase, as voltage increases.

3.6. Effect of the post-deposition annealing time

According to the structural, morphological, and electrochemical characterization performed in the previous section, the film annealed at 600 °C, LNMO_600, exhibits the features related to disordered spinel LNMO structure. So far, the thin film crystallization processes were carried out by annealing in air up to the desired temperature and maintaining it for 1 hour.

Table 3.2: Samples used for the study of the effect of the duration of the post-deposition thermal treatment.

	Annealing time (h)	Annealing temperature (°C) and specifications
LNMO_600_0.5h	0.5	In air at 600 °C with a 5 °C·min ⁻¹ ramp rate
LNMO_600_1h	1	
LNMO_600_2h	2	

In this section the effects of annealing at 600 °C for 0.5, 1, and 2 hours are studied. For this purpose, SEM, XRD, and electrochemical tests were conducted. These samples are referred to hereafter as LNMO_600_0.5h, LNMO_600_1h, and LNMO_600_2h, respectively. **Table 3.2** lists the samples used in this section.

3.6.1. Surface morphology and structural characterization

Figure 3.16 shows the evolution of the surface morphology of the LNMO films as a function of the annealing time at 600 °C. The surface of the LNMO_600_0.5h sample, see **Figure 3.16a**, consists mostly of flake-shaped particles with length and width of 500 and ~70 nm, respectively.

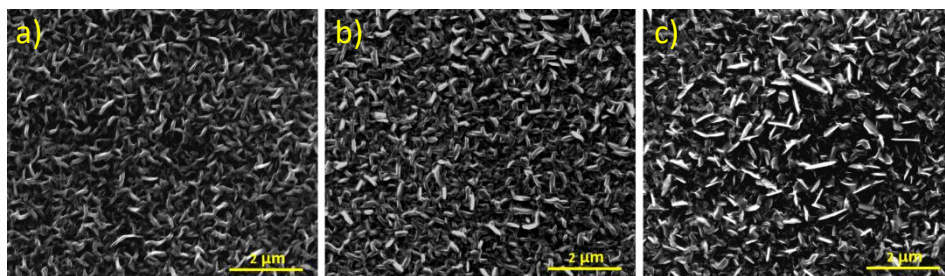


Figure 3.16: SEM images corresponding to a) LNMO_600_0.5h, b) LNMO_600_1h, and c) LNMO_600_2h.

By increasing the annealing time to 1 hour, the surface did not change significantly. In the sample LNMO_600_1h (**Figure 3.16b**) the surface was also

mostly full of flake-shape crystallites. However, in the longer-lasting annealing, a slight surface morphology change is observed with respect to the previous two samples: the crystallite length increases up to $1\ \mu\text{m}$ as seen in **Figure 3.16c**.

In order to verify if this small morphological difference is correlated with a crystallinity change of the samples, an XRD analysis was performed (see **Figure 3.17**). LNMO phase diffractogram, PDF 01-070-4215 reference corresponding to the cubic system with disordered Fd-3m (227) spinel, matched well with the reflections observed for all studied samples. In the LNMO_600_2h film, a new weak peak at $2\theta = 44.3^\circ$ is observed which matches well with the LNMO (400) diffraction line. However, in this sample, the LNMO reflections are accompanied by two additional reflections ($2\theta = 30.3^\circ$ and 35.6°) corresponding to $\gamma\text{-Fe}_2\text{O}_3$ phase, which could be originated by the Fe diffusion from the substrate.^[23]

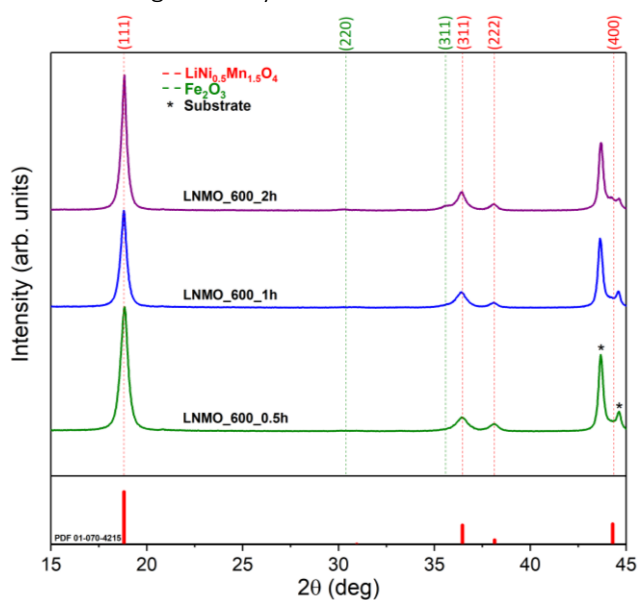


Figure 3.17: XRD pattern of LNMO_600_0.5h, LNMO_600_1h and LNMO_600_2h samples. Red, and green dashed lines correspond to miller indexes of spinel LNMO and $\gamma\text{-Fe}_2\text{O}_3$ maghemite phases.

3.6.2. Electrochemical characterization

Figure 3.18 shows the electrochemical results obtained from the LNMO thin films annealed for different times. In **Figure 3.18a** the first three cycles at C/10 in the 3.5 to 5 V vs Li/Li^+ voltage range, for LNMO_600_0.5h, LNMO_600_1h, and LNMO_600_2h are gathered. Strikingly, besides the double Nickel plateaus at 4.68 V vs Li/Li^+ and 4.76 V vs Li/Li^+ observed in all the samples, an unexpected

non-reversible plateau appeared in the first charge at around 4 V vs Li⁺/Li. Interestingly, the duration of this electrochemical process progressively increases with the annealing time of the samples. It is more than plausible that the presence of Fe₂O₃ phases in the thin films is at the origin of this plateau, this issue will be discussed further in the next section.

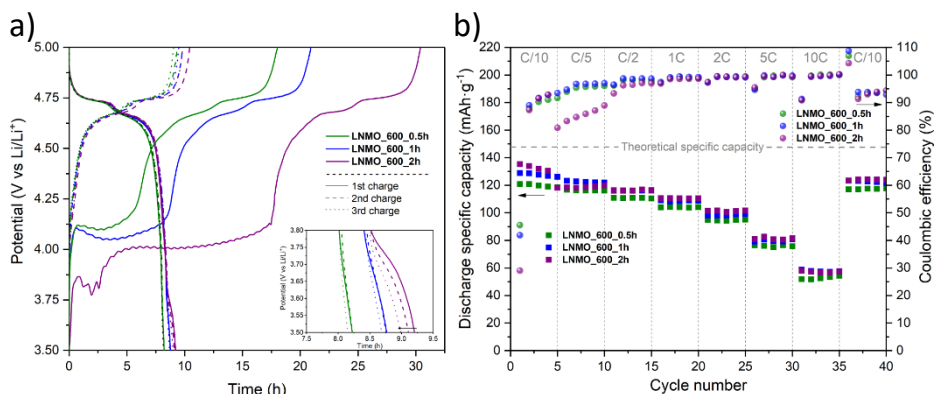


Figure 3.18: Electrochemical behavior of LNMO_600_0.5h, LNMO_600_1h and LNMO_600_2h, a) first three cycles (charge-discharge) at C/10, and b) discharge specific capacity at different C-rates, along with the coulombic efficiency.

The specific discharge capacity, along with the CE of each cycle, for all samples is represented in **Figure 3.18b**. As it can be observed, the C-rate performance was similar for all samples, indicating that the Li-ion diffusion through the spinel lattice of the samples annealed at different times not a limiting factor. At low C-rate (C/10), the obtained discharge specific capacities are 132.1, 127.6, and 119.8 mAh·g⁻¹ for LNMO_600_2h, LNMO_600_1h, and LNMO_600_0.5h, respectively. The increase in capacity in the LNMO_600_2h case, apart from higher crystallinity of the LNMO phase as seen in **Figure 3.17**, maybe due to an extra irreversible plateau at ~3.75 V vs Li/Li⁺ in the discharge (see inset graph in **Figure 3.18a**), resulting in a higher discharge capacity than the other two samples. This phenomenon may occur due to the presence of Li_xMnO₂ formed during the annealing process.^[23] The loss of specific discharge capacity is however similar in all the cases. At 1C, the capacity retention observed was 86.8%, 85.0% and 83.69% for the LNMO_600_0.5h, LNMO_600_1h and LNMO_600_2h, respectively. At a high rate (10C), these values reached 43.8%, 44.9%, and 42.9% by increasing the annealing time. It is important to highlight that more than 95% of their initial capacity was recovered in all cases when returning to C/10, confirming the good electrochemical stability of the LNMO after the C-rate. Regarding the CE, during the first cycles, the values were low, particularly

relevant in the case of the LNMO_600_2h sample. The formation of the secondary phases together with the electrolyte decomposition process occurring predominantly during the charge may be the source of such low values. Nevertheless, after the first cycles, the CE is steadily maintained above 90% during the whole C-rate capability test.

As we concluded in the previous section, the existence of secondary phases affects significantly the electrode performance. In this sense, and taking into account the higher specific capacity obtained for the LNMO_600_1h sample, the standard annealing process will be set for 1h at 600 °C.

3.6.3. In-depth elemental distribution analysis

However, the atom interdiffusion beneath the film surface cannot be excluded. To shed light on this, a 1.7 μm thick LNMO_600_1h sample was fabricated to qualitatively study in-depth elemental distribution. SEM EDS line scan performed along the film cross-section (see **Figure 3.19a**) allowed the detection of Cr and Fe in the SS substrate, as expected considering their high concentration, but also of Cr and Fe traces in the LNMO film. Particularly, the presence of this species decreases exponentially going from the SS/LNMO interface to the LNMO surface as seen in **Figure 3.19b**. In order to further explore the effect of diffusion, different LNMO thicknesses are deposited and analyzed in the next section.

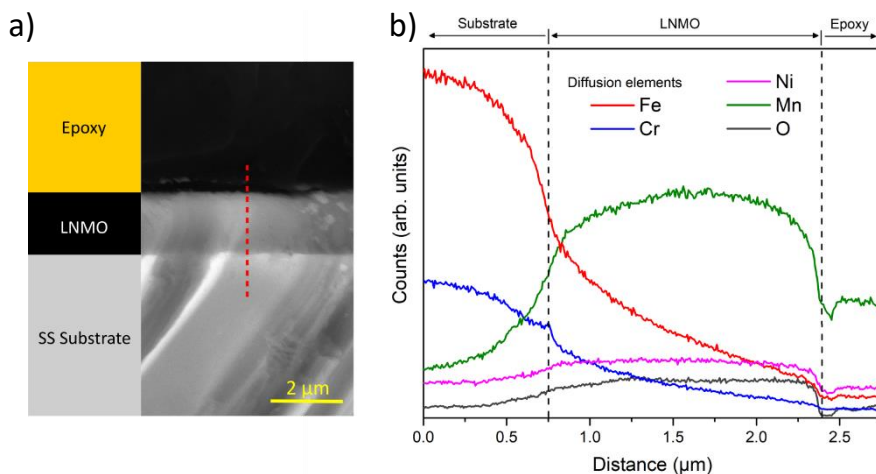


Figure 3.19: a) SEM cross-section micrograph of a 1.7 μm thick sample annealed at 600 °C for 1 hour, and corresponding sketch. The red dashed line outlines the scanned region using SEM EDS. b) In-depth distribution of Mn, Ni, O, Fe and Cr as detected by SEM EDS measured along the red dashed line shown in a). Black dashed-lines identify the SS/LNMO and LNMO/epoxy interfaces.

It is interesting to note that although the highest diffusion element was iron, in the substrate/cathode interface appears a small peak confirming the increase of chromium concentration.³ **Figure 3.20a** shows the EELS mapping of Cr distribution, wherein a thin Cr-abundant layer can be distinguished in the interface. This layer was further studied by using TEM, **Figure 3.20b**. With this microscopy method, we could determine an 8.3 nm Cr-layer between the substrate and the polycrystalline cathode (see Fast Fourier Transformation-FFT inset graph).

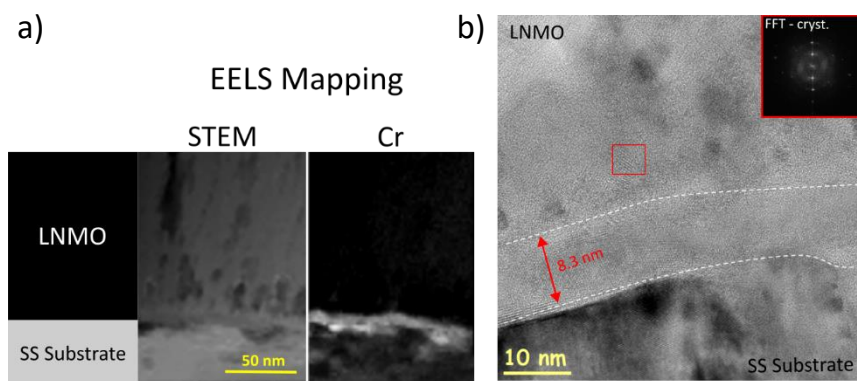


Figure 3.20: a) STEM cross-section micrograph of sample_600_1h with a corresponding sketch and Cr distribution along the interface. b) TEM image of the SS/LNMO interface, white dashed lines delimit a layer with different crystallinity. Inset figure correspond to the FFT of the LNMO.

3.7. Effect of the thin film thickness

As mentioned in the previous section, the diffusion of Fe decreases exponentially inside the LNMO layer (see **Figure 3.19**). The effect of LNMO film thickness deposited by sputtering in the structural and morphological properties of the films is analyzed and correlated with its electrochemical performance as cathode in Li|LNMO batteries.

The deposition processes of 0.5h, 1h, 2h, and 10h duration were carried out, leading to the deposition of 270 nm, 540 nm, 1080 nm, and 5.4 μm thick films, respectively. These samples, summarized in **Table 3.3**, will henceforth be referred to, in a rounded sense, as LNMO_250, LNMO_500, LNMO_1000, and LNMO_5000. In order to achieve the optimal crystallographic structure, the LNMO thin films underwent a post-annealing treatment at 600 $^{\circ}\text{C}$ in air for 1h with a 5 $^{\circ}\text{C}\cdot\text{min}^{-1}$ ramp rate in a commercial furnace.^[24]

³ The electronic microscopy works corresponding to the analysis of Cr diffusion have been carried out at *CIC nanoGUNE* by Dr. Francisco Bonilla within the MONBASA project.

Table 3.3: Samples used for the study of the effect of the thin film thickness.

	Duration (h)	Thickness (nm)	Thermal treatment specifications
LNMO_250	0.5	270	
LNMO_500	1	540	600 °C in air for 1h
LNMO_1000	2	1080	with a 5 °C·min ⁻¹ ramp
LNMO_5000	10	5400	rate

3.7.1. Surface morphology and structural characterization

Directly correlated to the maximum achievable areal capacity, the thickness of the LNMO layer is a fundamental parameter for the electrochemical performance of the battery. Here, we first analyze the evolution of LNMO crystallinity and morphology as a function of film thickness. For this purpose, XRD, SEM and Raman spectroscopy were used, prior to the electrochemical study.

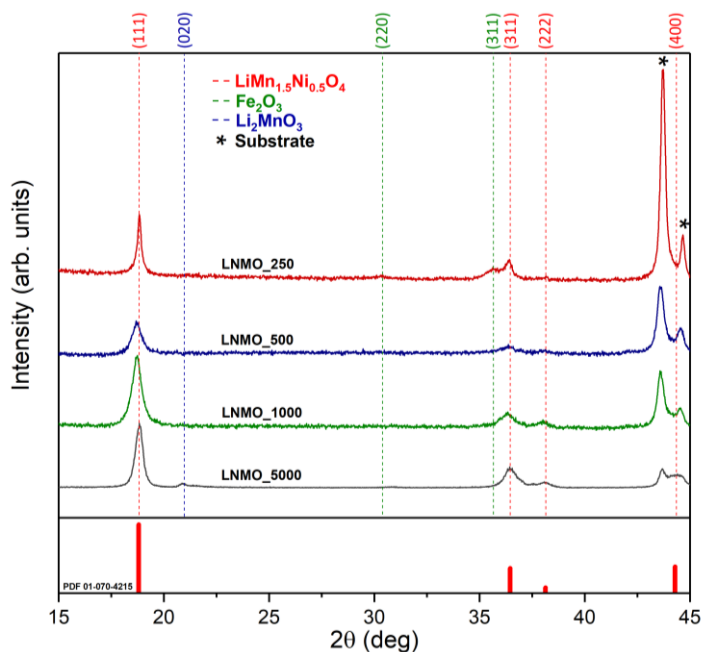


Figure 3.21: XRD pattern of LNMO_250, LNMO_500, LNMO_1000 and LNMO_5000 thin film cathodes. Stars identify the reflection corresponding to α - and γ -phases of the SS substrate. Red, blue, and dark green dashed lines correspond to miller indexes of spinel LNMO (PDF 01-070-4215), γ - Fe_2O_3 maghemite and detrimental Li_2MnO_3 phases, respectively. In the lower part of the figure, the pattern corresponding to standard PDF card used as reference for the LNMO is reported.

The XRD patterns of LNMO_250, LNMO_500, LNMO_1000 and LNMO_5000 films after annealing at 600 °C are shown in **Figure 3.21**, where reflections ascribed to the SS substrate^[23] are marked with an asterisk; as expected, the SS peak intensities are heavily influenced by the LNMO film thickness. In all cases, a series of reflections matching with the $\text{LiNi}_{0.5}\text{Mn}_{1.5}\text{O}_4$ spinel phase, cubic system with disordered Fd-3m (227), could be identified (see red dotted vertical lines highlighting LNMO reflections in **Figure 3.21**). However, significant differences were detected as a function of the thickness. In LNMO_250, the thinnest studied film, only two diffraction peaks at $2\theta = 18.8^\circ$ and 36.4° corresponding to the (111) and (311) LNMO spinel reflections were observed, accompanied by two additional reflections ($2\theta = 30.3^\circ$ and 35.6°) that would correspond to undesired $\text{Y-Fe}_2\text{O}_3$ maghemite secondary phase. As discussed later, this secondary phase could be related to Fe diffusion from the substrate towards the LNMO film taking place during annealing.^[24] For thicker films, this secondary phase disappears, and new peaks at $2\theta = 38.1^\circ$ and 44.3° are observed. These could be identified as the LNMO (222) and (400) diffraction lines. In the case of LNMO_1000 and LNMO_5000 films, the reflections associated to LNMO become more intense and narrower with respect to LNMO_500. Finally, it should be noted the appearance of a small peak at around $2\theta = 20.8^\circ$ in the thickest LNMO_5000 sample, which can be associated to the presence of a Li_2MnO_3 secondary phase, probably originated by an oxygen deficiency in the sample.^[44] Notably, secondary oxide phases such as Li-Fe-O ,^[15] Fe-Ni-Mn-O ^[45] or Li-Fe-Mn-O ^[23] were also reported in the past in similar systems, fact that could alter the conductance of the film by blocking the transport of electrons or ions and, ultimately affect the electrochemical performance of the cathode.^[23,36]

Figure 3.22 shows the evolution of the surface morphology of the LNMO films as a function of the thickness. The morphology of LNMO_250 and LNMO_500 is similar, consisting of a dense surface composed of flake-shaped crystalline grains of about 250 nm in the long axis (**Figure 3.22a** and **Figure 3.22b**). The surface morphology changes for the LNMO_1000 film (**Figure 3.22c**) in which the flake-like particles increase in length by forming rectangular structures. The rectangular structure was most evident in the LNMO_5000 sample which is the thickest sample (**Figure 3.22d**).

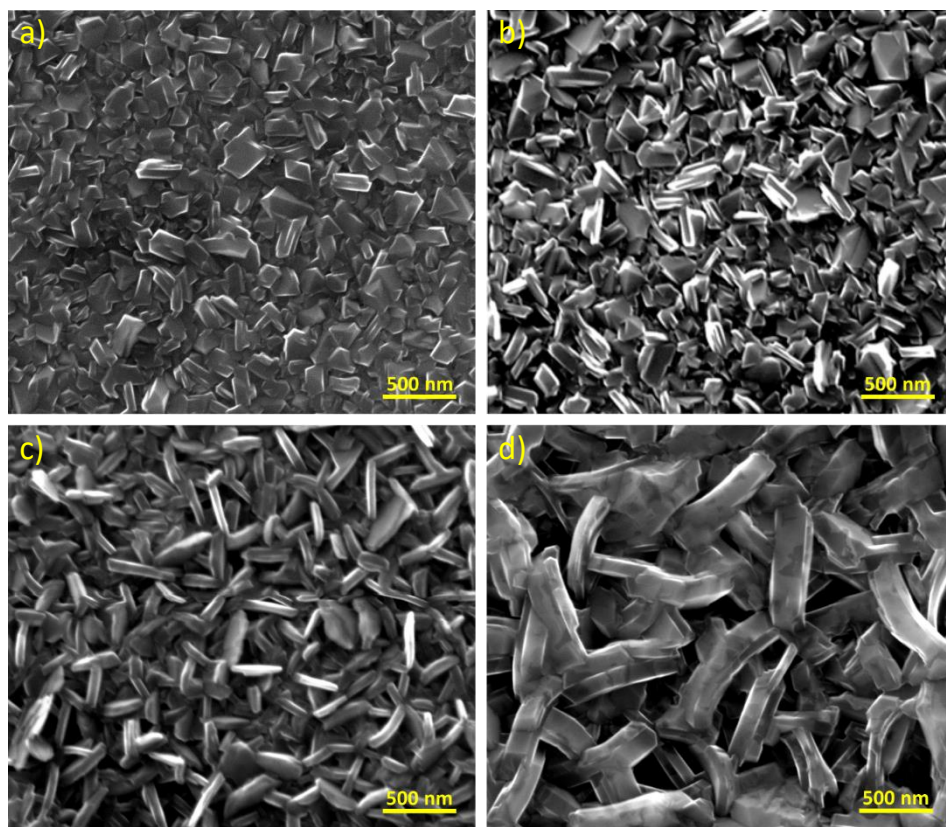


Figure 3.22: SEM images corresponding to a) LNMO_250, b) LNMO_500, c) LNMO_1000, and d) LNMO_5000 thin film cathodes after annealing in air at 600 °C.

The formation of interconnected, large and elongated (up to 1000 nm long and close to 200 nm wide) crystallites resulted in a considerable surface aspect change with respect to thinner samples. Indeed, the surface morphology of the LNMO_5000 appears to be less dense than the previous ones; however, as evidenced from the cross-sectional imaging shown in **Figure 3.23**, the film presents a highly dense structure in the inner $\sim 4 \mu\text{m}$ of the film, while the porosity seems to be ascribed only to the outermost 900 nm of the film.

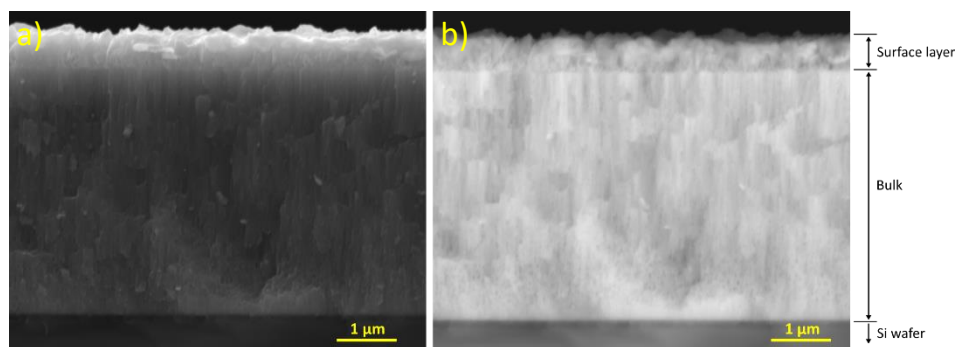


Figure 3.23: Cross-section of the LNMO_5000 deposited on silicon (100) single crystal and annealed to 600 °C, a) SE and b) BSE.

The structural evolution upon thickness variation is further analyzed by Raman spectroscopy, as shown in **Figure 3.24**. As mentioned above, this technique is particularly interesting to study LNMO, since it allows to distinguish between the ordered ($P4_332$) and disordered ($Fd-3m$) spinel LNMO phase structures.^[4] According to literature,^[46] the spinel structure presents vibrational modes at 640 (A_{1g}), 600 ($F_{2g(3)}$), 500 ($F_{2g(2)}$), 404 (E_g) and 343 ($F_{2g(1)}$) cm^{-1} , as highlighted in **Figure 3.24**. As previously discussed, the clearest distinction between the ordered and the disordered spinel is usually the double peak at 600 cm^{-1} .^[47] Looking at **Figure 3.24**, the spectra obtained for LNMO_250, LNMO_500 and LNMO_1000 films are in agreement with the presence of a disordered spinel phase, for which optimum electrochemical properties are expected as compared to its ordered counterpart.^[48] Notably, no sign of the Fe_2O_3 secondary phase was observed in the thinnest LNMO_250 sample (further analyzed later). The spectrum obtained for the LNMO_5000 significantly differs and requires a more detailed examination. A strong shift of A_{1g} and $F_{2g(3)}$ modes has been already reported in the literature in LNMO samples with additional presence of Li_2MnO_3 phase, which could be argued as well in our case.^[26,44] However, the same criteria is not applicable to $F_{2g(2)}$ mode, which is barely displaced. It is more likely to conceive that these modes correspond to the Li_2MnO_3 secondary phase itself, which overlap with those of the LNMO.^[49] This hypothesis matches well with the presence of the vibration modes located at 250 cm^{-1} , 327 cm^{-1} , 372 cm^{-1} , 417 cm^{-1} and 441 cm^{-1} , that can be associated as well to the Li_2MnO_3 .^[50] Therefore, Raman results confirm the presence of Li_2MnO_3 secondary phase in the thickest film, LNMO_5000, fact that strongly influences the short-range ordering of the spinel LNMO.

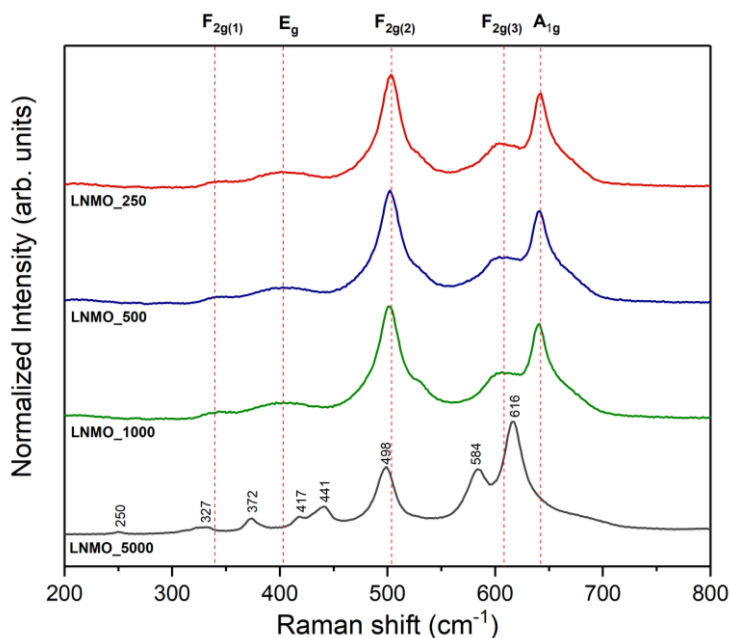


Figure 3.24: Raman spectra corresponding to LNMO_250, LNMO_500, LNMO_1000 and LNMO_5000 thin film cathodes. Dashed red lines indicate the expected LNMO vibrational modes.

3.7.2. Electrochemical characterization

The electrochemical results obtained for the studied LNMO thin films are collected in **Figure 3.25**. **Figure 3.25a** shows the discharge areal capacity, in $\mu\text{Ah}\cdot\text{cm}^{-2}$, of the four samples at different C-rates. As it can be observed, at the lowest C-rate ($C/10$), LNMO_5000 cathodes reached a discharge areal capacity of $267.9 \mu\text{Ah}\cdot\text{cm}^{-2}$, whereas for LNMO_1000, LNMO_500 and LNMO_250 films the maximum capacity is reduced to $52.6 \mu\text{Ah}\cdot\text{cm}^{-2}$, $23.3 \mu\text{Ah}\cdot\text{cm}^{-2}$ and $15.4 \mu\text{Ah}\cdot\text{cm}^{-2}$, respectively. Interestingly, the obtained values perfectly match the expected reduced thickness being the 19.6%, 8.7% and 5.7% of the LNMO_5000 capacity, respectively. Therefore, no significant effects of the Li_2MnO_3 and Fe_2O_3 secondary phases found in the thickest and thinnest samples respectively are observed at this C-rate. In all cases, increasing the C-rate results in a decrease of the capacity retention, due to the worsening of the (de)insertion efficiency of Li-ions into the crystal structure of LNMO. However, the loss in areal capacity is different depending on the sample. At $C/5$, the capacity retention was 90.7%, 98.4%, 98.6% and 93.0% compared to $C/10$, for the LNMO_5000, LNMO_1000, LNMO_500 and LNMO_250, respectively. A further decrease of capacity was observed at $C/2$ and $1C$, being 60.5%, 88.1%, 92.2% and 79.7% in the latter C-rate

as the thickness decreases. Looking at these results, it seems that the secondary phases observed in LNMO_5000 (Li_2MnO_3) and LNMO_250 (Fe_2O_3) impairs the quality of the LNMO cathodes affecting the electrochemical performance at high C-rates, particularly relevant for the thickest LNMO_5000 sample.^[15] Meanwhile, LNMO_1000 and LNMO_500, where disordered spinel structures free of impurities were obtained, present the best results in terms of capacity retention. It should be noted, though, that the particularly bad capacity retention of the thickest LNMO_5000 sample could be also associated to kinetic effects, since more sluggish processes are expected for thicker electrode layers owing to the increased diffusion lengths (more time will be required for the (de)insertion process during (dis)charge). In fact, the discharge areal capacity follows a linear trend with the electrode thickness for low C-rates, whereas this trend is lost at high C-rates. **Figure 3.26** shows the statistical study carried out over 20 samples from 250 to 5500 nm. At high C-rates (10C), although one could argue a slight dependency in the thinner samples, the linearity is practically lost. Indeed, the discharge areal capacity of the thicker ones tends to zero. Finally, it is also important to highlight that almost full initial capacity was recovered in all cases when returning to C/10, showing good electrochemical stability of the LNMO at high current densities.

To better observe the electrochemical performance of each thin film electrode, the corresponding specific discharge capacity, along with CE of each cycle, is represented in **Figure 3.25b**. Interestingly, at C/10 the discharge specific capacity was similar for all thickness (48.2 - 55.5 $\mu\text{Ah}\cdot\text{cm}^{-2}\cdot\mu\text{m}^{-1}$ range), indicating that, at low C-rates, the Li-ion diffusion through the spinel lattice is not a limiting factor, regardless of the layer thickness. Moreover, this observation supports the assumption that secondary phases do not play a significant role in the discharge specific capacity, at least at this low C-rate. As for the CE, low values were obtained in the first cycle of all electrodes, being the LNMO_250 and LNMO_500 the electrodes delivering the lowest CE values. This can be ascribed to electrolyte decomposition processes related to the substrate induced impurities predominantly occurring during the first charge and will be further analyzed later. Nonetheless, after the initial cycles, the CE is steadily maintained close to 100% during the whole C-rate capability test. The underperformance of the thickest LNMO_5000 film at high C-rates is also clearly observable in **Figure 3.25b**, with remarkable differences, in terms of capacity decay at increasing C-rates, between the thickest electrode and the other three. Notably, the best performing cathode in terms of specific capacity is the LNMO_500. This excellent behavior is ascribed to a good balance between the absence of secondary phases and the reduced thickness that favors fast kinetics.

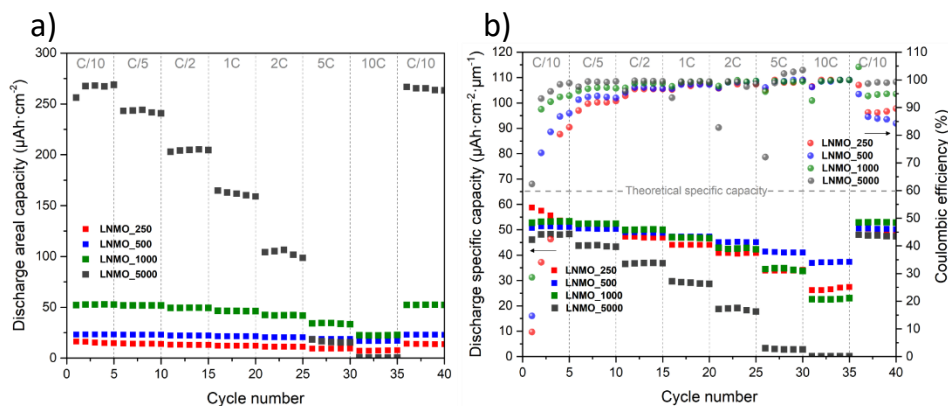


Figure 3.25 Discharge a) areal and b) specific capacities of LNMO_250 (red squares), LNMO_500 (blue squares), LNMO_1000 (green squares) and LNMO_5000 (black squares) films at different C-rate. In b) coulombic efficiency values are reported as well.

To better observe the electrochemical performance of each thin film electrode, the corresponding specific discharge capacity, along with coulombic efficiency (CE) of each cycle, is represented in **Figure 3.25b**. Interestingly, at C/10 the discharge specific capacity was similar for all thickness (48.2 - 55.5 $\mu\text{Ah}\cdot\text{cm}^{-2}\cdot\mu\text{m}^{-1}$ range), indicating that, at low C-rates, the Li-ion diffusion through the spinel lattice is not a limiting factor, regardless of the layer thickness. Moreover, this observation supports the assumption that secondary phases do not play a significant role in the discharge specific capacity, at least at this low C-rate. As for the CE, low values were obtained in the first cycle of all electrodes, being the LNMO_250 and LNMO_500 the electrodes delivering the lowest CE values. This can be ascribed to electrolyte decomposition processes related to the substrate induced impurities predominantly occurring during the first charge and will be further analyzed later. Nonetheless, after the initial cycles, the CE is steadily maintained close to 100% during the whole C-rate capability test. The underperformance of the thickest LNMO_5000 film at high C-rates is also clearly observable in **Figure 3.25b**, with remarkable differences, in terms of capacity decay at increasing C-rates, between the thickest electrode and the other three. Notably, the best performing cathode in terms of specific capacity is the LNMO_500. This excellent behavior is ascribed to a good balance between the absence of secondary phases and the reduced thickness that favors fast kinetics.

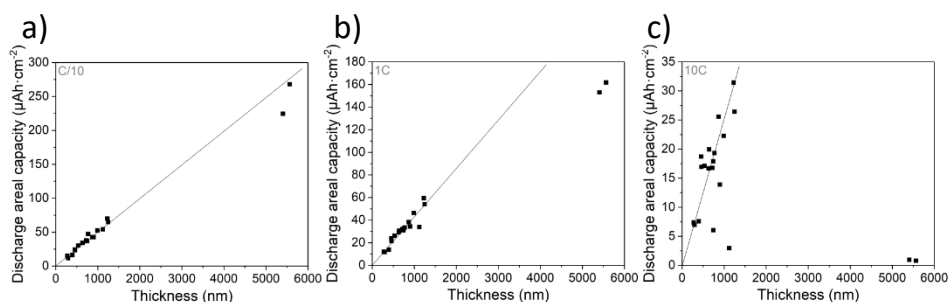


Figure 3.26: Evolution of the discharge areal capacity as a function of thickness at different C-rates, a) C/10, b) 1C and c) 10C.

The long-term stability of the LNMO thin film electrodes was tested by cycling the cells at 1C for more than 300 cycles, see **Figure 3.27**. As it can be observed in this figure, the capacity drops relatively fast for the LNMO_5000 and LNMO_250, whereas it is well preserved for the intermediate cases. Indeed, for the thickest LNMO_5000 sample, the discharge areal capacity drops steadily from 173.0 $\mu\text{Ah}\cdot\text{cm}^{-2}$ to 116.5 $\mu\text{Ah}\cdot\text{cm}^{-2}$, while, for the thinnest LNMO_250 sample, the discharge areal capacity decreases especially in the first 30 cycles (from 11.5 $\mu\text{Ah}\cdot\text{cm}^{-2}$ to 7.1 $\mu\text{Ah}\cdot\text{cm}^{-2}$) and afterwards remains practically stable (reaching 4.95 $\mu\text{Ah}\cdot\text{cm}^{-2}$ after 300 cycles). The latter can be ascribed to the electrolyte decomposition process (SEI formation) occurring at the cathode surface. It is expected to be larger in the case of LNMO_250 with respect to the thicker samples due to the high surface-to-volume ratio, having higher repercussion during initial cycles. In contrast, the capacity decay of the thickest sample might likely relay on the slow kinetics at 1C, associated also with the purity of the film. Eventually, the capacity retention for the four samples after 300 cycles is 43.1%, 98.0%, 96.5% and 67.3% for LNMO_250, LNMO_500, LNMO_1000 and LNMO_5000, respectively. In terms of CE, it is maintained above 95% in all the cases, although a certain trend towards higher values is observed with increasing thickness. Importantly, these results go in line with previous observations, since the parasitic reactions reflect less on the cycling performance of the thicker layers due to their lower surface-to-volume ratio.

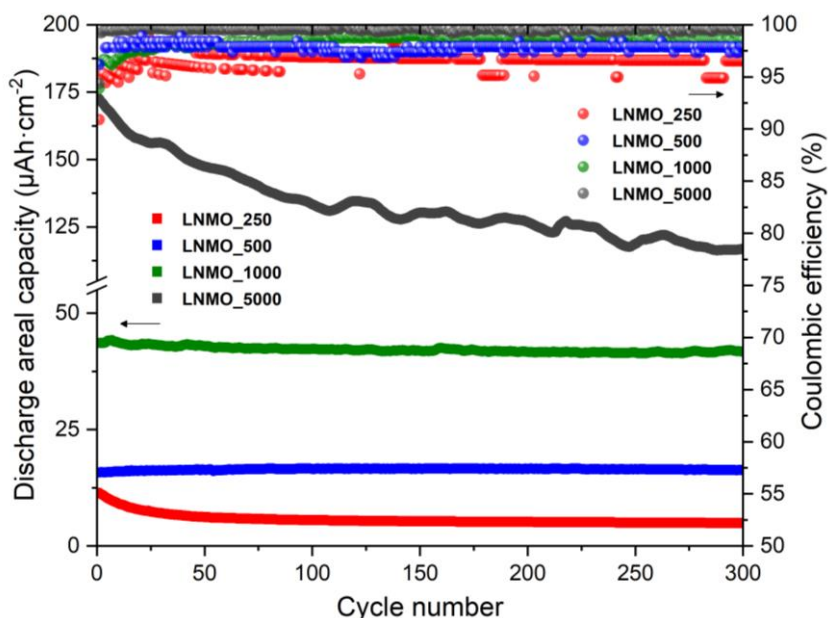


Figure 3.27: Discharge areal capacity of LNMO_250 (red squares), LNMO_500 (blue squares), LNMO_1000 (green squares) and LNMO_5000 (black squares) thin film cathodes cycled at 1C as a function of cycle number, along with coulombic efficiency (circles with the same color code). In order to visualize better the values of thinner samples, a break was introduced from 55 to 105 $\mu\text{Ah}\cdot\text{cm}^{-2}$.

3.7.3. Fe interdiffusion from the stainless steel substrate

As discussed in previous sections, two main secondary phases were detected in the thickest and thinnest films prepared, *viz.* Li_2MnO_3 phase in LNMO_5000 and $\gamma\text{-Fe}_2\text{O}_3$ in LNMO_250 samples. While the former could be associated to phase instabilities derived from slight off-stoichiometries or preferential elemental distribution in thick deposited films,^[26] the latter could be directly ascribed to the effect of Fe diffusion from the substrate, either during cathode deposition at high temperature or during post-deposition annealing.^[23]

In order to confirm the diffusion effect, further analysis of the LNMO_250 sample was conducted by XPS so as to determine the presence of Fe. **Figure 3.28** shows the XPS survey spectra of the LNMO_250 film surface. The main detected elements are Li, O, Mn, and Ni from the LNMO, as well as C from unavoidable surface contamination.^[24] Nevertheless, the presence of Fe is also found even in the outermost surface region of the 250 nm-thick film, see inset of **Figure 3.28**.^[51] This evidences a significant Fe diffusion from the substrate into the LNMO cathode. Importantly, it should be noted that, according to these results, atomic

interdiffusion beneath the film surface cannot be excluded in the rest of the thicker samples.

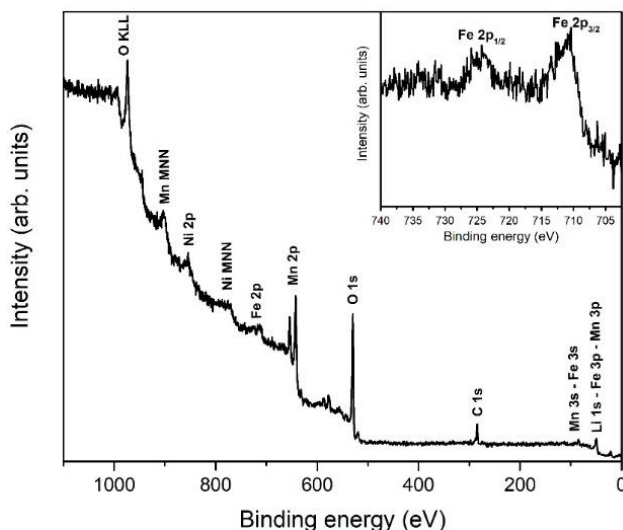


Figure 3.28: XPS survey spectrum of LNMO_250. The inset graph shows the Fe 2p signal region.

As mentioned above, low values of CE were obtained in the first cycles, especially in the case of the LNMO_250. To illustrate that, **Figure 3.29** shows the first three cycles at C/10 (from 3.5 V vs Li/Li⁺ to 5 V vs Li/Li⁺) of LNMO_250, LNMO_500, LNMO_1000 and LNMO_5000. As it can be observed in this figure, double plateaus at 4.65 V vs Li/Li⁺ and 4.76 V vs Li/Li⁺ appear during (dis)charge in all the samples, corresponding to Ni²⁺/Ni³⁺ and Ni³⁺/Ni⁴⁺ redox reactions and indicating a successful lithium (de)insertion. Nevertheless, in the first charge, an unexpected non-reversible plateau at around 4 V vs Li/Li⁺ could be observed for LNMO_250, LNMO_500 and LNMO_1000 films. Note that the duration of this unwanted electrochemical process was found to decrease progressively with thickness, see the different time scale (x axis) in each case. This plateau could be attributed to the presence of Fe₂O₃ phases in the thin films, ascribed to the electrolyte decomposition process related to this secondary phase occurring predominantly during charge (see more details in next section).^[34] This parasitic reaction is virtually eliminated in the case of LNMO_5000, where the effect of Fe diffusion from the substrate is expected to be smaller due to the significantly increased thickness. Still, a small irreversible plateau is found at around 4.2 V vs Li/Li⁺. In this case, the plateau could be related to the electrochemical activity of Mn³⁺/Mn⁴⁺, associated to the presence of the Li₂MnO₃ secondary phase in this case (see **Figure 3.21** and **Figure 3.24**).^[16,23]

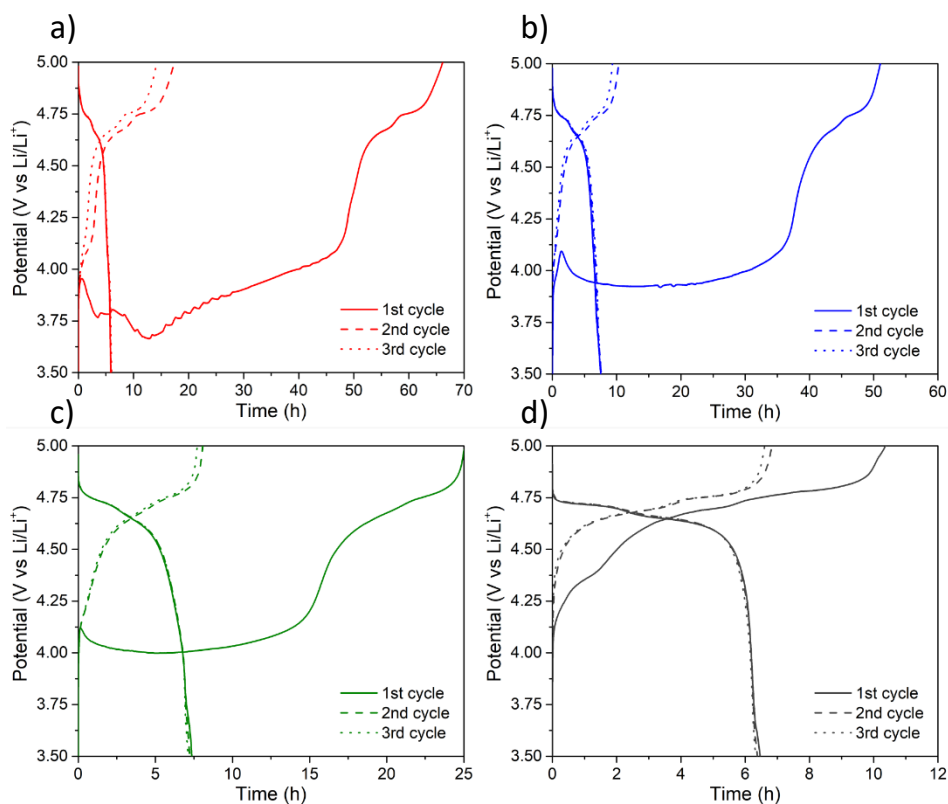


Figure 3.29: First three cycles at $C/10$ of a) LNMO₂₅₀, b) LNMO₅₀₀, c) LNMO₁₀₀₀, and d) LNMO₅₀₀₀ thin film cathodes.

To shed light on the possibility that the initial plateau observed in the thinner samples is caused by the presence of iron oxides in the thin film, bare SS substrates (without LNMO deposition) were subjected to study, under similar conditions than the LNMO films under consideration. This way, SS substrates were annealed at 600 °C and compared with the non-annealed counterparts, **Figure 3.30**. First, the structural evolution was tested by XRD and Raman (**Figure 3.30a** and **Figure 3.30b**, respectively). As it can be observed, no new reflections were observed by XRD with annealing, whereas significant changes were detected by Raman. Due to the metallic nature of the bare SS substrate before annealing, only a baseline Raman spectrum was observed. After annealing, the existence of a secondary non-metallic phase formed on the surface could however be confirmed. The appearance of a series of vibrational modes at 227, 250, 295, 418, 511, 623, 836, 957, 1075, 1126 and 1334 cm^{-1} could be attributed to a mix of α - and γ - Fe_2O_3 phases, hematite and maghemite, respectively.^[52]

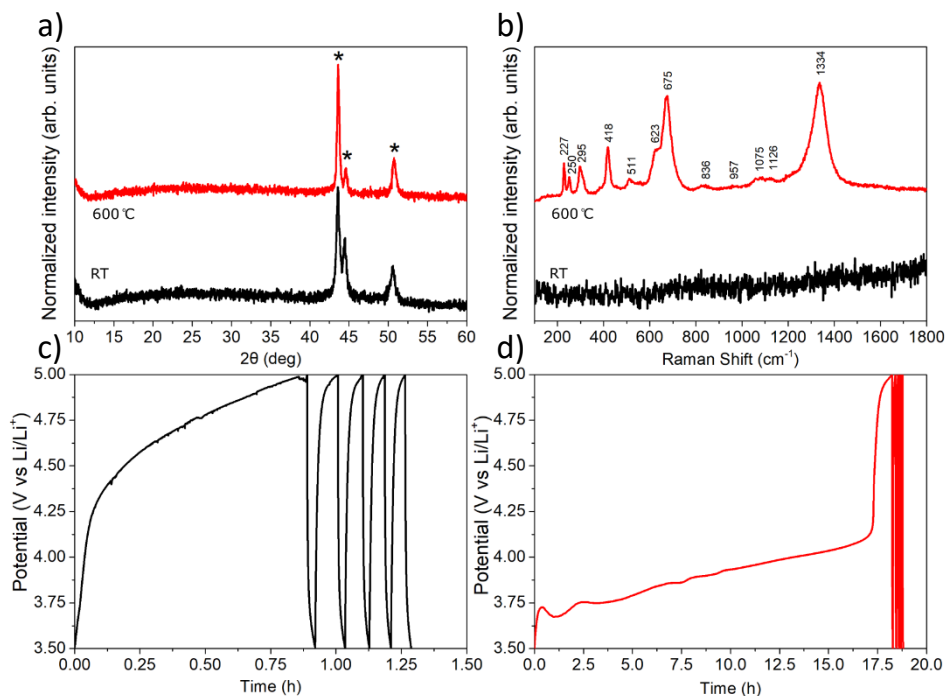


Figure 3.30: Comparison of the annealing effect on the SS substrate, a) XRD pattern after annealing, b) Raman spectrum after annealing, c) electrochemical performance before annealing, and d) electrochemical performance after annealing.

Then, the two types of SS discs (before and after annealing) were assembled in a coin cell following the same procedure used for the LNMO electrochemical characterization. The charge-discharge program was set in the battery tester with similar currents as for a C/10 rate for the LNMO_500 films and was kept for 5 consecutive cycles. The electrochemical response obtained is included in **Figure 3.30c** (non-annealed) and **Figure 3.30d** (annealed). As observed, the sample without annealing did not show any redox reaction, whereas the sample after annealing presented a similar initial irreversible plateau as the one observed in the **Figure 3.29**. Hence, the first charge irreversible plateau observed in the LNMO samples could be ascribed to electrochemical reaction between the new formed Fe_2O_3 secondary phase and the liquid electrolyte.^[34] In this way, the following chapter will analyze the possible diffusion barrier coatings at the cathode-substrate interface in order to avoid interdiffusion.

3.8. Comparison with commercial cathode

After studying the structural, morphological, and electrochemical properties of the fabricated LNMO thin films, it is interesting to evaluate our optimum LNMO cathode by comparing its cycling performance with a commercially available electrode from *Customcells*®. **Table 3.4** lists the features of this slurry mixture synthesized commercial cathode.

Table 3.4: Customcell's cathode features as provided by the manufacturer

Active material content (%)	Specific capacity ($\text{mAh}\cdot\text{g}^{-1}$)	Thickness (μm)	Current collector	Nominal voltage (V vs Li/Li ⁺)
86	130	76	Al foil	4.6

The comparison between the commercial and the thin film LNMO was firstly introduced by Dr. J. Rikarte.^[37] In the conducted experiments the two cathodes were assembled using the same amount of electrolyte, approx. 180 μl . The low cyclability (150 cycles) obtained by the commercial cathode (See Comm_180 μl trend in **Figure 3.31**) could be explained due to the low amount of electrolyte used in relation to its active material mass load, that is two order of magnitude higher than LNMO thin film (17.25 and 0.45 $\text{mg}\cdot\text{cm}^{-2}$, respectively). According to the literature, the low quantity of the electrolyte leads to the loss of capacity and lifetime.^[53,54] In this section, the commercial cathode using a higher amount of electrolyte is considered to verify if it is the limiting factor. For this purpose, the commercial cathode was assembled in a 3-electrode Swagelok system, maintaining the two-electrode format, and filling the third electrode cavity with the electrolyte, in total 700 μl .

Figure 3.31 shows the normalized discharge capacities and coulombic efficiencies of LNMO_1000 and commercial LNMO cathodes (Comm_180 μl and comm_700 μl) cycled at 1C as a function of cycle number. Before the long cycling, a SEI formation cycling procedure was set as two cycles at each C-rate, namely, C/10, C/5, and C/2.

The test was stopped when discharge capacity decreased down to 80% of its initial values (88.1, 78.6, and 81.9 $\text{mAh}\cdot\text{g}^{-1}$ for LNMO_1000, Comm_180 μl , and Comm_700 μl , respectively), the percentage that usually determines the utilization limit of a Li-ion battery. The results show that, despite increasing the amount of electrolyte, the Comm_700 μl cell has poor cyclability, even worse than

Comm_180 μ l; the discharge capacity decreases abruptly, reaching the limit after 99 cycles. Instead, LNMO_1000 last longer with respect to commercial cathodes and reaches the lower limit after 934 cycles. Concerning CE, values obtained for commercial cells are very high and stable (in both cases close to 99.5%), while those calculated for LNMO_1000 are relatively low and oscillate in the range from 97.5% to 98.5%.

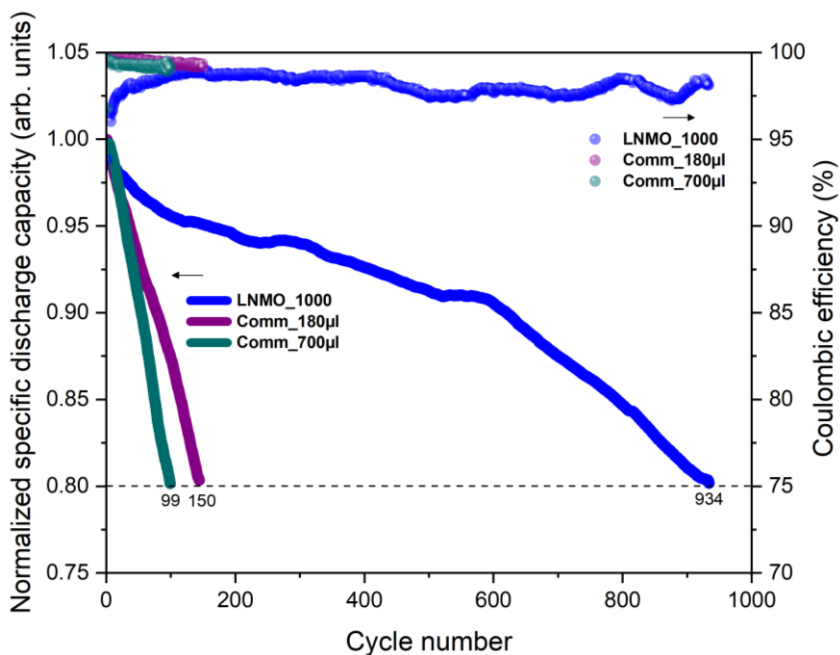


Figure 3.31: Normalized specific discharge capacity and coulombic efficiency of LNMO_1000, Comm_180 μ l and Comm_700 μ l cycled at 1C as a function of cycle number. Plotted until capacity reached 80% of its initial value.

In spite of the increased amount of electrolyte, the poor cyclability of commercial LNMO can be related to the parasitic reactions of the electrolyte with binders and conductive additives used in the formulation of the commercial cathode.^[55] It has been reported that the liquid electrolyte used in this work can react with C additives, hastening its degradation.^[55] As a result, an increasing number of active particles become progressively disconnected from the binders (PVDF, polyvinylidene fluoride) and conductive additives (C-65 carbon) network during cycling, leading to capacity fading. This is more pronounced as the amount of electrolyte increases. Conversely, this effect is avoided in the case of LNMO thin film because it consists of 100% active material. Then, the large difference observed in the cyclability of the two considered systems confirms the dramatic

effect that C-based conductive additive used in the commercial cathodes formulation can have on their performance.

To visualize the C/PVDF network and the active material particles distribution, **Figure 3.32a** shows the SEM micrographs of the commercial electrode surface, where the typical mixture of ceramic particles (with size from 1 to 3 microns) with carbon powder and polymer binder are clearly distinguished visually and elementally (see **Figure 3.32b**). Looking at the EDS analysis of the orthorhombic particles the presence of Mn, Ni, and O (Li is not detectable by this technique) is detected, which could agree with the LNMO composition of the active material. The analysis outside these oxide grains reveals a big quantity of carbon and a presence of fluorine, which could be related to the conductive carbon additive and PVDF binder.

In conclusion, the main reason for achieving better cyclability in the sputtered thin film than in the two commercial cells is that the LNMO thin film only consists of active material, so those parasitic reactions are avoided. Therefore, the expected CE of LNMO_1000 should be higher than Comm_180 μl and Comm_700 μl . Surprisingly the opposite result was obtained. A possible explanation for the pronounced difference observed in cycling performance may likely rely on the fact that the contribution to charge capacity of electrolyte decomposition is expected to be larger in the case of LNMO_1000 with respect to the commercials due to the high surface-to-volume ratio, typical of thin film electrodes.

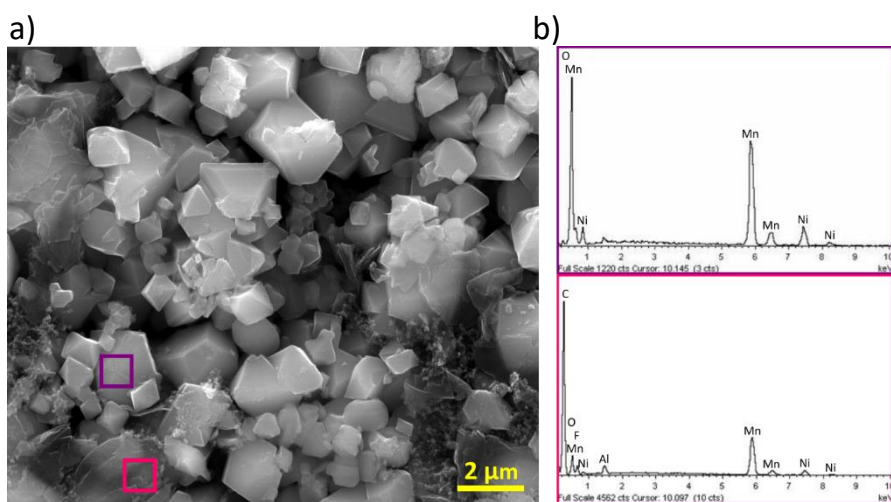


Figure 3.32: a) SEM image of the commercial LNMO electrode surface, b) EDS analysis on the LNMO grain (purple square) and on the cover material (pink square).

3.9. Conclusions

In this chapter, we successfully optimized the deposition of a high-voltage LNMO thin film on stainless steel substrate by AC magnetron sputtering. But, due to the amorphous nature of the as-deposited sample, a post-deposition thermal treatment was required in order to obtain the spinel LNMO phase.

The effect of the temperature was analyzed from 300 °C up to 900 °C. The thin film undergoes a progressive crystallization and surface morphology changes as the temperature increases. The first signs of crystallinity start to be visible at 300 °C, nevertheless, it remains electrochemically inactive. It takes up to 450 °C for the redox activity to become noticeable for the LNMO phase in the CV: Nickel oxidation from 2⁺ to 3⁺ and from 3⁺ to 4⁺. The expected pure disordered spinel LNMO was achieved after annealing at 600 °C, delivering 118.98 mAh·g⁻¹ at C/10 and being able to reach almost 95% of its initial value at 1C. This electrochemical performance is found to be in line with other LNMO films obtained using similar techniques and growth parameters. The LNMO phase integrity was highly disturbed by increasing the temperature up to 750 °C, under this annealing condition two identified phases are coexisting in the deposited thin film, leading to several redox reactions corresponding to the LNMO and LFMO phases. The well-defined octahedral grains on the surface of the sample annealed up to 900 °C is the consequence of the domination of the whole XRD pattern by the secondary phases. Resulting in fast discharge specific capacity drop at high C-rates and the absence of any relevant electrochemical activity. Concluding that high temperature is not suitable to make high-quality LNMO cathode, the interaction between LNMO and SS substrate deteriorates structural and electrochemical properties.

As seen in the EDS line study of the LNMO layer annealed for 1 hour at 600 °C, the diffusion of Fe decreases exponentially inside the LNMO layer, this way, we have analyzed the effect of thickness in the performance of LNMO thin film cathodes deposited on SS substrates. On one side, it was found that the thickness has a direct impact on the surface morphology and crystallinity of the cathode film, with the appearance of rougher surfaces and secondary phases in the thicker films. Marked differences are also found in the electrochemical performance between the thinnest and thicker electrodes. Whereas the areal capacity is clearly improved when increasing the mass loading (thick films), the performance at high C-rates is however compromised, ascribed to sluggish kinetics and the presence of secondary phases. Meanwhile, thinner films outperform at high C-rates both in terms of specific and areal capacity. On the other side, a clear detrimental effect of the substrate was found, related to an

unwanted Fe diffusion towards the film and leading to the formation of Fe_2O_3 secondary phases upon annealing. This is evidenced by the appearance of an irreversible plateau during the first charge in the samples up to $1\ \mu\text{m}$ in thickness, and particularly affects the performance of the thinnest LNMO films, where the plateau is significantly longer in duration and lower performance is also observed at high C-rates.

Finally, the fabricated $1\ \mu\text{m}$ LNMO film is compared with a *Customcell's* cathode. The LNMO thin film shows outstanding cycling performance compared to a commercial. This remarks an intrinsic advantage of thin films with respect to synthesized electrodes related to the absence of any conductive additives and binders.

To sum up, the obtained results confirm the suitability of AC magnetron sputtering for the fabrication of thin film cathodes. However, further experiments are needed to ensure the improvement of the LNMO electrochemistry performance: i) deposition of a diffusion barrier interlayer between substrate and cathode to avoid contaminant diffusion, ii) insertion of a cathode protective coatings to minimize possible side reactions at LNMO surface, and iii) switch to the solid electrolyte to overcome limitations typical of liquid ones.

References in Chapter 3

- [1] D. Liu, W. Zhu, J. Trottier, C. Gagnon, F. Barray, A. Guerfi, A. Mauger, H. Groult, C. M. Julien, J. B. Goodenough, K. Zaghib, *RSC Adv.* 2014, 4, 154.
- [2] T. F. Yi, J. Mei, Y. R. Zhu, *J. Power Sources* 2016, 316, 85.
- [3] X. Fang, M. Ge, J. Rong, Y. Che, N. Aroonyadet, X. Wang, Y. Liu, A. Zhang, C. Zhou, *Energy Technol.* 2014, 2, 159.
- [4] L. Wang, H. Li, X. Huang, E. Baudrin, *Solid State Ionics* 2011, 193, 32.
- [5] H. Konishi, K. Suzuki, S. Taminato, K. Kim, S. Kim, J. Lim, M. Hirayama, R. Kanno, *J. Power Sources* 2014, 246, 365.
- [6] S. H. Su, K. F. Chiu, H. J. Leu, *Thin Solid Films* 2014, 572, 15.
- [7] M. Atanasov, J. L. Barras, L. Benco, C. Daul, *J. Am. Chem. Soc.* 2000, 122, 4718.
- [8] M. Kunduraci, J. F. Al-Sharab, G. G. Amatucci, *Chem. Mater.* 2006, 18, 3585.
- [9] J. Zheng, J. Xiao, X. Yu, L. Kovarik, M. Gu, F. Omenya, X. Chen, X. Q. Yang, J. Liu, G. L. Graff, M. S. Whittingham, J. G. Zhang, *Phys. Chem. Chem. Phys.* 2012, 14, 13515.
- [10] K. Hoshina, K. Yoshima, M. Kotobuki, K. Kanamura, *Solid State Ionics* 2012, 209–210, 30.
- [11] M. Gellert, K. I. Gries, J. Zakel, A. Ott, S. Spannenberger, C. Yada, F. Rosciano, K. Volz, B. Roling, *Electrochim. Acta* 2014, 133, 146.
- [12] M. Mohamedi, M. Makino, K. Dokko, T. Itoh, I. Uchida, *Electrochim. Acta* 2002, 48, 79.
- [13] J. C. Arrebola, Á. Caballero, L. Hernán, M. Melero, J. Morales, E. R. Castellón, *J. Power Sources* 2006, 162, 606.
- [14] H. Xia, S. B. Tang, L. Lu, Y. S. Meng, G. Ceder, *Electrochim. Acta* 2007, 52, 2822.
- [15] Y. Wang, G. Yang, Z. Yang, L. Zhang, M. Fu, H. Long, Z. Li, Y. Huang, P. Lu,

- Electrochim. Acta* 2013, *102*, 416.
- [16] L. Baggetto, R. R. Unocic, N. J. Dudney, G. M. Veith, *J. Power Sources* 2012, *211*, 108.
- [17] R. D. Arnell, P. J. Kelly, *Surf. Coatings Technol.* 1999, *112*, 170.
- [18] S. Swann, *Phys. Technol.* 1988, *19*, 67.
- [19] I. Safi, *Surf. Coatings Technol.* 2000, *127*, 203.
- [20] Y. Wang, Q. Peng, G. Yang, Z. Yang, L. Zhang, H. Long, Y. Huang, P. Lu, *Electrochim. Acta* 2014, *136*, 450.
- [21] J. Li, L. Baggetto, S. K. Martha, G. M. Veith, J. Nanda, C. Liang, N. J. Dudney, *Adv. Energy Mater.* 2013, *3*, 1275.
- [22] L. Baggetto, N. J. Dudney, G. M. Veith, *Electrochim. Acta* 2013, *90*, 135.
- [23] J. H. Kim, J. Park, K. Park, S. H. Cho, Y. C. Park, C. Kim, I. D. Kim, K. Park, H. S. Kim, *J. Electroceramics* 2019, *42*, 104.
- [24] J. Rikarte, I. Madinabeitia, G. Baraldi, F. J. Fernández-Carretero, V. Bellido-González, A. García-Luis, M. A. Muñoz-Marquez, *Adv. Mater. Interfaces* 2021, *8*, 2002125.
- [25] J. A. Thornton, *Annu. Rev. Mater. Sci.* 1977, *7*, 239.
- [26] M. Létiche, M. Hallot, M. Huvé, T. Brousse, P. Roussel, C. Lethien, *Chem. Mater.* 2017, *29*, 6044.
- [27] P. Swift, *Surf. Interface Anal.* 1982, *4*, 47.
- [28] T. L. Barr, S. Seal, *J. Vac. Sci. Technol. A Vacuum, Surfaces, Film.* 1995, *13*, 1239.
- [29] T. Ohzuku, R. J. Brodd, *J. Power Sources* 2007, *174*, 449.
- [30] L. Pauling, S. B. Hendricks, *J. Am. Chem. Soc.* 1925, *47*, 781.
- [31] M. Létiche, M. Hallot, M. Huvé, T. Brousse, P. Roussel, C. Lethien, *Chem. Mater.* 2017, *29*, 6044.
- [32] M. Kunduraci, J. Al-Sharab, G. Amatucci, *Chem. Mater* 2006, *18*, 3585.

- [33] J. Lee, N. Dupre, M. Avdeev, B. Kang, *Sci. Rep.* 2017, 7, 1.
- [34] L. Wang, H. Li, M. Courty, X. Huang, E. Baudrin, *J. Power Sources* 2013, 232, 165.
- [35] Z. N. Taylor, A. J. Perez, J. A. Coca-Clemente, F. Braga, N. E. Drewett, M. J. Pitcher, W. J. Thomas, M. S. Dyer, C. Collins, M. Zanella, T. Johnson, S. Day, C. Tang, V. R. Dhanak, J. B. Claridge, L. J. Hardwick, M. J. Rosseinsky, *J. Am. Chem. Soc.* 2019, 141, 7333.
- [36] A. N. Filippin, M. Rawlence, A. Wäckerlin, T. Feurer, T. Zünd, K. Kravchyk, M. V. Kovalenko, Y. E. Romanyuk, A. N. Tiwari, S. Buecheler, *RSC Adv.* 2017, 7, 26960.
- [37] J. Rikarte Ormazabal, Doctoral Thesis, Surfaces & Interphases in Thin-Film & Conventional Li-Ion Batteries, Euskal Herriko Unibertsitatea, 2019.
- [38] F. Nobili, S. Dsoke, M. Minicucci, F. Croce, R. Marassi, *J. Phys. Chem. B* 2006, 110, 11310.
- [39] V. J. Ovejas Benedicto, Doctoral Thesis, Determination of the State of Health of Li-Ion Batteries : The Irreversible Entropy Production Approach, Universitat Politècnica de Catalunya, 2017.
- [40] F. Croce, F. Nobili, A. Deptula, W. Lada, R. Tossici, A. D'Epifanio, B. Scrosati, R. Marassi, *Electrochem. commun.* 1999, 1, 605.
- [41] M. D. Levi, G. Salitra, B. Markovsky, H. Teller, D. Aurbach, U. Heider, L. Heider, *J. Electrochem. Soc.* 1999, 146, 1279.
- [42] M. Zarrabeitia, Doctoral Thesis, Low and High Voltage Stability of Na-Ion Battery Materials : Study of Structural , Transport and Interfacial Properties, Euskal Herriko Unibertsitatea, 2016.
- [43] E. Barsoukov, J. R. Macdonald, *Impedance Spectroscopy: Theory, Experiment, and Applications*, Wiley, 2005.
- [44] M. Hallot, A. Demortière, P. Roussel, C. Lethien, *Energy Storage Mater.* 2018, 15, 396.
- [45] H. Xia, L. Lu, Y. S. Meng, *Appl. Phys. Lett.* 2008, 92, 3.
- [46] N. Amdouni, K. Zaghib, F. Gendron, A. Mauger, C. M. Julien, *Ionics (Kiel)*. 2006, 12, 117.

- [47] M. Börner, P. Niehoff, B. Vortmann, S. Nowak, M. Winter, F. M. Schappacher, *Energy Technol.* 2016, *4*, 1631.
- [48] J. H. Kim, A. Huq, M. Chi, N. P. W. Pieczonka, E. Lee, C. A. Bridges, M. M. Tessema, A. Manthiram, K. A. Persson, B. R. Powell, *Chem. Mater.* 2014, *26*, 4377.
- [49] Q. Wu, V. A. Maroni, D. J. Gosztola, D. J. Miller, D. W. Dees, W. Lu, *J. Electrochem. Soc.* 2015, *162*, A1255.
- [50] D. Yu, K. Yanagida, *J. Electrochem. Soc.* 2011, *158*, A1015.
- [51] T. Yamashita, P. Hayes, *Appl. Surf. Sci.* 2008, *254*, 2441.
- [52] I. S. Molchan, G. E. Thompson, R. Lindsay, P. Skeldon, V. Likodimos, G. E. Romanos, P. Falaras, G. Adamova, B. Iliev, T. J. S. Schubert, *RSC Adv.* 2014, *4*, 5300.
- [53] J. Li, C. Ma, M. Chi, C. Liang, N. J. Dudney, *Adv. Energy Mater.* 2015, *5*, 1.
- [54] F. J. Günter, C. Burgstaller, F. Konwitschny, G. Reinhart, *J. Electrochem. Soc.* 2019, *166*, A1709.
- [55] B. P. N. Nguyen, N. Mariage, R. Fredon, E. M. Kelder, B. Lestriez, *J. Electrochem. Soc.* 2015, *162*, A1451.
- [56] "The London Metal Exchange," can be found under <https://www.lme.com/>, 2021.

Chapter 4

Improvement of $\text{LiNi}_{0.5}\text{Mn}_{1.5}\text{O}_4$ (LNMO) thin film cathode

4.1. Introduction

Many investigations in the field of electrode materials are geared towards improving the cycling performance of the LNMO cathode. Such studies are mostly focused on the substrate or current collector modification, the insertion of surface protective layers, or the alteration of the intrinsic properties of the cathode material (*i.e.* composition, structure, etc.).

As highlighted in the previous chapter, films grown on SS substrate can suffer from chemical diffusion of Fe and Cr triggered by the postdeposition annealing. The addition of an interlayer coating between the SS substrate and the cathode could be effective in preventing such atomic migration, working as diffusion barrier and current collector simultaneously. Besides those requirements, the coating must be able to withstand high temperatures in air during the postdeposition thermal treatment required by LNMO. One of the most promising materials is platinum, sometimes in combination with an additional adhesion layer. It guarantees good electrical conductivity while suppressing diffusion;^[1,2] however, due to its elevated cost, it is important to identify cheaper alternative materials to produce economically viable thin film batteries. Gold has been proposed as a cost-affordable coating, achieving good electrochemical performance,^[3] however, despite gold might be a commonly used material in applications with high added value, it might not be feasible in a market-driven by low-cost policies. Filippin *et al.* demonstrated the suitability of chromium nitride

and Ni-Al-Cr superalloy as stable positive electrode current collector.^[4,5] Among them, CrN possesses a good combination of inertness and electronic conductivity, being the first property useful to withstand the thermal treatment without degradation while the latter is useful to improve the electrical contact between the current collector and the electrode. Alternatively, the low manufacturing cost, the natural abundance of the constituting elements, its high electrical conductivity, and oxidative stability at high potentials (5.0 V vs Li/Li⁺) in LiPF₆-based electrolytes, render titanium nitride a suitable material for commercial use as a high-voltage current collector.^[6] Plus, it is a well-known and widely used as barrier compatible with semiconductor technology.^[7]

This chapter will also address the integration of a cathode protective layer to minimize the eventual side reactions that take place between the LNMO and the conventional liquid electrolyte, improving the discharge capacity, the cycling stability, and the rate capability at high voltages.^[8] Therefore, these passivation layers must be able to reduce the decomposition of the electrolyte and to stabilize the SEI,^[9–11] to prevent the dissolution of Mn²⁺,^[12] and to scavenge unwanted HF.^[13,14] Looking at the reported literature, a wide variety of coating materials for LNMO cathode has been studied: SiO₂,^[15] ZnO,^[12] Al₂O₃,^[16] Bi₂O₃,^[17] ZrO₂,^[18] V₂O₅,^[19] Ta₂O₅,^[20] Li₃PO₄,^[21] Au,^[22] Ag,^[23] polyimide,^[24] conductive carbon,^[25] and graphene oxide.^[26] Among them, the surface isolation using metal oxide layers seems to be more effective as a barrier to block direct contact between the electrolyte while the electrode and acting as HF scavengers at the same time.^[16]

4.2. Main objectives of the chapter

This chapter is focused on the improvement of the LNMO cathode. On one hand, the effectiveness in preventing contaminant diffusion from the substrate by the insertion of different diffusion barrier interlayers in the current collector/cathode interface is analyzed. On the other hand, the optimal thickness of protective Al₂O₃ layers is studied to minimize the side reactions between LNMO surface and the liquid electrolyte.

4.3. Current collector/cathode interface: coating of the stainless steel substrate

Considering the negative effect of Fe-diffusion on the electrochemical properties of the electrode discussed in the previous chapter, this section is oriented to prevent the diffusion of transition metals from the substrate towards the cathode during the thermal treatment at 600 °C in air. The development of an effective

diffusion barrier layer between the SS substrate and the LNMO is considered for this purpose.

316L SS discs (*Hohsen Corp.*, diameter 16 mm, thickness 0.5 mm), typically employed as spacers in CR2032 coin cells, were coated with four different diffusion barrier layers: Au, CrN, TiN, and Al. The last two, according to their crystallinity, have the additional purpose of inducing the oriented growth of the LNMO according to their crystallinity. This study was carried out as part of the MONBASA project. **Figure 4.1** shows the details of each deposition (thickness, deposition method, and manufacturer). The CrN, TiN, and Al films were deposited by magnetron sputtering, while the Au was electroplated. The following section explains the experimental set-up of the CrN deposition, which was carried out at *Tecnalia*'s facilities.



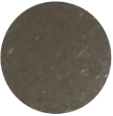


	SS	Au	CrN	TiN	Al
					
Thickness (nm)	-	1500	1500	300-500	280-300
Deposition method	-	Electroplating	Mag. Sput. ^{DC}	Mag. Sput. ^{HIPIMS}	Mag. Sput. ^{DC}
Manufacturer	-	<i>Global Coats</i>	<i>Tecnalia</i>	<i>Nano4Energy</i>	<i>Genco</i>

Figure 4.1: Appearance of the four deposited layers along with the SS substrate. Also are included the used deposition technique in each case, the layer thickness, and the manufacturer of the deposition.

After the deposition of all the diffusion barriers, LNMO films were deposited in each coated substrate by employing the optimized setup described in the previous chapter and subsequently annealed at 600 °C, 5 °C·min⁻¹ heating ramp, during one hour in a commercial furnace (*Carbolite*) and then left to cool down slowly inside the oven switched off.

Unfortunately, the LNMO film on the TiN-coated SS substrate delaminated, see **Figure 4.2**. In the SEM micrograph presented in **Figure 4.2b** it can be seen how the newly deposited layer of LNMO, **Figure 4.2a**, is detached from the surface of the TiN. This may be due to the growth of TiO_x oxides between the TiN grains that weaken the interlayer. Hence rendering necessary the cleaning of the substrate surface before the deposition of the cathode.

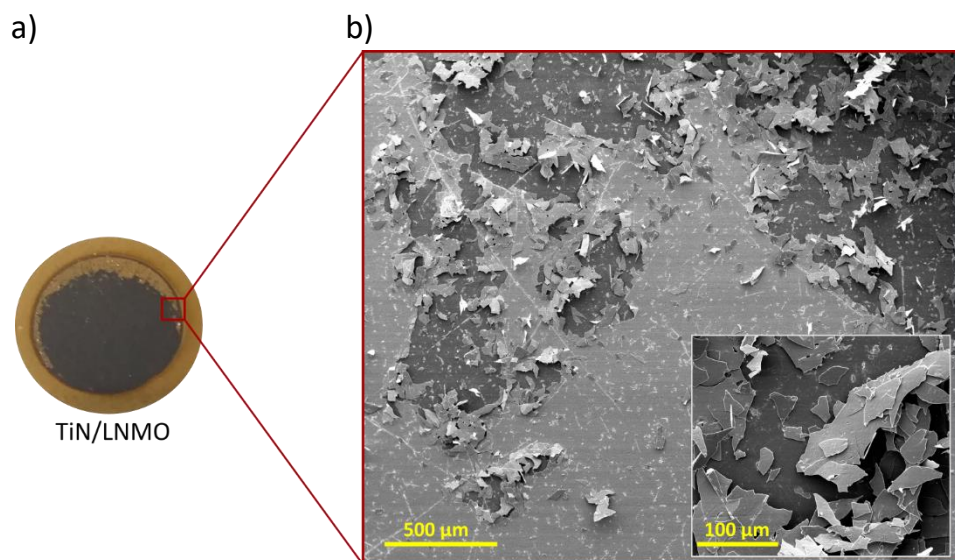


Figure 4.2: a) As-deposited LNMO thin film on TiN-coated SS substrate, and b) SEM image of the weak adherence part (zoomed in inset graph).

A circular ion source (IMC75) was installed in the deposition chamber for pre-sputtering of the substrate surface for both, adhesion increase and surface activation by ion bombardment, see **Figure 4.3**. The LNMO coating process using 15 minutes long preliminary ion etching with pure Ar and 30 mA of ion current was carried out on SS/TiN substrates. Regrettably, the ion etching process did not improve the adhesion and the LNMO coating detached even faster. The reported literature suggests the use of the ion source during deposition, as the bombardment of the metal substrate by high-energy ions can mix substrate atoms with coating ones.^[27] However, following this approach, the LNMO deposition and crystallization would be altered, not being comparable with the study done so far. Hence, considering the limited number of TiN samples, the analysis has been performed by depositing the LNMO directly in TiN-coated SS substrate without preconditioning, as shown in **Figure 4.2**.

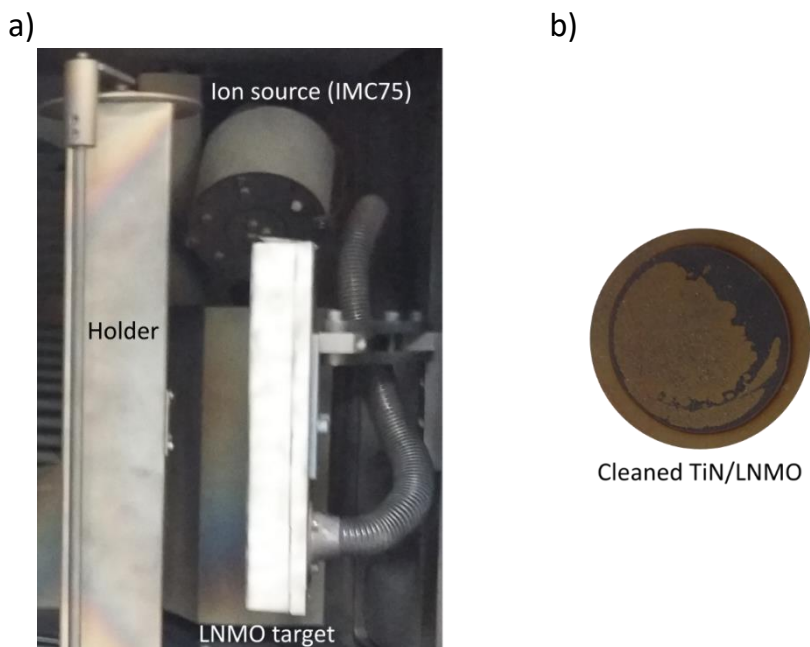


Figure 4.3: a) IMC75 ion source placed facing the substrate inside the chamber of the magnetron sputtering at *TecNALIA*, and b) as-deposited LNMO thin film on cleaned TiN-coated SS substrate.

4.3.1. Experimental set-up of CrN coating

CrN was deposited by DC semi-industrial *CemeCon CC800/8* reactive magnetron sputtering at *TecNALIA*. The employed experimental set-up is shown in **Figure 4.4**, the system is composed of four rectangular magnetrons with metallic Cr targets (*CemeCon AG*), and the substrates were posted on the rectangular faces of roundabout holders.

Following the evacuation of the chamber down to $2 \cdot 10^{-5}$ mbar and an etching process to clean the SS surface, a mixture of Ar, N₂, and Kr gases was leaked into the chamber, each one with a constant flow rate of 50 sccm, achieving a constant working pressure of $4.7 \cdot 10^{-3}$ mbar. The four metallic Cr targets were biased at 1000 W ($5.68 \text{ W} \cdot \text{cm}^{-2}$), while substrates were rotated in a planetary system to ensure coating uniformity and to guarantee complete coverage of the SS substrate, see w_1 and w_2 in **Figure 4.4**. The CrN deposition rate was $28 \text{ nm} \cdot \text{min}^{-1}$, as measured after deposition with a Bruker Dektak 150 stylus profilometer. This magnetron sputtering process was performed to grow a $\sim 1.5 \text{ } \mu\text{m}$ thick layer of CrN, so the thickness of the nitride and the Au coating are comparable.

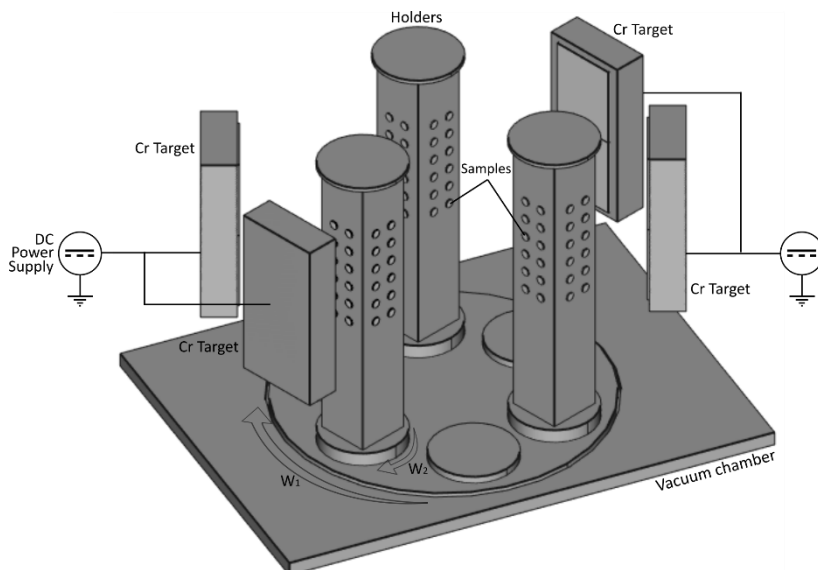


Figure 4.4: Schematic view of the magnetron sputtering configuration for CrN deposition at Tecnalia.

4.3.2. Structural characterization

Figure 4.5 shows the diffraction patterns collected from Au-, CrN-, TiN- and Al-coated SS substrates, as deposited (Au_RT, CrN_RT, TiN_RT, and Al_RT) and after annealing up to 600 °C without cathode (Au_600, CrN_600, TiN_600, and Al_600), as well as with 1 μm thick LNMO cathode deposited on top (Au_LNMO_600, CrN_LNMO_600, TiN_LNMO_600, and Al_LNMO_600). **Table 4.1** shows a summary of all the samples used in this section.

Table 4.1: Samples used for the characterization of the coatings as diffusion barrier.

Coating	As deposited on SS	After annealing (600 °C for 1h in air)	LNMO + annealing (600 °C for 1h in air)
Au	Au_RT	Au_600	Au_LNMO_600
CrN	CrN_RT	CrN_600	CrN_LNMO_600
TiN	TiN_RT	TiN_600	TiN_LNMO_600
Al	TiN_RT	TiN_600	Al_LNMO_600

The reflections ascribed to the SS substrate^[28] were found in all RT samples (marked with an asterisk) except in the Au_RT, see **Figure 5.4a**. There, only two intense peaks were observed at $2\theta = 38.4^\circ$ and $2\theta = 44.5^\circ$, corresponding to Au

(111) and (200) diffraction lines (ref. PDF 00-001-1172). After annealing, new reflections at slightly higher 2θ position than the Au peaks appeared, being even more intense and narrower (note that in order to see the rest of the contributions, the graph has been zoomed). This feature is originated by the formation of FeAu alloy, probably as a result of the diffusion of Fe from the substrate. Fuse *et al.* already reported a higher peak shift when the Fe concentration increases with respect to Au.^[29] The unwanted Fe_3O_4 magnetite and Fe_2O_3 hematite secondary phases assigned to the rest of the reflections (PDF 00-0024-0672 and PDF 01-076-5948, respectively) complete the phase identification. The intensity of these phases decreases in Au_LNMO_600 sample, where the LNMO spinel phase is hardly distinguishable due to the overlapping of different reflections.

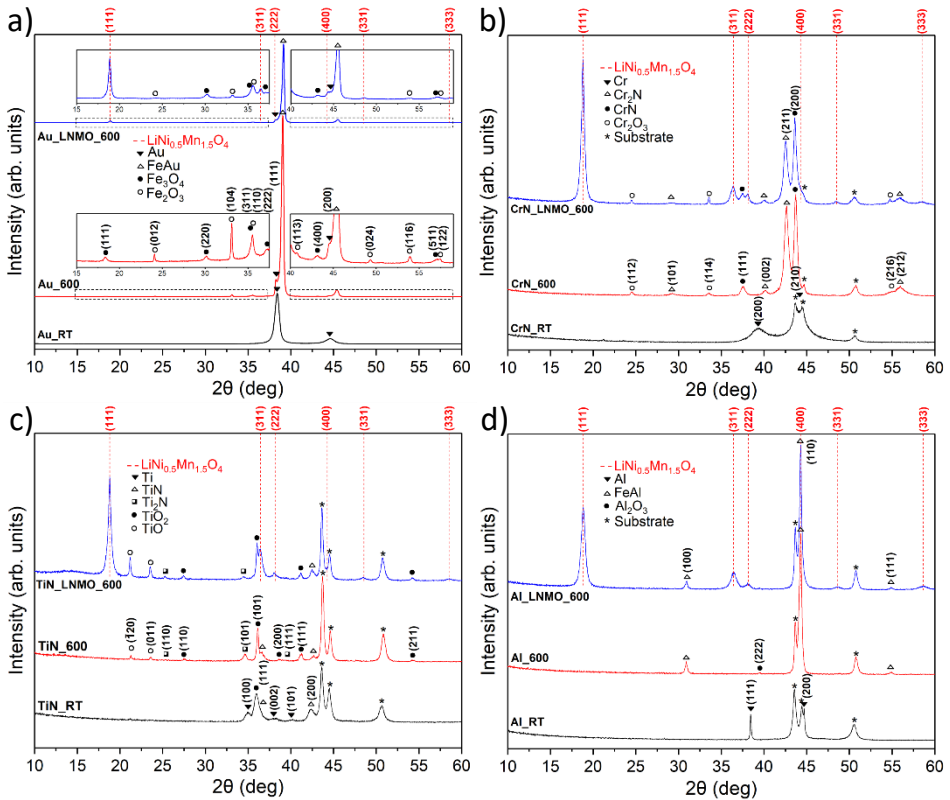


Figure 4.5: XRD pattern of as deposited coatings, after annealing up to 600 °C and annealed with LNMO: a) Au, b) CrN, c) TiN, and d) Al. Red dashed lines correspond to miller indexes of spinel LNMO. The triangles, the circles, and the square are used to identify the crystalline structure of the elements and/or the alloys of the different coatings.

In the as deposited CrN coating (**Figure 5.4b**), the SS substrate reflections are accompanied by broad and weaker diffraction peaks at $2\theta = 39.5^\circ$ and $2\theta = 44.3^\circ$, which could correspond to Cr diffraction lines (PDF 03-065-3316). The phases related to CrN become noticeable when the sample is annealed to 600°C , taking precedence over those of the SS substrate. The new contributions at 29.2° , 40.2° , 42.5° , and 55.9° in the CrN_600 sample can be related to hexagonal $\beta\text{-Cr}_2\text{N}$ (PDF 00-035-0803), and those at 37.5° and 43.7° to cubic CrN (PDF 00-011-0065).^[4] Besides the chromium nitride mix, a chromium oxide phase can also be found in the diffractogram, *i.e.* peaks at 24.5° , 33.5° , and 54.9° are attributed to Cr_2O_3 (PDF 00-001-1294). The contribution of this phase becomes a little bit more intense in the CrN_LNMO_600 sample. Moreover, the LNMO spinel phase is identified in this case, in perfect agreement with previously shown results in Chapter 3, with no signs of Fe secondary phases probably due to the barrier effect of the CrN layer.

As deposited TiN coating films exhibited, along with SS substrate contribution, a mixed structure of (111) and (200) orientations (COD 1100035). Besides the peaks corresponding to TiN, reflections at 34.9° , 38.3° and 40.1° of metallic titanium (PDF 00-001-1197) appear, as well as rutile- TiO_2 evidence at 36.1° (PDF 00-004-0551) which overlaps with TiN (111) reflection. Even if new traces of Ti_2N (PDF 00-017-0386) are found, the TiN peaks are maintained at 600°C , but the presence of titanium oxide is increased.^[30] In TiN_600, the metallic titanium has triggered the formation of TiO (PDF 00-023-1078) and new reflections of rutile- TiO_2 , *i.e.* peaks at 27.5° , 41.2° , and 54.3° , appear. In the TiN_LNMO_600 sample, the contribution of titanium oxide phases becomes more intense, analogously to chromium oxide formation in the CrN coating (see above). In this case, Fe-related phases do not appear, and the peaks corresponding to the LNMO are visible.

In the Al_RT sample, the peaks appearing at $2\theta = 38.5^\circ$ and $2\theta = 44.6^\circ$ other than those corresponding to the SS substrate confirm the presence of metallic aluminum (COD 4313217). However, this contribution quickly disappears when annealing around its melting temperature (660°C)^[4] which, in conjunction with the probable diffusion of Fe, the (100), (110), and (111) reflections of the newly formed FeAl alloy appear (PDF 00-001-1257).^[31] A small alumina contribution is also visible at $2\theta = 39.5^\circ$. Even so in the Al_LNMO_600 sample, the LNMO spinel phase is clearly identified along with the reflections of the previously mentioned FeAl alloy.

Figure 4.6 shows the Raman spectra of annealed LNMO thin film on Au-, CrN-, TiN-, and Al-coated SS substrates. As mentioned in the previous chapter, this technique is useful for determining whether the LNMO spinel corresponds to the ordered or disordered phase.^[11,45] As it can be observed, the spectra obtained for all the cases (Au_LNMO, CrN_LNMO, TiN_LNMO, and Al_LNMO), regardless of the secondary phases observed in XRD, match well with the desired disordered spinel structure. The vibrational modes corresponding to this disordered spinel, 640 (A_{1g}), 600 ($F_{2g(3)}$), 500 ($F_{2g(2)}$), 404 (E_g) and 343 ($F_{2g(1)}$) cm^{-1} are highlighted in the figure.^[34] Only a small shoulder is detected in Au_LNMO sample around 570 cm^{-1} , which in fact can be related to the structural changes induced by Fe diffusion.

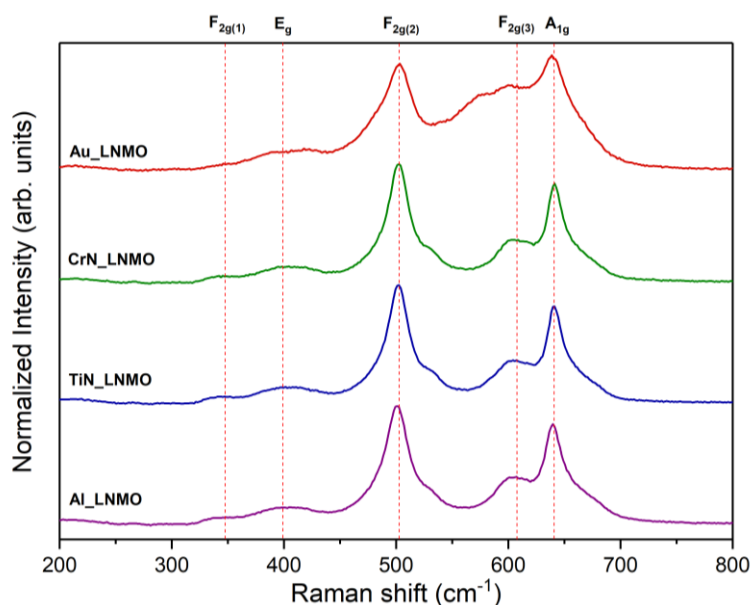


Figure 4.6: Raman spectra corresponding to Au_LNMO, CrN_LNMO, TiN_LNMO, and Al_LNMO samples. Dashed fiducial lines indicate the vibrational modes associated to the LNMO disordered phase.

4.3.3. Surface morphology and compositional analysis

The surface morphology of the annealed LNMO thin film on Au-, CrN-, TiN-, and Al-coated SS substrates was studied by SEM as can be seen on the micrographs of **Figure 4.7**: a) Au_LNMO, b) CrN_LNMO, c) TiN_LNMO, and d) Al_LNMO.

The Au_LNMO sample surface morphology presents rectangular-like particles (long- and short-axis of 1000 nm and 200 nm long, respectively), see **Figure 4.7a**. The observed morphology is compatible with the observed XRD pattern

characterized by intense and narrow reflections. Conversely, the CrN_LNMO sample consists of a dense surface with more compact particles, composed of mostly cubic-shaped crystalline grains of about 200-250 nm in length (**Figure 4.7b**). This is comparable with the morphology reported in the literature under similar experimental conditions.^[4] The surface morphology analysis of TiN_LNMO, carried out in the part that the LNMO layer had not detached, shows dense cubic shaped crystalline grains of about 200 nm, as CrN_LNMO sample, partially full of flake-like protruding particle sheets (**Figure 4.7c**). Al_LNMO case resembles Au_LNMO but with thinner and shorter particles, which are around 400 nm in the long-axis and 50 nm in the short-axis, see **Figure 4.7d**.

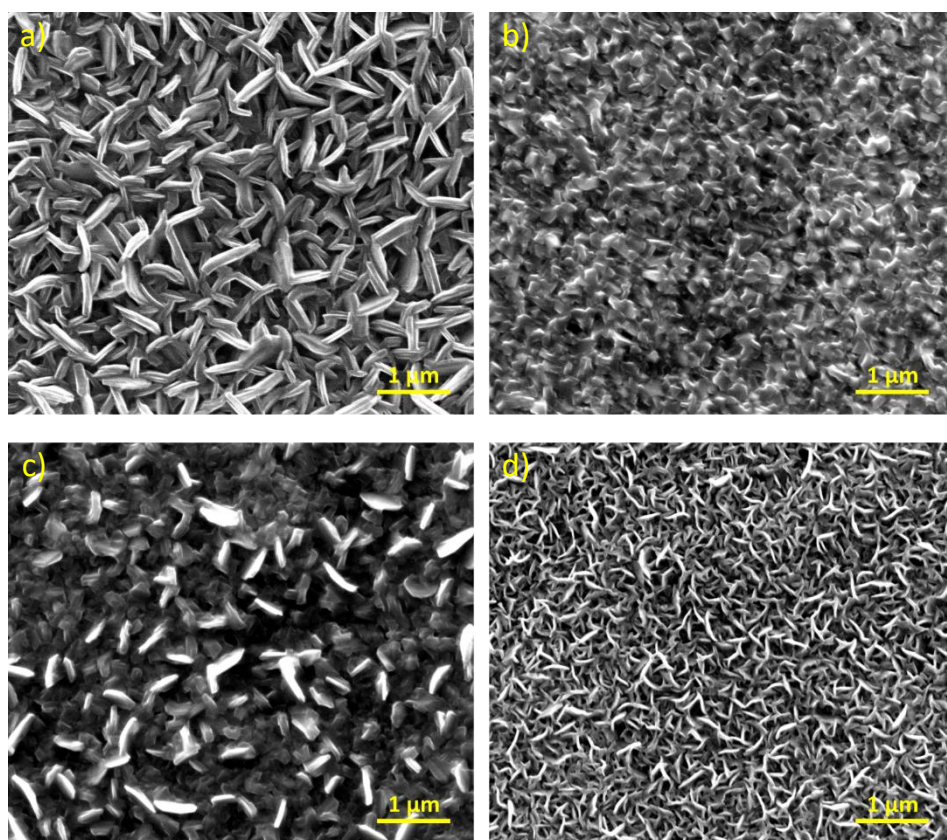


Figure 4.7: SEM micrographs corresponding to a) Au_LNMO, b) CrN_LNMO, c) TiN_LNMO, and d) Al_LNMO.

Interestingly, **Figure 4.8a,b** shows the cracks formed in the LNMO layer deposited on Al-coated SS substrate after annealing. Created as a result of the thermal stresses caused by a difference in the thermal expansion coefficient (α) between

two materials joined together.^[35] These cracks appear only in the aluminum coating due to its high thermal expansion coefficient value, $23 \cdot 10^{-6} \text{ } ^\circ\text{C}^{-1}$, compared to the bare substrate and the other coatings ($16 \cdot 10^{-6}$, $14 \cdot 10^{-6}$, $9.4 \cdot 10^{-6}$, and $9.3 \cdot 10^{-6} \text{ } ^\circ\text{C}^{-1}$ for SS, Au, CrN, and TiN, respectively).^[35] The ceramic cathode, with a much lower thermal expansion coefficient (α_{LNMO}) than aluminum (α_{Al}), is subjected to higher tension stress than with the other coatings, causing a plastic deformation on the metallic material and cracking in the ceramic, as schematically illustrated in **Figure 4.8c**.^[35,36]

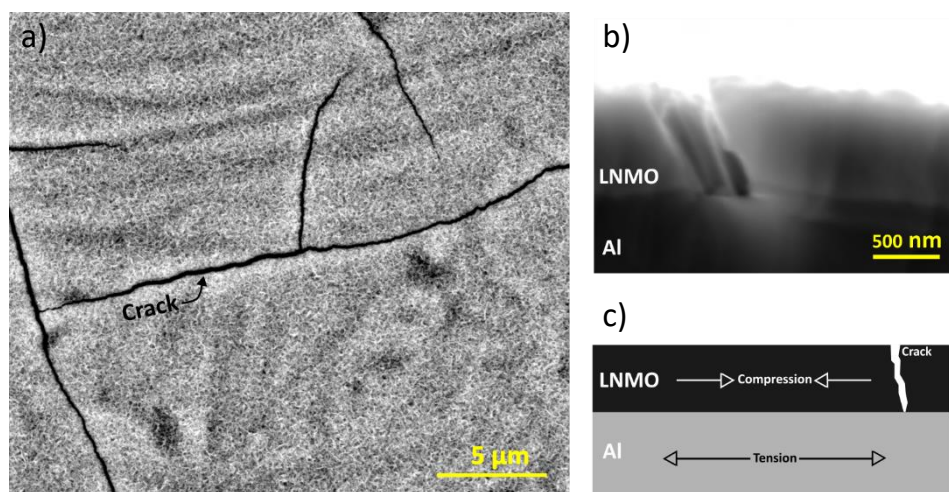


Figure 4.8: a) Top-view SEM BSED image of the Al_LNMO, b) cross-section of LNMO deposited on Al substrate, and c) schematic illustration of thermal stress in joint interface and cracking mode due to difference of thermal expansion coefficient ($\alpha_{\text{LNMO}} < \alpha_{\text{Al}}$).

In order to analyze the effectiveness of the SS substrate coatings as diffusion barrier, an elemental characterization was performed using EDS. This technique is suitable to compare the concentration of the constitutive elements (except Li) up to 1-2 μm depth of LNMO thin film deposited on bare, Au-, CrN-, TiN-, and Al-coated SS substrates. From quantitative analysis, the atomic concentration of the elements is normalized to 1.5 Mn, thus comparing with the LNMO theoretical values ($\text{LiNi}_{0.5}\text{Mn}_{1.5}\text{O}_4$). The obtained values of the coating elements, LNMO elements (Mn, Ni, and O), and the diffusion impurities (Fe) are listed in **Table 4.2**.

Looking at **Table 4.2**, it can be seen that for the reference sample, SS_LNMO, the concentration of Fe is similar to that of Ni, being the latter in accordance with the stoichiometric LNMO composition (as in the rest of the samples). In the Al_LNMO, almost the same amount of Fe as in the reference sample is observed, meaning that the Al coating is not very effective as a barrier layer. Even worse is

the Au_LNMO sample case, which doubles the amount of detected iron that could be oxidized as observed from the oxygen concentration increase. Although the metal layer thickness is 1.5 μm , it is not only unable to stop the diffusion, but it is vulnerable to the formation of new Fe-alloys (see XRD result in the previous section). In contrast, the CrN and TiN coatings hinder the Fe diffusion. The CrN_LNMO sample displays the same concentration of LNMO elements as the reference sample, rendering CrN a good candidate to avoid diffusion and obtain a good electrochemical performance. Note that the oxygen signal is more reduced than in the case of as deposited LNMO sample, see **Table 3.1** of the previous chapter, this is mainly due to the removal of surface contamination after annealing.

Table 4.2: Stoichiometry of LNMO deposited and annealed on the bare SS substrate (SS_LNMO), and Au- (Au_LNMO), CrN- (CrN_LNMO), TiN- (TiN_LNMO), and Al-coated (Al_LNMO) SS substrate determined from EDX analysis, normalized to 1.5 Mn.

	Mn	Ni	O	Fe	Cr	Au	Ti	Al
SS_LNMO	1.50	0.58	2.40	0.59	0.20	-	-	-
Au_LNMO	1.50	0.57	5.70	1.23	0.39	0.59	-	-
CrN_LNMO	1.50	0.54	2.26	0.02	0.84	-	-	-
TiN_LNMO	1.50	0.52	3.72	0.10	0.04	-	0.64	-
Al_LNMO	1.50	0.60	2.50	0.43	0.14	-	-	0.32

4.3.4. Electrochemical characterization

Finally, the effect of the addition of diffusion barriers in the electrochemical performance of LNMO cathodes was analyzed. **Figure 4.9a** shows the first three cycles of the corresponding Au_LNMO, CrN_LNMO, TiN_LNMO, and Al_LNMO sample at C/10 (from 3.5 V vs Li/Li⁺ to 5 V vs Li/Li⁺). In this way, a correlation between the diffused Fe as detected by EDS and the electrochemical performance at the first cycle can be established.

As seen for CrN_LNMO (**Figure 4.9b**), the previously observed initial plateau at *ca.* 4.0 V vs Li/Li⁺ does not appear on the first charge, thus confirming the absence of Fe-containing secondary phases leading to unwanted electrochemical behavior in this film. Instead, only a small irreversible plateau at 4.2 V vs Li/Li⁺ could be observed, which could be directly attributed to a certain electrochemical activity of Mn³⁺/Mn⁴⁺ reaction (as commented in the previous chapter for the thicker LNMO_5000 film). Moreover, the electrochemical cycling shows the two high voltage transitions near 4.65 and 4.75 V vs Li/Li⁺ due to the

successive oxidation of Ni^{2+} to Ni^{3+} and Ni^{4+} , respectively, indicating a successful lithium (de)insertion.

In the samples where the Fe signal was detected, Au_LNMO and Al_LNMO (**Figure 4.9a,d**), the non-reversible plateau at around 4 V vs Li/Li^+ could be observed, with a similar length in both cases. In addition, the Au_LNMO sample shows a new irreversible reaction at 4.57 V vs Li/Li^+ that can be related to the Au/Au^+ oxidation process.^[22] Anyway, the double plateau corresponding to the nickel redox process is observed in Au_LNMO, while it is not seen for Al_LNMO. This can be due to its high internal resistance since its IR drop is about 0.41 V (much higher than the other cases), possibly caused by the traces of Al_2O_3 as detected in the XRD analysis (**Figure 4.5**). In fact, some authors have reported the formation of electrically insulating LiAlO_2 after annealing up to 450 °C.^[4,37] The pronounced decrease in the discharge specific capacity during the first three cycles may also be produced by the presence of those alloys.

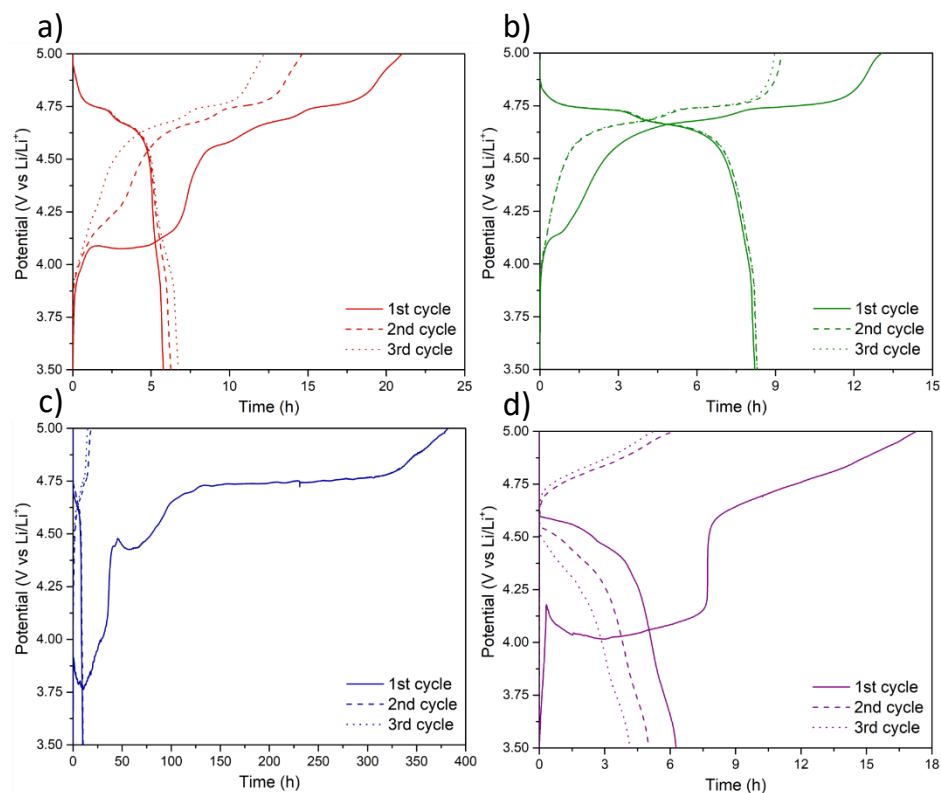


Figure 4.9: The initial three cycles of a) Au_LNMO, b) CrN_LNMO, c) TiN_LNMO, and d) Al_LNMO at C/10.

Finally, for the TiN_LNMO sample (**Figure 4.9c**) several observations can be made: i) the presence, again, of the non-reversible plateau at around 4 V vs Li/Li⁺ (lasting around 10h), ii) the appearance of an intermediate plateau at 4.43 V vs Li/Li⁺, iii) the small plateau at 4.68 V vs Li/Li⁺ corresponding to Ni²⁺/Ni³⁺ that is probably followed by a long Ni³⁺/Ni⁴⁺-related plateau at 4.73 V vs Li/Li⁺ (note the different x-axis scale), and iv) the 0.3 V of IR drop. The latter feature can be due to the presence of the low conductive-TiO₂, as detected by the XRD analysis, usually employed as electrical insulator.^[38] Owing to the reduced amount of cathode active material the electrochemical reactions last longer at the same C-rate, being more evident in the parasitic reactions of the secondary phases, even the LNMO's specific reactions.

Figure 4.10 shows the discharge specific capacity at different C-rates of the Au_LNMO, CrN_LNMO, TiN_LNMO, and Al_LNMO samples, compared to the corresponding 1000 nm-thick LNMO thin film electrode (SS_LNMO, comparable thickness - mass loading).

So far, the most promising coating is CrN, see **Figure 4.10b**. Notably, the discharge specific capacity at lower C-rates (below 1C) is like SS_LNMO, *e.g.*, 122.1 mAh·g⁻¹ for CrN_LNMO and 118.9 mAh·g⁻¹ for SS_LNMO at C/10 with a capacity retention of 89.9% and 88.2% at 1C, respectively. Slight differences arise at higher C-rates (10C), where the electrode with CrN interphase outperforms the CrN-free one: CrN_LNMO presents a capacity of 66.8 mAh·g⁻¹ which is equivalent to the retention of 54.7% vs initial C/10, whereas SS_LNMO delivers only 50.6 mAh·g⁻¹, *i.e.* 42.6% of capacity retention. In terms of CE, both samples present a similar evolution upon cycling, with CE > 90% from the second cycle and steadily improving up to nearly 100% at 1C. The only difference is found in the first cycle, with a marked improvement on the CrN-coated sample due to the absence of the irreversible Fe plateau.

At C/10, the discharge specific capacity of the Au_LNMO sample (**Figure 4.10a**) grows progressively from a rather small value of 84.9 mAh·g⁻¹ to 106.8 mAh·g⁻¹, equaling the SS_LNMO at C/5 (*e.g.*, 113.7 mAh·g⁻¹ for Au_LNMO and 117.2 mAh·g⁻¹ for SS_LNMO). The formation of impurities within LNMO film can affect electrode performance, becoming more evident when the SEI is being formed (during initial cycles). This is also evident in the CE, which increases from 26.8% up to 59.9% during the first five cycles at C/10. Note that the CE of the first cycle is as low as SS_LNMO. Despite the initial CE improvement, it does not exceed 95% until 1C, but achieving around 100% at 5C. The capacity retention at 1C considering the value at C/5, is 87.6%, very close to 89.4% of SS_LNMO. As in the previous case, Au_LNMO improves the performance of the non-coated sample

at higher C-rates, where Au-coated sample presents a capacity of $67.2 \text{ mAh}\cdot\text{g}^{-1}$, while the SS_LNMO gives only $50.6 \text{ mAh}\cdot\text{g}^{-1}$. When the cell is cycled back to C/10, the capacity at C/5 is recovered ($113.5 \text{ mAh}\cdot\text{g}^{-1}$). However, the value of the CE drops to 69.4%, which is 25% below SS_LNMO. As cycle times increase, parasitic reactions tend to become more pronounced.

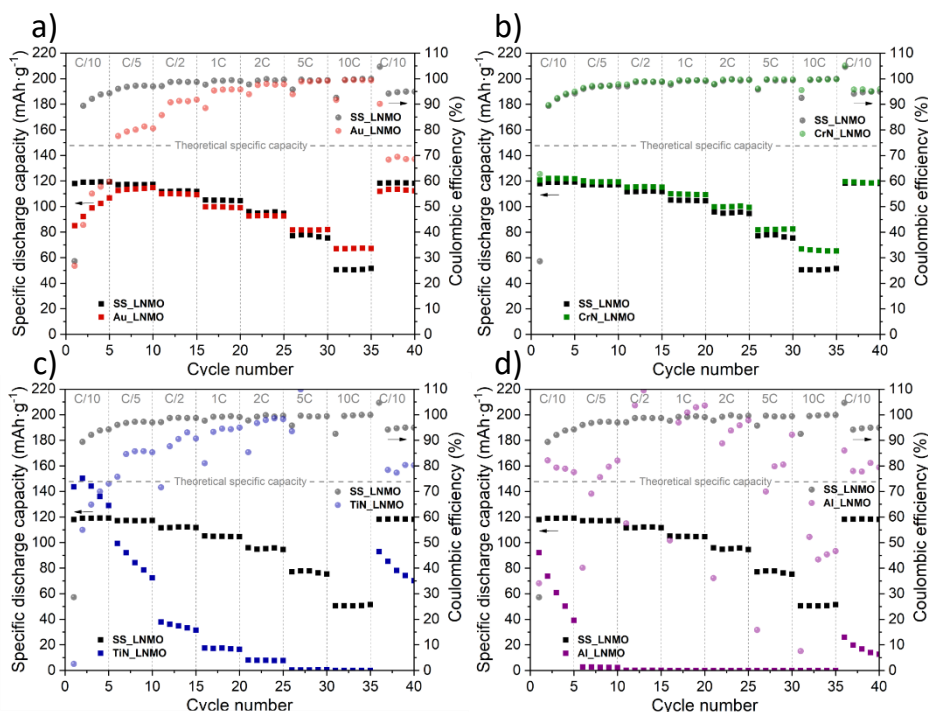


Figure 4.10: Discharge specific capacity (filled squares) and corresponding coulombic efficiency (filled circle) of a) Au_LNMO, b) CrN_LNMO, c) TiN_LNMO, and d) Al_LNMO compared with SS_LNMO at different C-rates. As reference, a dashed line indicates the theoretical specific capacity of the LNMO, which is equal to $146.6 \text{ mAh}\cdot\text{g}^{-1}$.

The discharge specific capacity of the TiN-coated sample decreases progressively from $143.6 \text{ mAh}\cdot\text{g}^{-1}$ at C/10 to $17.1 \text{ mAh}\cdot\text{g}^{-1}$ at C, falling by 88.1% (Figure 4.10c). Although the reversibility of the reactions in the following cycles is improved, the capacity drops to zero at 5C. Even so, when it returns to C/10, it recovers 64.1% of its initial value. However, this specific capacity decrease by 24.4% in the next 5 cycles. In terms of CE, TiN_LNMO sample presents a similar evolution upon cycling until 5C than Au_LNMO. Note that at high C-rates, as the capacity is zero, the CE value goes out of range. The increasing delamination of the LNMO thin film from the TiN-coated substrate during cycling is not excluded as a cause of the capacity decay. Moreover, the high probability of TiO_2 to form $\text{Li}_4\text{Ti}_5\text{O}_{12}$ in a

lithium environment is already reported in the literature,^[39] hindering the (de)intercalation of lithium.

The Al-coating (**Figure 4.10d**) is not suitable to improve the electrochemical performance of the non-coated LNMO sample. The low discharge specific capacity obtained in the first cycle at C/10, *i.e.*, $92.2 \text{ mAh}\cdot\text{g}^{-1}$, rapidly drops to $39.2 \text{ mAh}\cdot\text{g}^{-1}$ in the first five cycles. By increasing the current, at C/5, is only able to provide $2.5 \text{ mAh}\cdot\text{g}^{-1}$, falling to zero at C/2. When cycling again at C/10, barely reaches $15 \text{ mAh}\cdot\text{g}^{-1}$. It seems that the alloys formed after annealing, such as electrically insulating Al_2O_3 and LiAlO_2 ,^[4,37] are detrimental to cycling, disrupting the lithium/electron (de)intercalation.

As seen in the studies carried out above, the addition of a CrN diffusion barrier layer prevents the Fe diffusion, as well as improves the electrochemical performance. The following section analyses how the diffusion along the CrN layer is decreasing and the possibility of reducing its thickness.

4.3.5. CrN layer in-depth study

An in-depth elemental distribution analysis by SEM EDS was performed on the film cross-section of a $1.71 \mu\text{m}$ -thick CrN layer after the thermal treatment in air at $600 \text{ }^\circ\text{C}$, see **Figure 4.11**.

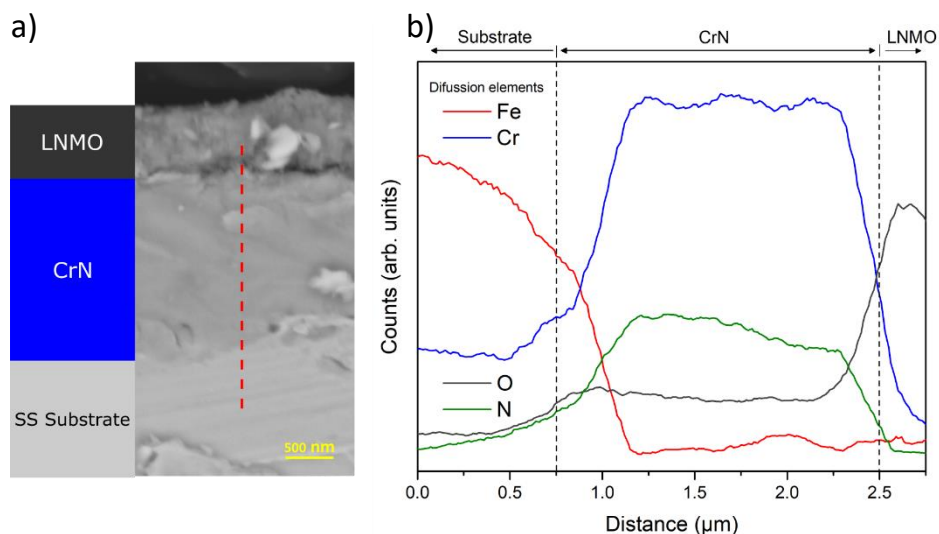


Figure 4.11: (a) SEM cross-section micrograph of CrN_LNMO and corresponding sketch. The red dashed line outlines the scanned region using SEM EDS. (b) In-depth distribution of Fe, Cr, O, and N as detected by SEM EDX measured along the red dashed line shown in (a). Black dashed lines identify the SS/CrN and CrN/LNMO interfaces.

As shown there, a rapid decrease in the concentration of Fe was detected when reaching the CrN interface, revealing that the CrN interlayer acts as a good diffusion barrier of Fe between the SS substrate and the LNMO film. The successful prevention of Fe diffusion through the CrN film was further confirmed by XPS, see **Figure 4.12**. The elemental analysis carried out on the surface of an annealed CrN layer corroborated the absence of iron, proving the effectiveness of CrN in preventing the Fe diffusion from the substrate. It is important to note here that the EDS analysis showed in **Figure 4.11** also evidenced a certain Cr diffusion towards the LNMO cathode. However, far from being a problem, it has been found in literature that the incorporation of this element in the LNMO cathode is an effective way to improve its electrochemical performance.^[4,40]

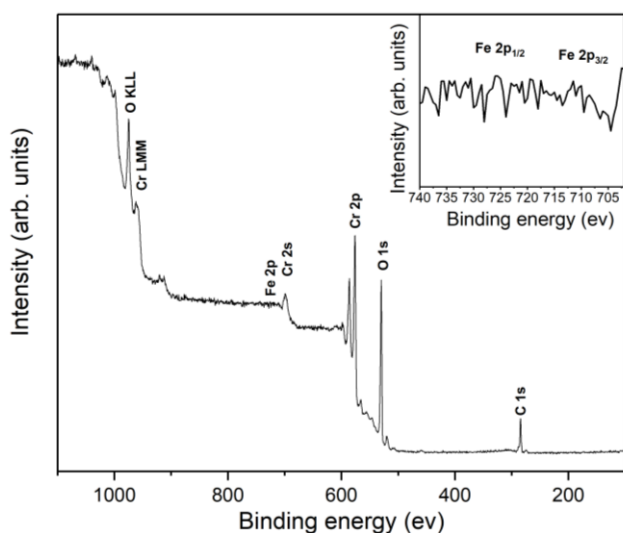


Figure 4.12: XPS survey spectra of the surface of 1.5 μm -thick CrN-coated SS substrate (The inset graph shows the binding energy region corresponding to Fe 2p photoemission line).

Looking at **Figure 4.11**, the Fe loading drops rapidly in the first few nanometers of the layer, suggesting that lower CrN-thickness would be able to prevent such Fe diffusion. Note that the formation of interlayers in the SS/CrN interface after annealing cannot be excluded. For the thickness study 1 μm -thick LNMO was deposited on 100, 250, 500, and 700 nm CrN-coated SS substrates. **Figure 4.13a** shows the first cycle at C/10 of the different thicknesses of CrN. Apart from the plateaus corresponding to $\text{Ni}^{2+}/\text{Ni}^{4+}$, only a small irreversible plateau at 4.2 V vs Li/Li⁺ can be seen in all samples during the first charge, without significant variations between each sample. This plateau is more likely due to the electrochemical activity of $\text{Mn}^{3+}/\text{Mn}^{4+}$, so it confirms that the diffusion of Fe has been avoided even in the thinnest sample. In this case, XPS measurements were

also performed to verify the absence of Fe on the CrN surface after annealing. **Figure 4.13b** shows the XPS survey of the 100nm-thick CrN layer. As can be seen in the inset graph, no traces of Fe are detected, thereby supporting the success of the CrN layer as diffusion barrier.

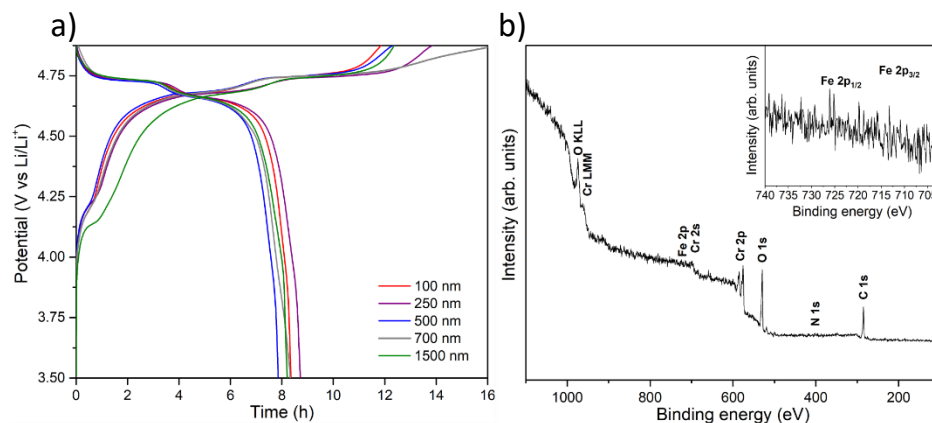


Figure 4.13: a) The first cycle of 1 μm -thick LNMO film deposited on top of a CrN (100, 250, 500, 700, and 1500 nm thick)-coated SS substrate, b) XPS survey spectra of 100 nm-thick CrN-coated SS substrate (the inset graph shows the Fe 2p signal region).

4.4. Cathode/liquid electrolyte interface: cathode protection coating

This section is oriented toward LNMO surface coating that prevent direct contact between the electrode and the liquid electrolyte. This stops electrolyte decomposition and ultimately improves cycle durability and rate capability. (*i.e.*, play the role of an SEI film). Surface coatings of Al_2O_3 have been known as an efficient strategy to treat different types of cathode materials.^[16,41] These coatings could be deposited by different techniques, being the reactive magnetron sputtering one of the most efficient technologies to achieve controllable thickness and composition.^[42,43]

4.4.1. Experimental set-up of Al_2O_3 coating and initial tests

The CemeCon CC800/8 magnetron sputtering system located in *Tecnalia* was used for the deposition of the Al_2O_3 coatings. The developed experimental set-up, based on the reactive sputtering mode, is shown in **Figure 4.14**. Two pure aluminum targets (one of them shielded to ensure better control of the deposition) and oxygen-argon mix as the reactive gas are used for the deposition. A reactive feedback control system (Speedflo[®] control - *Gencoa*) was used to

guarantee the reliability and reproducibility of the reactive process condition in all performed processes.

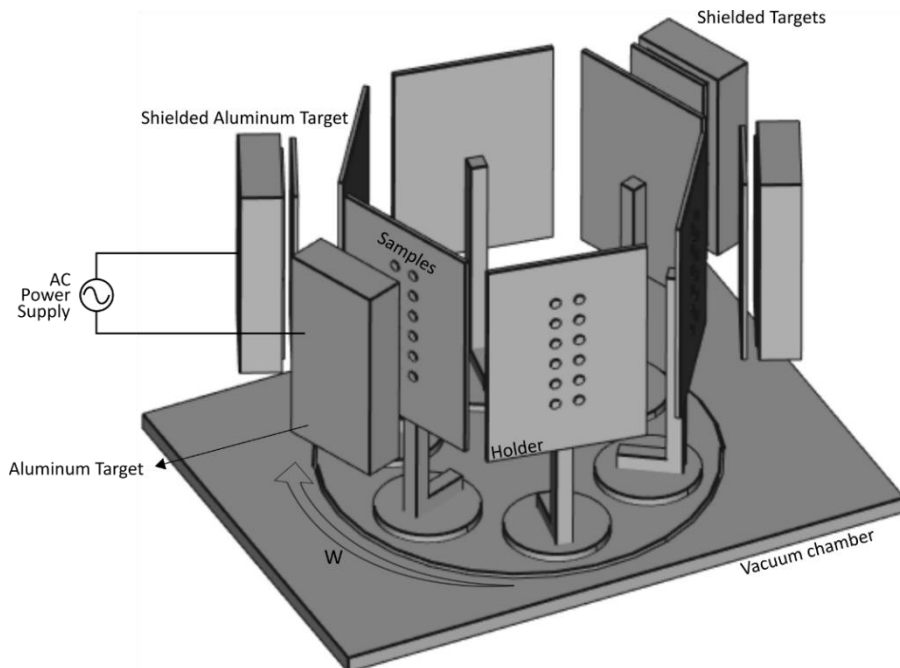


Figure 4.14: Schematic view of the CemeCon CC800/8 magnetron sputtering system at *Tecnalia*.

Before the deposition test, the process chamber was evacuated down to a base pressure of $2 \cdot 10^{-5}$ mbar. The substrate-to-target distance was set at 80 mm and the holders were rotating at 1.15 rpm to ensure coating uniformity (see w in **Figure 4.14**). Note that in this case, the substrates were always oriented to the target, thus making it easier to control the process. A mixture of Ar and O₂ was introduced in the chamber (167 sccm and 10 sccm, respectively) that resulted in working pressures of $4.88 \cdot 10^{-3}$ mbar. AC power of 500 W was applied in both targets with $8.3 \text{ W} \cdot \text{s}^{-1}$ ramp rate.

The optimal position of the substrates on the holder was determined by analyzing the deposition rate at different heights within the holder. For this purpose, 5 silicon substrates masked with a Kapton strip were placed at different heights within the holder before the start of a deposition process with the selected conditions for 1 h. Once the films were grown on the Si substrates, the thickness of the films was measured at the step edge of the Kapton shadow mask by means of a stylus profilometer. As the required thickness for this application is typically a few nm-thick, the deposition rate per turn performed was counted. Thus,

Figure 4.15 shows the deposition rate per turn as a function of the sample position on the holder.

The first silicon was positioned at 20.75 cm from the base of the sample holder, obtaining a value of $0.99 \pm 0.04 \text{ nm}\cdot\text{turn}^{-1}$. This value increases as moving toward the center of the holder, achieving $1.19 \pm 0.02 \text{ nm}\cdot\text{turn}^{-1}$ at 24.5 cm. In addition, the small measurement error indicates a more uniform film at this point. This value decreases again to $0.99 \pm 0.03 \text{ nm}\cdot\text{turn}^{-1}$ at 28.75 cm, where the last silicon has been positioned.

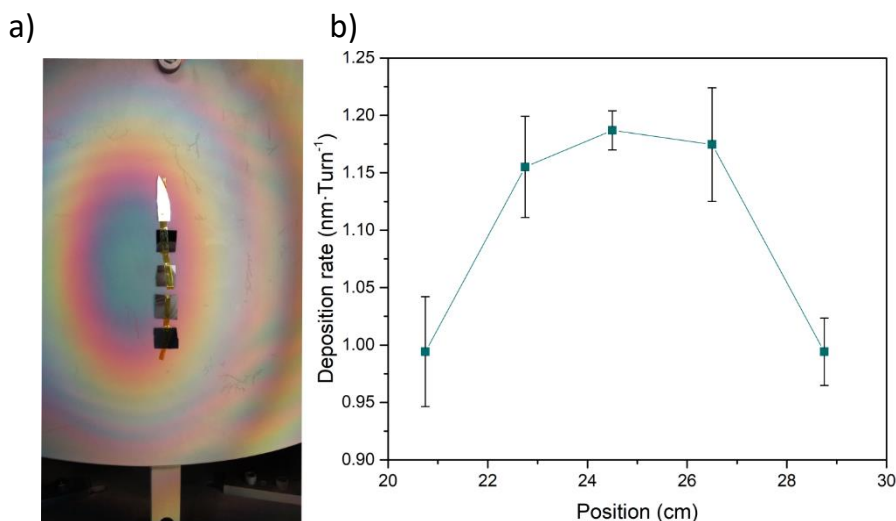


Figure 4.15: a) Position of the substrates on the sample holder, and b) the corresponding deposition rate along the holder.

4.4.2. Surface morphology and structural characterization

This section shows the morphological and structural characterization of the layer deposited for 1h in the previous process. Field emission scanning electron microscopy (FESEM) images⁴ of Al_2O_3 film deposited on different substrates are presented in **Figure 4.16**. The analyzed substrates include silicon (100) single crystal, as deposited LNMO and LNMO annealed to 600 °C (both deposited on Si wafer). The film homogeneously covers the Si and LNMO surface of the studied samples, with no signs of crystallization. Still, some small differences could be observed in the morphology. While the surface of the sample deposited on Si

⁴ The microscopy works corresponding to this section have been conducted in the Advanced Research Facilities (SGIker) - EHU/UPV. We acknowledge SGIker for offering access to their instruments and expertise.

wafer was smooth, a granulated surface was obtained in the films deposited on LNMO (as deposited and annealed). Among these last two cases, the annealed LNMO coating is the one that displays the largest grains (around 400 nm in diameter vs 100 nm of the non-annealed sample).

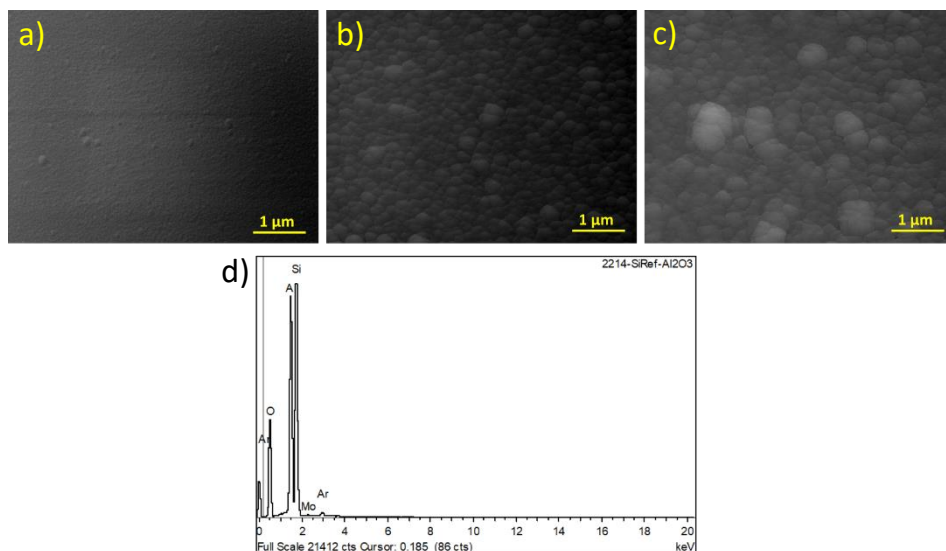


Figure 4.16: FESEM images of Al₂O₃ film deposited on a) silicon wafer, b) as-deposited LNMO, and c) annealed LNMO. d) EDS signal of Al₂O₃ deposited on silicon wafer.

To verify whether the deposited film contains the desired elements, bulk elemental analysis of Al₂O₃ film deposited on Si wafer was carried out by means of EDS study (**Figure 4.16d**). With this technique, the presence of Al and O in the film was confirmed.

The XRD measurement performed on the Al₂O₃ coating deposited on non-annealed LNMO reveals the amorphous nature of the film, see **Figure 4.17**. Only those broad peaks related to the base of the measurement platform were observed, *i.e.*, 2θ angles of 13.2°, 29.7°, and 42.3°. Meanwhile, no peaks associated with Al₂O₃ crystallinity could be identified, confirming its amorphousness. This result is in agreement with the reported literature on Al₂O₃ protective coating.^[44]

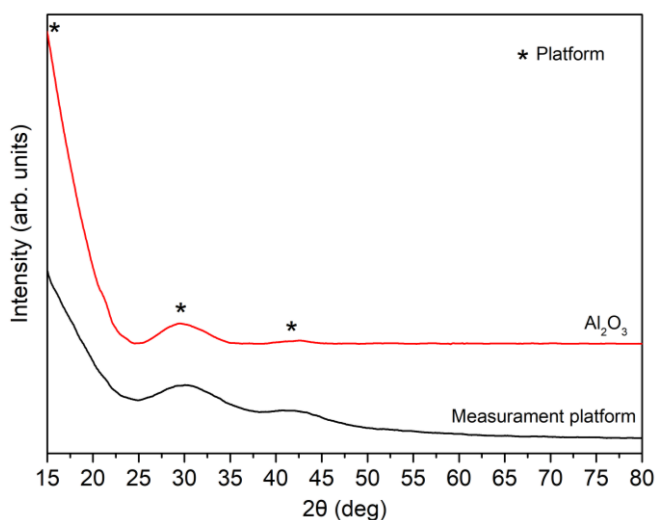


Figure 4.17: XRD pattern of Al_2O_3 deposited on Si wafer compared with the measurement platform's signal.

4.4.3. Electrochemical characterization of different Al_2O_3 thickness

Like many metal oxides, Al_2O_3 does not have good electronic conductivity; hence agglomeration or increased thickness of the coating becomes detrimental to the conductivity of the electrode. Therefore, tight control of the thickness is needed to achieve the optimum properties. Typically, values in the range from 5 to 10 nm are presented as optimum for this application.^[16,41]

The thickness of the coating is controlled by counting the time the substrate passes in front of the magnetron head. In total, two different thicknesses were analyzed in this work. For this purpose, the previously annealed SS/LNMO samples (600 °C for 1h in air atmosphere) were placed in the center of the holder. The Al_2O_3 depositions conducted are a 4-turn process, which is equivalent to 3.5 minutes long process, and a 14-turn or 12 minutes process. The expected thicknesses for each process are 4.75 and 16.65 nm, respectively. Determining such small thickness by profilometer can be problematic. Therefore, the real thickness of the samples was calculated by means of ellipsometry.⁵ As can be seen in **Table 4.3**, the thickness of the thinnest one differs from the expected value, while the thickest film is similar. This means that the deposition of the first layers has been faster than expected, matching the calculated thickness

⁵ The ellipsometry measurements were performed at *CIC nanoGUNE*. We acknowledge them for offering access to their instruments and expertise.

afterward. These samples will be referred to hereafter as LNMO_Al₂O₃_4T and LNMO_Al₂O₃_14T.

Table 4.3: Al₂O₃ deposition processes carried out at *Tecnalia*. The table includes the number of turns made, the duration of the processes, the expected thickness considering the deposition rate, and the thickness measured by ellipsometry.

	Turns	Duration (min)	Expected thickness (nm)	Real thickness (nm)
LNMO_Al ₂ O ₃ _4T	4	3.5	4.75	8.09 ± 0.33
LNMO_Al ₂ O ₃ _14T	14	12	16.65	17.03 ± 0.39

The electrochemical results obtained for the uncoated LNMO sample (LNMO_bare), LNMO_Al₂O₃_4T, and LNMO_Al₂O₃_14T are shown in **Figure 4.18**. Looking at the discharge specific capacity at low C-rates (**Figure 4.18a**), it can be observed that at C/10 the value was similar in samples LNMO_bare and LNMO_Al₂O₃_14T, while it was slightly reduced in the case of LNMO_Al₂O₃_4T (113.3, 110.1, and 96.6 mAh·g⁻¹, respectively). Interestingly, it can be concluded that at low rates the alumina layer does not deteriorate the discharge specific capacity. At C, the highest capacity retention belonged to the uncoated LNMO, 95.5% versus 87.1% and 83.0% of the LNMO_Al₂O₃_4T and LNMO_Al₂O₃_14T samples, respectively. This can be attributed to the lower ohmic resistance of bare LNMO if compared with Al₂O₃-coated LNMO, so higher specific capacity values can be achieved when operated at higher current densities. At the highest C-rate, the discharge specific capacity of the thicker Al₂O₃ coating sample was reduced by 22.4% with respect to the other two samples, which achieved a similar capacity value (around 58 mAh·g⁻¹). The increase in the electrical insulator layer thickness leads to a poorer surface charge transfer or Li-ion solid-state conduction kinetics, resulting in a lower specific capacity.^[11,12] Nevertheless, when cycling back to C/10, the capacity retention of LNMO_bare and LNMO_Al₂O₃_4T samples was below 98.5%, while LNMO_Al₂O₃_14T almost achieves 100%. The thicker Al₂O₃ coating has the positive effect to reduce the irreversible losses related to the electrolyte and cathode reactions.^[12] This phenomenon was also highlighted in the CE values, being more evident at low C-rates. The best CE at the initial C/10 cycles corresponds to the LNMO_Al₂O₃_14T sample, reaching > 99% at C/2. The LNMO_bare and LNMO_Al₂O₃_4T samples followed a similar trend, reaching over 98% at 2C. As expected, when cycled again at C/10, LNMO_Al₂O₃_14T achieved 93% compared to 88% for LNMO_bare and LNMO_Al₂O₃_4T.

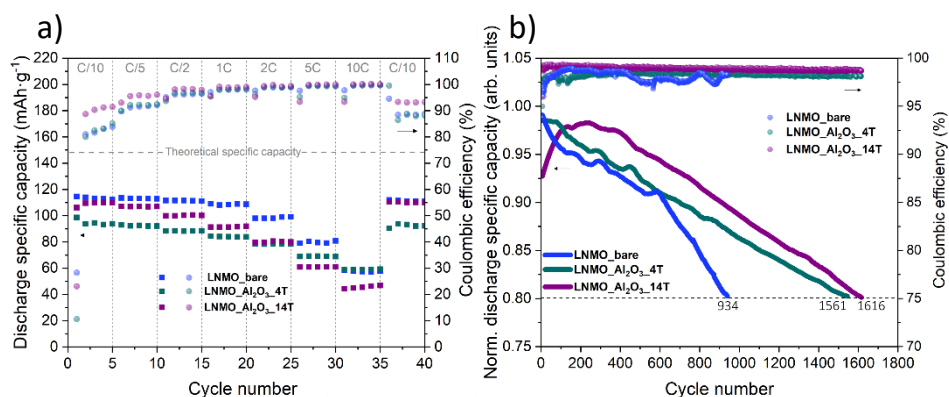


Figure 4.18: a) Discharge specific capacity and corresponding coulombic efficiency at different c-rates, and b) normalized specific discharge capacity and coulombic efficiency cycled at 1C as a function of cycle number of LNMO_bare, LNMO_Al₂O₃_4T, and LNMO_Al₂O₃_14T.

Figure 4.18b shows the normalized discharge specific capacities and coulombic efficiencies of LNMO_bare and Al₂O₃ coated LNMO samples (LNMO_Al₂O₃_4T and LNMO_Al₂O₃_14T) cycled at 1C as a function of cycle number. Before the long cycling, an SEI formation cycling procedure was set as two cycles at each C-rate, namely, C/10, C/5, and C/2.

The test was stopped when discharge capacity decreased down to 80% of its initial values, a percentage that usually determines the utilization limit of a Li-ion battery. After 20 cycles the CE followed LNMO_Al₂O₃_14T > LNMO_Al₂O₃_4T > LNMO_bare trend (99.2, 98.1 and 97.3 %, respectively). Thus, it is evident that the incorporation of the alumina film enhances the CE, which improves the thicker the layer is. As a result, the LNMO_bare performed 934 cycles before falling to 80% of its initial capacity, while the Al₂O₃ coated LNMO samples improved their cyclability reaching 1561 cycles in the thinnest case, and 1616 in the thickest.

4.5. Conclusions

In this work, the addition of Au, CrN, TiN, and Al diffusion layers in the current collector/cathode interface in order to solve the unwanted Fe diffusion towards the LNMO and the subsequent Fe₂O₃ secondary phase formation upon annealing was analyzed. Successful prevention of the Fe diffusion was attained in the CrN case, translated as an improvement of the electrochemical performance on the first cycle, by the disappearance of the initial plateau. Better capacity retention was also observed in the CrN-protected sample at high C-rates. These results

pave the way towards the use of LNMO thin film cathodes in functional microbatteries, fabricated on cost-effective stainless-steel substrates.

In addition, the insertion of cathode protective coatings to minimize possible side reactions at LNMO surface with liquid electrolyte was also analyzed. For this purpose, different thicknesses of Al_2O_3 coatings were grown, 3.5- and 12-minute processes. Discharge capacity at higher C-rates decreased along with the Al_2O_3 coating thickness. Conversely, in terms of coulombic efficiency, the thickest Al_2O_3 -coated electrode showed the highest values, particularly at low C-rates. The cathode shielding was evident in the long cycling, where the Al_2O_3 -coated samples outperformed the non-protected LNMO sample cycle life, especially the sample with thicker Al_2O_3 film. This latter sample represents a compromise solution between the suppression of the side reactions on the LNMO surface and the decrease in the ionic conductivity, leading to a trade-off between improved CE and a slight decrease in the specific capacity.

References in Chapter 4

- [1] C. F. Xiao, J. H. Kim, D. Choi, Y. C. Park, J. H. Kim, J. Park, Y. J. Kim, H. S. Kim, *J. Alloys Compd.* 2019, *801*, 550.
- [2] J. H. Kim, J. Park, J. Y. Cheong, A. Song, K. B. Chung, Y. C. Park, I. D. Kim, Y. J. Kim, K. Park, H. S. Kim, *Ceram. Int.* 2018, *44*, 20093.
- [3] M. Gellert, K. I. Gries, J. Zakel, A. Ott, S. Spannenberger, C. Yada, F. Rosciano, K. Volz, B. Roling, *Electrochim. Acta* 2014, *133*, 146.
- [4] A. N. Filippin, M. Rawlence, A. Wäckerlin, T. Feurer, T. Zünd, K. Kravchyk, M. V. Kovalenko, Y. E. Romanyuk, A. N. Tiwari, S. Buecheler, *RSC Adv.* 2017, *7*, 26960.
- [5] A. N. Filippin, T. Y. Lin, M. Rawlence, T. Zünd, K. Kravchyk, J. Sastre-Pellicer, S. G. Haass, A. Wäckerlin, M. V. Kovalenko, S. Buecheler, *RSC Adv.* 2018, *8*, 20304.
- [6] S. Wang, K. V. Kravchyk, A. N. Filippin, R. Widmer, A. N. Tiwari, S. Buecheler, M. I. Bodnarchuk, M. V. Kovalenko, *ACS Appl. Energy Mater.* 2019, *2*, 974.
- [7] J. Baumann, T. Werner, A. Ehrlich, M. Rennau, C. Kaufmann, T. Gessner, *Microelectron. Eng.* 1997, *37–38*, 221.
- [8] S. Lv, M. Li, X. Luo, J. Cheng, Z. Li, *J. Alloys Compd.* 2020, *815*, 151636.
- [9] T. Noguchi, I. Yamazaki, T. Numata, M. Shirakata, *J. Power Sources* 2007, *174*, 359.
- [10] Y. Kim, N. J. Dudney, M. Chi, S. K. Martha, J. Nanda, G. M. Veith, C. Liang, *J. Electrochem. Soc.* 2013, *160*, A3113.
- [11] J. Li, L. Baggetto, S. K. Martha, G. M. Veith, J. Nanda, C. Liang, N. J. Dudney, *Adv. Energy Mater.* 2013, *3*, 1275.
- [12] L. Baggetto, N. J. Dudney, G. M. Veith, *Electrochim. Acta* 2013, *90*, 135.
- [13] Y. K. Sun, Y. S. Lee, M. Yoshio, K. Amine, *Electrochem. Solid-State Lett.* 2002, *5*, 99.
- [14] Z. Chen, Y. Qin, K. Amine, Y. K. Sun, *J. Mater. Chem.* 2010, *20*, 7606.

- [15] Y. Fan, J. Wang, Z. Tang, W. He, J. Zhang, *Electrochim. Acta* 2007, 52, 3870.
- [16] X. Fang, M. Ge, J. Rong, Y. Che, N. Aroonyadet, X. Wang, Y. Liu, A. Zhang, C. Zhou, *Energy Technol.* 2014, 2, 159.
- [17] J. Liu, A. Manthiram, *Chem. Mater.* 2009, 21, 1695.
- [18] H. M. Wu, I. Belharouak, A. Abouimrane, Y. K. Sun, K. Amine, *J. Power Sources* 2010, 195, 2909.
- [19] J. Wang, S. Yao, W. Lin, B. Wu, X. He, J. Li, J. Zhao, *J. Power Sources* 2015, 280, 114.
- [20] L. Ben, H. Yu, Y. Wu, B. Chen, W. Zhao, X. Huang, *ACS Appl. Energy Mater.* 2018, 1, 5589.
- [21] Y. Wu, L. Ben, H. Yu, W. Qi, Y. Zhan, W. Zhao, X. Huang, *ACS Appl. Mater. Interfaces* 2019, 11, 6937.
- [22] J. Arrebola, A. Caballero, L. Hernán, J. Morales, E. Rodríguez Castellón, J. R. Ramos Barrado, *J. Electrochem. Soc.* 2007, 154, A178.
- [23] J. Arrebola, A. Caballero, L. Hernán, J. Morales, E. R. Castellón, *Electrochem. Solid-State Lett.* 2005, 8, 4.
- [24] J. H. Cho, J. H. Park, M. H. Lee, H. K. Song, S. Y. Lee, *Energy Environ. Sci.* 2012, 5, 7124.
- [25] T. Yang, N. Zhang, Y. Lang, K. Sun, *Electrochim. Acta* 2011, 56, 4058.
- [26] X. Fang, M. Ge, J. Rong, C. Zhou, *J. Mater. Chem. A* 2013, 1, 4083.
- [27] Y. A. Melnik, A. S. Metel, *J. Phys. Conf. Ser.* 2016, 830.
- [28] J. H. Kim, J. Park, K. Park, S. H. Cho, Y. C. Park, C. Kim, I. D. Kim, K. Park, H. S. Kim, *J. Electroceramics* 2019, 42, 104.
- [29] H. Fuse, N. Koshizaki, Y. Ishikawa, Z. Swiatkowska-Warkocka, *Nanomaterials* 2019, 9.
- [30] H. Y. Chen, F. H. Lu, *J. Vac. Sci. Technol. A Vacuum, Surfaces, Film.* 2005, 23, 1006.
- [31] M. Yildirim, M. V. Akdeniz, A. O. Mekhrabov, *Metall. Mater. Trans. A Phys.*

- Metall. Mater. Sci.* 2012, 43, 1809.
- [32] M. Létiche, M. Hallot, M. Huvé, T. Brousse, P. Roussel, C. Lethien, *Chem. Mater.* 2017, 29, 6044.
- [33] T. F. Yi, J. Mei, Y. R. Zhu, *J. Power Sources* 2016, 316, 85.
- [34] P. B. Samarasingha, N. H. Andersen, M. H. Sørby, S. Kumar, O. Nilsen, H. Fjellvåg, *Solid State Ionics* 2016, 284, 28.
- [35] M. B. Uday, M. N. Ahmad-Fauzi, A. M. Noor, S. Rajoo, *Join. Technol.* 2016, DOI 10.5772/64524.
- [36] J. Lemus, R. A. L. Drew, *Br. Ceram. Trans.* 2000, 99, 200.
- [37] T. K. Li, D. H. L. Ng, *Mater. Sci. Eng. A* 2007, 445–446, 652.
- [38] M. K. Nowotny, T. Bak, J. Nowotny, *J. Phys. Chem. B* 2006, 110, 16270.
- [39] G. Izquierdo, A. R. West, *Mater. Res. Bull.* 1980, 15, 1655.
- [40] D. W. Shin, C. A. Bridges, A. Huq, M. P. Paranthaman, A. Manthiram, *Chem. Mater.* 2012, 24, 3720.
- [41] Y. Wang, Q. Peng, G. Yang, Z. Yang, L. Zhang, H. Long, Y. Huang, P. Lu, *Electrochim. Acta* 2014, 136, 450.
- [42] S. Prasanna, R. G. Mohan, S. Jayakumar, M. D. Kannan, V. Ganesan, *Thin Solid Films* 2012, 520, 2689.
- [43] S. Prasanna, G. Krishnendu, S. Shalini, P. Biji, G. Mohan Rao, S. Jayakumar, R. Balasundaraprabhu, *Mater. Sci. Semicond. Process.* 2013, 16, 705.
- [44] X. Huang, K. Chen, Y. Liu, *J. Electrochem. Soc.* 2019, 166, A5081.

Chapter 5

Synthesis and characterization of LiPON thin film solid electrolyte

5.1. Introduction

Despite the progress made in the development of new materials, nowadays the most used inorganic solid-state electrolyte material in thin film form is still LiPON. Its stability against metallic Li and negligible electronic conductivity ($>10^{14} \Omega \cdot \text{cm}$) are key aspects here, while their main drawback is the relatively low ionic conductivity ($2 \cdot 10^{-6} \text{ S} \cdot \text{cm}^{-1}$ at room temperature).^[1] However, it is to be noted that a drastic thickness reduction of the electrolyte layer ($< 1 \mu\text{m}$) eventually permits its practical use, regardless of the lower conductivity.

LiPON was first fabricated by magnetron sputtering and introduced in ASSBs as a solid electrolyte in the 1990s by Bates et al.^[2-4] Since then, research efforts on this solid electrolyte have been primarily focused on increasing its ionic conductivity by varying deposition conditions, such as the sputtering power, N_2 pressure, and substrate temperature.^[5-7] Taking into account all the studies done so far, this chapter focuses on the deposition of LiPON by RF magnetron sputtering analyzing how the N_2 flow rate affects the deposited electrolyte.

5.2. Main objectives of the chapter

This chapter is focused on the characterization of LiPON thin film solid electrolyte deposited by RF magnetron sputtering at *CIC energiGUNE*.

This study includes the determination of the best N₂ flow rate for the optimal LiPON layer, in terms of ionic conductivity measured by means of EIS. Moreover, the obtained films were characterized morphologically by SEM, structurally by XRD, and in terms of surface composition by XPS.

5.3. Experimental set-up and initial deposition tests

As described in the experimental part, the magnetron sputtering system available at *CIC energiGUNE*, see **Figure 5.1**, is composed of 2 target-holder configurations that require 2" diameter targets, another one for 3" diameter targets (further details are given below), and an ion source that is used to clean the surface of the substrate prior to deposition by ionic bombardment or to improve deposition.^[8] These cathodes can be powered via DC and RF power supplies. As described in Chapter 2, we know that the DC mode can sputter only electrically conductive targets and would not be able to sputter electrically insulating targets such as the LiPON-based electrolyte. Therefore, bearing in mind that in RF mode we can sputter off insulating materials, this mode was used for the solid electrolyte deposition during this chapter. The main drawback for RF sputtering is the low deposition rates. To solve this problem, we have integrated a full-face erosion technology (FFE75), provided by *Gencoa Ltd.*, in where the whole target surface is sputtered via a motor-driven dynamic plasma scanning. In this way, it was possible to increase the deposition rate and the homogeneity of the thin film along the deposition area.

The selected target material was a 3" Li₃PO₄ circular target (*Toshima Manufacturing Co.*). Using this target, the ignition of the plasma, visible to the naked eye, was obtained even at relatively low power density, *i.e.* 0.5 W·cm⁻². For the deposition, a power density of 1.09 W·cm⁻² was applied to the target, and the substrate-to-target distance was maintained at 90 mm with an incident angle of 45°. To improve the uniformity, during the sputtering process, the substrate holder was rotating as indicated in **Figure 5.1** and a constant working pressure of 4.5·10⁻³ mbar was kept in the process chamber. These selected values enabled performing sputtering without any risk of target cracking due to thermal stress while guaranteeing reasonable deposition rate values. In this sense, it is important to consider that for this kind of ceramic target, a low ramping power rate is also needed to avoid the target fracture.

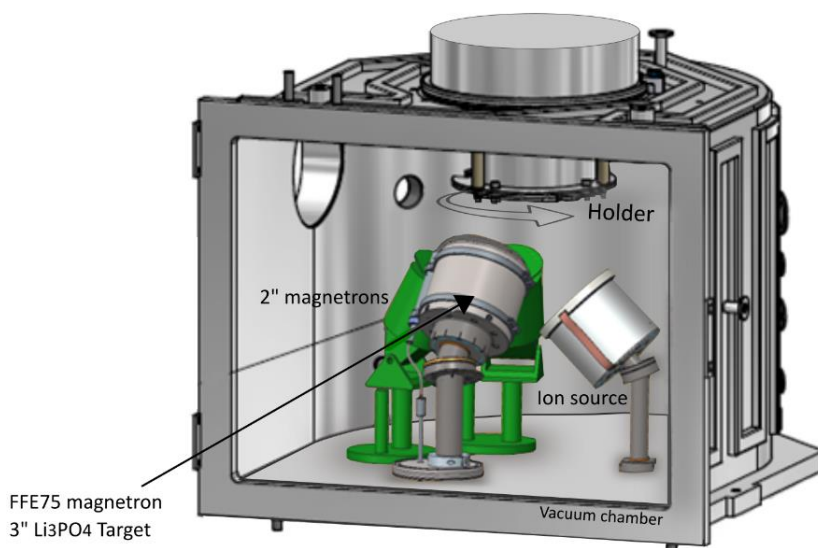


Figure 5.1: Schematic view of the magnetron sputtering configuration at *CIC energiGUNE*.

In order to analyze the role of the nitrogen concentration on the solid electrolyte, different percentages of pure nitrogen (N_2) flow rates were used: 0%, 25%, 50%, 75%, and 100%. Note that for a more accurate analysis, the chamber pressure was equal in the different processes. **Table 5.1** shows the N_2 flow rate values used to obtain the desired percentage, along with the respective Ar flow rate. These samples are henceforth referred as LiPON_0, LiPON_25, LiPON_50, LiPON_75, and LiPON_100, respectively.

Table 5.1: Ar- N_2 flow-rate values used for each sample.

Sample	N_2 percentage (%)	N_2 flow rate (sccm)	Ar flow rate (sccm)
LiPON_0	0	-	25.00
LiPON_25	25	3.70	18.75
LiPON_50	50	7.40	12.50
LiPON_75	75	11.10	6.25
LiPON_100	100	14.50	-

Once the sputterability of the target was verified, films were grown on atomically flat Si (100) single crystal substrates for morphological, structural, and elemental characterization; and on a 10 x 10 x 0.5 mm dielectric MgO (100) single crystal substrates (*CrysTec GmbH*) to evaluate the electrolyte ionic conductivity. The thin

film deposition processes carried out for this chapter lasted 16 hours. The first analysis consisted of the film thickness determination by cross-sectional SEM of the films grown on Si substrates, this analysis revealed that the deposition rate varies from sample to sample (**Figure 5.2**). The highest deposition rate, $1.38 \pm 0.04 \text{ nm}\cdot\text{min}^{-1}$, corresponds to the LiPON_0 sample which is deposited using only argon. The reason for this might be nested on the difference in the atomic radius of the two used gases, being Ar the process gas with the largest atomic radius: 0.88 \AA versus 0.75 \AA for N, which will result in increased collision probability of the Ar ion with the target atoms. In this way, as the percentage of Ar is decreased and N_2 is introduced, the deposition rate falls. Although during the intermediate percentages of gas mixtures, the deposition rate remains almost constant, around $1.28 \pm 0.01 \text{ nm}\cdot\text{min}^{-1}$, decreasing to $1.24 \pm 0.05 \text{ nm}\cdot\text{min}^{-1}$ when only N_2 is employed.

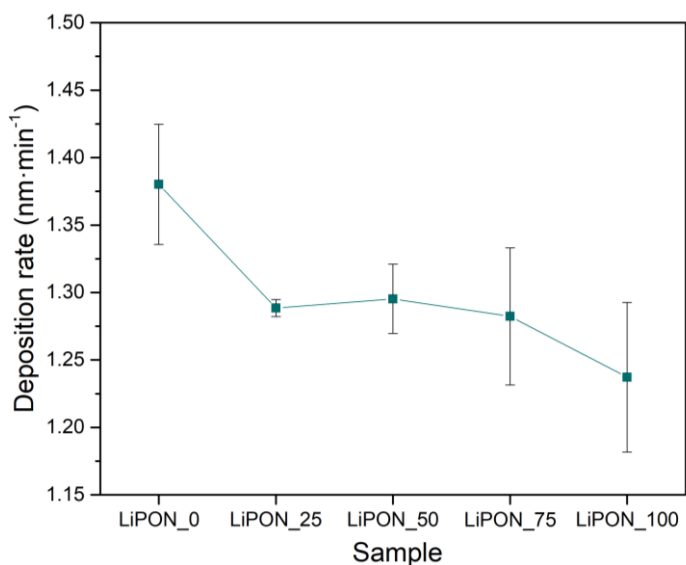


Figure 5.2: Deposition rate of LiPON processes carried out as a function of the Ar: N_2 concentration ratio.

As an example of the deposited layer, **Figure 5.3** shows the cross-section of the sample LiPON_50. Where a uniform, defect-free, and dense coating can be seen, without visible pinholes or cracks. Further in-depth characterizations of the samples are described in the next section.

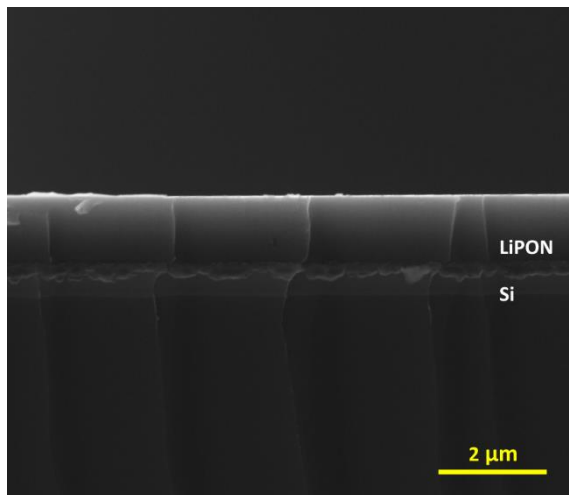


Figure 5.3: Cross-section image of LiPON_50.

5.4. Characterization of LiPON films

The results showed in this section include the analysis of the surface morphology, the crystalline structure, the ionic conductivity, and the elemental characterization of the deposited samples.

5.4.1. Surface morphology

Figure 5.4 shows the top-view SEM images of the deposited samples: a) LiPON_0, b) LiPON_25, c) LiPON_50, d) LiPON_75 and e) LiPON_100. First, all the deposited films presented a smooth and highly dense structure regardless of the background species, with no signs of crystallization (no crystallites could be identified in the images), as reported in the literature.^[9,10] Still, some small differences could be observed in the morphology. While the surface of the sample deposited only with argon is granulated, a smoother surface was obtained with increasing nitrogen content. Although an increase of spherical features is observed on the surface of the LiPON_75 sample, from a morphological point of view, all films presented the desired dense and homogeneous structure required.

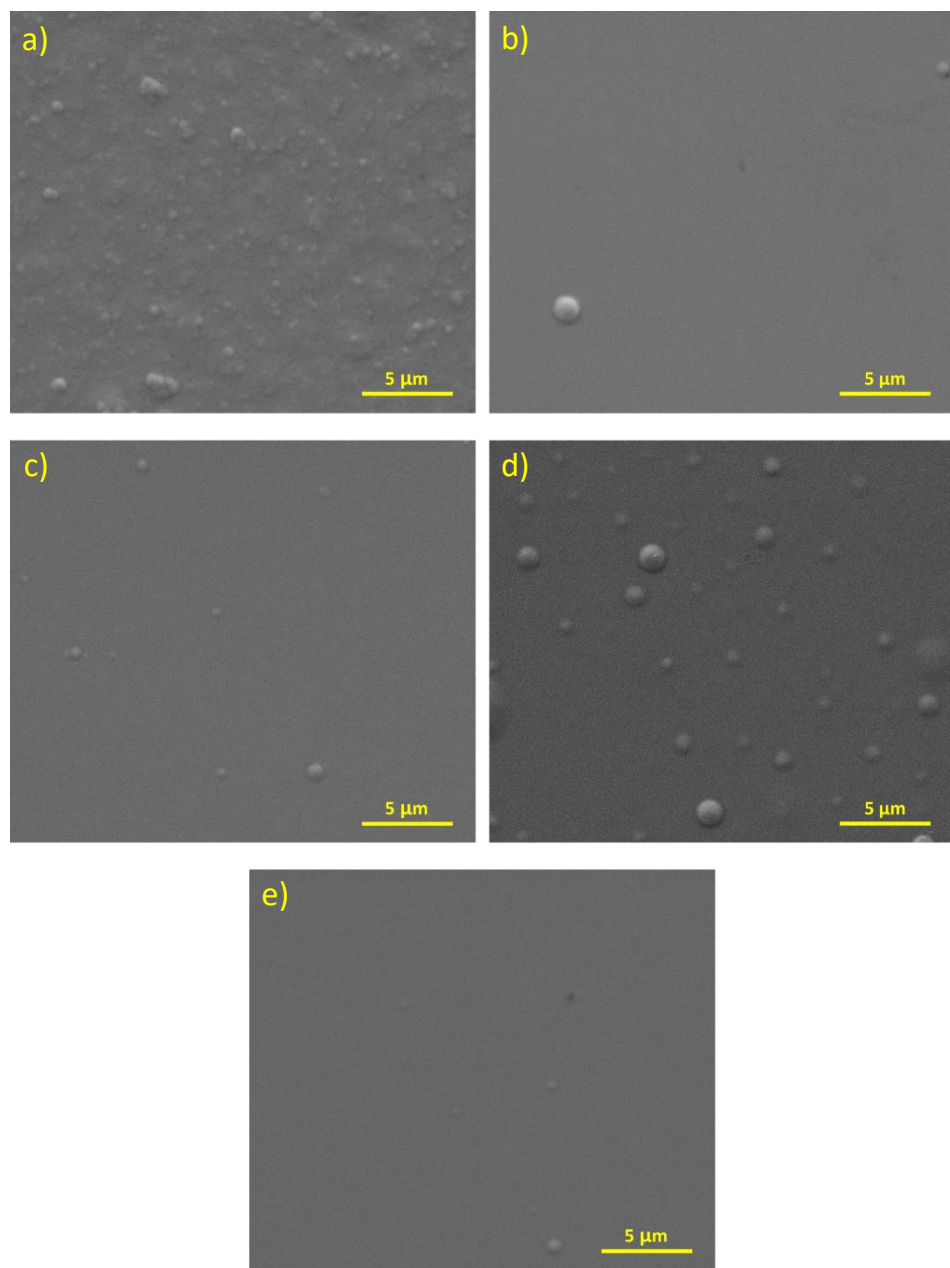


Figure 5.4: Top-view SEM images of LiPON thin films deposited with different Ar-N₂ content a) LiPON_0, b) LiPON_25, c) LiPON_50, d) LiPON_75 and e) LiPON_100, respectively.

The sudden increase of the spherical features in the sample LiPON_75, without evidencing any clear correlation with the respective gas percentages, can be associated with the sensitive character of the sample. Belous et al. and Chen et al. reported that the instability of LiPON when exposed to air can induce cracks and degradation on the surface after a short time (*approx.* 2 min).^[11,12] **Figure 5.5** shows how the surface of the LiPON_75 and the LiPON_0, degrade after two weeks of air exposure. As can be seen in the cross-section of the LiPON_75 (**Figure 5.5a**), vertical column formations have grown on the surface (see inset graph), which could be due the further evolution of the spherical features seen above. In the same way, on the surface of LiPON_0 (**Figure 5.5b**) a volcanic-shape structure was formed.

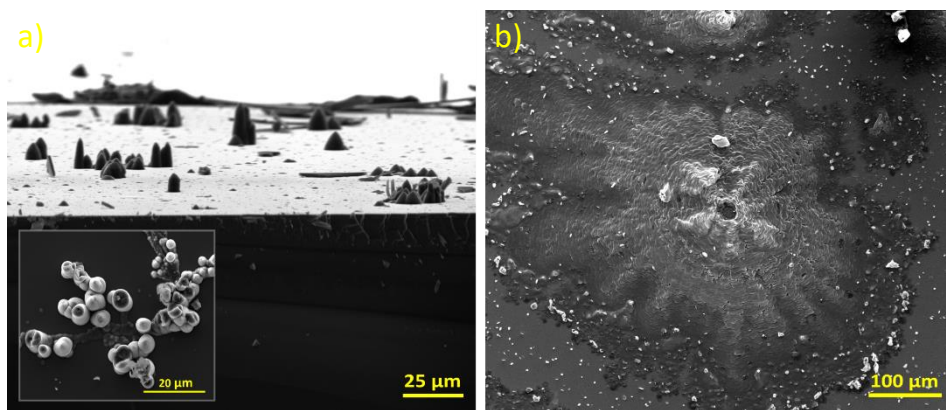


Figure 5.5: SEM images of LiPON thin films after two weeks of air-exposure a) top-view and cross-section (inset graph) of LiPON_75, and b) top-view of LiPON_0.

It is very important to avoid any pinholes or cracks in the electrolyte since they can lead to short-circuiting of the battery. Therefore, the samples once deposited were introduced in an air-sensitive transfer arm and were stored in an inert atmosphere glove box (O_2 and H_2O concentration below 0.1 ppms).

5.4.2. Structural characterization

For the crystallographic structure study, the XRD diffractograms were collected in the 10° to 65° 2θ range with a step size of 0.02° 2θ . These data confirmed the expected amorphous nature of the LiPON thin films prepared in this work (**Figure 5.6**). Only those peaks related to the silicon substrate and Kapton film used for sample protection during the measurement (see reference substrate in black) were observed for all the samples. Meanwhile, no peaks associated with electrolyte crystallinity could be identified, confirming the amorphousness of the LiPON film. This statement is in line with the reported literature on LiPON thin

film layers deposited by RF magnetron sputtering.^[13,14] It is worth noting the presence of orthorhombic SiO₂ (ref. COD 4110502),^[15] identified at 10.6°, 12.8°, 15.1°, and 18.9° 2θ that has been formed during deposition, as these are not detected in the bare Si substrate. In any case, the SiO₂ formation would be associated with the use of Si as substrate and would not be present when moving to the functional SS substrate.

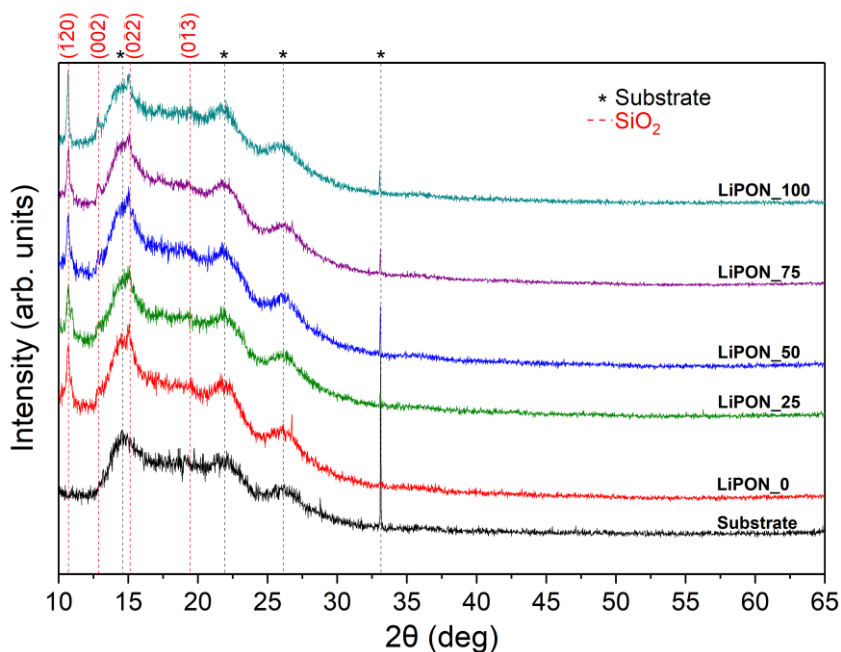


Figure 5.6: XRD patterns for all LiPON samples. Black and red dashed lines correspond to substrate and SiO₂ phase, respectively.

5.4.3. Ionic conductivity

The in-plane ionic conductivity of the thin films was measured by EIS using a two-probe method. 6 x 1 mm and 440 nm-thick electrical copper contacts were deposited on the surface of the sample by DC magnetron sputtering using a shadow mask (**Figure 5.7**). These contacts were grown using a Cu target biased at 2.27 W·cm⁻². A total of 44 sccms of Ar flow-rate were leaked in the process chamber while keeping a constant working pressure of 7.8·10⁻³ mbar during the sputtering process that lasted 0.5 h.

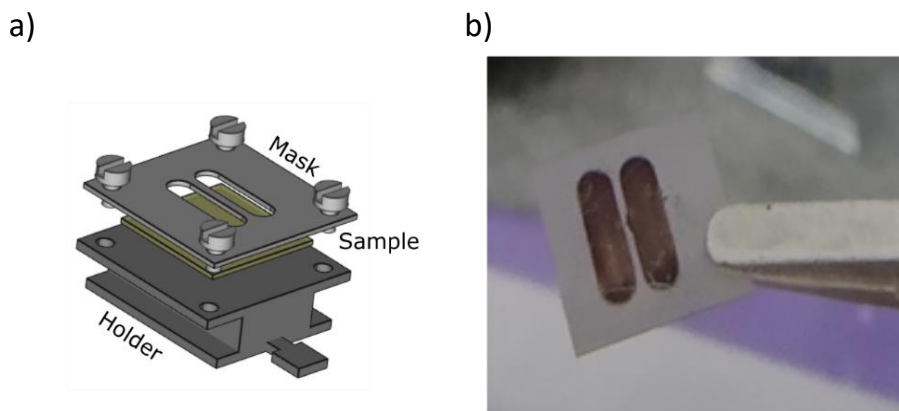


Figure 5.7: Cu deposition on LiPON samples a) drawing of sample holder and mask arrangement, and b) image of the deposited Cu contacts.

As mentioned in the experimental methods chapter, the ionic conductivity can be determined from the resistance of the material, in a selected frequency range, applying **Equation 2.11** ($\sigma=d/(R \cdot L \cdot t)$).^[16] For the implementation of the EIS measurements, a Linkam HFS600E-PB4 stage was used. The experiment was carried out with the help of a Biologic EC-Lab potentiostat in a frequency range from 7 MHz to 100 mHz, with 10 points per decade and a sinus amplitude of 20 mV. The initial measurements were performed at room temperature (RT) in a controlled Ar atmosphere within the chamber.

Figure 5.8a shows the schematic illustration of the setup for the electrical measurement of the film samples, including the dimensions and layout of the Cu contacts (note that **equation 2.11** depends directly on these values). Nyquist plots obtained from a LiPON₁₀₀ film at RT are shown in **Figure 5.8b**. At high frequencies, positive values of imaginary impedance were always obtained, which is usually ascribed to artifacts associated to the measuring setup, including cables-induced inductances. Following that, the expected behavior associated to a resistor in series to an RC element (resistor-capacitor in parallel) was difficult to assess at mid-to-low frequencies. The measuring error at this low temperature was considerably high; note the scattering observed in the measured values, as well as the high resistance values obtained, in the order of 10 MΩ. This evidenced the need of higher temperatures for a proper analysis of the LiPON ionic conductivity.

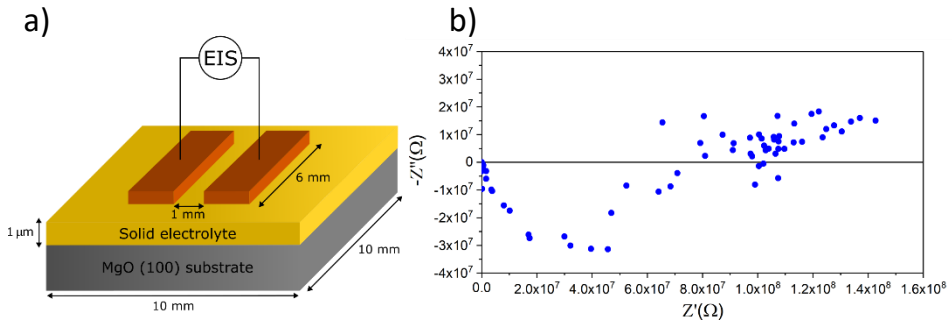


Figure 5.8: a) Schematic illustration of the setup for the electrical measurement of the film samples, and b) Nyquist plots obtained for a LiPON₁₀₀ film at RT.

The impedance measurements were performed at temperatures of $100\ ^\circ\text{C}$, $150\ ^\circ\text{C}$, $200\ ^\circ\text{C}$, and $250\ ^\circ\text{C}$ in a chamber with controlled Ar atmosphere. Nyquist plots obtained for a LiPON₁₀₀ film at different temperatures are reproduced in **Figure 5.9** (the $100\ ^\circ\text{C}$ has not been graphed to show the other plots with better resolution). As it can be observed, the quality of measurements was clearly improved at higher temperatures compared to the RT results.

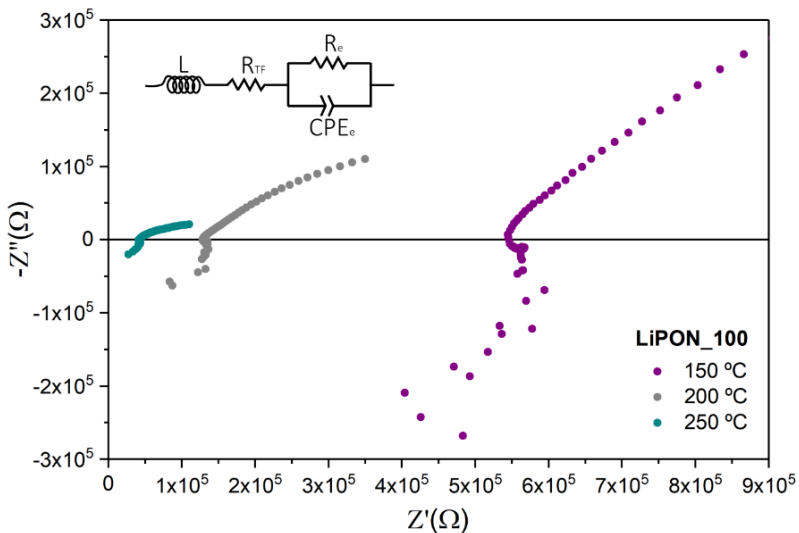


Figure 5.9: Obtained electrochemical impedance spectra of LiPON₁₀₀ thin film electrolyte at $150\ ^\circ\text{C}$, $200\ ^\circ\text{C}$, and $250\ ^\circ\text{C}$, along with the used equivalent circuit.

Again, a setup-associated inductance (L) was always observed at high frequencies followed by a resistive contribution (R_{TF}), in series to a (R_e - CPE_e) contribution at lower frequencies (see the corresponding equivalent circuit in the figure inset).

The series resistance R_{TF} is interpreted as the ohmic resistance associated with the Li^+ conduction through the thin film, whereas the low-frequency contribution is associated with electrode-related phenomena. Moreover, note that the expected electronic resistance associated with contacts and cables, incorporated in the R_{TF} contribution, is much lower than that associated with the Li^+ mobility and can thus be neglected.

The temperature dependence of the electrolyte resistivity is widely studied in the reported literature,^[17,18] being a thermally activated conduction mechanism that follows the Arrhenius equation, **equation 5.1**.^[19,20]

$$\sigma = \frac{\sigma_0}{T} e^{-Ea/K \cdot T} \tag{5.1}$$

Where σ_0 is the pre-exponential factor related to the number of charge carriers, T is the temperature in Kelvin, k is the Boltzmann constant, and Ea is the activation energy of the diffusion.

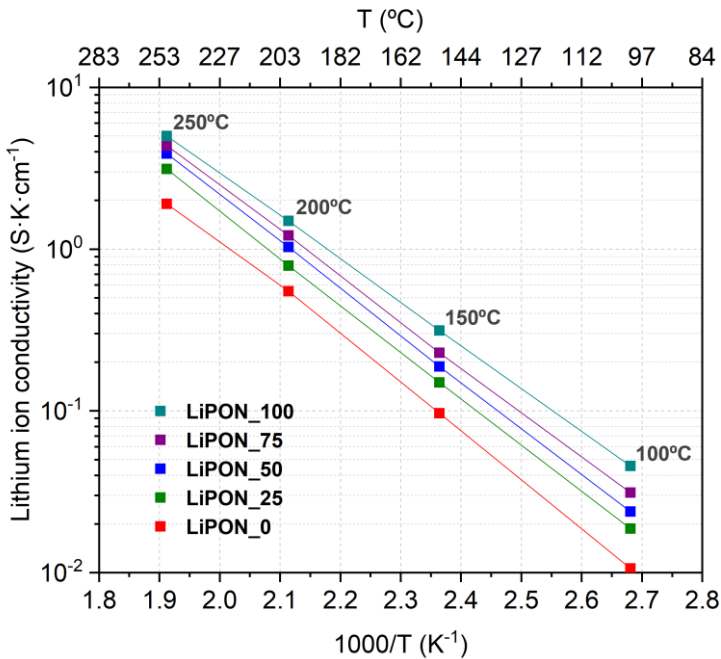


Figure 5.10: Arrhenius plots of the ionic conductivity of LiPON_0, LiPON_50 and LiPON_100 glasses.

Figure 5.10 includes the Arrhenius representation the ionic conductivity calculated from the measured impedance at different temperatures, for the five samples under study. Two clear observations can be drawn from this figure. First,

the ionic conductivity of LiPON significantly increases with the incorporation of nitrogen, reaching a maximum value of $9.56 \cdot 10^{-2} \text{ S}\cdot\text{cm}^{-1}$ at 250 °C for the LiPON_100 film. Second, the activation energy is slightly reduced, from 0.585 eV to 0.530 eV for the LiPON_0 and 100, respectively (see **Table 5.2**). These results match well with previous observations in literature, since N substitution in the Li_3PO_4 glass structure seems to reduce the non-bridging vs bridging P-O bonds ratio, favoring the Li^+ hopping through the LiPON network.^[7,21] Also, from a processing perspective, the results suggest that an N_2 -saturated background pressure during sputtering deposition is preferred for the incorporation of the optimum amount of N in the LiPON system.

The ionic conductivity at room temperature was then estimated by extrapolating the obtained fittings for the five different films, assuming no phase change and pure Arrhenius behavior^[22] from RT to the measuring temperature range, up to 250 °C. The obtained values are summarized in **Table 5.2**, together with the measured conductivity at 150 °C as well as the activation energy of each sample.

Table 5.2: Ionic conductivity and activation energy of all samples at 150 °C and RT.

	150 °C Ionic Conductivity ($\text{S}\cdot\text{cm}^{-1}$)	RT Ionic Conductivity ($\text{S}\cdot\text{cm}^{-1}$)	Activation Energy (eV)
LiPON_0	$2.28 \cdot 10^{-4}$	$3.84 \cdot 10^{-7}$	0.585
LiPON_25	$3.63 \cdot 10^{-4}$	$7.07 \cdot 10^{-7}$	0.575
LiPON_50	$4.44 \cdot 10^{-4}$	$9.05 \cdot 10^{-7}$	0.572
LiPON_75	$5.63 \cdot 10^{-4}$	$1.35 \cdot 10^{-6}$	0.555
LiPON_100	$7.42 \cdot 10^{-4}$	$2.48 \cdot 10^{-6}$	0.530

As it can be observed in **Table 5.2**, the best performing film, LiPON_100, reaches a conductivity of $2.48 \cdot 10^{-6} \text{ S}\cdot\text{cm}^{-1}$, in good agreement with literature (see *e.g.* Bates et al.^[23] and Fleutot et al.^[7] who measured $\sim 2 \cdot 10^{-6} \text{ S}\cdot\text{cm}^{-1}$ and $\sim 3 \cdot 10^{-6} \text{ S}\cdot\text{cm}^{-1}$, respectively, at 25 °C in films deposited also by sputtering Li_3PO_4 in pure N_2). These results validate, from a Li^+ -ion mobility perspective, the use of LiPON_100 as solid electrolyte in this work.

5.4.4. Analysis of the surface composition

In order to identify any change related to the insertion of nitrogen into the structure, a surface elemental characterization was performed using XPS. In order to make it clearer, this section is focused on the analysis of three of the

deposited samples: Using only Ar (LiPON_0), 50% Ar and 50% N₂ (LiPON_50), and using only N₂ (LiPON_100).

Figure 5.11 shows the XPS spectra of the specific regions corresponding to N 1s, O 1s, P 2p, and Li 1s of the selected samples. All the spectra were acquired using a non-monochromatic Mg K_α X-ray source operated at 100 W and setting the photoelectron analyzer at 0.1 eV of step size and pass energy of 30 eV. The binding energy of all acquired spectra was calibrated using the aliphatic carbon signal which was set at 284.6 eV.

As expected, the major difference between N-containing and N-excluding films becomes visible when analyzing the N 1s region. While the film deposited without N₂ background gas (LiPON_0) shows no peak in this region, the other two samples are characterized by a broad signal that can be resolved with two different components. This matches well with previous reports,^[7,9] and they can be associated with doubly coordinated nitrogen -N= (N_d) and triply coordinated nitrogen -N< (N_t) expected in the LiPON structure, respectively (see **Figure 5.12**). Additionally, a weak peak at higher binding energy (around 403 eV) can be seen, probably corresponding to O-N=O (N_o).^[24] In both cases, N_d presents a more intense signal than the N_t contribution, indicating a relatively higher concentration in the glass structure, being the N_d/N_t ratio about 2.39 for LiPON_50 and 3.42 for LiPON_100. Notably, an increase of doubly coordinated nitrogen is observed when the amount of nitrogen in the system is increased. When comparing the two nitrated samples, namely LiPON_50 and LiPON_100, a clear shift towards lower binding energies can be observed when increasing N content. This way, the doubly coordinated nitrogen shifts from 397.14 eV in the case of LiPON_50 to 396.80 eV in the case of LiPON_100, while the less intense triply bonded nitrogen contribution shifts from 398.76 eV to 398.46 eV. N_o also presents a similar shift, from 402.97 eV for LiPON_50 to 402.90 eV for LiPON_100. This shift can be associated with a decrease of the surface charge load associated with the electro-insulating nature of these oxides.^[25]

The analysis of the O 1s spectrum has been carried out using the model proposed by Brow et al.^[26] The main contribution at lower binding energies (*ca.* 533 eV) corresponds to the non-bridging oxygen (O_{NB}), whereas the shoulder located at higher binding energies (around 531 eV) is corresponding to bridging oxygen (O_B). As described in the literature,^[3,27] the first contribution could be interpreted as the sum of two types of non-bridging oxygens present in lithium phosphate oxide and oxynitride structures, P=O and P-O⁻...Li⁺. Nevertheless, the difficulty of distinguishing these bonds leads us to treat them as a single resonant pair.

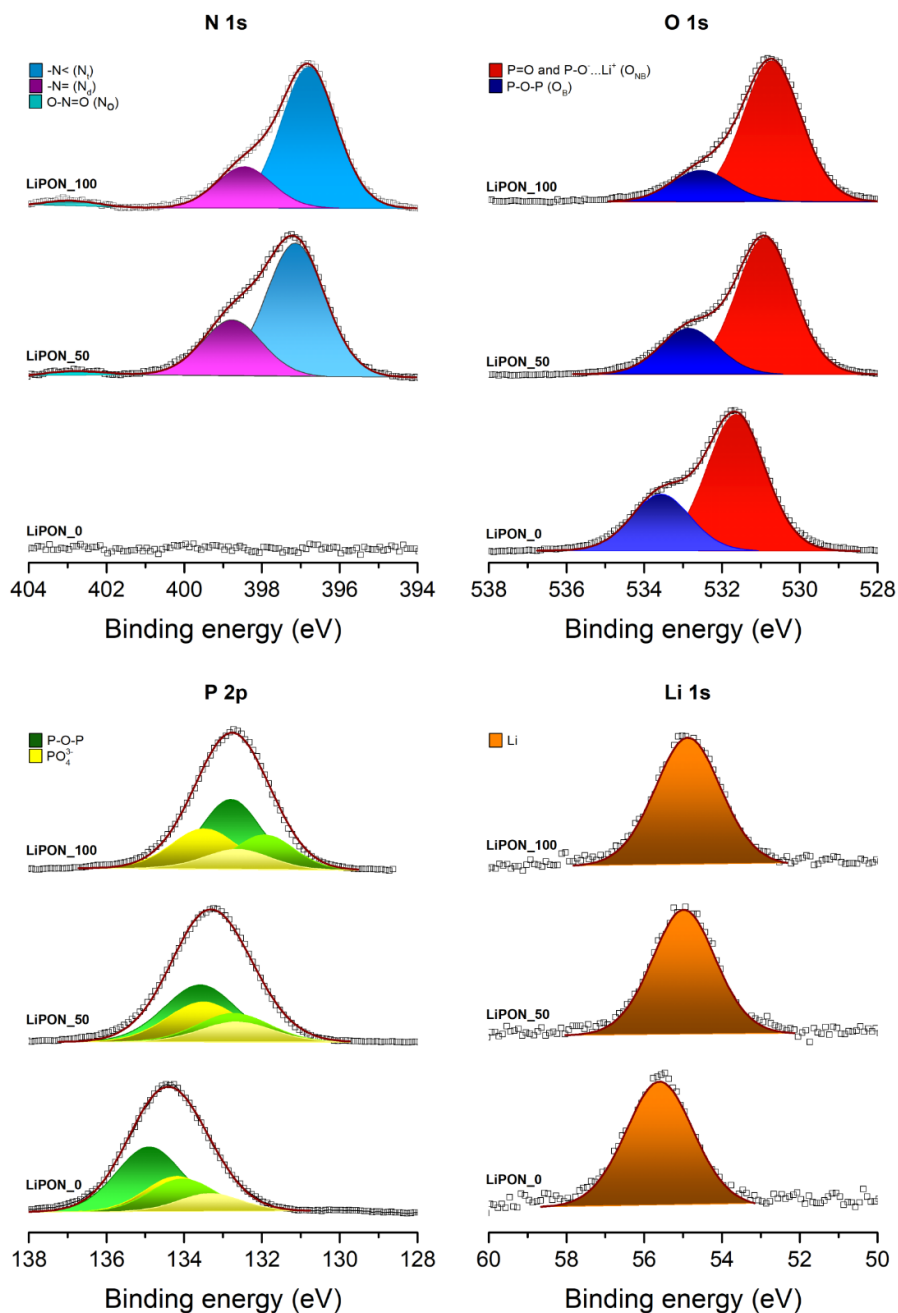


Figure 5.11: XPS profiles deconvolution of the regions N 1s, O 1s, P 2p, and Li 1s for LiPON_0, LiPON_50 and LiPON_100 samples. Note that the ordinate axis which corresponds to the normalized photoelectron intensity in arb. units have not been incorporated in the graph for a better visualization.

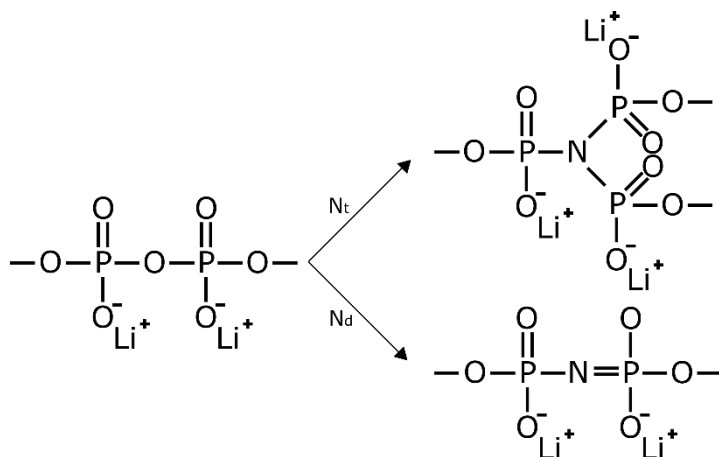


Figure 5.12: Partial structure of nitride Li_3PO_4 thin film glass with the incorporation of $-\text{N}<$ and $-\text{N}=\text{}$.

Like the above-mentioned case, introducing nitrogen into the system entails a slight displacement towards low binding energies for both the non-bridging ($533.57 > 532.84 > 532.54$ eV for LiPON_0, LiPON_50 and LiPON_100, respectively) and bridging ($531.64 > 530.90 > 530.72$ eV) oxygens. Similarly, as the nitrogen is inserted in the phosphate base glass, the area of O_B decreases in relation to that of O_{NB} . In the sample LiPON_0, the $\text{O}_B/\text{O}_{\text{NB}}$ ratio is 0.42, close to the theoretical ratio of 0.50 for a metaphosphate glass,^[26] while with 50% of nitrogen the ratio is reduced to 0.33 and with 100% finally to 0.22. In order to provide a theoretical estimation of the efficiency of nitrogen incorporation in the LiPON structure, two structural models will be used. The first one is related to the specific region of O 1s and was proposed by Brow and co-workers,^[3,26] **Equation 5.2.**

$$\frac{O_B}{O_{\text{NB}}} = \frac{1-3z_i/4}{1/y_0-3z_i/4} \quad (5.2)$$

Where y_0 is the $\text{O}_B/\text{O}_{\text{NB}}$ ratio for the non-nitrided sample (LiPON_0) and z_i is the ratio N/P of the nitrided sample under consideration. In this model, it is assumed that nitrogen has no preference in replacing either bridging or non-bridging oxygens, *i.e.* equal numbers of these species are replaced during nitridation.

The second model, proposed by Marchand and co-workers,^[27] relates the amount of doubly coordinated nitrogen (N_d) and triply coordinated nitrogen (N_t) in the sample under consideration with the amounts of non-bridging oxygen (O_{NB}) and bridging oxygen (O_B), based on the substitution of 3O^{2-} by 2N^{3-} , **Equation 5.3.**

$$\frac{N_d}{N_t} = \frac{O_{BN} + (1/2)OB}{(3/2)OB} \quad (5.3)$$

Table 5.3 collects the obtained experimental ratios of O_B/O_{NB} as well as N_d/N_t and compares them with the expected theoretical values of the analyzed samples. As it can be observed, the values obtained from the theoretical models for nitrated LiPON_50 and LiPON_100 films match well with the experimental ones, suggesting efficient nitrogen incorporation into the films for both cases.

Table 5.3: Experimental and theoretical ratios of lithium phosphate oxide and oxynitride glasses.

	O_B/O_{NB}	N_d/N_t	$(O_B/O_{NB})_{\text{Theoretical}}^{[26]}$	$(N_d/N_t)_{\text{Theoretical}}^{[27]}$
LiPON_0	0.42	-	-	-
LiPON_50	0.33	2.39	0.29	2.32
LiPON_100	0.22	3.42	0.18	3.33

A quasi-symmetrical spectrum was obtained in the specific region of P 2p for the three films as can be seen in the **Figure 2.11**, with no shape evolution upon nitration. The corresponding peaks could be fitted with two doublet components, with spin-orbit splitting around 0.89 eV between $2p_{3/2}$ and $2p_{1/2}$. The first species at lower binding energy could be related to a PO_4^{3-} tetrahedral environment, whereas the second doublet could correspond to a P–O–P.^[7] The shift, however, is larger than those found for the other elements and is believed to be due to the replacement of P–O bonds by P–N bonds. Reducing the average ionic charge on the phosphorus ions results in a decrease in the binding energy.^[7,26] Thus, as nitrogen is inserted, the P-O-P doublet will tend to decrease more the binding energies ($2p_{1/2}$ peaks located at $134.04 > 132.73 > 131.93$ eV for LiPON_0, LiPON_50 and LiPON_100, respectively) than PO_4^{3-} species ($133.34 > 132.65 > 132.62$ eV), being mostly attributed to the electro-insulating nature of the system in the latter doublet case.

Figure 5.13 shows the quantitative evolution of the O/P and N/P ratios with nitrogen incorporation, calculated from the sum of their respective areas. As can be observed, the oxygen content decreases with the introduction of nitrogen (from 4.98 to 2.81), and vice versa in the case of nitrogen content (from 0 to 0.92). This matches well with the expected behavior, the O/P and N/P values obtained by Fleutot et al.^[7] ranges from 4.3 to 3.0 and from 0 to 1, respectively. And thus, it confirms the successful substitution of oxygen by nitrogen in the system, as commented before.

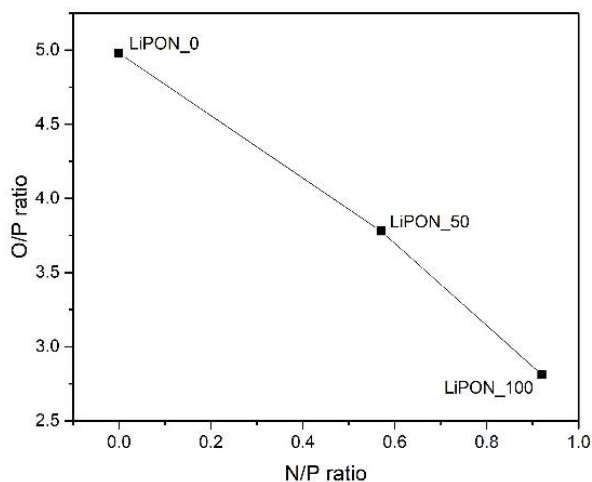


Figure 5.13: Quantitative evolution of O/P and N/P ratios with nitrogen incorporation.

Finally, looking back to **Figure 5.11**, similarly to the previous case, Li 1s spectra show a quasi-symmetrical shape. They are analyzed with a single lithium element, suffering in turn from the displacement observed in the previous cases, $55.60 > 54.98 > 54.88$ eV for LiPON_0, LiPON_50, and LiPON_100, respectively.

5.5. Conclusions

In this chapter, we successfully deposited LiPON thin films by RF magnetron sputtering varying the concentration of Ar and N₂ process gases in order to study the role of N₂ in the structure.

All the deposited films presented a smooth and highly dense structure with no signs of crystallization. Only small differences could be appreciated in the morphology related to the introduction of the N₂. While the surface of the sample deposited only with argon is granulated, a smoother surface was obtained with increasing nitrogen content.

The reflections observed in the XRD data correspond to the substrate, the formed SiO₂ secondary phase, and the Kapton protection used for the measurement. Therefore, the absence of LiPON-related peaks confirmed the expected amorphous nature of the thin films prepared in this work.

The ionic conductivity at RT was estimated for the five different films, assuming no phase change and pure Arrhenius behavior from RT to the measuring temperature range, up to 250 °C. Irrespective of the analyzed temperatures, all samples significantly increase their ionic conductivity with the incorporation of

nitrogen, reaching a maximum value of $9.56 \cdot 10^{-2} \text{ Scm}^{-1}$ at $250 \text{ }^\circ\text{C}$ for the LiPON_100 film. This sample achieves the higher ionic conductivity at RT, $2.48 \cdot 10^{-6} \text{ S}\cdot\text{cm}^{-1}$. On the contrary, the activation energy slightly reduces its value with the incorporation of nitrogen, ranging from 0.585 eV to 0.530 eV for the LiPON_0 and 100, respectively. These results suggest that an N_2 -saturated background pressure during sputtering deposition is preferred for the incorporation of the optimum amount of N in the LiPON system.

For a more in-depth analysis of the impact of N_2 , elemental analysis was performed by XPS. As expected, differences were observed with nitrogen insertion, particularly in the N 1s spectra. While the film deposited without N_2 background gas (LiPON_0) shows no peak in this region, the other two samples are characterized by a broad signal that can be resolved with N_d and N_t components. The behavior of these two components along with the oxygen components (O_B and O_{NB}) for nitrated LiPON_50 and LiPON_100 samples match well with the proposed O-substitution theoretical models, suggesting efficient nitrogen incorporation. In a similar way, it can be concluded by using the N/P and O/P ratios that the oxygen content decreases with the introduction of N_2 , and vice versa in the case of nitrogen content.

The next step to be taken, as the ideal $\text{N}_2\%$ was already determined, is to deposit the LiPON_100 on the LNMO/SS tandem and the final implementation of the all-solid-state thin film high voltage battery.

References in Chapter 5

- [1] N. J. Dudney, *J. Power Sources* 2000, *89*, 176.
- [2] J. B. Bates, N. J. Dudney, G. R. Gruzalski, R. A. Zuhr, A. Choudhury, C. F. Luck, J. D. Robertson, *Solid State Ionics* 1992, *53–56*, 647.
- [3] B. Wang, B. S. Kwak, B. C. Sales, J. B. Bates, *J. Non. Cryst. Solids* 1995, *183*, 297.
- [4] N. J. Dudney, B. J. Neudecker, *Curr. Opin. Solid State Mater. Sci.* 1999, *4*, 479.
- [5] C. H. Choi, W. I. Cho, B. W. Cho, H. S. Kim, Y. S. Yoon, Y. S. Tak, *Electrochem. Solid-State Lett.* 2002, *5*, 14.
- [6] H. Y. Park, S. C. Nam, Y. C. Lim, K. G. Choi, K. C. Lee, G. B. Park, S. R. Lee, H. P. Kim, S. B. Cho, *J. Electroceramics* 2006, *17*, 1023.
- [7] B. Fleutot, B. Pecquenard, H. Martinez, M. Letellier, A. Levasseur, *Solid State Ionics* 2011, *186*, 29.
- [8] J. Rikarte Ormazabal, Doctoral Thesis, Surfaces & Interphases in Thin-Film & Conventional Li-Ion Batteries, Euskal Herriko Unibertsitatea, 2019.
- [9] Y. Su, J. Falgenhauer, A. Polity, T. Leichtweiß, A. Kronenberger, J. Obel, S. Zhou, D. Schlettwein, J. Janek, B. K. Meyer, *Solid State Ionics* 2015, *282*, 63.
- [10] N. Suzuki, T. Inaba, T. Shiga, *Thin Solid Films* 2012, *520*, 1821.
- [11] Y. Chen, Z. Tang, S. Yang, Y. Wang, D. Chu, *Mater. Technol.* 2015, *30*, A58.
- [12] A. G. Belous, O. I. V'Yunov, L. L. Kovalenko, O. Bohnke, C. Bohnke, *Russ. J. Electrochem.* 2014, *50*, 523.
- [13] C. S. Nimisha, K. Y. Rao, G. Venkatesh, G. M. Rao, N. Munichandraiah, *Thin Solid Films* 2011, *519*, 3401.
- [14] Z. Hu, D. Li, K. Xie, *Bull. Mater. Sci.* 2008, *31*, 681.
- [15] A. Cantín, A. Corma, M. J. Diaz-Cabanas, J. L. Jordá, M. Moliner, *J. Am. Chem. Soc.* 2006, *128*, 4216.

- [16] K. R. Cooper, *ECS Trans.* 2011, *41*, 1371.
- [17] D. Li, Z. Ma, J. Xu, Y. Li, K. Xie, *Mater. Lett.* 2014, *134*, 237.
- [18] S. Jacke, J. Song, L. Dimesso, J. Brötz, D. Becker, W. Jaegermann, *J. Power Sources* 2011, *196*, 6911.
- [19] L. Le Van-Jodin, F. Ducroquet, F. Sabary, I. Chevalier, *Solid State Ionics* 2013, *253*, 151.
- [20] L. Meabe Iturbe, Doctoral Thesis, Innovative Polycarbonates for Lithium Conducting Polymer Electrolytes, Euskal Herriko Unibertsitatea, 2019.
- [21] N. Mascaraque, J. L. Fierro, A. Durán, F. Muñoz, *Solid State Ionics* 2013, *233*, 73.
- [22] L. Li, X. Xue, S. Liu, H. Zhou, *Ionics (Kiel)*. 2017, *23*, 1451.
- [23] J. B. Bates, N. J. Dudney, G. R. Gruzalski, R. A. Zuhr, A. Choudhury, C. F. Luck, J. D. Robertson, *J. Power Sources* 1993, *43*, 103.
- [24] T. Pichonat, C. Lethien, N. Tiercelin, S. Godey, E. Pichonat, P. Roussel, M. Colmont, P. A. Rolland, *Mater. Chem. Phys.* 2010, *123*, 231.
- [25] M. A. Carrillo Solano, M. Dussauze, P. Vinatier, L. Croguennec, E. I. Kamitsos, R. Hausbrand, W. Jaegermann, *Ionics (Kiel)*. 2016, *22*, 471.
- [26] R. K. Brow, M. R. Reidmeyer, D. E. Day, *J. Non. Cryst. Solids* 1988, *99*, 178.
- [27] R. Marchand, D. Agliz, L. Boukbir, A. Quemerais, *J. Non. Cryst. Solids* 1988, *103*, 35.

Chapter 6

All solid-state high voltage thin film battery

6.1. Introduction

The all solid-state thin film microbattery can be defined as a stack of thin film battery components that are sequentially deposited with the desired geometry following a layer-by-layer fashion. It was in 1994 when Bates and co-workers developed and patented a thin film microbattery fabricated by magnetron sputtering at ORNL.^[1] Notably, this coating technique is still nowadays one of the most used method for processing thin-film components. Its suitability and reliability to work with almost any type of material (conductor/insulator, crystalline/amorphous) has been demonstrated in the fabrication of different components of the battery: in positive electrodes such as LiMn_2O_4 ,^[2] LiCoO_2 ,^[3] and LiFePO_4 ;^[4] in amorphous $\text{Li}_2\text{PO}_2\text{N}$ ^[5] and garnet-structure like $\text{Li}_7\text{La}_3\text{Zr}_2\text{O}_{12}$ ^[6] solid electrolytes; in negative electrodes as $\text{Li}_4\text{Ti}_5\text{O}_{12}$,^[7] and SnO_2 ,^[8] and for metallic current collectors such as Ag, Cu or Al.^[9] This is evidenced in the previous chapters by the success in depositing the positive electrode (LNMO) and the solid electrolyte (LiPON).

In this thesis, we have opted for the integration of lithium as the battery anode due to its high theoretical specific capacity and the lowest negative electrochemical potential.^[10,11] Being up to the challenge of the increasing demands of a new generation of high energy density, long-lasting powering devices which out-perform the widespread Li-ion battery technology.^[12,13]

However, the poor interconnection of the solid-solid electrode-electrolyte interface is often cited as the main limitation for full exploitation of the electrochemical properties of the electroactive materials.^[10] The poor adherence generated by discontinuities at the interface results in limited diffusion paths of Li ions.^[14] Moreover, the appearance of detrimental reaction products at the battery inner interfaces, predominantly between Li metal and the solid electrolyte, is usually behind the high internal resistance of the cell that ultimately reduces the cell performance.^[15] In this regard, it is worth mentioning that low interface resistance in solid-state thin film batteries with LMNO electrode and Li₃PO₄ electrolyte has already been demonstrated. However, the Li metal-solid electrolyte interface is still an open question.^[16]

6.2. Main objectives of the chapter

This chapter characterizes the last missing battery component: the anode. Once all components have been analyzed separately, the focus was placed on the building up of a thin film ASSB. The battery is comprised of a high voltage cathode LNMO, a ceramic electrolyte, LiPON (both deposited by magnetron sputtering), and a Li anode (thermally evaporated). All them sequentially deposited on the SS substrate, starting with the cathode. In particular, the study emphasized on the characterization of the battery electrochemical performance.

6.3. Lithium anode

The selected anode was deposited at *CIC energiGUNE* by thermal evaporation using metallic crucibles that contained the evaporation material.^[17] During the deposition, a circular shadow mask with a centered 12 mm diameter hole was used (**Figure 6.1a**), the same surface area as LNMO. Before the lithium deposition, the evaporation chamber was evacuated down to a base pressure below $1 \cdot 10^{-8}$ mbar, the substrate-to-crucible distance was set at 50 mm, and a current of 12 A was applied to the metallic crucible that contains the lithium. During the deposition, a working pressure of $5 \cdot 10^{-8}$ mbar was maintained for a total of 24 h of processing (~ 1 μm thick thin film). **Figure 6.1b** shows the aspect of lithium once deposited.

For the transport and handling of the air-sensitive samples, air-tight transfer arms and inert atmosphere glove box (Ar filled, with H₂O and O₂ concentrations below 0.1 ppm) were used.

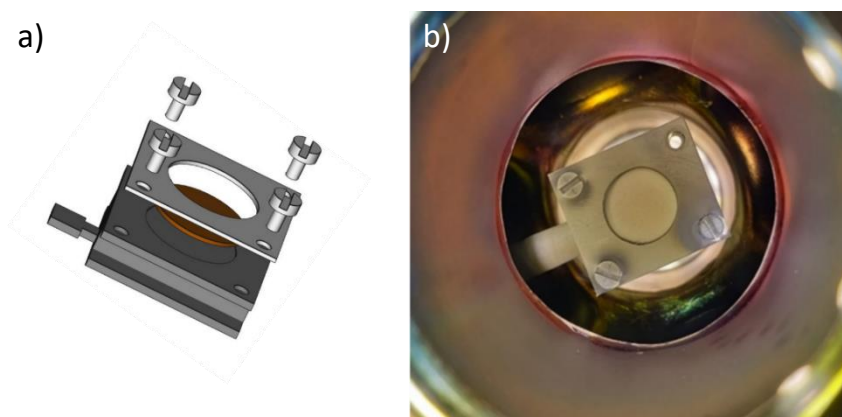


Figure 6.1: a) Concentric 12 mm hole-mask used for lithium deposition, b) as-deposited lithium in the thermal evaporator.

6.3.1 Characterization of the evaporated lithium anode

Prior to the assembly of a full cell with all components, the evaporated lithium thin films were characterized. In this section, we focused on the study of its morphological, elemental, and electrochemical properties.

Morphological and compositional characterization

Figure 6.2 shows the top view SEM image of the evaporated lithium on SS substrate. The film presented a granulated and highly dense structure. The lithium surface roughness is induced by the SS substrate, as well as the black spots, which correspond to traces of alumina used during substrate processing.

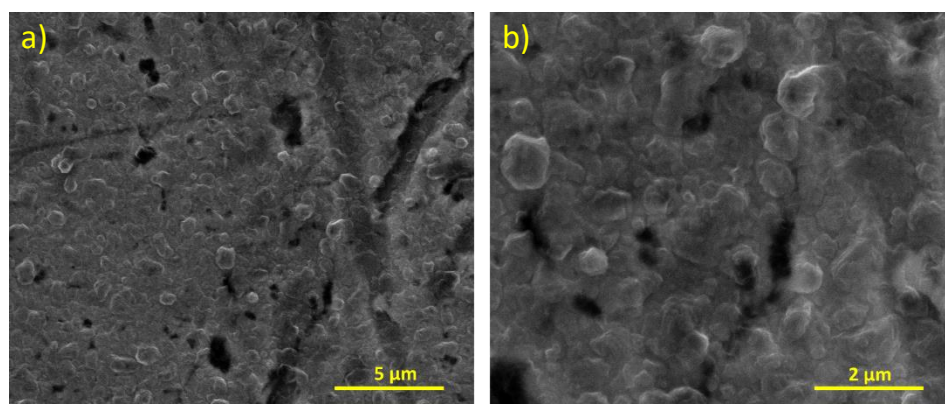


Figure 6.2: Top view SEM images of the evaporated lithium on SS substrate sample, performed at different magnifications, a) 12000x and b) 30000x.

In order to validate the viability of the thermal evaporation process, the elemental characterization of the as-deposited lithium was carried out using XPS, with a non-monochromatic Mg K_{α} source operated at 100 W. **Figure 6.3** shows the survey spectrum, along with the Li 1s, O 1s and C 1s regions acquired with higher resolution. The atomic concentration values were calculated from the areas of each element in the survey (considering the corresponding relative sensitive factor and the equipment transmission function). Looking at these atomic concentration values, it can be concluded that the layer practically consists of lithium (49.9% of the normalized atomic concentration), oxygen (37.9%) and, with lower concentration, carbon (7.5%). Besides the adventitious carbon and surface oxides, some fluorine traces were also detected. Because of its low atomic concentration (4.7%), this cross-contamination is probably coming from the Viton gaskets used in the XPS chamber. It is conceivable that the surface mainly consists of oxides and carbonate species. This is confirmed in the O 1s and C 1s regions, where Li_2CO_3 and $\text{Li}_2\text{O}/\text{Li}_2\text{O}_2$ appear. Based on these deconvolutions, it is also possible to determine the different species that are usually overlapping in the Li 1s region. These include LiOH , Li_2CO_3 , $\text{Li}_2\text{O}/\text{Li}_2\text{O}_2$, LiF , and to a significantly lesser extent Li^0 . All contaminants resulting from the reaction of Li with traces of O_2 , CO_2 , F and H_2O even when not exposed to air.

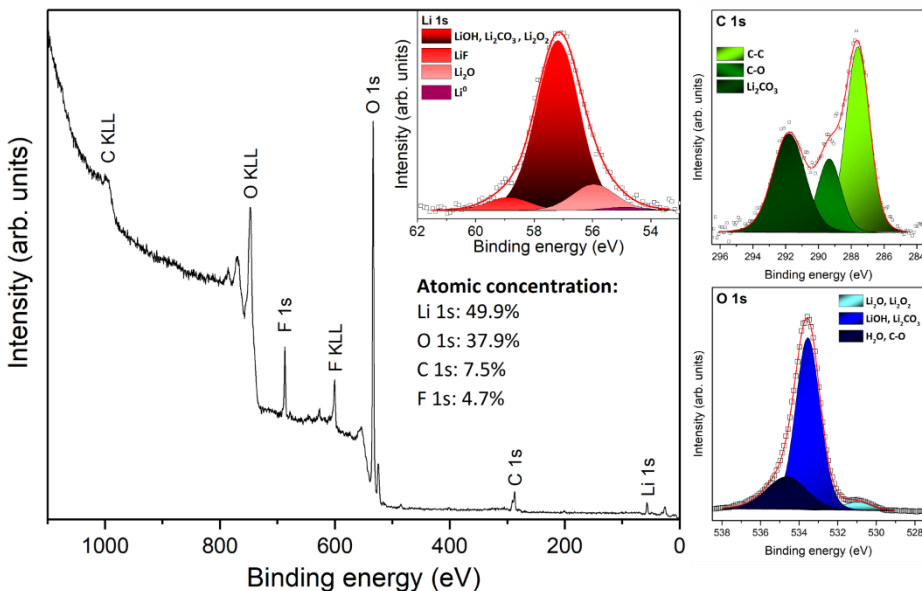


Figure 6.3: XPS survey spectra, Li 1s (inset graph), C 1s, and O 1s regions of the evaporated lithium deposited on SS substrate (Mg K_{α} source). The normalized surface atomic concentration is also shown in the figure.

Electrochemical characterization

For the electrochemical analysis, the lithium was evaporated on SS substrate (using 14 mm \emptyset mask) and was mounted in an air-tight CR2032 coin cell against the already characterized LNMO thin film and with a 1 M of LiPF_6 in EC:DMC (1:1, v/v) liquid electrolyte in a glass fiber as separator (*i.e.* same test performed in Chapter 3, but instead of using lithium foil, evaporated lithium was used).

Figure 6.4 shows the rate capability and the corresponding CE of the evaporated lithium in the range from C/20 to C, and back to C/20. It is worth mentioning that, in this case, we opted for slower C-rates, typically used for solid-state electrolytes.^[18,19] At C/20 the discharge specific capacity was $113.9 \text{ mAh}\cdot\text{g}^{-1}$, like the lithium foil case ($119.0 \text{ mAh}\cdot\text{g}^{-1}$ at C/10), indicating that, at low C-rates, the Li-ion insertion through the LNMO does not depend on the used anode. At C/10 and C/5, the capacity retention observed was 91.6% and 85.0%, respectively. However, as the C-rate increases to C/2, the discharge specific capacity drops abruptly from $96.9 \text{ mAh}\cdot\text{g}^{-1}$ to $27.1 \text{ mAh}\cdot\text{g}^{-1}$. At 1C, the specific discharge capacity has lost 89.0% of its initial value. Moreover, the initial capacity is not recovered when cycled back to C/20, where only $23.9 \text{ mAh}\cdot\text{g}^{-1}$ are delivered. This value decreases as it cycles at C/20, reaching a value of $9.7 \text{ mAh}\cdot\text{g}^{-1}$ in the 15th cycle at C/20 (cycle 40 in total). The unstable anode-electrolyte interface may be behind the underperformance of the evaporated lithium. The same reactions affecting the lithium foil are also expected for evaporated lithium, but in this case, these reactions can affect the whole thin film.^[17] This reduction of active lithium is also confirmed by the CE evolution, which follows a similar trend as with lithium foil, starting from low efficiency in the first cycles (39.5%) and reaching values $>97\%$ at C/5. At C/2, along with the capacity decay, the CE becomes unstable, remaining at values of 89.9% and 85.5% at the final C/20. Additionally, the non-uniformity of the anode, see **Figure 6.6**, could contribute to this fast degradation. Notwithstanding, the integration of the solid electrolyte is expected to reduce the unwanted reactions between the organic liquid electrolyte and the lithium anode, thus improving its electrochemical performance.

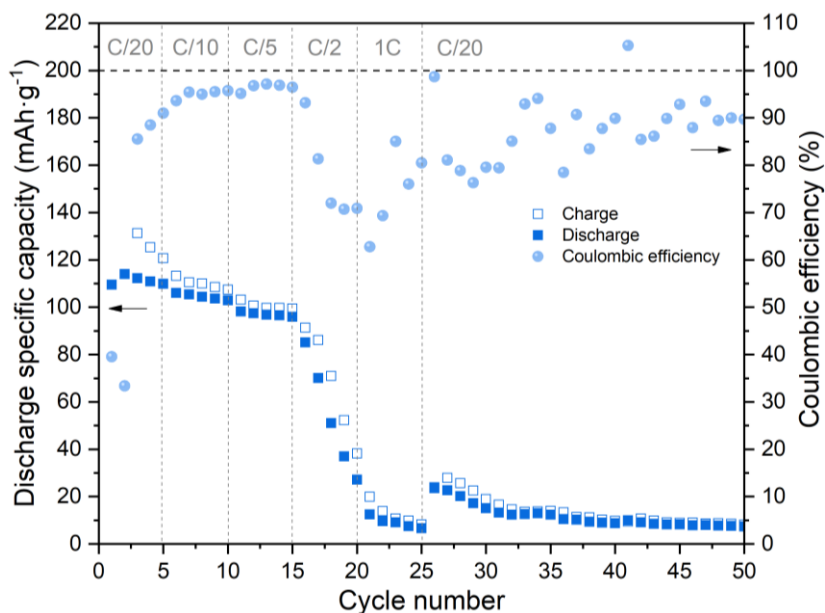


Figure 6.4: Charge (hollow squares), discharge (filled squares) specific capacities, and corresponding coulombic efficiency (filled circle) at different C-rates for LNMO||Li thin film cells assembled with conventional liquid electrolyte and separator.

6.4. Sequential deposition of ASSB components

LNMO thin film cathode was the first component to be deposited at *Tecnalia* by MF-AC magnetron sputtering on top of SS substrates and required a post-annealing process in order to achieve the desired crystallographic structure: 600 °C for 1h in air using a heating ramp of 5 °C·min⁻¹ and cooling down slowly inside the switched-off oven, as described in Chapter 3. As discussed in Chapter 4, the use of CrN-coated SS substrates can prevent the diffusion of Fe from the substrate to the LNMO. For this reason, its implementation in the ASSB is also discussed. In some SS discs, the CrN passivation layer was deposited by DC magnetron sputtering at *Tecnalia*, prior to the deposition of the cathode.

On top of the positive electrode, the LiPON thin film solid electrolyte was deposited at *CIC energiGUNE* by RF magnetron sputtering using pure N₂ as process gas along with a Li₃PO₄ target, as described in Chapter 5. No shadow masks were used for the electrolyte, thus a full coverage of the SS/LNMO or SS/CrN/LNMO sample was needed.

Finally, the lithium thin film was deposited over the solid electrolyte by means of thermal evaporation at *CIC energiGUNE*, as explained above.

In **Figure 6.5a** the ASSB stack once deposited is shown, where each component of the battery can be differentiated. **Figure 6.5b** shows the cross-sectional SEM image of the thin film battery. The whole cathode/electrolyte/anode cell stack has a thickness below 5 μm . This cross-sectioning image was obtained out using silicon as the substrate due to its handling advantages in terms of ease of cleavage (note that this substrate is not the one used for functional ASSB). The uniform 500 nm thick CrN layer with granular morphology was deposited on the Si substrate and would act as a current collector (CC). This interlayer was not present in all the tests performed in this chapter (e.g. in **Figure 6.5a**). On top of the CC, a columnar layer of LNMO with an approximate thickness of 1 μm and, on top of the latter, a smooth surface film of LiPON can also be observed in **Figure 6.5**. The good adhesion between the different defect-free and uniform thin films, with no evidence of any intermediate newly formed layer, can also be inferred from this figure. For the anode, a non-uniform surface was obtained (see also **Figure 6.6**). Besides, the Li thin film was covered with a titanium layer, deposited by DC magnetron sputtering, in order to avoid the interaction/degradation of Li metal under the SEM electron beam.^[17]

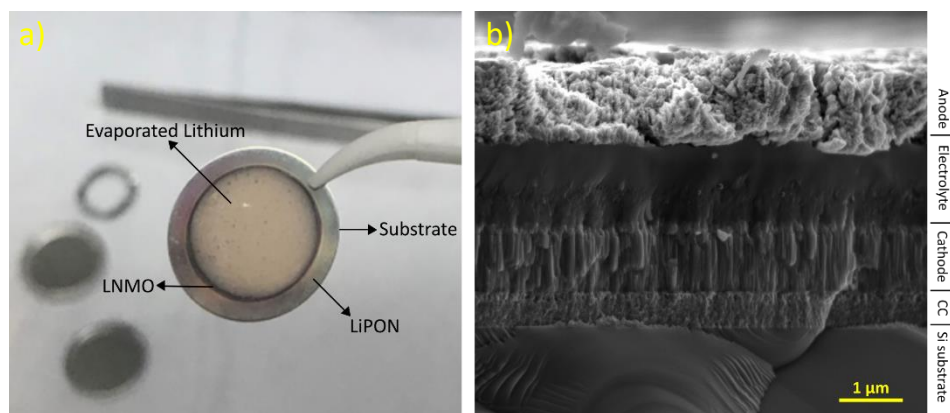


Figure 6.5: a) Appearance of the ASSB full cell. Different layers can be identified depending on the diameter of the masks used to deposit them, b) cross-sectional SEM image of the battery stack deposited on Silicon substrate and with a CrN interlayer used as diffusion barrier and CC.

For the compositional analysis, the EDS mapping results are presented in **Figure 6.6**. The detected elements were Si, Cr, N, Ni, Mn, P, and O (Li cannot be detected with this technique). Silicon signal appears in the bottom part of the image and corresponds to the substrate used for the cross-sectional analysis. The first deposited layer is CrN, where it is easily differentiated by the Cr-rich layer on the top of the Si-wafer. In the intermediate layer, Ni and Mn signals are detected, along with more oxygen, related to the uniform LNMO layer. Some diffusion of

the elements towards the anode can be observed. When lithium is deposited on the surface of the solid electrolyte, it tends to react with each of the elements present (P, O, and N), leading to the formation of Li_3PO_4 , Li_3P , Li_3N , and Li_2O .^[15]

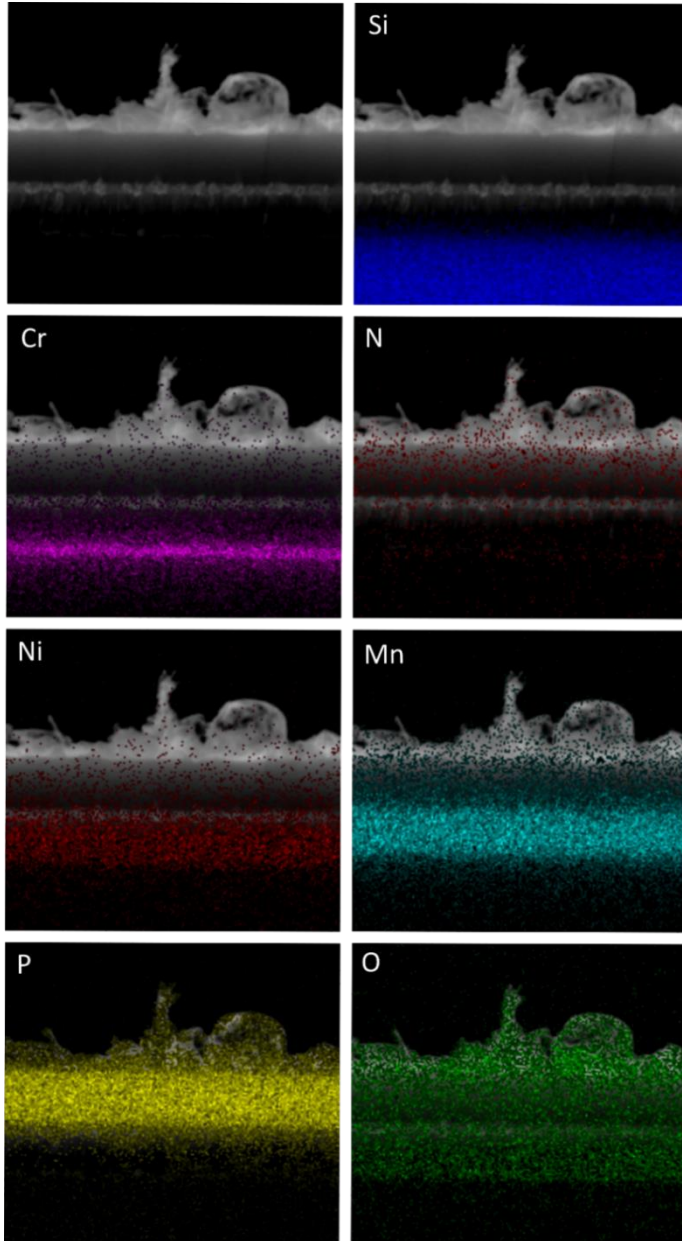


Figure 6.6: EDS mapping images obtained for Si, Cr, N, Ni, Mn, P, and O in the ASSB cross-section analysis.

6.5. Initial tests of the all solid-state thin film battery

Figure 6.7 shows the OCV measurement of the SS/LNMO/LiPON/Evaporated Li sample. Its initial value of 1.7 V vs Li/Li⁺ decreases steadily, reaching a voltage of only 1 V vs Li/Li⁺ after an hour and a half of measurement. This decreasing tendency might be ascribed to internal cell short-circuit. The roughness of the SS substrate may cause pinholes in the coatings, that will ultimately result in the localized electric contact between anode and cathode. Note that the thin films cross sections analyzed in this thesis have so far been deposited on flat silicon substrate. As for the LNMO deposition, the sample holder was not rotated to ensure the maximum deposition rate, however this resulted in regions of the SS substrate that were not properly exposed. Since the electrochemical tests had been performed with liquid electrolytes, this coverage problem was not noticed in the previous phases of this research, and it has only arisen when generating solid-solid interfaces. The inset graph of **Figure 6.7** shows an example of how these pinholes are developed at the bottom of the SS substrate holes.^[20]

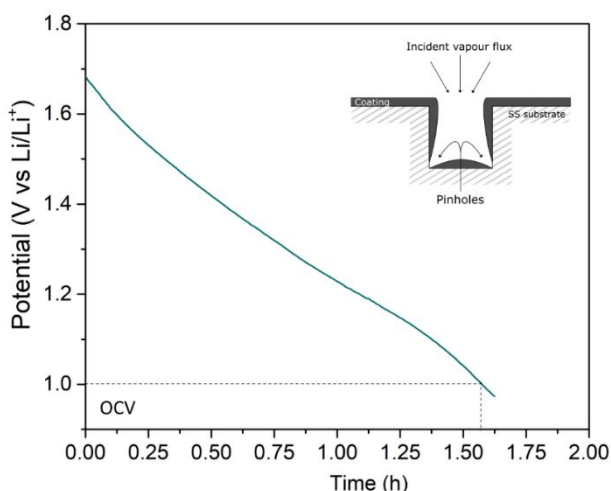


Figure 6.7: OCV measurement of the ASSB. The inset graph illustrates the pinholes formed in the grooves of the SS substrate.

Therefore, it is required to smooth the surface of the substrate to avoid short-circuiting of the battery. For this purpose, the SS substrate surface was hand-polished by using a rotational grinding machine with different SiC polishing foils, and polishing cloths with diamond suspension monocrystalline (DSM) grains.⁶ In **Table 6.1** are listed the values of the roughness average, the maximum height of

⁶ This process was carried out by the *Materialographic Laboratory* (Lab_services Division) at *Tecnalia*.

the profile, and the average maximum height obtained with a stylus profiler. The average roughness is reduced by 94% after polishing, with maximum peaks of 33.35 ± 2.16 nm versus the more than 500 nm of the starting substrate. The mirror polish type finish was achieved.

Table 6.1: Surface roughness parameters, with their corresponding errors, of the polished and non-polished SS substrates. Where R_a is the roughness average, R_t is the maximum height of the profile, and R_z is the average maximum height of the profile.

	R_a (nm)	R_t (nm)	R_z (nm)
Non-polished SS substrate	39.09 ± 2.04	503.33 ± 87.33	302.64 ± 30.21
Polished SS substrate	2.33 ± 0.31	33.35 ± 2.16	22.22 ± 5.79

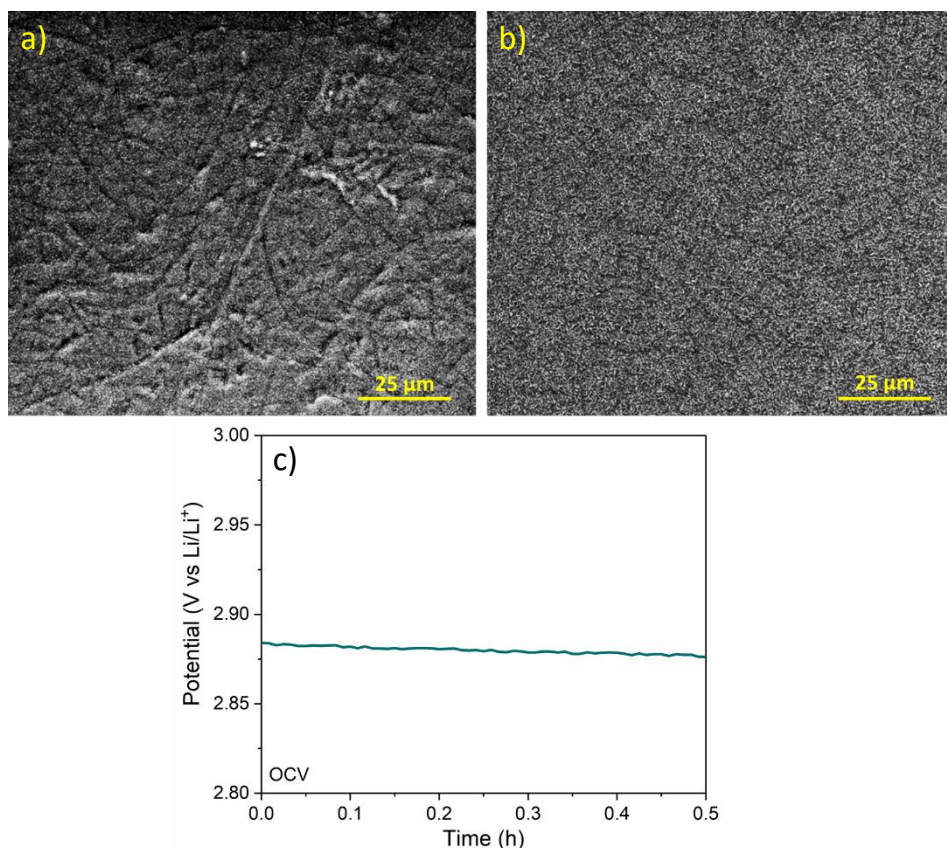


Figure 6.8: Top view SEM image of annealed LNMO deposited on a) non-polished, and b) polished SS substrates. In addition to c) OCV measurement of the polished ASSB.

Figure 6.8 shows the top view SEM image of annealed LNMO on both, a non-polished and a polished SS substrate. As can be seen, the LNMO induces the roughness of the substrate surface (**Figure 6.8a**), being flat after polishing it (**Figure 6.8b**). **Figure 6.8b** presents the OCV measurement of the polished SS/LNMO/LiPON/Evaporated Li sample as a guarantee that no pinholes were developed. In the case of the polished ASSB the OCV kept constant at 2.88 V vs Li/Li⁺ in the measured 30 minutes, while in the case of the non-polished ASSB the OCV decreased by 15.5% of its initial value in the same period of time. Therefore, from now on, all the SS substrates used were polished before the deposition of the battery stack.

6.6. Interface effect study of the all solid-state thin film battery

This section compares the electrochemical performance of the ASSB cells with the conventional lithium foil and with the evaporated lithium described above as anode, in both cases using LNMO and LiPON as cathode and solid electrolyte, respectively. Moreover, the effect of incorporating a drop of liquid electrolyte (1 M of LiPF₆ in EC:DMC, 1:1) in the interface between the solid electrolyte and the lithium foil to improve the contact is also analyzed (note that this implementation does not apply to evaporated lithium). These samples are hereinafter referred to as ASSB_Foil, ASSB_Drop_Foil, and ASSB_ThinFilm (**Figure 6.9**).

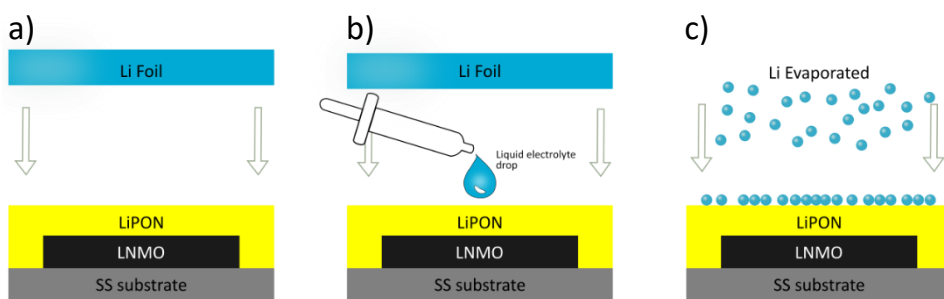


Figure 6.9: Schematic diagrams of the tested cell structures, a) Polished SS Substrate/LNMO/LiPON/Li Foil (ASSB_Foil), b) Polished SS Substrate/LNMO/LiPON/liquid electrolyte drop/Li Foil (ASSB_Drop_Foil), and c) Polished SS Substrate/LNMO/LiPON/Evaporated Li (ASSB_ThinFilm).

The electrochemical characterization of lithium foil ASSBs were carried out in CR2032 coin cells (ASSB_Foil, and ASSB_Drop_Foil), whereas the evaporated lithium ASSB (ASSB_ThinFilm), in order to improve the electrical contacts, was assembled in a pouch cell system, see **Figure 6.10**.

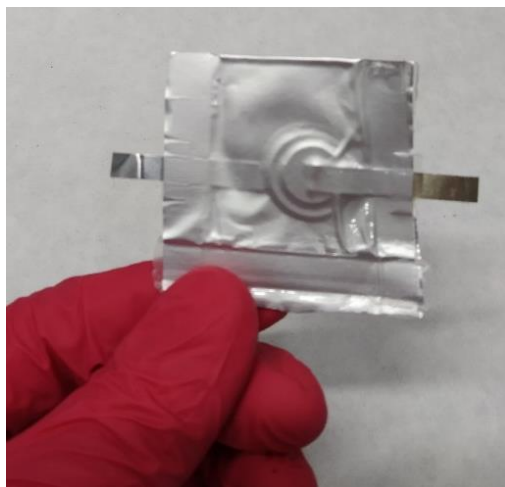


Figure 6.10: Evaporated lithium ASSB pouch cell system (ASSB_ThinFilm). The used electrical contacts were aluminum (cathode) and Nickel (anode).

All cells were connected to a potentiostat, in a laboratory with controlled temperature (25°C), to perform galvanostatic cycling. For these tests, as in previous cases, the voltage window of the cells was set in the 3.5 to 5 V vs Li/Li⁺ range and at current rates in the C/20 to C range.

Figure 6.11 shows the discharge specific capacity and the corresponding CE of ASSB_Foil, ASSB_Drop_Foil, and ASSB_ThinFilm at different C-rates. At C/20, the discharge specific capacity of ASSB_Foil was 33.0 mAh·g⁻¹, much lower than the other two samples. When the drop of liquid electrolyte is introduced, ASSB_Drop_Foil, the initial value at C/20 reached 121.1 mAh·g⁻¹. Although this value decreases rapidly over the first 5 cycles at this C-rate, losing 52.9% of its initial value. This may be due to the irreversible reactions triggered by the liquid electrolyte that occur at the interlayers during the first few cycles, leading to the formation of an SEI. This deterioration was not that evident in the case of thin film, ASSB_ThinFilm, in the fifth cycle only loses 15.6% of its initial value (80.5 mAh·g⁻¹). At C/10, the highest discharge specific capacity value corresponds to ASSB_ThinFilm, 48.8 mAh·g⁻¹, better than the 40.9 mAh·g⁻¹ and 16.4 mAh·g⁻¹ of ASSB_Drop_Foil and ASSB_Foil, respectively. By increasing the C-rate to C/5, the ASSB_ThinFilm, ASSB_Drop_Foil, and ASSB_Foil cells retain 52.5%, 51.8%, and 25.0%, respectively, of their capacities at C/10. Losing at C/2 the 85.2% in the thin film case, the 89.3% in the lithium foil with drop case, and almost 100% in the lithium foil without drop case. Although the capacity reduces in all three cells to zero at 1C, they recover 94.6%, 52.9%, and almost 100% (ASSB_ThinFilm, ASSB_Drop_Foil, and ASSB_Foil, respectively) of their initial specific discharge

capacities upon cycling back to C/20 (note that these values were calculated based on the first cycle at C/20). In the last long cycling at C/20, the discharge specific capacity values (ASSB_ThinFilm > ASSB_Drop_Foil > ASSB_Foil) remain relatively stable. As can be seen, the liquid electrolyte drop enhances ion diffusion between the lithium foil and the LiPON. Even so, the result can be improved by using evaporated lithium. Unfortunately, in cycle 37 the ASSB_ThinFilm begins to lose the specific discharge capacity, short-circuiting the battery. The facility of dendrite formation in evaporated lithium versus the lithium foil may be the cause of this deterioration.^[17]

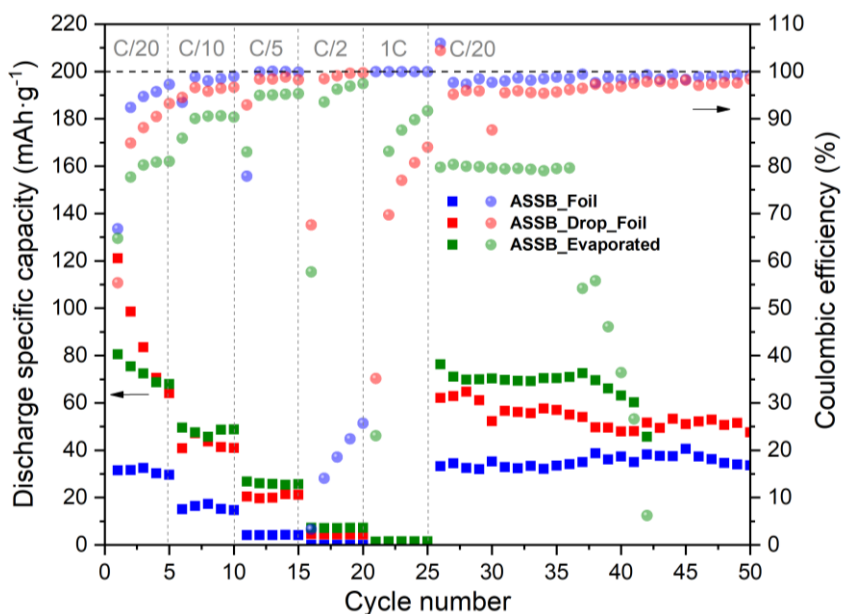


Figure 6.11: Discharge specific capacity (filled squares) and corresponding coulombic efficiency (filled circle) at different C-rates of ASSB_Foil, ASSB_Drop_Foil, and ASSB_ThinFilm.

Regarding the CE, low values were obtained in the first cycle, particularly in the case of the ASSB_Drop_Foil (55.4%, versus 64.8% and 66.8% of ASSB_ThinFilm and ASSB_Foil, respectively). This is ascribed to the liquid electrolyte decomposition process in the anode interface at high voltages occurring predominantly during the charge.^[21] Note that in this case, the CE is not as low as the cells cycled only with liquid electrolyte in the previous chapters (check section 3.6.3). In this case, as shown below (**Figure 6.12a**), there is no evidence of the long non-reversible plateau at around 4 V vs Li/Li⁺ during the first charge attributed to the presence of Fe. The LiPON, besides its role as solid electrolyte, also acts as a cathode protector.^[22,23] For the rest of the cycle, ASSB_Foil shows a CE of 97.31% in the last cycle at C/20, exceeding 98% at C/10 and reaching almost

100% at C/5. While ASSB_Drop_Foil was below 94% in the last cycle at C/20, at C/10 it got 96.6% and 98.8% at C/5. Furthermore, higher CE for the ASSB_Foil than for the ASSB_Drop_Foil was observed during long cycling at C/20, 98.9%, and 97.3%, respectively. In the case of ASSB_ThinFilm, the CE remains below the other two cells, up to 81.0% during the first cycling stage at C/20, reaching a maximum value of 97.4% at high C-rates (C/2) and around 80% during the last long cycling at C/20. A possible explanation for the pronounced difference observed in the CE may likely rely on the high reactivity of the evaporated lithium with the solid electrolyte, in addition, it is expected to trigger more unwanted reactions in the ASSB_ThinFilm than in ASSB_Foil due to the high surface-to-volume ratio, typical of thin film electrodes.

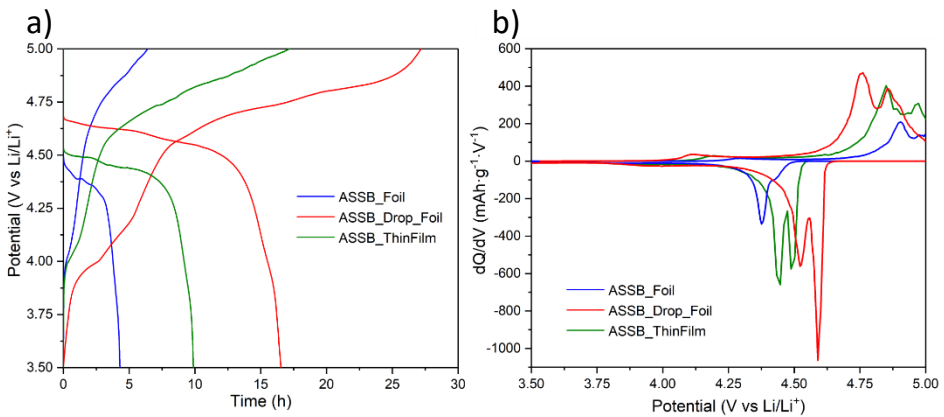


Figure 6.12: a) The First cycle measured at C/20, and b) dQ/dV vs voltage curves derived from the third charge/discharge cycle at C/20 of ASSB_Foil, ASSB_Drop_Foil, and ASSB_ThinFilm cells.

In order to analyze the redox reactions and voltage hysteresis between the charge and discharge of the battery, differential capacity curves (dQ/dV) were used (Figure 6.12b).^[24] In all three cells, during charge (from 3.5 to 5 V vs Li/Li⁺) and discharge (from 5 to 3.5 V vs Li/Li⁺), two high voltage transitions can be distinguished related to the successive oxidation of Ni²⁺ to Ni³⁺ and Ni⁴⁺. In addition, another capacity contribution corresponding to the presence of Mn³⁺ (redox pair Mn^{3+/4+}) at around 4 V vs Li/Li⁺ is also revealed, particularly in ASSB_Drop_Foil cell.^[25] In the case of ASSB_Foil, the nickel-related redox peaks appear during the charge at 4.90 and 4.97 V vs Li/Li⁺ (Ni^{2+/3+} and Ni^{3+/4+}, respectively), while during discharge at 4.37 and 4.43 V vs Li/Li⁺, the second transition being less pronounced than the first one. This voltage difference leads to a hysteresis of 0.53 V, higher than in the other two cells: 0.26 V in the ASSB_Drop_Foil case, and 0.39 V in the ASSB_ThinFilm. These results prove that the liquid electrolyte drop at the interface between the Li foil anode and LiPON

electrolyte can effectively weaken the polarization during charge and discharge, most probably due to an improvement of the lithium-ion migration. Importantly, the evaporated lithium reduces this polarization without the need of introducing any liquid component, thus improving battery safety.

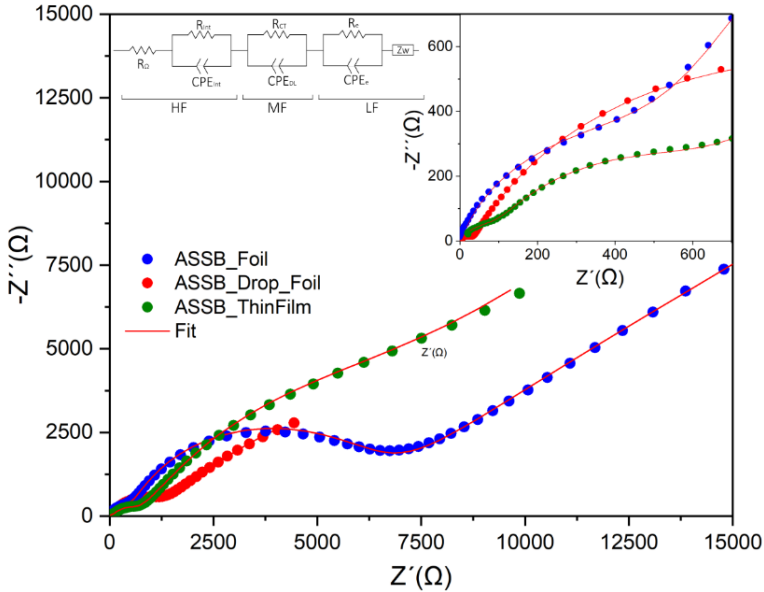


Figure 6.13: Nyquist plots of ASSB_Foil, ASSB_Drop_Foil, and ASSB_ThinFilm, along with the equivalent circuit and the fitted data.

For a better analysis of the internal resistance, the electrochemical impedance spectroscopy (EIS) study was carried out. The data were collected in the 100 mHz – 7 MHz frequency range once the cell was assembled. **Figure 6.13** shows the Nyquist plots of ASSB_Foil, ASSB_Drop_Foil and ASSB_ThinFilm fitted with the proposed equivalent circuit (see inset drawing). For sake of clarity, the zoomed graph is gathered in the right-inset graph. The impedance curves show a semicircle at HF, followed by a more prominent semicircle at MF and ending with a semicircular tail at LF. A possible explanation of the equivalent circuit could be as follows: the HF contribution is originated by the R_{int} - CPE_{int} contribution of interfacial layers in series with the electrolyte ohmic resistance (R_Ω), corresponding to the Li^+ resistance across the electrolyte (the expected electronic resistance associated with contacts and cables was neglected). The semicircle at MF is ascribed to a charge-transfer resistance and a double layer capacitance (R_{CT} - CPE_{DL}), both connected in parallel. And finally, the LF range is ascribed to an RC semicircle associated with bulk electronic resistance (R_e) and charge accumulation capacitance (CPE_e), along with the Warburg diffusion

element (Z_w) that accounts for the sloping line ascribed to the solid-state diffusion of Li^+ in the crystal.

Table 6.1 collects the fitted values for the high-frequency part, which is the one ascribed to the interface. Since different samples are involved, the results have been normalized with respect to the area for resistance (area-specific resistance, ASR) in $\Omega\cdot\text{cm}^2$ and capacity in $\text{F}\cdot\text{cm}^2$.

Table 6.1: Values corresponding to the Interfacial layer ($R_{\text{Int-C}_{\text{Int}}}$) contribution, charge-transfer resistance and a double layer capacitance ($R_{\text{CT-C}_{\text{DL}}}$), and respective time constants ($\tau = R\cdot C$).

	ASSB_Foil	ASSB_Drop_Foil	ASSB_ThinFilm
R_{Int} ($\Omega\cdot\text{cm}^2$)	530.1	30.4	105.4
C_{Int} ($\text{F}\cdot\text{cm}^2$)	$3.2\cdot 10^{-9}$	$2.6\cdot 10^{-8}$	$1.1\cdot 10^{-8}$
τ_{Int} (sec.)	$1.7\cdot 10^{-6}$	$7.8\cdot 10^{-7}$	$1.2\cdot 10^{-6}$
R_{CT} ($\Omega\cdot\text{cm}^2$)	6198.8	1070.0	697.9
C_{DL} ($\text{F}\cdot\text{cm}^2$)	$2.8\cdot 10^{-8}$	$4.3\cdot 10^{-6}$	$1.8\cdot 10^{-7}$
$\tau_{\text{CT-DL}}$ (sec.)	$1.7\cdot 10^{-4}$	$4.6\cdot 10^{-3}$	$1.3\cdot 10^{-4}$

The different RC contributions of the three cells could be compared based on the value of τ . In the first contribution, the three samples are roughly of the same order of magnitude (10^{-6}), suggesting that they correspond to the same interfacial feature. Particularly, they refer to the formation of a passivating layer on the electrode/electrolyte interface. The value of the resistance (R_{Int}) follows this trend for the different cells: $\text{ASSB_Drop_Foil} < \text{ASSB_ThinFilm} \ll \text{ASSB_Foil}$. In the ASSB_Foil, the poor contact between the lithium and the solid electrolyte makes the formation of the SEI layer between them highly resistive. By improving the contact by adding liquid electrolyte the R_{Int} was reduced to $30.4 \Omega\cdot\text{cm}^2$. Resulting in a significant improvement of the SEI. The ASSB_ThinFilm achieved an intermediate resistance, exactly $105.4 \Omega\cdot\text{cm}^2$. The interfacial reactions between evaporated lithium anode and solid electrolyte seem to be more active than those corresponding to the lithium foil. This high reactivity, and the absence of contaminating species that are typically present on the surface of commercial lithium foil, helps the formation of a better SEI, thus improving contact.

The τ of the second semicircle also coincides in all three samples ($\sim 10^{-4}$). Interestingly, a lower charge-transfer resistance was obtained in the case of the evaporated lithium, $697.9 \Omega \cdot \text{cm}^2$ vs $1070.0 \Omega \cdot \text{cm}^2$ and 6198.8 for ASSB_Drop_Foil and ASSB_Foil cells, respectively. This improvement in the pass-through of Li ions could be caused by a larger contact surface. The fact that lithium is deposited directly on the LiPON surface, without the need to introduce a bonding medium, results in a more active area for the reactions. The higher resistance of ASSB_Drop may also be due as well to the fact that there are two media through which the Li must pass (two charge transfers; from Li to liquid and from liquid to LiPON). In the case of ASSB_Foil, the roughness and stiffness of the Li foil makes the active surface smaller, what would be behind the highest charge transfer resistance observed.

For a better interpretation, **Figure 6.14** shows a schematic representation of the anode/electrolyte interface of ASSB_Foil, ASSB_Drop_Foil, and ASSB_ThinFilm. In the ASSB_Foil case, where the lithium foil is placed directly on top of the solid electrolyte, the Li-ion diffusion paths are limited by the voids created in the interface due to the poor adhesion between the Li foil and the LiPON.^[14] When a drop of liquid electrolyte is added, the voids are filled improving their contact although adding an extra media for the Li to cross. In the case of ASSB_ThinFilm, the lithium was evaporated, avoiding possible voids due to the adaptation of the lithium atoms on the roughness of the LiPON.

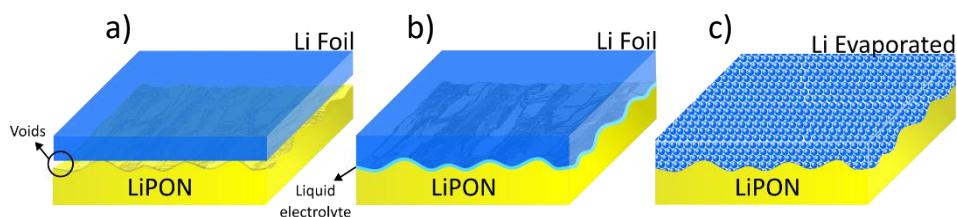


Figure 6.14: Schematic illustration of the anode/solid electrolyte interface of a) ASSB_Foil, b) ASSB_Drop_Foil, and c) ASSB_ThinFilm.

6.6.1. CrN passivation layer in the current collector/cathode interface

As discussed in the previous chapter, the addition of a protective CrN interphase between the current collector and the cathode was required to avoid the interdiffusion of the unwanted Fe during the thermal treatment. So far, the consequences of this diffusion have been analyzed with liquid electrolyte. In this section, instead, the focus is on studying its effects using the solid electrolyte.

Figure 6.15 shows the three samples under study, named from now on as ASSB_Foil_CrN, ASSB_Drop_Foil_CrN, and ASSB_ThinFilm_CrN from left to right.

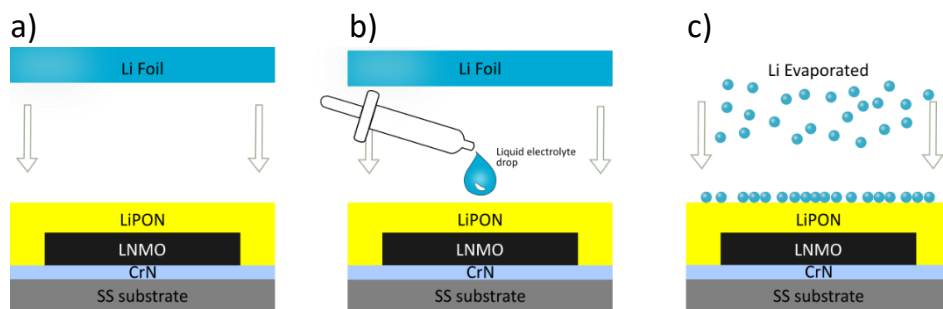


Figure 6.15: Schematic diagrams of the tested cell structures, a) Polished SS Substrate/CrN/LNMO/LiPON/Li Foil (ASSB_Foil_CrN), b) Polished SS Substrate/CrN/LNMO/LiPON/liquid electrolyte drop/Li Foil (ASSB_Drop_Foil_CrN), and c) Polished SS Substrate/CrN/LNMO/LiPON/Evaporated Li (ASSB_ThinFilm_CrN).

The electrochemical results obtained for the studied samples are collected in Figure 6.16. The C-rate study was carried out between C/20 and C, setting the voltage window of the cells in the 3.5 to 5 V vs Li/Li⁺ range. As it can be observed, at the lowest C-rate (C/20), ASSB_Foil_CrN full cell reached a discharge specific capacity of 12.5 mAh·g⁻¹, whereas for ASSB_Drop_Foil_CrN and ASSB_ThinFilm_CrN cells the maximum capacity is increased to 82.8 mAh·g⁻¹ and 73.6 mAh·g⁻¹, respectively. In contrast with the CrN-free cycled cells, the evaporated lithium improves the performance of the lithium foil in the initial cycles at C/20. However, in this case also, due to the initial irreversible reactions, the capacity loses 46.3 and 27.5 % in the first 5 cycles at C/20, respectively. A further decrease of capacity was observed at C/10, where the capacity retention was 18.6%, 25.6%, and 36.0% vs first cycle at C/20, for the ASSB_Foil_CrN, ASSB_Drop_Foil_CrN, and ASSB_ThinFilm_CrN, respectively. At C/5, the specific capacity of ASSB_Foil_CrN drops to zero, remaining around 12 mAh·g⁻¹ the ASSB_Drop_Foil_CrN and ASSB_ThinFilm_CrN. But as for CrN-free cells, they decay also to zero when cycling at 1C. The specific capacity value was recovered by cycling again to C/20, obtaining 12.2, 47.6, and 66.3 mAh·g⁻¹ for ASSB_Foil_CrN, ASSB_Drop_Foil_CrN, and ASSB_ThinFilm_CrN, respectively. It can be concluded that the evaporated lithium cell achieves better electrochemical results than the lithium foil cells. Although, as in the previous case, the capacity of ASSB_ThinFilm_CrN drops when reaching cycle 35. Even so, the implementation of the CrN layer has not been as effective as expected, achieving lower specific capacity values than the free-CrN cells.

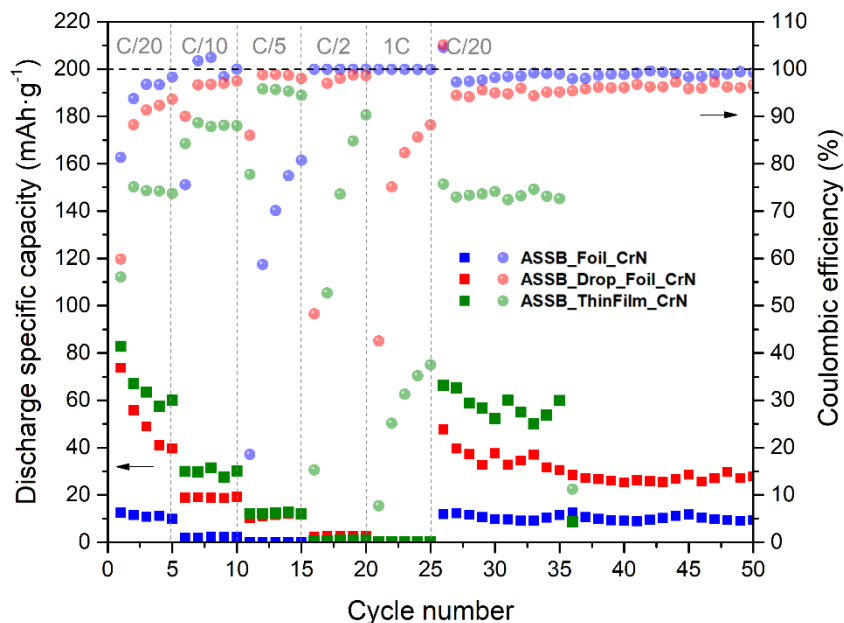


Figure 6.16: Discharge specific capacity (filled squares) and corresponding coulombic efficiency (filled circle) at different C-rates of ASSB_Foil, ASSB_Drop_Foil, and ASSB_ThinFilm.

To better observe the electrochemical performance of each thin film electrode, the corresponding CE of each cycle is also represented in **Figure 6.16**. Low values of CE were obtained in the first cycle of all electrodes, being the ASSB_Drop_Foil_CrN and ASSB_ThinFilm_CrN the electrodes delivering the lowest CE values. As reported in the previous section, they are not as low as in cells cycled with only liquid electrolyte. As there was no liquid electrolyte or a good interfacial contact, the CE of ASSB_Foil_CrN was kept at high values until its capacity drops to zero. Nonetheless, after the initial cycles, the CE of ASSB_Drop_Foil and ASSB_ThinFilm_CrN was increased exceeding 90% at C/5. In general, though a better specific capacity was obtained during the C-rate, the CE of ASSB_ThinFilm_CrN was lower than the other two cells. In the long cycling at C/20 these values differed by almost 20%. This can be ascribed to the high reactivity of the evaporated lithium and its higher surface-to-volume ratio, especially affecting low C-rates.

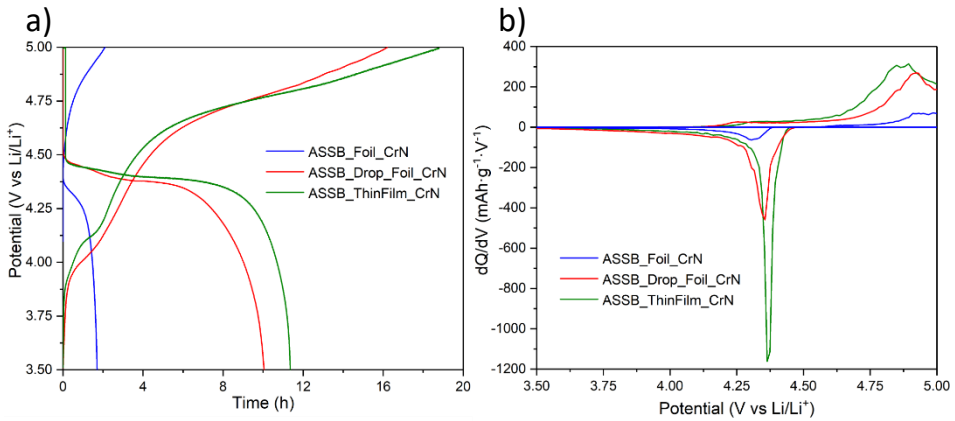


Figure 6.17: a) First cycle measured at C/20, and b) dQ/dV vs voltage curves derived from the third charge/discharge cycle at C/20 of ASSB_Foil_CrN, ASSB_Drop_Foil_CrN, and ASSB_ThinFilm_CrN cells.

Figure 6.17 shows the first cycle and the dQ/dV curves of the three samples under study. As in the previous case, during the charge is no evidence of the long non-reversible plateau at around 4 V vs Li/Li⁺ attributed to the interdiffusion of Fe from the substrate (see **Figure 6.17a**). Therefore, the plateau observed around this voltage in ASSB_ThinFilm_CrN and ASSB_Drop_Foil_CrN correlates with the presence of Mn³⁺.^[25] Furthermore, in these samples is where the plateaus of the redox reactions related to the successive oxidation of Ni²⁺ to Ni³⁺ and Ni⁴⁺ are most readily distinguishable, being these more prominent in the discharge. The voltage difference of these plateaus between charge and discharge leads to hysteresis in the third cycle of 0.67 V, 0.60 V, and 0.49 V for ASSB_Foil_CrN, ASSB_Drop_Foil_CrN, and ASSB_ThinFilm_CrN, respectively. Thus, the cell with the evaporated lithium showed the lowest polarization (see **Figure 6.17b**), improving the migration of ions between electrodes. Even though in this case the evaporated lithium was the highest, it is much lower than the result obtained by ASSB_ThinFilm.

For a better understanding of the effect of the CrN layer, we proceeded to perform the EIS. **Figure 6.18** shows the Nyquist plots of ASSB_Foil_CrN, ASSB_Drop_Foil_CrN, and ASSB_ThinFilm_CrN. In this case, the equivalent circuit proposed in the previous section could also be applied. The fitting result has been incorporated in the same graph.

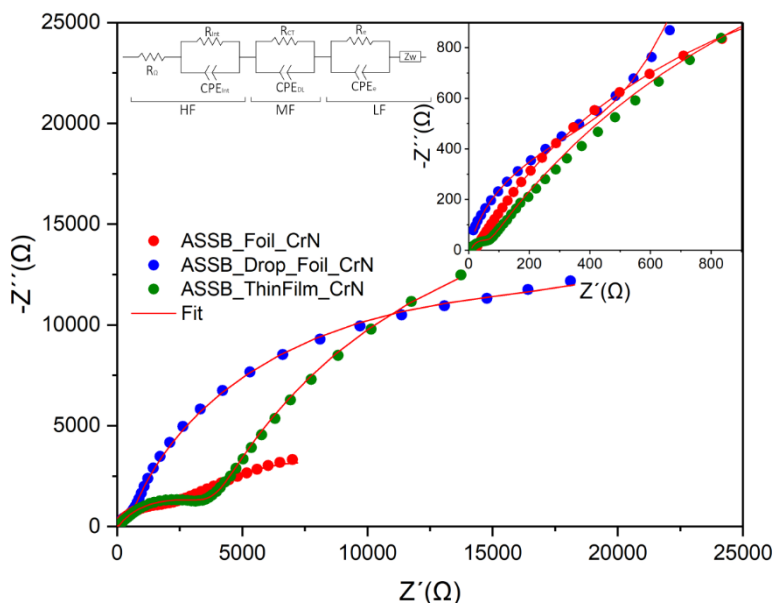


Figure 6.18: Nyquits plots of ASSB_Foil_CrN, ASSB_Drop_Foil_CrN, and ASSB_ThinFilm_CrN, along with the equivalent circuit and the fitted data.

The **Table 6.2** presents the fitted values corresponding to the HF part, typically related to the interfaces. Namely, R_{int} - CPE_{int} contribution of interfacial layers and charge-transfer resistance and a double layer capacitance (R_{CT} - CPE_{DL}).

As in the previous case, both τ (τ_{int} and τ_{CT-DL}) match in the three cases. The first contribution, which is about 10^{-6} , is ascribed to the formation of the SEI on the electrode/electrolyte interface. As it happens with CrN-free cells, the highest resistance corresponds to ASSB_Foil_CrN. The SEI formation is enhanced by inserting a drop of liquid electrolyte, as the resistance is reduced from 509.8 to 25.1 $\Omega \cdot \text{cm}^2$ for ASSB_Foil_CrN and ASSB_Drop_Foil_CrN, respectively. Like the previous case, the ASSB_ThinFilm_CrN achieved an intermediate resistance of 50.1 $\Omega \cdot \text{cm}^2$. It is concluded that the incorporation of the CrN layer does not affect the formation of the SEI. In any case, since it is the same CrN layer, it will affect all three samples in the same way.

The second contribution correspond to a τ of 10^{-3} - 10^{-4} , as in the CrN-free cells. Again, ASSB_Drop_Foil_CrN and ASSB_ThinFilm_CrN show a much lower resistance than ASSB_Foil_CrN, 2410.3, 4422.8, and 19422.4 $\Omega \cdot \text{cm}^2$, respectively. Unexpectedly, a lower charge-transfer resistance was obtained in the case of ASSB_Drop_Foil_CrN than ASSB_ThinFilm_CrN. The discrepancy with previous data may be due to a non-optimized Li deposition process, resulting in fewer

active reactions. The ASSB_ThinFilm_CrN sample was exposed in the glove box much longer than the other samples. During this time, although the atmosphere inside the glove box is controlled, the surface of the high reactive evaporated Li could have oxidized, leading to the increase in resistance. Thus, it is necessary to control the storage time of the evaporated lithium samples inside the glove box.

Tabla 6.2: Values corresponding to the Interfacial layer ($R_{\text{Int-C}_{\text{Int}}}$) contribution, charge-transfer resistance and a double layer capacitance ($R_{\text{CT-C}_{\text{DL}}}$), and respective time constants ($\tau = R \cdot C$).

	ASSB_Foil_CrN	ASSB_Drop_Foil_CrN	ASSB_ThinFilm_CrN
R_{Int} ($\Omega \cdot \text{cm}^2$)	509.8	25.1	50.1
C_{Int} ($\text{F} \cdot \text{cm}^{-2}$)	$2.0 \cdot 10^{-9}$	$1.9 \cdot 10^{-8}$	$2.0 \cdot 10^{-8}$
τ_{Int} (sec.)	$1.0 \cdot 10^{-6}$	$4.8 \cdot 10^{-7}$	$1.0 \cdot 10^{-6}$
R_{CT} ($\Omega \cdot \text{cm}^2$)	19422.4	2410.3	4422.8
C_{DL} ($\text{F} \cdot \text{cm}^{-2}$)	$1.2 \cdot 10^{-8}$	$4.1 \cdot 10^{-6}$	$8.0 \cdot 10^{-7}$
$\tau_{\text{CT-DL}}$ (sec.)	$2.4 \cdot 10^{-4}$	$9.9 \cdot 10^{-3}$	$3.5 \cdot 10^{-3}$

6.7. Conclusions

In this chapter, we successfully build-up a high voltage all solid-state thin film battery by sequentially depositing the optimized thin film battery components. Moreover, the morphological, elemental, and electrochemical characterization of the thermally evaporated lithium anode on stainless steel substrate is also presented.

The dense layers of evaporated lithium showed a granular surface, with an inherent roughness of the substrate. Its high reactivity was evidenced by the presence of traces of lithium carbonates and oxides. Substances formed by contact of O_2 , CO_2 , and H_2O , even without exposure to air. Its electrochemical characterization was carried out cycling a cell with LNMO thin film cathode and commercial organic electrolyte (1 M of LiPF_6 in EC:DMC, 1:1). The specific capacity at initial low C-rates is similar to that of lithium foil cycled in the same way. However, at the end of the test when cycling back at the initial C-rate this value is not recovered. The unstable anode-electrolyte interface and the anode

consumption were behind the underperformance of this system. Despite this, the integration of the solid electrolyte is expected to reduce the unwanted reactions, improving the electrochemical performance.

After building up the cathode and solid electrolyte tandem on a stainless steel substrate, a comparison of the electrochemical performance of the microbattery using evaporated lithium as well as lithium foil was performed. The lack of contact between the lithium foil and the LiPON limits the Li^+ diffusion between the anode and the electrolyte, thereby impairing the electrochemical performance of the cell. The addition of a liquid electrolyte drop provides a homogeneous interface, reaching $121.1 \text{ mAh}\cdot\text{g}^{-1}$ at $C/20$. The low coulombic efficiency of evaporated lithium cell was found to be caused by the inhomogeneous interface between LiPON and Li. However, the high specific capacity achieved, even better than by using liquid electrolyte, proves the outstanding success of this thesis work.

In contrast, the implementation of the CrN interlayer was not as effective as expected. In this case, the substitution of the liquid electrolyte with the solid electrolyte was not hampered by the interdiffusion of Fe from the substrate to the LNMO. The specific capacity achieved with such incorporation was lower, showing a higher internal resistance than for the CrN-free cells.

References in Chapter 6

- [1] J.B.Bates, G.R.Gruzalski, N.J.Dudney, C.F.Luck, X. Yu, *Solid State Ionics* 1994, 70–71, 619.
- [2] K. Jayanth Babu, P. Jeevan Kumar, O. M. Hussain, *Appl. Nanosci.* 2012, 2, 401.
- [3] C. M. Julien, A. Mauger, O. M. Hussain, *Materials (Basel)*. 2019, 12, 1.
- [4] V. A. Sugiawati, F. Vacandio, C. Perrin-Pellegrino, A. Galeyeva, A. P. Kurbatov, T. Djenizian, *Sci. Rep.* 2019, 9, 11172.
- [5] J. B. Bates, N. J. Dudney, G. R. Gruzalski, R. A. Zuhr, A. Choudhury, C. F. Luck, J. D. Robertson, *J. Power Sources* 1993, 43, 103.
- [6] S. Lobe, C. Dellen, M. Finsterbusch, H. G. Gehrke, D. Sebold, C. L. Tsai, S. Uhlenbruck, O. Guillon, *J. Power Sources* 2016, 307, 684.
- [7] A. Kumatani, S. Shiraki, Y. Takagi, T. Suzuki, T. Ohsawa, X. Gao, Y. Ikuhara, T. Hitosugi, *Jpn. J. Appl. Phys.* 2014, 53.
- [8] W. H. Lee, H. C. Son, H. S. Moon, Y. I. Kim, S. H. Sung, J. Y. Kim, J. G. Lee, J. W. Park, *J. Power Sources* 2000, 89, 102.
- [9] X. Q. Tan, J. Y. Liu, J. R. Niu, J. Y. Liu, J. Y. Tian, *Materials (Basel)*. 2018, 11.
- [10] S. Xia, X. Wu, Z. Zhang, Y. Cui, W. Liu, *Chem* 2019, 5, 753.
- [11] Z. Jiang, Q. Han, S. Wang, H. Wang, *ChemElectroChem* 2019, 6, 2970.
- [12] M. Armand, M. Tarascon, *Nature* 2008, 451, 652.
- [13] G. Qian, X. Liao, Y. Zhu, F. Pan, X. Chen, Y. Yang, *ACS Energy Lett.* 2019, 4, 690.
- [14] J. H. Kim, C. Xiao, J. Han, Y. Joo, S. Yagi, H. Kim, *Ceram. Int.* 2020, 46, 9960.
- [15] A. Schwöbel, R. Hausbrand, W. Jaegermann, *Solid State Ionics* 2015, 273, 51.
- [16] H. Kawasoko, S. Shiraki, T. Suzuki, R. Shimizu, T. Hitosugi, *ACS Appl. Mater. Interfaces* 2018, 10, 27498.

- [17] A. Etxebarria Dueñas, Doctoral Thesis, Study of Li Metal Anode Surface: Interaction with Atmospheric Gases and Impact of Impurities in Electrochemistry, Euskal Herriko Unibertsitatea, 2020.
- [18] Y. Iriyama, C. Yada, T. Abe, Z. Ogumi, K. Kikuchi, *Electrochem. commun.* 2006, 8, 1287.
- [19] H. Nakazawa, K. Sano, M. Baba, N. Kumagai, *J. Electrochem. Soc.* 2015, 162, A392.
- [20] P. M. Martin, *Handbook of Deposition Technologies for Films and Coatings*, Elsevier Inc., 2010.
- [21] P. Jehnichen, K. Wedlich, C. Korte, *Sci. Technol. Adv. Mater.* 2019, 20, 1.
- [22] Y. Kim, N. J. Dudney, M. Chi, S. K. Martha, J. Nanda, G. M. Veith, C. Liang, *J. Electrochem. Soc.* 2013, 160, A3113.
- [23] L. Baggetto, R. R. Unocic, N. J. Dudney, G. M. Veith, *J. Power Sources* 2012, 211, 108.
- [24] J. A. Coca, Doctoral Thesis, Electrochemical and Surface Study of Lithium-Rich Transition Metal Oxides Used as Cathodes in Lithium-Ion Batteries, University of Liverpool, 2019.
- [25] M. Gellert, K. I. Gries, J. Zakel, A. Ott, S. Spannenberger, C. Yada, F. Rosciano, K. Volz, B. Roling, *Electrochim. Acta* 2014, 133, 146.

Chapter 7

General conclusions and perspectives

7.1. General conclusions

In this work, an all solid-state high voltage Li-ion thin film battery comprised of an LNMO cathode grown on a stainless steel current collector, a LiPON solid electrolyte, and a lithium anode has been developed. Before assembling up the full cell, each electroactive component of the battery has been characterized separately. The morphological, structural, and electrochemical studies carried out have confirmed the suitability of each component prior to its subsequent implementation in the full cell.

Starting with the cathode, LNMO thin films were prepared using mid-frequency alternating current dual technology-based magnetron sputtering system. The thin films deposited at room temperature on stainless steel substrates were amorphous and electrochemically inactive, so postdeposition annealing at 600 °C was needed to induce the optimum crystallization into the electrochemically active LNMO disordered spinel phase. The phase integrity of the cathode was highly altered after increasing the temperature up to that value. The electrochemical performance of the optimized thin film electrodes, tested using a commercial liquid electrolyte (1 M of LiPF₆ in EC:DMC, 1:1), is found to be in line with previous LNMO films grown using other sputtering techniques. Nonetheless, the optimized thin film electrodes show outstanding cycling performance when compared to conventional cathodes. This highlights the great potential of the LNMO as electroactive material, and maybe any other electroactive material, when there is absence of conductive additives and binders in the electrode formulation. In addition, MF-AC dual magnetron sputtering is

proposed as a top candidate for industrial production of thin film battery components.

Unfortunately, temperature-induced Fe diffusion from the stainless steel substrate towards the LNMO film was found to occur, leading to the formation of Fe₂O₃ secondary phases upon thermal treatment of the LNMO thin film. This is evidenced by the appearance of an irreversible plateau during the first charge in the samples up to 1 μm thick, particularly affecting the performance of the thinnest LNMO films, where the plateau is significantly longer in duration and lower performance is also observed at high C-rates. Moreover, the observation of unwanted secondary phases in the thickest films may limit the maximum effective thickness for real applications, specially at high C-rates. In order to solve the issues originated by the Fe interdiffusion, the addition of Au, CrN, TiN, and Al coatings as diffusion barriers layer was investigated. A successful prevention of the Fe diffusion was attained with CrN overlayers deposited on the stainless steel substrate, which ultimately resulted in an improvement of the first cycle electrochemical performance, where the initial plateau disappeared. A better capacity retention was also observed in the CrN-protected sample at high C-rates. Interestingly, the implementation of the CrN layer had not been as effective as expected with the solid electrolyte, achieving lower specific capacity values and higher internal resistance than the CrN-free cells.

Among the improvements concerning the cycling of the cathode, it is worth mentioning the insertion of a cathode protective coating to minimize possible side reactions at LNMO surface with the liquid electrolyte. The coating of the LNMO with a nanometric Al₂O₃ layer reduces the main irreversible reactions on the surface of the cathode, while considerably increasing the coulombic efficiency. Although the specific capacitance is further decreased due to the low ionic conductivity of the given coating, the Al₂O₃-coated sample outperforms the non-protected LNMO sample cycle life. By changing from liquid to solid electrolyte, side reactions are expected to be minimized, making the application of this protective coating unnecessary.

The LiPON solid electrolyte thin film was deposited on atomically flat Si (100) single crystal substrates by RF magnetron sputtering using different concentrations of Ar and N₂ gases for each process. All the deposited samples show smooth and highly dense structure with no signs of crystallization. The amorphous nature of the LiPON films was confirmed with XRD diffractogram, in where the only visible reflections correspond to substrate related phases and to the protective Kapton film used to cover air sensitive samples. The in-plane ionic conductivity of the thin films was measured by EIS using a two-probe method.

The high measuring error at RT evidenced the need of higher temperatures for a proper analysis of the LiPON ionic conductivity. These measurements were carried out by assuming no phase change and pure Arrhenius behavior from RT to 250 °C. The ionic conductivity increased with temperature, being higher in samples deposited with a larger nitrogen percentage. As a result, the highest ionic conductivity at RT of $2.48 \cdot 10^{-6} \text{ S} \cdot \text{cm}^{-1}$ correspond to the N₂-saturated sputtering process, in good agreement with literature. Regarding the activation energy, the trend was the other way around and it slightly reduced with nitrogen incorporation, ranging from 0.585 eV to 0.530 eV for the only-Ar and only-N₂ processes, respectively. Indicating that a N₂-saturated background pressure is preferred for the incorporation of the optimum amount of N in the LiPON. A better understanding of the elemental composition of each sample was provided by XPS. The main differences were observed in the N 1s spectra. The sample grown only with Ar shows no peaks in this region, whereas the samples grown using a 50:50 or 0:100 concentration of Ar:N₂ in the process gas present a broad signal that can be resolved with N_d and N_t components and, furthermore, is in agreement with the proposed O-substitution theoretical models, hence suggesting efficient nitrogen incorporation.

Lithium anode thin films of approximately 1 μm were prepared by thermal evaporation on a stainless steel substrate. The deposited films presented a granulated and highly dense structure, with a substrate induced roughness. Because of the high reactivity of the evaporated lithium, it was seen by XPS that the surface mainly consists of oxides and carbonate species, *viz.* Li₂CO₃ and Li₂O/Li₂O₂. These contaminants result from the reaction of Li with traces of O₂, CO₂ and H₂O even without being exposed to air. Its electrochemical performance was determined by cycling vs LNMO cathode with liquid electrolyte. It was found that at C/20 the discharge specific capacity was similar to the lithium foil case, *i.e.* 113.9 mAh·g⁻¹. These indicate that at low C-rates the Li-ion insertion in the LNMO does not depend on the used anode. Unfortunately, the low loading of evaporated lithium resulted in low cycle life. In any case, it is a proof of concept of the functionality of lithium thin film anodes.

Finally, the layer-by-layer growth of a monolithic high voltage all solid-state thin film battery by combining the optimized functional films (cathode and electrolyte) was performed. Each component was deposited on a polished stainless steel substrate by using a set of shadow masks that ensured the proper dimensions of the cell components so as to avoid short-circuit. **Figure 7.1** shows the nominal voltage of the assembled high voltage pouch cell system.

To validate the successful implementation of the thin film battery, a comparison of the electrochemical performance of the microbattery using evaporated lithium as well as lithium foil (commonly employed) was done. The lithium foil exhibits poor adherence to the solid electrolyte, requiring the addition of a drop of liquid electrolyte to improve the contact and thus the electrochemical behavior. The performance of the evaporated lithium, grown on top of the rough solid electrolyte, highlights the unnecessary addition of liquid components for achieving high specific capacities. This is a prove of success of this thesis work.

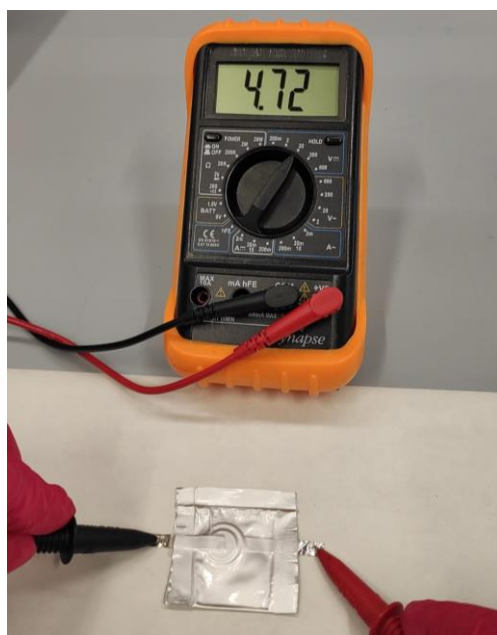


Figure 7.1: Nominal voltage measurement of the pouch cell assembled all solid-state high voltage thin film battery.

7.2. Perspectives

At the laboratory level, among all the different attempts that were made to obtain a functional monolithic all solid-state battery, one stands out: the cell composed of SS/LNMO/LiPON_50/evap. Li that achieved a specific capacity of $100 \text{ mAh}\cdot\text{g}^{-1}$ at $C/10$, reaching almost 100% of CE at relatively high C-rates. This resulted in an energy and volumetric energy densities of $332.9 \text{ Wh}\cdot\text{kg}^{-1}$ and $1212.4 \text{ Wh}\cdot\text{l}^{-1}$, respectively. Values close to the upper limit, or even higher in the case of volumetric energy density, of the estimations made in the first chapter (Table 1.1). The reproducibility of the cell, however, turned out to be a major challenge.

Monitoring and characterizing lithium deposition by thermal evaporation is not straightforward. Its high reactivity means that it must be treated with utmost precaution. Thus, the interface between LiPON and lithium is a key factor for the improvement of the electrochemical properties of the thin film ASSB cells. In order to characterize the evolution of the solid electrolyte/anode interface degradation with increasing ASSB cycle number a study is proposed by combining the air-free FIB/SEM, and the cryo STEM EELS techniques. This will enable the observation of the possible formation and growth of Li dendrites and how Li stripping/plating affects the mechanical stability of the electrolyte over the cycle life of the battery. Moreover, one of the paths to further improve the electrochemical performance could be the insertion of an Al_2O_3 interlayer, minimizing the eventual unwanted reactions and providing a homogeneous interface between LiPON and Li.

Another possible route for improvement could be the substitution of the lithium anode with $\text{Li}_4\text{Ti}_5\text{O}_{12}$ (LTO), often used in ASSBs in combination with LiPON. Our colleague Dr. G. Baraldi has succeeded in depositing a defect-free LTO thin film electrode by means of RF reactive magnetron at room temperature, achieving good electrochemical performance in LTO || Li battery ($83 \mu\text{Ah}\cdot\text{cm}^{-2}\cdot\mu\text{m}^{-1}$ at C/10). The annealing-free battery component processing is a desired requirement for the manufacture of our ASSB. Thus, internal diffusion between the different components of the battery is prevented. Moreover, improved Li-ion diffusion kinetics have been demonstrated in the epitaxial LTO thin films prepared by PLD, displaying even better electrochemical performance than polycrystalline LTO films.

The low specific capacity obtained at high C-rates is also an open discussion. For a better characterization or improvement of the cell, further experiments could be considered by varying the LiPON thickness. The thinnest possible thickness able to avoid short-circuiting would be optimal to enhance the migration of the lithium ions between the electrodes.

In this thesis, a functional ASSB thin film has been grown on a rigid stainless steel substrate. There are stainless steel sheets with a thickness of 0.02 mm that would allow a flexible thin film ASSB. Moreover, the use of masks and selective etching processes allow defining the shape of the functional area of each cell component. Thus, these approaches are likely to increase the range of future applications, such as wearable electronics, autonomous sensors, RFID tags, data smart cards, and in high added-value batteries for aerospace applications, such as satellites.

APPENDIX

A.1 List of abbreviations

AC	Alternating Current
AE	Auger Electrons
arb. Units	Arbitrary units
ASSB	All-Solid-State Batteries
BSE	Backscattered Electrons
CC	Current Collector
CE	Coulombic Efficiency
CMA	Cylindrical Mirror Analyzer
COD	Crystallography Open Database
CPP	Cast Polypropylene
CV	Cyclic Voltammetry
CVD	Chemical Vapor Deposition
DC	Direct Current
DMC	Dimethyl Carbonate
DSM	Diamond Suspension Monocrystalline
EC	Ethylene Carbonate
EDS	Energy-Dispersive X-Ray Spectroscopy
EELS	Electron Energy Loss Spectroscopy
EIS	Electrochemical Impedance Spectroscopy
EM	Electron Microscopy
FAT	Fixed Analyzer Transmission

FEG	Field Emission Gun
FESEM	Field Emission Scanning Electron Microscopy
FRR	Fixed Retard Ratio
HDI	Human Development Index
HF	High Frequency
HIPIMS	High-Power Impulse Magnetron Sputtering
HSA	Hemispherical Electrostatic Analyzer
IMFP	Inelastic Mean Free Path
IOT	Internet of Things
IPS	Infinite Power Solutions
LAGP	$\text{Li}_{1+x}\text{Al}_x\text{GeM}_{2-x}(\text{PO}_4)_3$
LATP	$\text{Li}_{1+x}\text{Al}_x\text{Ti}_{2-x}(\text{PO}_4)_3$
LCMO	LiCoMnO_4
LCO	LiCoO_2
LF	Low frequency
LFPO	LiFePO_4
LIB	Li-ion batteries
LIPON	Lithium Phosphorous Oxynitride
LLTO	$\text{Li}_{3x}\text{La}_{2/3-x}\text{TiO}_3$
LLZO	$\text{Li}_7\text{La}_3\text{Zr}_2\text{O}_{12}$
LMO	LiMn_2O_4
LNMO	$\text{LiMn}_{1.5}\text{Ni}_{0.5}\text{O}_4$
LTO	$\text{Li}_4\text{Ti}_5\text{O}_{12}$
MF	Mid Frequency

MONBASA	Monolithic Batteries for Spaceship Applications
NMC	$\text{Li}(\text{Ni}_x\text{Mn}_y\text{Co}_z)\text{O}_2$
OCV	Open Circuit Voltage
ORNL	Oak Ridge National Laboratory
PA	Polyamide
PDF	Powder Diffraction File Database
PEO	Polyethylene Oxide
PET	Polyethylene Terephthalate
PLD	Pulsed Laser Deposition
PVD	Physical Vapor Deposition
PVDF	Polyvinylidene Fluoride
RF	RadioFrequency
RFID	Radio Frequency Identification
RT	Room Temperature
SE	Secondary Electrons
SEI	Solid Electrolyte Interphase
SEM	Scanning Electron Microscopy
SMA	Spherical Mirror Analyzer
SMT	Surface-Mount Technology
SS	Stainless Steel
STEM	Scanning Transmission Electron Microscopy
SZM	Structure Zones Model
TEM	Transmission Electron Microscopy
UHV	Ultra-High Vacuum Chamber

UN	United Nations
WRI	World Resources Institute
XPS	X-Ray Photoelectron Spectroscopy
XRD	X-Ray Diffraction

A.2 List of contributions

A.2.1 Conferences

- ✚ **Power Our Future 2017.** The 3rd International Forum on Progress and Trends in Battery and Capacitor Technologies.

MONBASA: EU H2020 project on the development of all-solid thin-film batteries for space applications. (**Poster**)

I. Madinabeitia, J. Rikarte, A. Etxebarria, G. Baraldi, A. Llordés, M.A. Muñoz-Márquez, F. Fernández-Carretero, A. García-Luis, V. Bellido-González, A. Zaldívar, S. Tiensuu.

- ✚ **III. IKERGAZTE.** Nazioarteko ikerketa Euskaraz (International Research in Euskera)

Tentsio altuko katodoak geruza meheko litio-ioi baterietarako. (**Oral**)

I. Madinabeitia, J. Rikarte, A. Etxebarria, G. Baraldi, A. Garcia-Luis, F. Fernandez-Carretero, M. A. Muñoz-Marquez.

- ✚ **Power our future 2019.** The 4th International Forum on Progress and Trends in Battery and Capacitor Technologies.

High-voltage $\text{LiNi}_{0.5}\text{Mn}_{1.5}\text{O}_4$ thin film cathode for Lithium-Ion microbatteries. (**Oral**)

I. Madinabeitia, J. Rikarte, G. Baraldi, F. Fernández-Carretero, A. García-Luis, M.A. Muñoz-Márquez.

A.2.2 Publications

- ✚ **AC Magnetron Sputtering: An Industrial Approach for High-Voltage and High-Performance Thin-Film Cathodes for Li-Ion Batteries**

J. Rikarte, I. Madinabeitia, G. Baraldi, F. Fernández-Carretero, V. Bellido-González, A. García-Luis, M. A. Muñoz-Márquez.

Accepted. March 2021 in Advanced Materials Interfaces 8 (10), 2002125
DOI:10.1002/admi.202002125

- ✚ **Growth parameters and diffusion barriers for functional high voltage thin film batteries based on spinel $\text{LiNi}_{0.5}\text{Mn}_{1.5}\text{O}_4$ cathodes**

I. Madinabeitia, J. Rikarte, G. Baraldi, F. Fernández-Carretero, I. Garbayo, A. Garcia-Luis, M. A. Muñoz-Márquez.

Manuscript under revision for ACS Applied Materials & Interfaces Manuscript ID: am-2021-18247a

- ✚ A comparative study of nitrogen doping on $\text{LiNi}_{0.5}\text{Mn}_{1.5}\text{O}_4$ sputtered thin films as high voltage cathode materials for Li-ion batteries

H. Darjazi, I. Madinabeitia, B. Acebedo, F. Fernández-Carretero, A. García-Luis, M. A. Muñoz-Márquez.

Manuscript in preparation.

- ✚ $\text{Li}_4\text{Ti}_5\text{O}_{12}$ thin-film electrodes sputtered on CrN-coated stainless steel substrate for cost-affordable microbatteries

G. Baraldi, I. Madinabeitia, R. Cid, E. Gonzalo, F. Bonilla, F. Fernández Carretero, A. García-Luis, M. A. Muñoz-Márqueza.

Manuscript in preparation.

All solid-state Li-ion batteries present key technological advantages that position them as a promising alternative to State-of-the-Art liquid electrolyte-based batteries, namely a wider electrochemical stability window, low toxicity, and hindered Li dendrite formation. These directly impact on the energy density, environmentally friendliness and safety, respectively. Importantly, all solid-state configurations also allow downscaling the whole battery to micrometric thin film components, paving the way towards the fabrication of compact microbatteries for low power energy supply. In this thesis, an all solid-state high voltage Li-ion thin film battery comprised of $\text{LiNi}_{0.5}\text{Mn}_{1.5}\text{O}_4$ cathode, a LiPON solid electrolyte, and a metallic lithium anode has been developed, supported on high-value stainless steel current collector substrates. Growing parameters, individual film properties and issues related to the internal solid-solid interfaces are deeply analyzed.

